Prediction of the Formation of Adiabatic Shear Bands in High Strength Low Alloy 4340 Steel through Analysis of Grains and Grain Deformation

by

Ioannis Polyzois

A Thesis submitted to the Faculty of Graduate Studies of

The University of Manitoba

In partial fulfilment of the requirements of the degree of

DOCTOR OF PHILOSOPHY

Department of Mechanical and Manufacturing Engineering

University of Manitoba

Winnipeg

ABSTRACT

High strain rate plastic deformation of metals results in the formation of localized zones of severe shear strain known as adiabatic shear bands (ASBs) which are a precursor to shear failure. The formation of ASBs in steel is shown to be a microstructural phenomenon which depends highly on the grain size, shape, and orientation in the microstructure prior to deformation. In this thesis, the formation of adiabatic shear bands (ASBs) in heat treated AISI 4340 steel was studied as a function of prior heat treatment, tempering temperature, testing temperature, and impact momentum using the Direct Impact Hopkinson Pressure Bar (DIHPB). Optical microscopic examination of the microstructure showed that ASBs formed more readily in steel heat treated to have a higher strength and hardness and a smaller initial grain size. Specimens which formed ASBs showed a progressive reorientation and elongation of the grain structure in the direction of maximum shear, followed by the appearance of a refined grain structure at the center of the bands.

Using the stress strain response data in the experimental investigation, a simulation model was developed in Matlab and explicit FEA software ANSYS and LSDYNA to simulate ASB formation in AISI 4340 steel on the microstructural level under high strain rate impact based on the grain size, shape, orientation, and microstructural material property inhomogeneity between the grains and the grain boundaries. The model uses the

Voronoi tessellation to generate prior austenite grains, and generates geometry for the martensite sub-grain lath blocks and a grain boundary geometry in a 2D axi-symmetric area representative of the cross section of the specimens. The model was discretized using the meshless Smooth Particle Hydrodynamics (SPH) method and the Johnson-Cook plasticity model parameters and rupture failure criteria were calculated for all tested heat treatments and simulated against experimental results at various impact momenta. Simulated stress-strain responses matched closely with experimental responses.

Comparing with experimental observations, the grain model provided a good representation of the kinematics of ASB formation on the microstructural level, based on grain size, shape and orientation. Simulation results showed a progressive reorientation and elongation of the grains in the direction of shear. Severe strain localization and ASB formation was shown to nucleate at the grain boundaries of the elongated grains, creating micro-voids, which grew and propagated as micro-cracks through the grains, separating them into smaller sizes. Under continued deformation, the grains would continue to elongate and refine. Final grain size is represented by the smallest cluster of intact SPH particles.

ACKNOWLEDGEMENTS

I wish to convey my sincere appreciation to my advisor, Professor M.N. Bassim, for his continued enthusiasm, valuable guidance, and ongoing support throughout this project.

I would like to extend my gratitude to the other members of my thesis committee, Professors A. Shalaby, I. Telichev, and Y. Luo for their valuable input towards improving my thesis.

I would also like to thank my external examiner Dr. Zhirui Wang for his invaluable feedback and suggestions towards the improvement of my thesis.

A special thanks go to Dr. J. Sorensen for providing access to his chemistry lab at the University of Manitoba and his help in developing the chemical etchants used in the experimental investigation

The financial support provided for this research by The Natural Sciences and Engineering Research Council (NSERC) and the University of Manitoba is greatly acknowledged.

Finally, I would like to extend my heartfelt thanks to my family, and my fiancée Rhanissa Hirawan for their unremitting love, support and encouragement.

TABLE OF CONTENTS

LIST OF FIGURES

LIST OF TABLES

NOMENCLATURE

List of Acronyms

AISI	American Iron and Steel Institute
ASB	Adiabatic Shear Band
ASTM	American Society for Testing and Materials
BCC	Body-Centered Cubic
BCT	Body-Centered Tetragonal
DIHPB	Direct Impact Hopkinson Pressure Bar
DRX	Dynamic Recrystallization
FCC	Face-Centered Cubic
FEA	Finite Element Analysis
GB	Grain Boundary
HSLA	High Strength Low-Alloy
HV	Vickers Hardness
JC	Johnson-Cook (Plasticity Model)
SAE	Society of Automotive Engineers
SPH	Smooth Particle Hydrodynamics

List of Common Symbols

G	Shear modulus
E	Elastic modulus
K	Bulk modulus
ν	Poisson's ratio
b	Burgers vector
α-Fe	Alpha iron (pure iron)
γ-Fe	Gamma iron (austenite)
α'-Fe	Martensite
C_0	Wave speed of sound
L_0	Initial length of specimen
A_0	Initial cross-sectional area of specimen
A	Johnson-Cook yield strength at $\varepsilon = 1$
B	Johnson-Cook strain hardening coefficient
$\bar{\varepsilon}^{pl}$	Equivalent plastic strain
n	Strain hardening coefficient
$\hat{T}$	Non-dimensional homologous temperature
T_m	Melting temperature
T_{ref}	Reference temperature (ambient)
m	Thermal sensitivity parameter

C	Johnson-Cook strain rate sensitivity parameter
$\bar{\dot{\varepsilon}}^{pl}$	Equivalent plastic strain rate
$\dot{\varepsilon}_o$	Johnson-Cook reference strain rate (=1)
D	Johnson-Cook damage parameter
$\bar{\varepsilon}_f^{pl}$	Johnson-Cook failure strain
C_P	Specific heat
χ	Taylor-Quinney coefficient

1. INTRODUCTION

High-strength low-alloy (HSLA) steels have been widely used in structures designed to handle large amounts of stress. These include gears, machine parts, cranes, bridges, naval ships, commercial and military vehicles and aircraft, and armor plates. They belong to a category of alloy steels that provides better mechanical and corrosion resistant properties when compared to plain carbon steels and can be heat-treated to improve toughness while maintaining high strength. However, like all steels, HSLA steels are predisposed to forming adiabatic shear bands (ASBs) when deformed under certain conditions. These adiabatic shear bands are zones of severe shear localization which form under deformation at high-strain rates and large strains and are a precursor to shear failure in metals.

The specific steel under investigation, AISI/SAE 4340 steel, is a medium carbon, high-strength low-alloy steel whose primary constituents are molybdenum for increased hardness and hardenability, as well as nickel and chromium for increased corrosion resistance. It can be heat-treated to impart a wide range of mechanical properties and is commercially available at low cost. Its heat treatability allows it to be a 'prototype' template for the behavior of many HSLA heat treatable steels.

Analyzing the formation of ASBs in metals has been primarily carried out through experimentation under high strain rate deformation at large strains. Experimentation has helped define a relationship between testing conditions, such as deformation strain rate and testing temperature, on ASB formation—classifying ASB formation as being dependent on deformation conditions [1-2]. However, the predisposition of HSLA steel to forming/not forming ASBs is highly dependent on the chemical composition of the constituent alloying elements as well as the phase distribution in the microstructure of the steel prior to deformation, which is controlled directly by its heat treatment [3]. These factors, in turn, control the mechanical properties of the metal. To this end, it can be shown that the formation and properties of ASBs in steel are related directly to its microstructure, and more specifically, the prior austenite grain size, its shape, orientation, and the properties of the sub grain microstructure structure.

1.1 Research Objectives

The main objective of this thesis was to develop a simulation model that could predict the formation of ASBs in steel and describe the microstructural mechanism of their formation based on grain size, shape, orientation, and the inhomogeneous distribution of material properties on the microstructural scale. To this end, the following steps were taken:

1) Conduct an extensive review of the literature to establish the existing mechanisms developed to describe microstructural evolution and ASB formation in metals subject to high strain rate deformation through evaluation of existing mathematical, empirical, and physical-based FEA models used to simulate grain structures, grain deformation and microstructural evolution.
2) Carry out an extensive experimental investigation which included a) high strain rate impact of specimens in order to map out the microstructural evolution, such as grain size, shape, and orientation and formation of ASBs at various heat treatments and testing conditions; b) a microscopic examination of the tested specimens for ASB formation; and c) dynamic stress-strain and hardness tests to examine the evolution of material properties in and around the formation of ASBs and to contribute to the development of the simulation model.
3) Develop a simulation model which can be used to simulate the microstructural mechanism of ASB formation and the evolution of the microstructure of steel under various heat treatments and testing conditions.

1.2 Research Methodology

To meet the research objectives an experimental program was designed to determine the effect of heat treatment temperature, tempering temperature, impact momentum, and testing temperature on the formation of ASBs and microstructural evolution in AISI 4340 steel. Cylindrical steel specimens were impacted using a modified Direct Impact Hopkinson Pressure Bar (DIHPB) and subsequently analyzed under optical microscopy to measure grain size, shape, and orientation in and around the formation of ASBs. Stress-strain data and hardness measurements were taken to correlate the physical properties of the steels with the formation of ASBs and were used in the development of the simulation model for simulating ASB formation on the microstructural scale. To meet the objectives of the experimental investigation, the following parametric variations were selected:

- Type of steel: AISI 4340
- Heat Treatments: (800°C, 900°C, 1000°C)/30mins, oil quenched & tempering at 400°C/90mins and 550°C/90mins, air cooled
- Impact momenta: 30kgm/s, 45kgm/s, 49kgm/s, 52kgm/s
- Testing Temperatures: 20°C, $0.3T_m$ = 428°C

In addition to the experimental investigation, a theoretical investigation was also carried out. This involved the development of a simulation model that can be used to simulate grain deformation behavior and ASB formation in AISI 4340 steel. It accounts for the inhomogeneous physical and geometrical properties of steel at the microscopic level; i.e.

grain size and grain composition, which are dependent on the heat treatment and pre-impact conditions of the metal. The geometry and properties of the material constituents are taken from experimental observations.

The simulation model was developed using MATLAB [4] and explicit dynamics software LSDYNA [5] and represents a 2D axi-symmetric area of grains through the cross section of a specimen. This area is tessellated by randomly oriented prior austenite grains whose initial size is based on the heat treatment temperature. The grain geometries are generated using a Voronoi tessellation [6, 7]. Each grain is further subdivided into geometrical representations of parallel blocks of lath martensite. The size and number of blocks changes with heat treatment and tempering temperatures. The models were meshed using the mesh-free Smooth Particle Hydrodynamics (SPH) formulation [8-10], which allows for large localized deformation. The Johnson-Cook plasticity model parameters [11-13] for each heat treatment were calculated and implemented along with the rupture failure criterion that defines shear failure. The Johnson-Cook plasticity model is an empirical model which defines metal deformation under highs strain rate deformation. The prior austenite grain boundaries were modeled by a thin layer separating the prior austenite grains and assigned physical properties having a higher hardness than the surrounding grains to account for the segregation of hard solute particles to the grain boundaries during heat treatment. The model was impacted using a rigid wall impactor of fixed mass at various initial

velocities. The resulting grain deformation and ASB formation was compared with observations and predictions from experimentation.

1.3 Need for Investigation

Adiabatic shear bands in metals are known to form under deformation at very high strain rates and at large strains and are a precursor to shear failure. There has been a constant push to improve the strength and reliability of metals and alloys for applications ranging from aerospace and military, to medicine and commercial use to reduce or eliminate the formation of ASBs. The formation of ASBs in metals has been extensively studied in the literature [1].

Several mechanisms have been proposed, based on experimental observations, to describe the formation of ASBs showing that they are dependent on the material property composition of the metals or more specifically their microstructure. These mechanisms include a) ASB formation from local material defects or inhomogeneities in the microstructure [14, 15]; b) ASB formation along favorably oriented grains [16]; c) ASB formation by the mechanism of dynamic recrystallization (DRX) [17-26] which is strongly affected by strain rate [27] and is accompanied by grain rotation, alignment and refinement

[24, 27]. Several studies have shown the formation of ultra-fine recrystallized grains within shear bands [18, 28-29].

Several studies have been published on the simulation of ASBs in metals [14, 30-37]. Many of these studies are limited in that they cannot properly simulate strain localization. They predict ASB formation by implementing material defects from which ASBs can form, or define ASB formation by the nucleation and propagation of a crack. The removal of failed elements results in an unrealistic relaxation of the surrounding material and gives a poor indication of the stress and strain distribution through the material.

Recently, some models have been developed to describe the experimentally observed mechanism of grain growth and dynamic recrystallization and grain refinement which include a mechanical subgrain rotation model for copper that accounts for the recrystallized grains observed in ASBs [30]; constitutive modeling of grain refinement due to continuous dynamic recrystallization in aluminum [38]; and a model for static recrystallization and grain growth in austenitic stainless steel during hot torsion at low strain rates [39].

The current research provides a new model that can simulate the microstructural mechanism of ASB formation and grain refinement in AISI 4340 steel, using existing FEA software, for a wide range of heat treatment and testing conditions. The data provided by this model also allows for a complete mapping of the behavior of all high-strength low alloy

steels with a similar composition to that of AISI 4340 steel and can be used to design a steel that leads to the reduction of ASBs while maintaining good mechanical properties.

1.4 Scope of Work

This thesis comprises of five chapters:

- Chapter 1 provides an introduction to the research topic; describes the methodology used to meet the objectives; highlights the need for investigation; and summarizes the shape of the work presented.
- Chapter 2 provides an extensive review of the literature. It starts by providing a background overview of the physical and microstructural properties of metals, starting with a basic understanding of crystalline structures, grains and grain boundaries, and the plastic deformation of metals at the microstructural level based on dislocation theory. An in-depth look into the effects of carbon and alloying elements on the properties of steel, as well as the effect of heat treatment and tempering temperatures on the microstructure of steel are discussed with reference to existing experimental observations in the literature. An overview of existing mechanisms developed to describe the formation of ASBs and resulting

physical properties is also presented. Finally, a background of the finite element theory used in this thesis, and review of current finite element models and methods used to simulate microstructural evolution and ASB formation is given.

- Chapter 3 covers the experimental work. The test method is described and the experimental results from heat treatment and impact testing of the specimens are presented. Optical micrographs of the microstructure at various heat treatments before and after testing are analyzed for the formation of ASBs. Grain sizes, geometry and characteristics are recorded along with stress-strain responses and hardness measurements which contribute to the development of the simulation model.
- Chapter 4 discusses the development of the simulation model used to simulate grain microstructural evolution under deformation and the formation of ASBs. It starts by providing an overview of the model formulation, including a complete mapping of the elastic, Johnson-Cook plasticity, and failure model parameters for all heat treatment temperatures and testing conditions. This is followed by the development of the lath grain model, which is comprised of grain geometry generated using the Voronoi tessellation, discretized using the SPH meshless method, and simulated using the Johnson-Cook model under various testing conditions. Simulation results are presented and simulated stress-strain responses

are compared with experimentation. The initiation and propagation of ASBs is discussed and compared with experimental results.

- Chapter 5 presents an extensive review of the results, comparing the findings between the experimentation and simulations and summarizing the key findings. It also provides a summary of possible future work and recommendations.

2. LITERATURE REVIEW

This chapter provides an overview of the literature. It begins with a discussion of the physical and microstructural properties of metals including a basic understanding of crystalline structures, grains and grain boundaries, and the plastic deformation of metals at the microstructural level based on dislocation theory. Grain size and grain boundary effects on the physical and mechanical properties of metals is also discussed.

An in-depth look into the effects of the heat treatment and tempering temperatures on the microstructure of steel is given with reference to existing experimental observations in the literature. Additionally, currently developed mechanisms for the formation of ASBs in metals is presented followed by a review of current research in the area of microstructural simulation and prediction of ASB formation.

2.1 The Lattice Structure of Metals

When molten metal solidifies, the atoms arrange themselves into definite patterns called crystal structures. The two most common crystal structures in metals are body-centered

cubic (BCC), and face-centered cubic (FCC), which represent the smallest unit of lattice points with the highest symmetry, shown in Fig. 1.

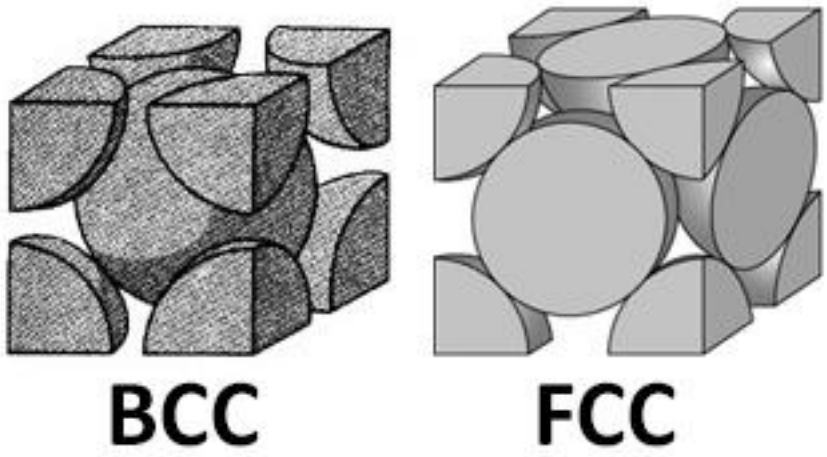

Fig. 1 BCC and FCC arrangement of atoms in a crystal structure of metal (illustration by this author)

These crystal structures grow uniformly in all directions within each developing crystal. As the metal cools, these crystals are confined by the adjacent developing crystals forming grains. The boundary between these growing crystals is called the grain boundary. Since each grain grows independently, the crystal lattices are oriented at various directions compared with adjacent grains.

Each atom in the lattice is held together by electromagnetic forces that act like springs. If a force or load is applied to the lattice, the bonds will stretch allowing the atoms to move slightly. When the load is removed, the bonds pull the atoms back into their original position,

indicating elastic deformation. If the applied force exceeds the metal's yield strength, the electromagnetic bonds will break and reattach to adjacent atoms causing permanent deformation. The lattice will be displaced by one or more atomic planes. This displacement in the lattice is called a dislocation of the lattice structure.

The shear stress required to plastically deform a single crystal whereby atomic planes slide over each other along the closest packed plane of atoms, was first defined by Frenkel in 1926 [40] as:

$$\tau = \frac{Gb}{2\pi a} sin \frac{2\pi x}{b} \qquad \textbf{Eq. 2-1}$$

where τ is the applied shear stress, G is the shear modulus, 'b' is the spacing between the atoms in the direction of the shear stress, 'a' is the spacing of the rows of atoms, and 'x' is the shear translation of the two rows away from the low-energy equilibrium position, as shown in Fig. 2.

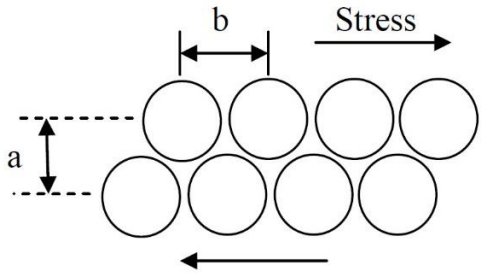

Fig. 2 Shear slip of two atomic planes in a simple crystalline structure (illustration by this author)

This stress is related to the flow stress, or the shear stress necessary to induce plastic deformation in solid metals. The sliding motion creates dislocations in the original microstructure of the crystal. Dislocations are 1D lattice defects or lattice imperfections which form as an absence or inclusion of atoms in one or more layers of the lattice. A representation of two types of dislocations in a simple cubic lattice; i.e. screw and edge, is shown in Fig. 3.

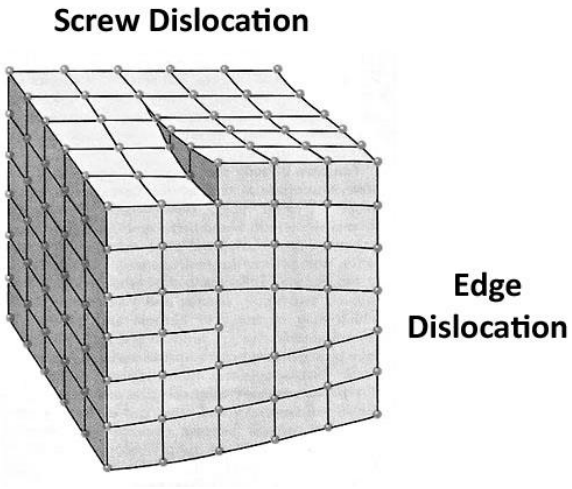

Fig. 3 Edge and screw dislocations in a crystal lattice (illustration by this author)

The positions and orientations of dislocations are commonly described by the Burgers vector, named after Dutch physicist Jan Burgers. The Burgers vector, commonly labelled as "b", is defined as the magnitude and direction of the lattice distortion of dislocation in a crystal lattice [41, 42]. For an edge dislocation the Burgers vector is normal to the line of dislocation and parallel for screw dislocation. Parameters such as strain energy of dislocations and the forces to move dislocations are dependent on the Burgers vector.

The applied resolved shear stress required to make a dislocation glide in a perfect crystal is known as the Peierls-Nabarro stress. It depends on the force-distance relationship between individual atoms and can be defined as the stress necessary for dislocations to move by one atomic space:

$$\tau_{PN} = \frac{Gb}{2c} exp\left(\frac{-\pi a}{c}\right) sin\left(\frac{2\pi x}{c}\right) \quad \textbf{Eq. 2-2}$$

where G is the shear modulus, ‘b’ is the Burgers vector, ‘c’ is the lattice spacing, and ‘a’ is the lattice parameter. This stress follows the same concept as the one created by Frenkel and can be related to the critical shear stress required to move dislocations by gliding which ultimately induces plastic deformation in the material.

Both BCC and FCC metals follow Hooke’s Law when deforming elastically. However, there are different factors that affect the behavioral responses of these metals when they undergo plastic deformation. Plastic deformation involves the gliding of dislocations along slip planes, or planes with the highest density of atoms (closest packed plane), induced by applying stresses which surpass the critical resolved shear stress required to move dislocations. The closest packed plane has the shortest Burgers vector. In metals, this deformation is controlled by the movement of dislocations past obstacles in the lattice caused by either increasing the applied stress or inducing thermal fluctuations [43, 44]. This stress controls the macroscopic yield in materials. The FCC lattice has 12 slip planes with shorter Burgers vector than BCC, while BCC metals have only six. Thus, FCC metals can undergo plastic deformation more easily at lower stresses than BCC metals.

In the 1950's Hall and Petch developed a series of equations that linked macroscopic yielding to the critical resolved shear stress for plastic deformation—basing their analysis on the pile-up of screw dislocations against obstacles in the lattice [45, 46]. They reported that when the macroscopic shear stress, resolved onto the slip plane in the direction of the Burgers vector, reaches a critical value, the dislocation in the pile-up is able to push past the obstacle. They labeled this critical shear stress the Hall-Petch shear stress defined as:

$$\tau_{HP} = \tau_0 + \frac{k_{HP}}{\sqrt{d}} \qquad \textbf{Eq. 2-3}$$

where

$$k_{HP} = \sqrt{\frac{\mu b \tau^*}{\pi}} \qquad \textbf{Eq. 2-4}$$

The term τ^* is the obstacle strength, 'd' is the spacing between obstacles, 'μ' is the elastic shear modulus, 'b' is the magnitude of the Burgers vector, and 'τ_o' is the resistance to dislocation motion in a material free of obstacles ($d = \infty$). Materials with stronger obstacles have higher k_{HP} so that their yield strength and hardness are more sensitive to changes in d. This can be measured experimentally through quasi-static tension tests. In a true stress-strain curve, the work or strain hardening is a result of the increasing amount of flow stress required to maintain plastic flow in the material. Material parameters such as crystal

structure, alloy composition, dislocation arrangement and grain size all affect the yield and flow stress of the metal.

In addition to linear 1D dislocations, there can exist lattice point defects such as substitutional and interstitial impurities, vacancies, and self-interstitials, shown in Fig. 4.

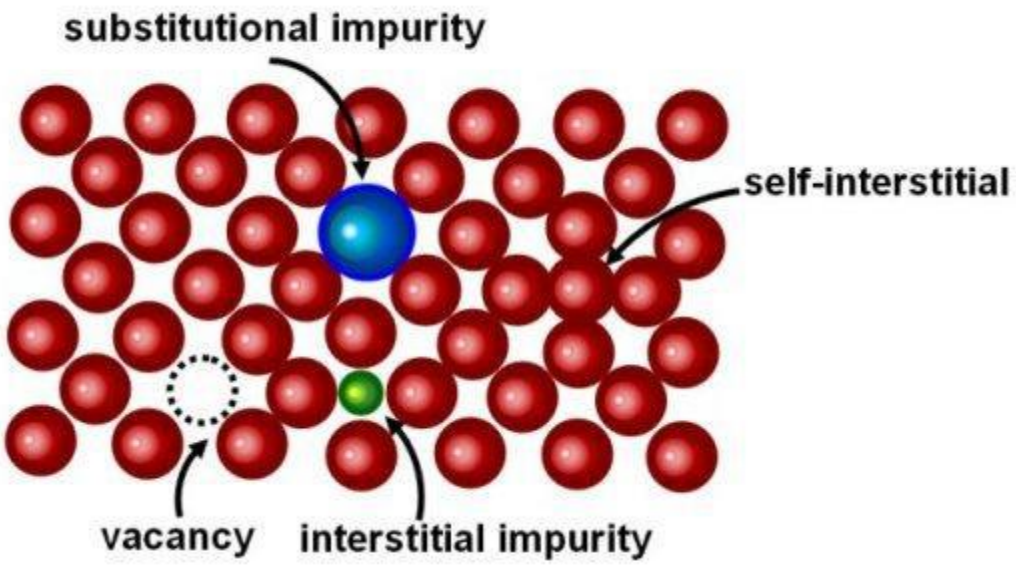

Fig. 4 Types of point defects in a crystalline lattice (illustration by this author)

The grain boundary is considered to be a 2D planar defect in the crystal structure. The high interfacial energy in most grain boundaries makes them preferred sites for the precipitation of new phases from the solid and segregation of solute atoms. Grain boundaries also disrupt the motion of dislocations through a material. During plastic deformation or when energy is applied to the lattice via a rise in temperature, dislocations will move through

the crystal lattice to the grain boundary. The mis-orientation at the grain boundary between grains inhibits the movement of dislocations from one grain to the next as it requires more energy for a dislocation to change directions and move into the adjacent grain. When the mis-orientation between two grains is small, the grain boundary can be described by a relatively simple configuration of dislocations (e.g., an edge dislocation wall) and is called a low-angle boundary. Large mis-orientations are called high-angle grain boundary and the larger the mis-orientation the more energy is required for dislocations to move across the grain boundaries. Low and high angle grain boundaries can be seen in Fig. 5.

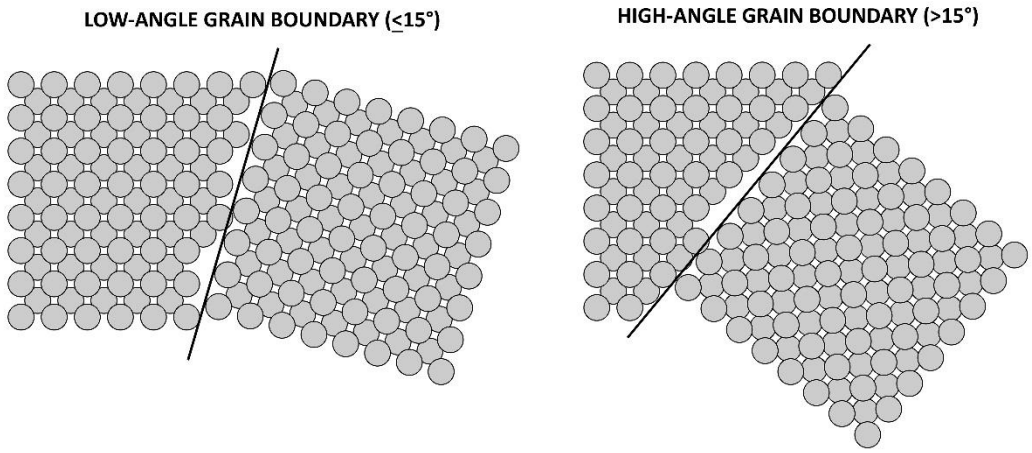

Fig. 5 High and low grain boundary angles (illustration by this author)

Dislocations will pile-up behind high angle grain boundaries and increase the surrounding stresses to the point that the dislocation is forced through the boundary in to the

neighboring grain. The grain boundary is also much more disordered than inside the grain, and prevents dislocations from moving in a continuous slip plane. Impeding this dislocation movement will hinder the onset of plasticity and hence increase the yield strength of the material.

At low temperature (T<0.5Tm) the grain boundaries act as strong obstacles to dislocation motion. Mobile dislocations can pile up against the grain boundaries and thus give rise to stress concentrations that can be relaxed by initiating localized slip. At high temperatures the grain boundaries function as sites of weakness. Grain boundary sliding more readily occurs, leading to plastic flow.

2.1.1 Effect of Grain Size on Mechanical Properties of Metals

The mechanical properties of metals, such as its hardenability, toughness, and strength, depend on grain size. The Hall-Petch equation [45] can also relate yield strength, σ, to the average grain diameter, d as

$$\sigma = \sigma_o + kd^{-0.5} \qquad \textbf{Eq. 2-5}$$

where σ_o is a material constant for the starting stress for dislocation movement and k is the strengthening coefficient, or Hall-Petch slope.

Eq. 2-5 is based on the dislocation theory where grain boundaries act as obstacles to slip dislocations, causing dislocations to pile up on their slip planes behind the grain boundaries. Dislocations that attempt to pass from one grain to the adjacent grain will have to change their direction of motion due to crystallographic mis-orientation. As dislocations generate repulsive stress fields, each successive dislocation will apply a repulsive force to the dislocation incident with the grain boundary such that additional pile up causes dislocation diffusion across the grain boundary, allowing further deformation in the material. Decreasing grain size decreases the amount of possible pile up at the boundary, resulting in an increase in the amount of applied stress necessary to move a dislocation across a grain boundary. The higher the applied stress to move the dislocation, the higher the yield strength. *There is then an inverse relationship between grain size and yield strength.*

The driving force for grain growth is the surface energy of the grain boundaries. As growth occurs the overall number of grains decreases as larger grains consume smaller grains [47]. The mean grain diameter is utilized as a measure of the grain size of an alloy. The Ideal Grain Growth Law relates average grain diameter, D^m, to initial grain size D_o^m, as follows,

$$D^m - D_o^m = kt$$ **Eq. 2-6**

where k is a constant of proportionality that relates heating temperature and activation energy for grain growth, and t is the holding time. Constant of proportionality, k, is defined as

$$k = k_o exp\left(\frac{-Q}{RT}\right)$$ **Eq. 2-7**

where k_o is a constant, T is the absolute temperature and Q is the activation energy for boundary mobility.

Thus according to Eq. 2-6 and Eq. 2-7 as temperature increases, the constant of proportionality between D_o and D both increase signifying an increase in grain size. *Thus, grain size increases with increasing temperature.*

Derby and Ashby [25] obtained a formula based on work by Sandstorm and Lagneborg [48] for the recrystallized steady-state grain size which is inversely proportional to the imposed strain rate of deformation. The formula defines the steady state grain size d_s as

$$d_s = \sqrt{\left(\frac{2^{n_c-1}\varepsilon_c \lambda g}{3\dot{\varepsilon}}\right)} \qquad \textbf{Eq. 2-8}$$

where n_c is the critical number of cell intersections within grain boundaries, ε_c is the characteristic strain to reach steady-state, λ is the steady-state subgrain size and *g* is the grain boundary growth rate. *Grain size thus decreases with increasing strain rate.*

2.2 The Elemental Alloying Properties of Steel

Steel is an alloy of carbon and iron where carbon makes up 0.12-2.0% of its weight. It also contains a number of other alloying elements which are added to obtain a desired alloying effect. The amount of carbon and alloying elements affects the mechanical and physical properties of the steel.

2.2.1 The Role of Carbon in Steel

The carbon content of steel affects its strength, hardness, ductility, and toughness. Carbon acts as a hardening agent that prevents the movement of dislocations that exist naturally in the iron atomic lattice or as a result of machining or manufacturing. The higher the carbon content the easier it becomes for steel to become harder and stronger through heat treatment.

2.2.2 Types of Steels Based on Carbon Content

Part of the classification of steel comes from its % carbon content which has a major effect on its hardenability (ability to be hardened through heat treatment), strength and toughness. Classification of steel based on carbon content is divided into three categories: low-carbon, medium-carbon, and high-carbon steels. These steels contain a minimal % of alloying elements.

2.2.2.1 Low-Carbon Steel

Low-carbon steel; also known as mild steel or plain-carbon steel, has a carbon content between 0.05-0.2% wt. [49]. Its low carbon content makes it malleable and ductile, with low strength. It is cheap and used in structural steel where large quantities of steel is needed. AISI/SAE classifications of steels in this category include AISI 1005-1026,1109-1119, 1211-1215 and 1513-1527 [50].

2.2.2.2 Medium-Carbon Steel

Medium-carbon steels contain between 0.2-0.4% carbon [49] and have a good balance of ductility and strength. These steels are typically used in large parts, forgings, and machined components; i.e. bolts, rods, crankshafts and tubing in the automotive industry.

Other parts include axles, gears, and components that require higher hardness and wear resistance. AISI/SAE classifications of steels in this category include AISI 1029-1053, 1137-1151, and 1541-1552.

2.2.2.3 High-Carbon Steel

High-carbon steels have a carbon content ranging between 0.5-1.0% C [49] and are extremely strong yet very brittle. They are used in parts that require high wear resistance. AISI/SAE classifications of steels in this category include AISI 1055-1095, 1137-1151, 1561-1572.

2.2.3 Alloying Elements of Steel

In addition to carbon, a number of alloying elements are added to steel in amounts ranging between 1.0% and 50% by weight to improve its mechanical and corrosion resistant properties. Common alloying elements include manganese, nickel, chromium, molybdenum, vanadium, silicon, and boron. Less common alloying elements include aluminum, cobalt, copper, cerium, niobium, titanium, tungsten, tin, zinc, lead, and zirconium. Each alloying element plays a role in improving the strength, hardness, toughness, wear resistance, corrosion resistance, and hardenability. Varying the amount of alloying elements, their distribution in the steel as either solute elements or as precipitated

phases, acts to hinder plastic deformation by hindering the movement of dislocations and controlling the hardness and strength. Alloy steels are used in highly demanding applications such as turbine blades of jet engines, in spacecraft, and nuclear reactors. Alloy steels are broken down into two categories: low-alloy steels and high-alloy steels.

2.2.3.1 Low-Alloy Steel

Low-alloy steels are steels whose main constituent alloying elements are nickel, chromium, and molybdenum and whose total content ranges between 2.07-8 wt. % [49]. These elements increase the hardenability of steel. Nickel increases strength, impact strength and toughness, while also improving the resistance to oxidation and corrosion. It increases toughness at low temperatures when added in small amounts [51]. Chromium is added for corrosion resistance in addition to improving strength and response to heat treatment. Molybdenum is added to increase strength, particularly at high temperatures. It binds with carbon easily and forms stable carbides in alloys, inhibits grain growth, and protects against corrosion caused by chlorides and sulphur chemicals. It is a valuable alloy metal for making cutting parts of machine tools and turbine blades of turbojet engines and rocket motors. AISI/SAE classification for low-alloy steels containing nickel chromium and molybdenum as main alloying elements include AISI 43XX, 47XX, 81XX, 86XX, 87XX, 88XX, 93XX, 94XX, where XX is the 0.XX % wt. carbon content [52].

2.2.3.2 High-Alloy Steel

High-Alloy steels are steels which contain more than 8% wt. alloying element. They are used mainly for corrosion resistance in aqueous media at or near room temperature and for service in hot gases and liquids at high temperatures (>650°C) [53]. Extremely high corrosion resistance is achieved by alloying >20% Cr. These alloys do not show phase changes during heating or cooling between room temperature and melting. Therefore they are not hardenable or heat treatable and the properties depend on the chemical composition rather than heat treatment.

2.2.4 AISI 4340 Steel

AISI 4340 steel is a medium-carbon (0.38% wt C) low-alloy nickel-chromium-molybdenum steel composed of (wt. %) 0.38-0.43% carbon (C), 0.60-0.80% Manganese (Mn), 0.035 (max) Phosphorus (P), 0.04% (max) Sulfur (s), 0.15-0.30% Silicon (Si), 0.70-0.90% Chromium (Cr), 1.65-2.00% Nickel (Ni), 0.20-0.30% Molybdenum (Mo). This steel has high hardenability and heat treatability giving it a wide range of achievable strength, hardness, toughness, or ductility. Typical tensile strength varies between 758 and 1882 MPa and elastic modulus between 190 to 210 GPa [54].

2.3 The Heat Treatment and Microstructure of Steel

Heat treating is a metalworking process used to alter the physical, mechanical, and sometimes chemical properties of a metal. Medium to high wt. % carbon, low-alloy steels can be heat treated to improve toughness, strength, hardness, or ductility by heating and cooling at different rates between room temperature and melting. Heat treatment techniques include quenching, tempering, annealing, and precipitation strengthening.

2.3.1 Allotropes/Phases of Iron in Steel

Heat treatment of steel works by changing the rate of heating or cooling and holding time at specific temperatures. Pure Iron can exist in several crystalline forms based on the heat treatment. These forms are called phases and four phases of iron exist at different temperatures—characterized as α, β, γ, and δ-Fe.

Ferrite, also known as α-Fe or alpha iron, is a phase of pure iron with a body-centered cubic (BCC) crystalline structure of iron atoms, shown in Fig. 6.

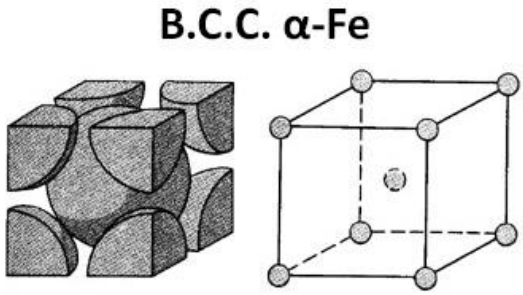

Fig. 6 Body-centered cubic crystalline structure of α-Fe (illustration by this author)

Iron makes up the majority of the composition of steel and gives it its magnetic properties. It is also the softest and most ductile phase. In pure iron, ferrite is stable below 910°C [55]. Above this temperature, α-Fe transforms to a face-centered cubic form of iron called austenite, or γ-Fe, shown in Fig. 7. Above this temperature austenite is stable.

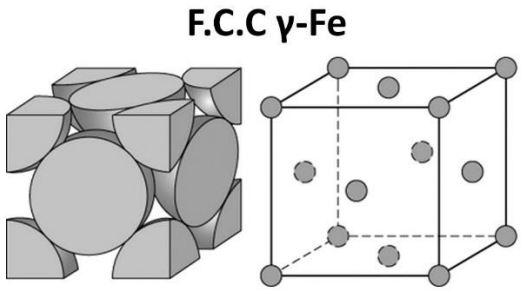

Fig. 7 Face-centered cubic crystalline structure of γ-Fe (illustration by this author)

Above 1400°C, up to the melting point at 1539°C, austenite transforms back to a stable BCC structure called delta-ferrite or δ-Fe.

The temperature at which iron changes phase in steel is dependent on the wt. % of carbon. Carbon also interacts with iron to form phases of iron and carbon. These include pearlite and cementite. The phases present at different temperatures with respect to % C is represented by the iron-carbon phase diagram [56], illustrated in Fig. 8.

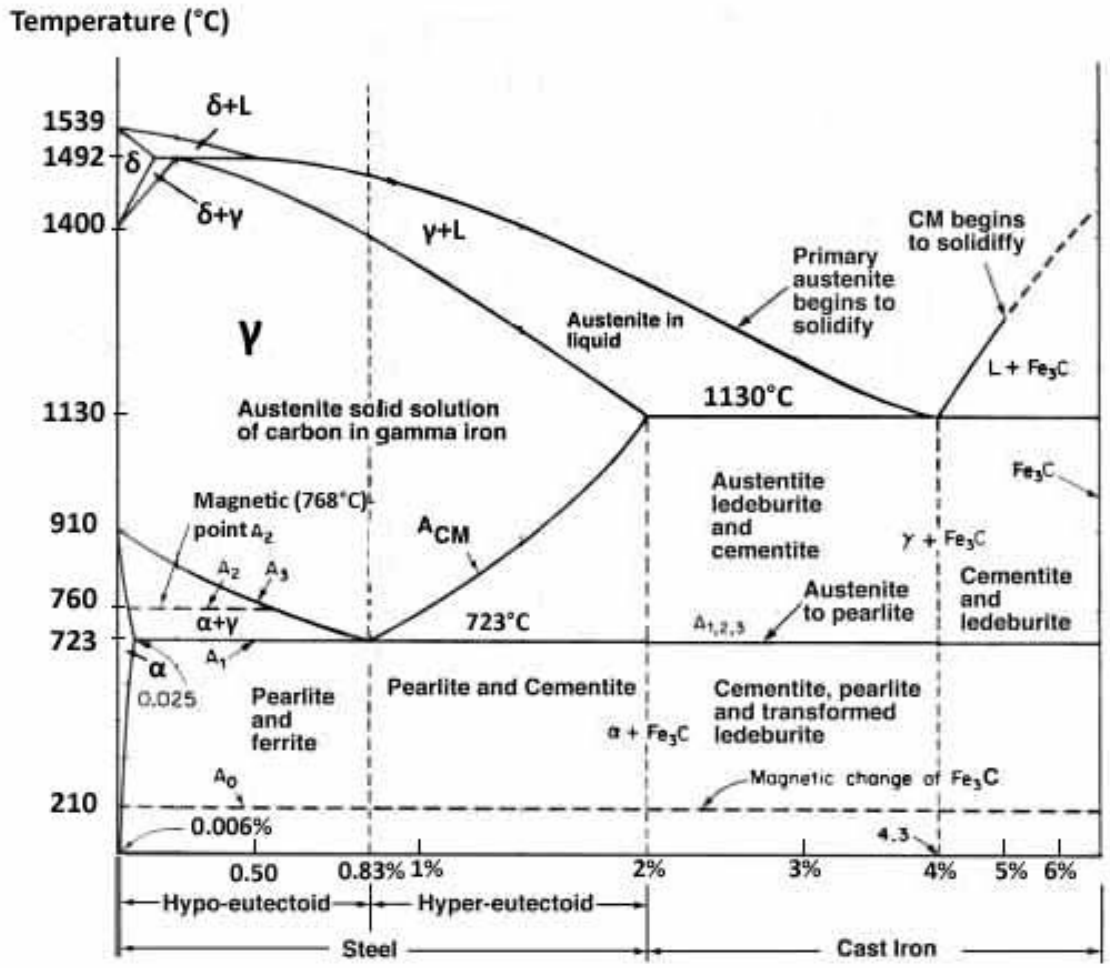

Fig. 8 The Iron-carbon phase diagram (illustration compiled by this author)

The iron-carbon phase diagram shows the phases which form in steel when it is slowly cooled. It does not give an indication as to the effects of heating and cooling rates. Steels with a carbon content below 0.83%, slowly cooled from above 723°C are composed of ferrite and pearlite. Pearlite is a two-phase lamellar (layered) structure composed of alternating layers of ferrite (88 wt %) and cementite [Fe_3C] (12 wt %) [57]. These steels are very ductile and can be draw into thin wires and bundled into rope. They are used as piano wires, ropes for suspension bridges, and steel cord for tire reinforcement. A steel with a lower wt. % carbon will form more ferrite and a higher % carbon will form more cementite.

Cementite, or iron-carbide Fe_3C / Fe_2C:Fe is 6.67 wt. % carbon and 93.3% iron. It has a complex orthorhombic crystal structure [55]. Carbon atoms are located in the interstitial sites of the Fe triangular prism, shown in Fig. 9.

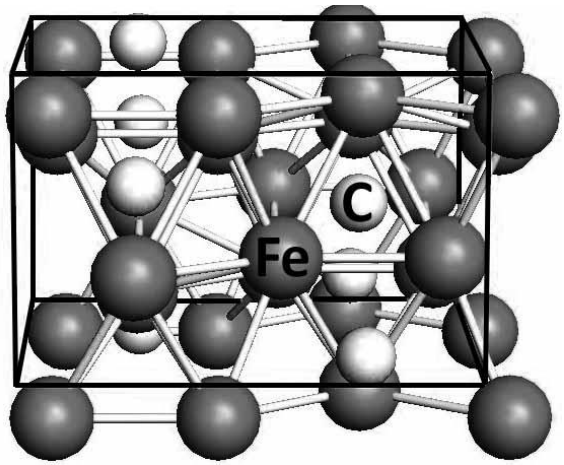

Fig. 9 Orthorhombic crystal structure of iron carbide Fe_3C (illustration by this author)

Cementite is a hard and brittle material and is classified as a ceramic in its pure form. Cementite forms because carbon has a low solubility in BCC ferrite. This gives pearlite its layered pattern. Carbon atoms are about twice the diameter of the interstitial gaps in the BCC structure of ferrite. When carbon atoms dissolve interstitially into BCC iron they become surrounded by a strong local strain field. As a result the solubility of carbon in BCC iron is very low, having a maximum solubility of about 0.02 wt % C at 723°C and 0.005% carbon at 0°C [55]. A representation of interstitially dissolved carbon in a crystal structure of α-Fe is shown in Fig. 10.

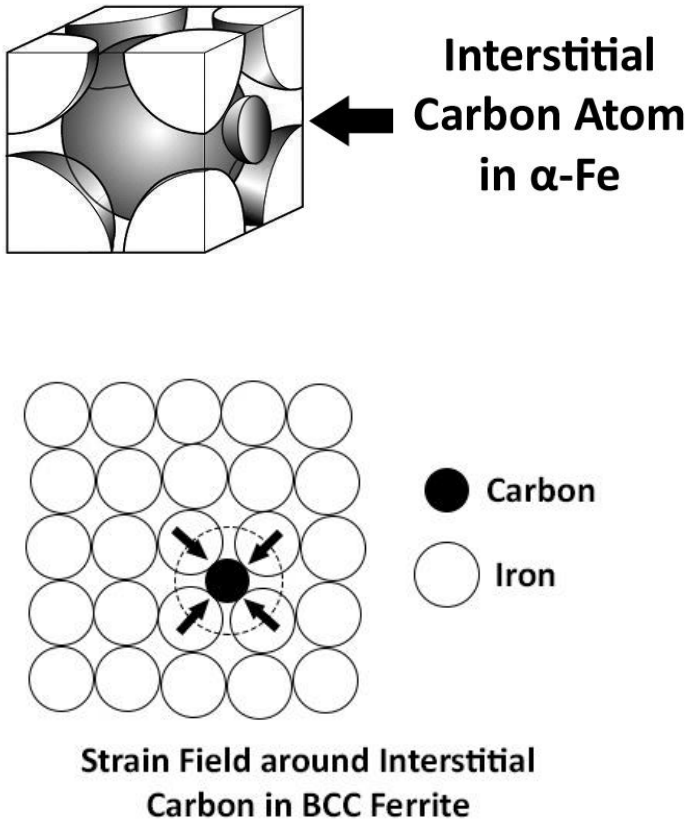

Fig. 10 Interstitial carbon atom in α-Fe (illustration by this author)

Above the austenization temperature, cementite dissolves into a solid solution of carbon and iron transforming BCC ferrite to an FCC austenite crystal structure. The interstitial points in the lattice are larger than in BCC and can accommodate more carbon atoms (as much as 2.04 wt % at 1146°C [55]).

2.3.2 Effect of High Temperature Heating, Grain Recovery & Grain Growth

At temperatures above austenization, there is a rapid recovery of the crystal structure within the grains, in which the grains reduce their stored energy by removal or rearrangement of defects, such as dislocations introduced into in the crystal structure by deformation.

At temperatures above $0.3T_m$, dislocations within the grains become mobile and are able to glide, cross-slip and climb [24]. If two dislocations of opposite Burgers vector meet, they effectively cancel out. This process is called dislocation annihilation. After annihilation, dislocations want to move into lower energy configurations and align into low-angle grain boundaries. The removal of dislocations from the grains is accompanied by a reduction in strength and an increase in toughness. This recovery process is also thought to be called static recrystallization.

The grain boundaries are considered to be walls of dislocation tangles between two misoriented-crystal structures. These walls contain a level of stored energy. Upon completion of the recovery process, further reduction of the stored energy is achieved by reducing the total grain boundary area by the process of grain growth. While recovery can occur as low as $0.3T_m$, grain growth requires a higher thermodynamic driving force and is typically achieved at temperatures above austenization [58]. Grain growth is accompanied

by a coarsening of the subgrain structure where their size increases and their number decreases.

2.3.3 Effect of Cooling Rate on the Microstructure of Carbon Steel

Cooling rate controls the rate of diffusion of carbon atoms in the iron solution. If cooled slowly, austenite will undergo a stable equilibrium transform to a mixture of BCC ferrite and pearlite or cementite, depending on carbon content. However, if rapid cooling is performed, called quenching, carbon does not have enough time to diffuse out of the FCC austenite resulting in a diffusionless or shear transformation to a hard and brittle distorted body-centered tetragonal (BCT) phase called martensite (α'-Fe)—a supersaturated phase of iron and carbon with the same composition as austenite. Martensite grows at speeds which approach the speed of sound, as high as 1100 m/s [59]. BCT martensite is distorted due to the presence of carbon atoms which occupy the interstitial lattice positions, shown in Fig. 11.

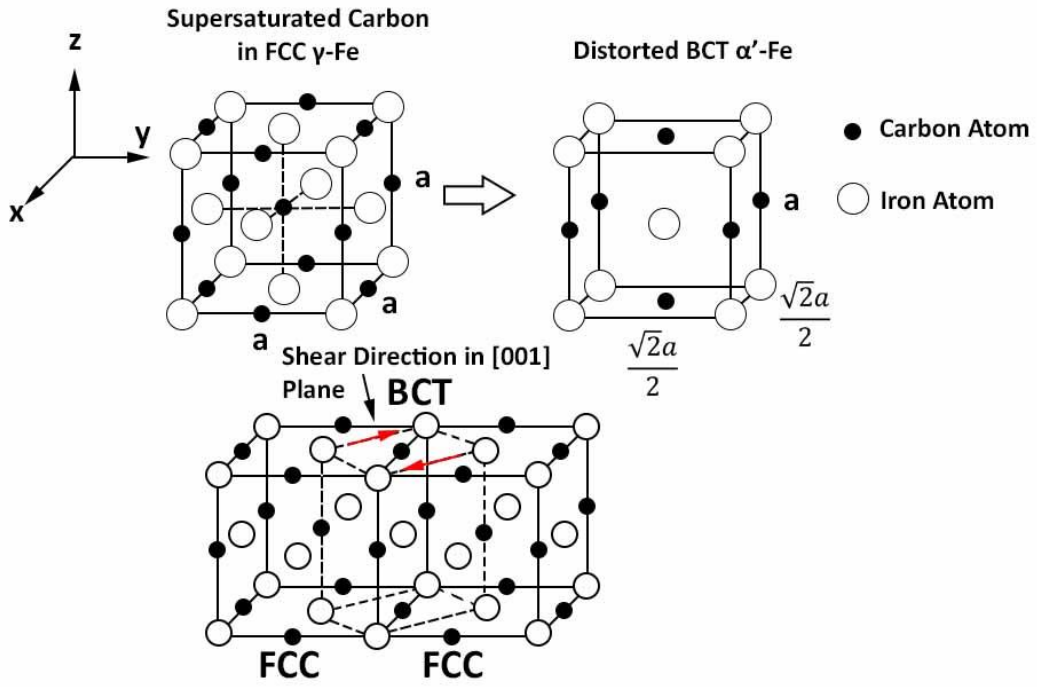

Fig. 11 BCT structure of martensite resulting from a diffusionless shear transformation from austenite upon rapid cooling. The BCT structure can be visualized inside two adjacent FCC crystal structures. Shear occurs on the close-packed plane (illustration by this author)

BCT martensite is metastable below the austenization temperature and wants to transform to a BCC structure by shrinking in the z-direction and expanding along the x- and y-directions so that the dimensions of the cubic structure are equal. Full transformation to BCC is prevented by the carbon atoms which sit in the interstitial positions of the BCT structure and cannot diffuse. However, there is a change in shape from FCC to BCT by a contraction of ~20% in the z-direction, and expansion of about 12% in the x and y-directions [59]. This change in shape appears as a simple shear parallel to a habit plane (interface

between austenite and martensite) and a uniaxial expansion (dilatation) normal to the habit plane. Steels with 0 wt. % C or steels which have been tempered at elevated temperatures to allow carbon to diffuse away from the structure, show the transformation of BCT martensite to stable BCC martensite also called tempered martensite which is softer and tougher but still retains a good level of hardness.

The shear transformation to BCT martensite increases the strain energy in the microstructure. This energy can be minimized by a shape deformation along the habit plane, categorized as either twinning or slip, visualized schematically in Fig. 12. Twinned martensite appears as plates and usually forms in high carbon steels while slip martensite appears as laths and forms in medium to low carbon steels [60]. The individual martensite laths are on a scale of a few nanometers in width.

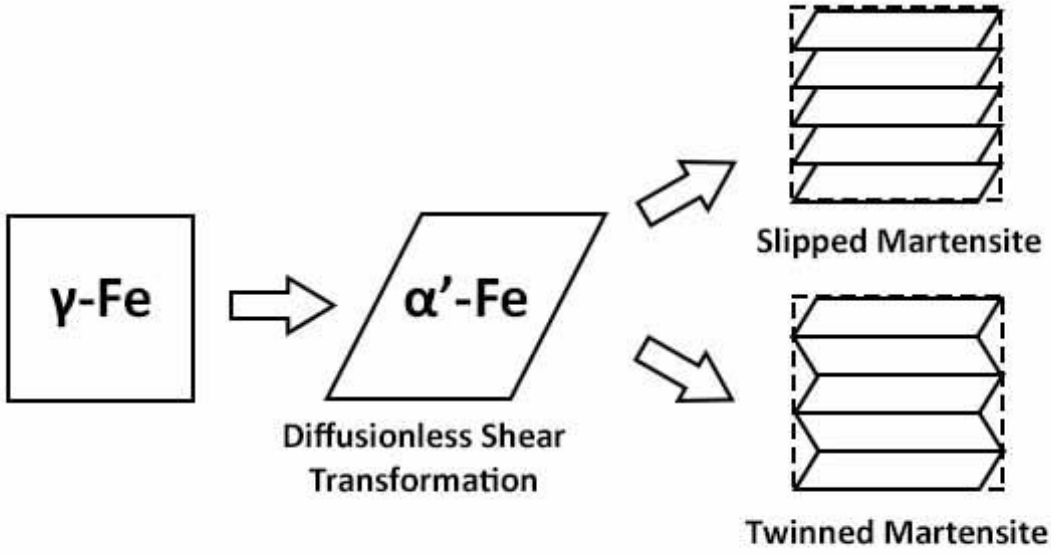

Fig. 12 Formation of Lath martensite by twinning and slip in the BCT martensite grains (illustration by this author)

The formation of martensite laths creates a large number of dislocations. The high amount of carbon atoms and dislocation density in the martensite laths gives them a very high strength and hardness but also makes them very brittle.

Martensite growth is limited by the structure of the parent austenite grain due to the diffusionless transformation. It grows by a shear displacive (as opposed to reconstructive) transformation of austenite where atomic movement cannot be sustained across the austenite grain boundaries [61]. Ordinary pearlitic/ferritic steels have phases which grow by

reconstructive transformation across the austenite grain boundaries. In doing so, they destroy the structure that exists at those boundaries and removes them as potential sources for the segregation of impurity atoms, like phosphorus.

The final microstructure of steel changes depending on cooling rate. A fast cooling rate will result in a high strength, high hardness, but brittle structure, while slow cooling can result in a softer, tougher steel. The effect of cooling rate on microstructure of carbon steel from temperatures above austenization, is shown in the continuous cooling transformation diagram, in Fig. 13. Slower cooling rates allow carbon to diffuse out of austenite and can form pearlite, ferrite, cementite, and the intermediary phase bainite [62], or a combination.

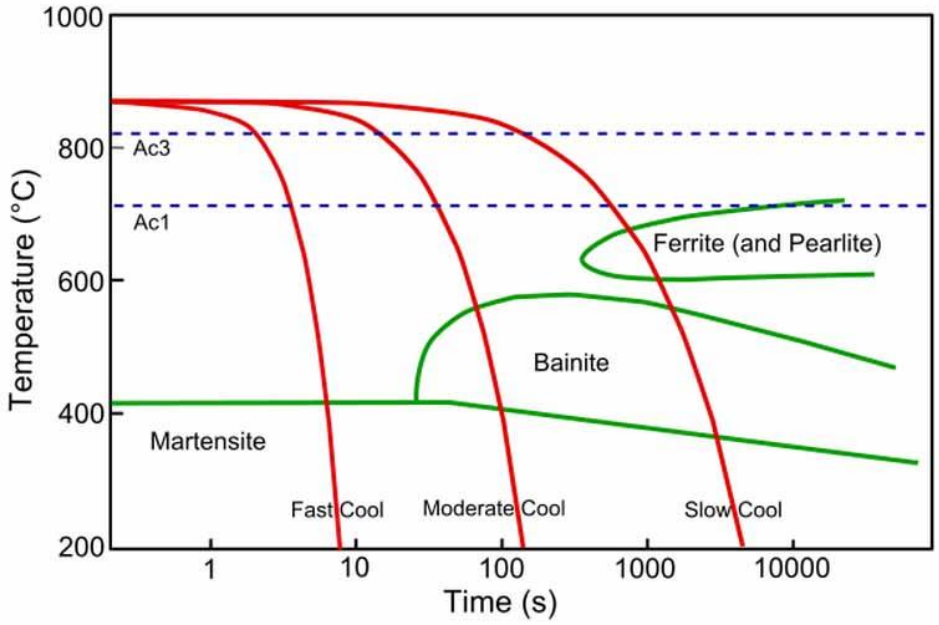

Fig. 13 Continuous cooling transformation (CCT) diagram for steel (image is public domain [62])

2.3.4 Effect of Tempering on the Microstructure of Steel

After quenching, steel becomes hard and brittle. This form of steel is not suitable for many applications requiring high toughness, ductility, and impact strength. This form of steel is also highly prone to cracking. By precisely controlling tempering temperature and time, a desired balance between hardness, strength, toughness, and ductility can be achieved. Tempering is a process of heat treating which is performed after hardening (quenching) by heating the metal to a temperature below the critical temperature (723°C for steel) before austenite begins to form, and holding for a specified time followed by controlled cooling or air cooling. Heating above the eutectoid temperature would destroy the martensite needed for hardness, which transforms back to austenite. The exact temperature and holding time determines the degree of retained hardness, and improved toughness and ductility, which also depends on the alloying elements and the phases which form.

The tempering temperature regulates the amount of thermal energy added to the system which promotes diffusion of carbon atoms. Higher temperatures will promote greater diffusion of carbon atoms and formation of carbides, resulting in softer more ductile steel with lower strength and hardness. Upon reheating to an elevated temperature, there is a diffusion of carbon atoms which changes the formation of the microstructure. These changes can be categorized into stages:

1) Between 60°C-260°C: At the lower temperatures, there is a precipitation of ε-carbides (transition iron carbides with a chemical formula between Fe_2C and Fe_3C) from the partial decomposition of BCT martensite [63-65]. Around 200°C, there is a decomposition of retained austenite, or metastable austenite which does not fully transform to hardened martensite upon quenching [66-68]. This retained austenite decomposes into bainite, ferrite, and cementite. AISI 4340 steel contains approximately 4 vol% of retained austenite upon quenching [69]. In this temperature range martensite is still very hard and has high strength although there is a slight reduction in brittleness. This range of tempering is suitable for steels used in tools where a high hardness and strength is required.
2) Between 260°C to 340°C: There is a *decrease* in ductility and an increase in brittleness due to the phenomena of tempered martensite embrittlement (TME). TME occurs due to precipitation of very fine but brittle cementite at the interlath boundaries of martensite. These cementites are in the shape of long needles or plates called Widmanstatten cementite. Impurities, such as phosphorus, or alloying elements like manganese can also increase embrittlement [70]. This embrittlement is permanent and can only be reversed by heating above the austenization temperature and quenching. Embrittlement occurs when tempering in the TME range

for longer than 60 minutes. Microstructures which suffer from TME fail by transgranular fracture with respect to the parent austenite grain.

3) Between 370° and 540°C: Ideal range for medium to high carbon steel to have high toughness at the expense of strength and hardness. Transition ε-carbides dissolve and are replaced by cementite. ($Fe_{2-3}C \rightarrow Fe_3C$). Additionally, carbon atoms diffuse from the prior austenite grain boundary and lath boundaries precipitate which contributes to the coarsening of the cementite.

4) Between 540°C and 600°C: Further increase in temperature leads to a spheroidizing of the cementite particles, annihilation of dislocations, and growth of martensite laths. This leads to a significant increase in toughness and ductility. The final microstructure is that of coarse cementite and soft BCC lath martensite.

5) Above 600°C: There is another embrittlement phenomena called temper embrittlement (TE). It is caused by the presence of specific impurities in the steel, which segregate to the prior austenite grain boundaries, the most common of which is phosphorus. Fracture surfaces of materials embrittled by phosphorus have an intergranular appearance. Alloying elements such as Ni, Cr, and Mn, increase the susceptibility to temper embrittlement while small additions of Mo, can inhibit it.

The response of alloyed steels to hardening and tempering varies according to their chemical composition. Certain alloying elements are added to not only improve the physical or mechanical properties of steel but also to inhibit grain growth in order to retain a high strength while also achieving a high toughness, promote the formation of stable carbides during tempering to improve toughness and reduce instability, reduce susceptibility to embrittlement, and improve hardenability by increasing the range of temperatures at which the steel can be heat treated. Through heat treatment by quenching and tempering, a good balance between strength and toughness can be achieved.

2.4 Adiabatic Shear Bands (ASBs)

When steels are deformed at high strain rates and larges strains, they are susceptible to failure through shear. All shear failure is preceded by the formation of adiabatic shear bands which are characterized by a severe shear localization in the material. ASBs measure anywhere between 5 and 500 μm [1]. The size and characteristics of the ASBs depends on the steel's mechanical and physical properties as well as the deformation stress and strain rate. Two types of ASBs have been shown to form in steels: deformed and transformed or 'white-etched' shear bands. Deformed bands appear in both hard and soft metals. In soft metals they are characterized by a severe reorientation of the microstructure in a large plastic

deformation zone in the direction of maximum shear, shown in Fig. 14. In harder metals they often precede or follow or even surround the formation of 'white-etched' bands and are characterized by a darkened zone, an example of which can be seen in Fig. 15, for a specimen of AISI 4340 steel which has fractured. This has also been confirmed in tests by Odeshi et al. [71].

Transformed bands, or 'white-etched' bands, named for their white appearance under optical microscopy, are characterized by a thinner more pronounced band which typically appears in harder and stronger metals. These bands exhibit a high hardness where microcracks are known to form at the center of the bands. A micrograph of a 'white-etched' transformed band in high strain rate impacted AISI 4340 steel are shown in Fig. 16.

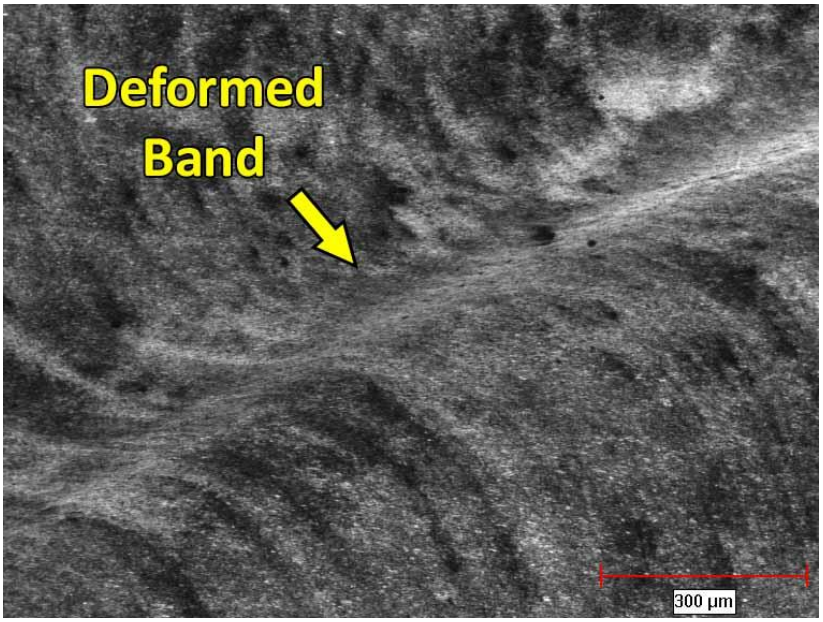

Fig. 14 Deformed band in heat treated AISI 4340 steel with high toughness, low strength, and low hardness (image taken by this author)

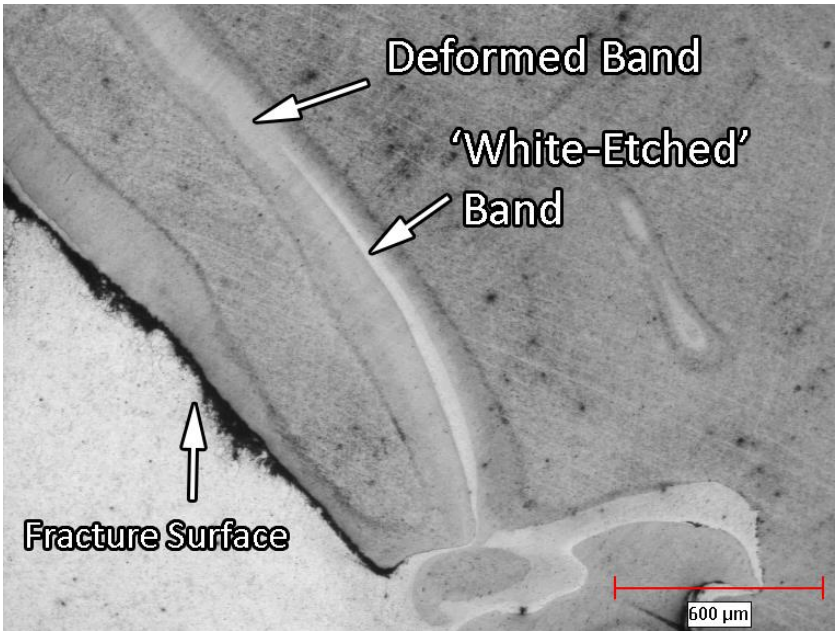

Fig. 15 Formation of deformed and 'white-etched' ASBs in a fractured specimen of AISI 4340 steel heat treated to have high hardness and strength (image taken by this author)

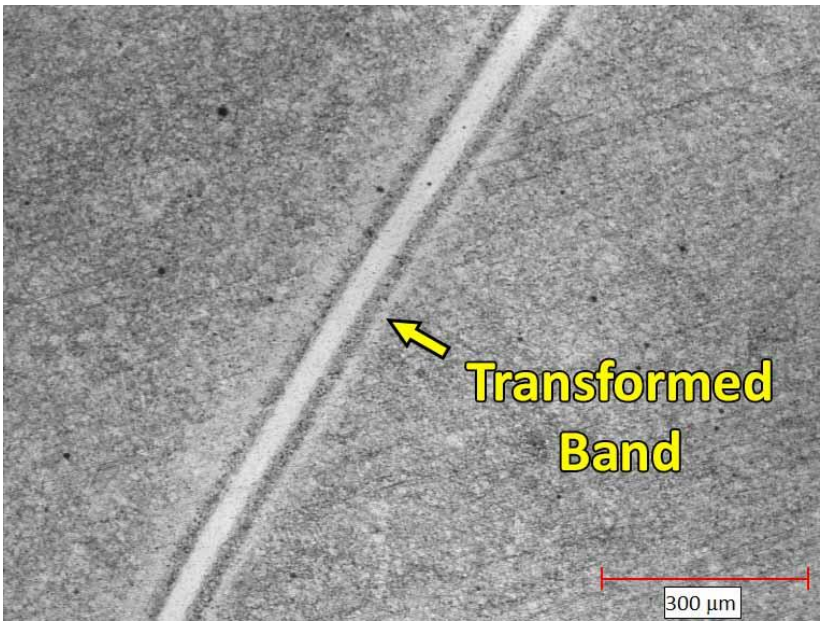

Fig. 16 White-etched ASB in AISI 4340 heat treated to have high strength and hardness subjected to high strain rate impact at large strains (image taken by this author)

ASBs are a 3D microstructural phenomena. They form in the direction of maximum shear which is dependent on the geometry of the steel being deformed. Typical tested geometries include rectangular prism (thin/thick plate impact/penetration), and cylindrical (cylindrical impact, rod impact, rod tension). The maximum shear directions for these geometries are shown in Fig. 17 indicated by the dotted lines. In the rectangular prism, Shear direction also appears along the diagonals of the faces.

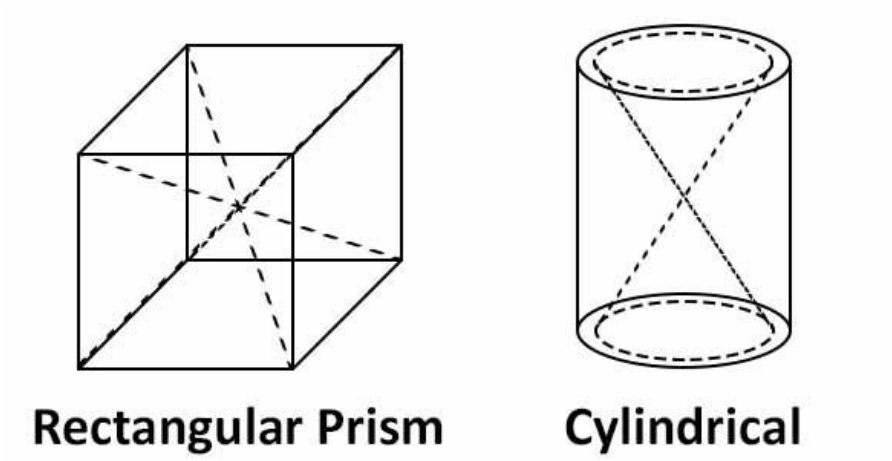

Fig. 17 Shear directions in typical geometrical specimens. (illustration by this author)

A steel's ability to resist ASB formation is dependent on its mechanical and physical properties which is controlled by its chemical composition and heat treatment. Also, the type of ASB which forms is directly related to the kinematics of its microstructure under deformation.

2.4.1 Mechanisms of ASB Formation

There have been several mechanisms which have been developed to explain the formation of ASBs in metals. They range from physical mechanisms based on dislocation

theory and observed microstructural deformation from experimentation to phenomenological theories from FEA simulations.

In studying the formation of ASBs in of AISI 4340 steel under high strain rate torsion, Feng and Bassim [14] suggested that local material defects or inhomogeneities inside the material will initiate ASBs. Bassim [15] suggested that differences in properties and microstructure cause the material to form ASBs. Local defects and in-homogeneities inside the material act as preferential sites for shear band initiation.

It has also been suggested that specific control of specimen geometry can affect the direction of formation and properties of ASBs. In studying the formation of ASBs in stainless steel, Xue et al. [72] used hat-shaped specimens to control the size, shape, and direction of the shear bands during deformation under high strain rate impact.

ASB formation has been shown to be affected by the size and orientation of grains within the microstructure of the metals prior to deformation. Nesterenko et al. [16] suggested that shear localization initiates along the grains which are favorably orientated. They also suggested that uneven distribution of grain size may act as a perturbation for the formation of ASBs. These authors concluded that larger grains deform initially and can act as preferential sites for shear localization. Meyers et al. [73] investigated the effect of grain size on the high strain rate behavior of copper and suggested that localization of plastic

deformation is observed for the coarse-grain sample while the copper sample with smaller grain size exhibited homogenous plastic deformation.

Recently, several studies have shown the formation of ultra-fine recrystallized grains within shear bands [18, 28, 29] and several authors have attributed this observation to the mechanism of dynamic recrystallization (DRX) [17-26]. The rate of dynamic recrystallization is strongly affected by strain rate [27]. Some authors have proposed mechanisms based on DRX to predict ASBs; many of which are rooted in the behavior of the grains during deformation, including grain rotation, alignment, and refinement [24, 27].

2.4.1.1 Dynamic Recrystallization and Grain Refinement

Recrystallization is a process by which deformed grains are replaced by a set of undeformed grains that nucleate and grow until the original grains are consumed. It is accompanied by a reduction in strength and hardness and increase in ductility. Metals which have been hardened, e.g. cold work, can be softened through recrystallization. It can occur during (dynamic) or after deformation (static). Recrystallization is thought to be thermally activated where the rate of nucleation of new stress-free grains is controlled by temperature. Recrystallization requires a critical temperature above which atomic rearrangement of the

microstructure can occur and a sufficient pre-deformation of the microstructure to provide sufficient stored energy to drive recrystallization. The amount of pre-deformation required is driven by a critical applied stress/strain rate and translates to a specific dislocation density inside the material. This dislocation density defines the amount of stored energy. The grain boundaries of a metal are the sites for nuclei of stress-free grains to form.

The mechanisms of recrystallization under static or low strain rate deformation have been well documented. Bailey and Hirsch [74] first proposed that recrystallization can be represented by a strain-induced boundary migration model (SIBM) where recrystallization is driven by the strain energy and dislocation density difference across an existing high-angle grain boundary in cold worked metal. This driving force causes a portion of the high angle grain boundary to migrate into the subgrain with a higher dislocation density. There is an elimination of dislocations as the high-angle grain boundary migrates through the microstructure, eliminating the dislocations and creating a small, strain-free nucleation point for the growth of new grains by grain-boundary migration.

Li [75] and Hu [76] showed that recrystallization in static annealing occurs through a process of subgrain coalescence whereby subgrains form and rotate to eliminate low angle-grain boundaries. This subgrain rotation produces large misorientations between other

subgrains causing the formation of high-angle grain boundaries and forming new recrystallized grains [77].

Recrystallization under high strain rate deformation has not been well studied due to the difficulty in measuring microstructural evolution under very fast deformation. The mechanism of recrystallization under these conditions have been developed based on analyzing the microstructure of ASBs which form under various conditions of deformation.

It has long been accepted that there is a rapid increase in temperature within adiabatic shear bands, hence the name ‘adiabatic’. However, studies have shown that the temperature rise in ASBs is not high enough to thermally soften or initiate a phase change in the metals [78, 79]. This has been confirmed experimentally by Duffy and Chi [19] and Marchand and Duffy [20] in studying the formation of ASBs in steel. These authors concluded that a different physical mechanism was causing a loss of material stability through local softening attributing the behavior to dynamic recrystallization (DRX). Chokshi and Meyers [21] describe DRX as a thermally activated process which involves the development of dislocation cells and subgrain structures where low angle grain boundaries transform into high angle grain boundaries (through grain rotation and elongation) during plastic deformation. This process is repeated continuously during deformation and eventually leads to the development of a steady-state recrystallized grain size. The heat generated inside the

ASB does not directly soften the material but contributes to the initiation of DRX. Several authors [16-18, 22, 23] also suggested that DRX is the mechanism behind the formation of transformed shear bands in metallic alloys.

Similarly, Doherty et al. [24] defines dynamic recrystallization as the formation of a new grain structure in a deformed material by the formation and migration of high angle grain boundaries (>15° misorientation) driven by the stored energy of deformation. Doherty et al. concluded that the degree of refinement is related to the number of stress free grains which form and is dependent on the total energy of deformation in the system. Metals which undergo DRX appear to have a very fine grain structure. The authors describe the process as the nucleation of new stress free grains in metal which is being deformed under stress. The new grains slowly consume the deformed matrix, lowering the energy of the system.

In studying FCC copper, Meyers and Pak [28] and Hines and Vecchio [18] showed that the microstructure within the shear band consists of fine recrystallized grains, with the finer grains located closer to the center of the band. In studying HY-100 steel, Cho et al. [27] showed that with increasing strain and strain rate, substantial dislocations were produced (dislocation multiplication) in the metal which then combined to form elongated cells (grains). Under an applied stress, the subgrains within the cells would gradually increase

their mis-orientation with respect to their neighbors and eventually breakdown into even finer subgrains.

Xu et al. [80] observed the formation of ASBs in 8090 Al-Li alloy using a split Hopkinson press bar. Subsequent analysis by transmission electron microscope revealed fine equi-axed grains located inside the ASB and proposed that they formed by the mechanism of dynamic recrystallization.

Medyanik et al. [81] developed a physical criterion for ASB formation and propagation based on the hypothesis that the material inside an ASB undergoes DRX under high temperature and high strain rate conditions. They described the onset condition of DRX in terms of a critical temperature. The authors claim that the process of DRX causes a dramatic change in the material's microstructure, considerably refining the microscopic grain size, and is accompanied by a sudden reduction of the dislocation density, finally leading to an instant softening. The authors show that when the temperature in the ASB reaches the critical value, T_{cr}, which is a function of a strain rate, instant softening occurs, which leads to stress collapse. Since DRX does not occur for low values of strain rate, they suggested that T_{cr} is equal to the melting temperature, T_m, for low strain rates when no DRX takes place, and is equal to T_{DRX} for the higher strain rates. Combining the two cases in a single function, the authors developed the following expression for the critical temperature when ASBs form:

$$T_{cr} = T_{DRX} + (T_m - T_{DRX})\frac{\dot{\varepsilon}_{DRX}}{\dot{\varepsilon}_{DRX} + \dot{\varepsilon}} \quad \textbf{Eq. 2-9}$$

where $\dot{\varepsilon}$ is the strain rate and $\dot{\varepsilon}_{DRX}$ is the strain rate when DRX initiates. Medyanik et al. suggested that the critical temperature for stress collapse and instant softening by DRX in metals is about 0.4-0.5 T_m.

In studying ASB formation in copper, Hines and Vecchio [18, 30] proposed that classic recrystallization behavior is too slow to account for the fine recrystallized grains inside ASBs. They proposed a model of progressive subgrain misorientation (PriSM) recrystallization based on the mechanically-assisted subgrain rotation that is kinetically possible under very fast deformation conducive to ASB formation. This model shows that the refined recrystallized grain structure inside the ASB is the result of the rotation of the recovered microstructure where dislocation annihilation causes the transformation of subgrain dislocation walls to grain boundaries.

Recently, in analyzing the microstructural evolution of ASBs in Ta and Ta-W alloy hat-shaped specimens under high strain rate deformation, Pérez-Prado et al. [82] showed no recrystallization inside the ASB, which is in contradiction to many recent reports in the literature [21, 28-29, 83-84] claiming that the refined grain structure inside the formation of ASBs is comprised of stress-free grains from recrystallization. Instead these authors show

that the previous models for ASB formation do not take into account the kinetics of the boundary refinement process and proposed that that ASBs form by a progressive subgrain misorientation (PriSM) recrystallization model.

These authors show that classical recrystallization models cannot account for the microstructural evolution in ASBs. The authors showed an elongation of the dislocation cells near the edge of the shear region and fine-scaled dislocation cells (0.2 μm) in diameter towards the center of the shear region. There was also a non-uniform deformation distribution inside the ASB. Diffraction analysis showed that the degree of misorientation between cells increased with decreasing cell size. Despite the high degree of misorientation, the microstructure in the ASB is not recrystallized due to the presence of large number of dislocations in the cell boundaries contradicting the definition of recrystallization which creates stress-free dislocation-free grains. The temperature rise inside the ASB was not high enough to initiate recrystallization.

In this thesis it will be shown that the grain microstructure kinetics play an important role in the formation of ASBs in steel and that the microstructure around the formation of ASBs is a result of the reorientation and elongation of the grains structure in the direction of maximum shear based on the mechanically-assisted subgrain rotation from the PriSM mechanism. Additionally, it will be shown that the degree of grain rotation depends on the

mechanical and physical properties of the steel controlled by the heat treatment; increasing in softer steels and decreasing in harder steels. A decrease in grain rotation is accompanied by a break-up of the grain structure which increases with increasing impact momentum and applied stress. The resulting refined grain structure inside the ASB is a result of a severely elongated subgrain structure which breaks-up into smaller grains and is accompanied by an increase in dislocation density, contrary to the mechanism of a recrystallized stress-free grain structure.

2.4.2 Experimentation on ASB Formation in Metals

Adiabatic shear bands in metals are known to form at very high strain rates and at large strains under deformation and are a precursor to shear failure. There has been a constant push to improve the strength and reliability of metals and alloys for applications ranging from aerospace and military, to medicine and commercial use to reduce or eliminate the formation of ASBs that form during high strain rate deformation. Modern testing methods for studying the dynamic response of materials under high strain rate or shock loading conditions include the planar impact test using a high velocity projectile [85, 86], Flyer-plate impact [87], the Taylor test [88, 89] which involved cylindrical shaped specimens impacting into fixed walls or two cylindrical specimens impacting into each other; and the

Kolsky bar [90] later modified to test in compression and called the split Hopkinson pressure bar based on work by John Hopkinson [91]. Modifications include the Torsional Hopkinson Bar which allows for deformation under pure shear.

2.4.2.1 The Split Hopkinson Pressure Bar (SHPB)

The Hopkinson bar test is the most commonly used method for determining the dynamic properties of materials during deformation, due to its low cost and high repeatability. Experimentation involving the use of the SHPB to analyze materials under high strain rate deformation has been extensively reported in the literature [92-94]. Applications include determining the dynamic strength of steel in offshore platforms subject to impact, defining the compressive strength of ceramics used in advance armors, evaluating pipeline and nuclear pressure vessel steels, and evaluating the strength of materials on pressurized hulls of the U.S. space station under impact from meteorites or other orbital debris impact. A simplified schematic of the SHPB apparatus is shown in Fig. 18.

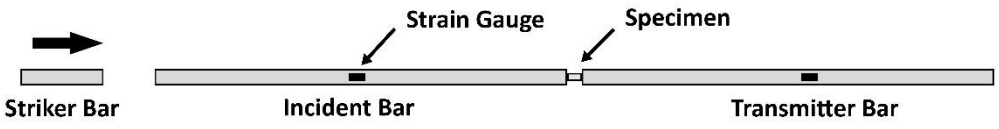

Fig. 18 Simplified Schematic of Split Hopkinson Pressure Bar (illustration by this author)

Information from the SHPB tested specimens is derived indirectly from the wave magnitude signals entering and leaving the specimen via strain gauges placed on the incident and transmitter bars. The incident bar strain gage reads the incident elastic strain wave from the striker bar $\varepsilon_I(t)$ and the resulting reflected wave from the specimen $\varepsilon_R(t)$. The transmitter bar strain gage reads the transmitted wave $\varepsilon_T(t)$. This can be seen in a wave propagation schematic shown in Fig. 19.

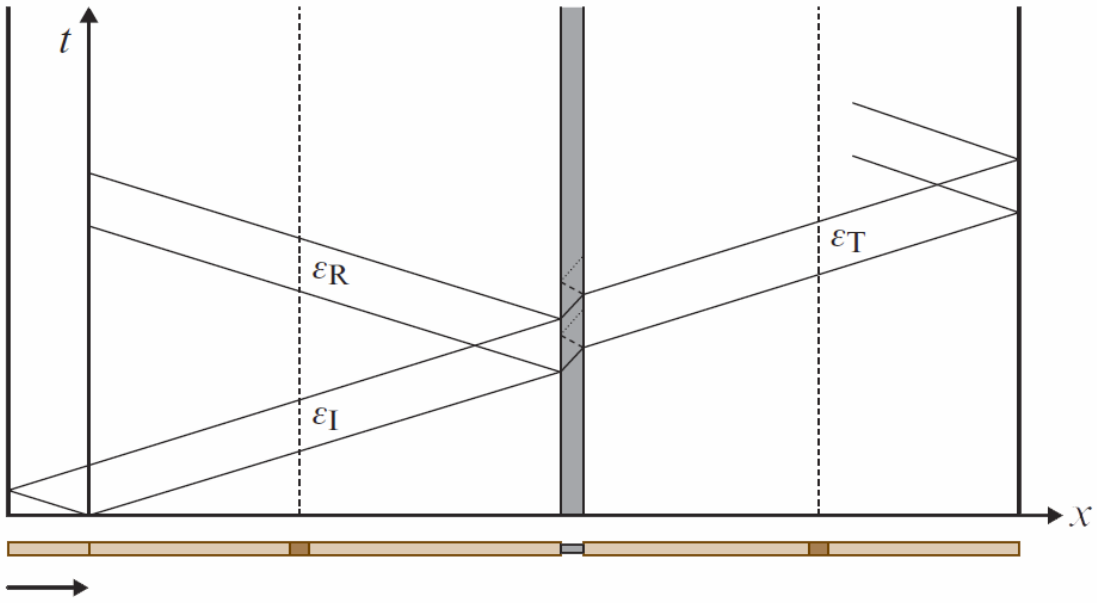

Fig. 19 Wave propagation through a two bar SHPB apparatus (illustration by this author)

These readings are translated into data that can be used to calculate the stress, strain and strain rate of deformation on the specimen which are calculated in Eq. 2-10.

$$\dot{\varepsilon}_s = \frac{2C_0}{L_0}\varepsilon_R(t)$$

$$\varepsilon_s = \frac{2C_0}{L_0}\varepsilon_R(t)\Delta t \qquad \textbf{Eq. 2-10}$$

$$\sigma_s = E\left(\frac{A}{A_0}\right)\varepsilon_T(t)$$

where C_0 is the wave speed of sound through the specimen, L_0 is the original length of the specimen, A_0 is the original cross-sectional area of the specimen, A is the area of the specimen at any time *t*, and E is the modulus of elasticity of the specimen. Under the SHPB configuration, specimens are deformed under a *constant load* and *constant strain rate*. The diameter of the specimen is kept close to the diameter of the incident and transmitting bars. A long incident bar allows for dispersal of the reflected wave so that the deformation of the specimen is controlled solely by the incident wave pulse from the initial impact. The SHPB is capable of achieving strain rates between 10^2 and 10^4 s^{-1}.

There have been modifications to the SHPB apparatus for special purpose dynamic techniques [92]. Song and Chen [95] modified the SHPB to handle high strain rate deformation in soft materials like polymers, polymeric foams and metallic foams.

Similarly, the SHPB has been modified to achieve much higher strain rates than 10^4 and has been used to test for deformation under shock conditions. Foster et al. [96] modified the driving force of the striker bar by replacing the firing mechanism with a pulse accelerometer which achieved a striker force up to 92.88g.

Some authors have been able to achieve controlled ASB formation by changing the geometry of the specimens tested. Andrade et al. [29] and Xue et al. [72] were able to induce ASB formation under impact conditions in the shear direction by using hat-shaped specimens.

2.4.2.2 The Modified Direct Impact Hopkinson Pressure Bar (DIHPB)

Experimentation at the University of Manitoba has shown that the conventional split Hopkinson bar apparatus cannot produce high enough strain rates and deformation at large enough strains to form ASBs in high strength alloys [97]. As a result the split Hopkinson bar apparatus was modified by removing the incident bar and allowing for direct impact of the striker bar onto the specimen. A schematic of the modified Direct Impact Hopkinson Pressure bar is shown in Fig. 20.

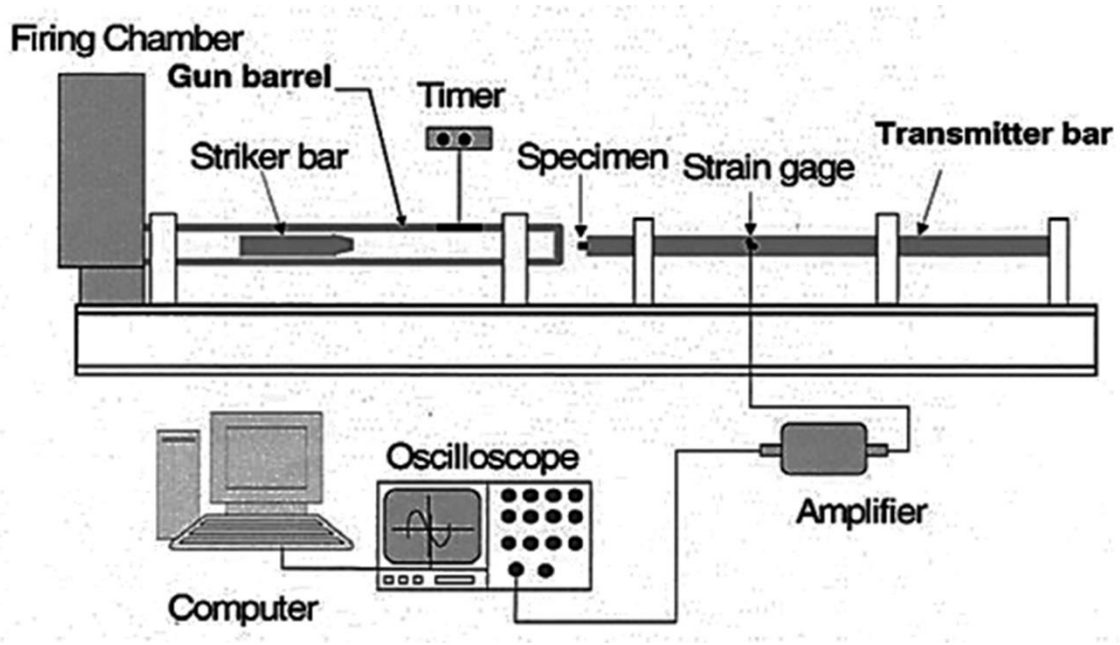

Fig. 20 Schematic of the Direct Impact Hopkinson Pressure Bar (DIHPB)

In this configuration the striker bar and transmitter bar diameters are increased and much larger than the specimen diameter. Fig. 21 shows the wave propagation in the DIHPB when a specimen is impacted. The loading rate and strain rate of deformation are no longer constant. The length of the striker bar is too small for the reflected stress pulses to disperse. Thus, the strain gauge on the transmitter bar reads multiple transmitted pulses.

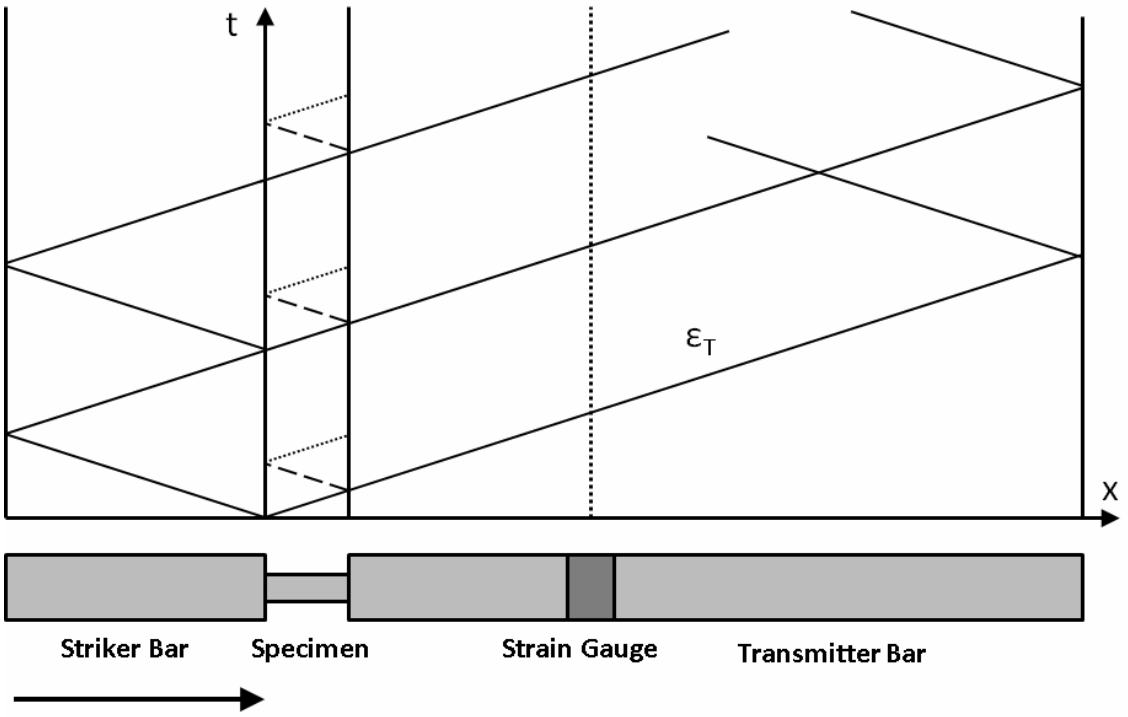

Fig. 21 Wave propagation in the DIHPB apparatus (illustration by this author)

The loading rate is only constant up to the time where the elastic compression wave has travelled from the impact end of the striker bar, reflected from the free end, and returned to the impact end. This time, $t_{\dot{\varepsilon}}$, is defined as

$$0 < t_{\dot{\varepsilon}} < \frac{(2l)}{C_0} \qquad \textbf{Eq. 2-11}$$

where C_0 is the wave speed of sound through the striker bar, and l is the length of the striker bar. After this point in time, the strain rate of deformation is diminished due to the

mechanical impedance mismatch between the striker and specimen. Measurement of the strain rate of deformation after $t_{\dot{\varepsilon}}$ is difficult and thus a constant strain rate is assumed.

2.5 Finite Element Modeling of Metal Deformation

In material science, finite elemental analysis is a powerful tool used to predict material deformation behavior at various length scales and conditions of deformation. Material models are a set of constitutive equations that describe material response under external stimuli such as stresses, forces, strains, or deformations. Model definitions range from a macroscopic scale, defining the stress and strain response of the material in the elastic and plastic range and is based on continuum mechanics; down to atomic scale defining the interaction of atoms in crystallographic unit cells and dislocations. Material failure can also be examined and modeled at various scales ranging from macroscopic characterized by a materials loss of load carrying or energy storage capacity; to mesoscale represented by the formation of voids; to the microscopic formation and propagation of cracks, and finally to atomic scale formation and propagation of dislocations.

2.5.1 Macroscopic Modeling

Early macroscopic material models were very simple, at best including basic relationships between work hardening, strain rate dependence, and thermal softening. They defined the behavior of metals as having an elastic region with perfectly plastic behavior and a linear work hardening [98]. However, these models were only a numeric fit to test data and their accuracy was questionable outside the limited range of this data. Development of material constitutive equations in the field of finite element modeling has evolved, driven by the need to improve efficiency of design in industries such as automotive, aeronautical, and military sectors. In their paper, Rusinek et al. [44] categorize macroscopic constitutive modeling into two main groups:

a) Physical-based Constitutive Models:

These models account for the physical aspects of the material behavior—most grounded on the theory of thermodynamics and kinetic slip and dislocation theory (e.g. Zerilli-Armstrong Model [98]; Feng & Bassim Model [14]). These types of models tend to use a larger number of material constants and their determination procedure follows physical assumptions. They more accurately describe the material behavior under a wider range of loading conditions.

b) Phenomenological Constitutive Models:

These models provide a definition of the material flow stress based on empirical observations—consisting of mathematical functions with lack of physical background that fit experimental observations. They are characterized by a reduced number of material constants and easy calibration. They are used in restricted applications, covering a limited range of strain rate and temperature, and exhibit reduced flexibility for certain materials. Examples of this type of constitutive model include the Johnson-Cook Material Model [11], and it's modification [12, 13].

2.5.2 Physical-based Constitutive Models

Most physical-based constitutive models created to describe the behavior of metals under plastic deformation at both low and high strain rates, bridge the gap between macroscopic continuum mechanics and atomic level dislocation mechanics. They take into account the factors that affect deformation and more specifically the resistance to deformation. These include: dislocations overcoming periodic lattice potentials, interactions between dislocations, interactions between dislocations and solute atoms, dislocations overcoming the long-range elastic stress field caused by grain boundaries, precipitates,

dislocation forests, and other defects, as well as dislocations overcoming the viscous drag [99]. An examples of a popular physical-based model used for defining high strain rate deformation of metals is the Zerilli-Armstrong model which is based on dislocation mechanics and defines the flow stress of both BCC and FCC metals [98]. However, this model is limited in that it cannot be used for strain rates that exceed the maximum elastic wave speed through the material, i.e. shockwave speeds.

2.5.3 The Empirical Johnson-Cook Constitutive Model

The most popular material constitutive model for simulating high strain rate plastic deformation of metals is the Johnson-Cook plasticity model. Although it is an empirical model that is heavily dependent on experimental data with a dependency on strain hardening law and strain rate, material data can be gathered quite easily. It is typically used in adiabatic transient dynamic simulations. This model was developed in 1983 by Johnson and Cook [11] to describe the behavior of several metals including Armco Iron, 4340 steel and OFHC copper during cylindrical impact loading.

2.5.3.1 Johnson-Cook Hardening Law

The Johnson-Cook hardening law defines how a metal hardens under plastic loading. Johnson-Cook hardening is isotropic, where the dynamic flow stress, σ_o, is assumed to be of the form:

$$\sigma_o = [A + B(\bar{\varepsilon}^{pl})^n]\left(1 - \hat{T}^m\right) \qquad \textbf{Eq. 2-12}$$

where $\bar{\varepsilon}^{pl}$ is the equivalent plastic strain, A is the yield strenth at a strain rate of 1/s, B is the strain hardening coefficient, n is the strain hardening exponent, m is the thermal sensitivity parameter and $\hat{T}$ is a non-dimensional homologous temperature defined as:

$$\hat{T} = \frac{\left(T - T_{ref}\right)}{\left(T_m - T_{ref}\right)} \qquad \textbf{Eq. 2-13}$$

The terms in the brackets of Eq. 2-12 define a power law relationship between true stress and effective plastic strain of the material. The term T_{ref} represents the ambient room temperature, and T_m is the melting temperature of the material.

2.5.3.2 Johnson-Cook Strain Rate Dependence

Johnson-Cook strain rate dependence assumes

$$\bar{\sigma} = \sigma_o(\bar{\varepsilon}^{pl}, T)R\left(\dot{\bar{\varepsilon}}^{pl}\right) \qquad \textbf{Eq. 2-14}$$

and

$$\dot{\bar{\varepsilon}}^{pl} = \dot{\varepsilon}_o exp\left[\frac{1}{C}(R-1)\right] \quad for\ \bar{\sigma} \geq \sigma_o \qquad \textbf{Eq. 2-15}$$

where $\bar{\sigma}$ is the yield stress at non-zero strain rate; $\dot{\bar{\varepsilon}}^{pl}$ is the equivalent plastic strain rate; $\dot{\varepsilon}_o$ is the reference strain rate used to determine A,B, and n which is most commonly set to equal 1, *C* is the strain rate sensitivity factor; and *R* is the ratio of the yield stress at non-zero strain rate to the quasi-static yield stress so that $R(\dot{\varepsilon}_o) = 1$. There is a logarithmic dependence on strain rate. The Johnson-Cook representation of the dynamic flow stress is thus:

$$\sigma_o = [A + B(\bar{\varepsilon}^{pl})^n]\left[1 + Cln\left(\frac{\dot{\bar{\varepsilon}}^{pl}}{\dot{\varepsilon}_o}\right)\right]\left(1 - \hat{T}^m\right) \qquad \textbf{Eq. 2-16}$$

2.5.4 The Modified Johnson-Cook Model and Improved Strain Rate Forms

The standard Johnson-Cook model of flow stress has a linear logarithmic relationship to strain rate. While this form is adequate, most materials exhibit a bi-linear or tri-linear dependence of strength on the logarithm of the strain rate, often seen at very high strain rates (>10^3 and >10^4 respectively) [100]. The modified Johnson-Cook model [12, 13] removes the logarithmic dependence of strain rate to avoid unwanted effects when $\dot{\varepsilon}_o < 1$ and defines the flow stress as

$$\sigma_o = [A + B(\bar{\varepsilon}^{pl})^n]\left[1 + \frac{\dot{\bar{\varepsilon}}^{pl}}{\dot{\varepsilon}_o}\right]^C \left(1 - \hat{T}^m\right) \quad \textbf{Eq. 2-17}$$

Finite element software LS-DYNA [5] provides alternative strain rate forms that define the strain rate dependence on flow stress. Depending on the materials selected, these forms may either improve or reduce the accuracy of the simulation. The best form can be chosen when analyzing the dynamic response data obtained from experimentation and comparing to the quasi-static response.

2.5.4.1 The Huh-Kang Strain Rate Form

In analyzing high strain rate impact of thin walled high strength steel sheet used in vehicles for crash-worthiness testing, Huh and Kang [101] proposed a strain-rate form that has a quadratic logarithmic dependence on plastic strain rate and is of the form:

$$1 + C_1 ln\dot{\varepsilon} + C_2 (ln\dot{\varepsilon})^2 \qquad \textbf{Eq. 2-18}$$

and replaces the single term linear logarithmic dependence on strain rate in the traditional Johnson-Cook model.

2.5.4.2 Allen-Rule-Jones Strain Rate Form

Allen et al. [102] proposed a strain-rate form that is an exponential of the effective plastic strain rate, $\dot{\varepsilon}^C$, similar to the form used in the modified Johnson-Cook model, based on data from Taylor-impact tests of various metals.

2.5.4.3 Cowper-Symonds Strain Rate Form

Cowper and Symonds [103] analyzed the rate effects in the impact loading of cantilever beams and devised the strain rate form

$$1 + \left(\frac{\dot{\varepsilon}}{C}\right)^{\frac{1}{P}} \qquad \textbf{Eq. 2-19}$$

as a two parameter exponential dependence on strain rate.

2.5.4.4 The Johnson-Cook Dynamic Failure Model

The Johnson Cook Dynamic Failure Model is used to model the initiation and progressive failure of ductile metals, and is based on the value of the equivalent plastic strain at element integration points. Failure is initiated when the damage parameter exceeds one. The damage parameter, D, is defined as

$$D = \sum \left(\frac{\Delta\bar{\varepsilon}^{pl}}{\bar{\varepsilon}_f^{pl}}\right) = \int_0^{\bar{\varepsilon}_f^{pl}} \frac{d\bar{\varepsilon}^{pl}}{\bar{\varepsilon}_f^{pl}} = 1 \qquad \textbf{Eq. 2-20}$$

where $\Delta\bar{\varepsilon}^{pl}$ is an increment of equivalent plastic strain, $\bar{\varepsilon}_f^{pl}$ is the strain at failure, and the summation is performed over all increments in the analysis. The failure strain is assumed to be dependent on the non-dimensional plastic strain rate $\frac{\dot{\bar{\varepsilon}}^{pl}}{\dot{\varepsilon}_o}$; a dimensionless pressure-deviatoric stress ratio or stress triaxiality, *p/q* (where *p* is the pressure stress ($[\sigma_1 + \sigma_2 + \sigma_3]/3$)

and q is the Mises stress); and the non-dimensional temperature $\hat{T}$, defined in the Johnson-Cook hardening model. The dependencies are assumed to be separable and are of the form:

$$\bar{\varepsilon}_f^{pl} = \left[d_1 + d_2 \exp\left(d_3 \frac{p}{q}\right)\right]\left[1 + d_4 ln\left(\frac{\dot{\bar{\varepsilon}}^{pl}}{\dot{\varepsilon}_o}\right)\right]\left[1 + d_5 \hat{T}\right] \quad \textbf{Eq. 2-21}$$

where d_1 through d_5 are failure parameters and $\dot{\varepsilon}_o$ is the reference strain rate. The modified Johnson-cook damage model becomes:

$$\bar{\varepsilon}_f^{pl} = \left[d_1 + d_2 \exp\left(d_3 \frac{p}{q}\right)\right]\left[1 + \frac{\dot{\bar{\varepsilon}}^{pl}}{\dot{\varepsilon}_o}\right]^{d_4}\left[1 + d_5 \hat{T}\right] \quad \textbf{Eq. 2-22}$$

Most materials experience an increase in plastic failure strain with increasing pressure deviatoric stress ratio. When the failure criterion is met there is an instantaneous failure. The material parameters d_1, d_2, d_3 and d_4 are determined by specimen tests under different triaxialities: pure compression tests (p/q = -0.3333), shear tests (p/q = 0), smooth tension tests (p/q = 1/3), notched transverse tests (p/q = 0.5). The damage parameters are obtained by fitting a curve of Eq. 2-22 through these points.

2.5.4.5 The Cockroft-Latham (CL) Fracture Criterion

The Cockroft-Latham (CL) tensile fracture criterion used in modeling sheet metal forming [104] assumes material failure occurs when the plastic work per unit volume, *W*, exceeds a critical value defined as

$$W = \int_0^{\bar{\varepsilon}_f^{pl}} \frac{\langle \sigma_1 \rangle}{\bar{\sigma}^{pl}} d\bar{\varepsilon}^{pl} \leq W_{CR} \qquad \textbf{Eq. 2-23}$$

$$\langle \sigma_1 \rangle = \begin{cases} \sigma_1 \; when \; \sigma_1 \geq 0 \\ 0 \; when \; \sigma_1 < 0 \end{cases}$$

where σ_1 is the maximum tensile principal stress, and $\bar{\varepsilon}_f^{pl}$ is the total equivalent plastic strain at fracture. This model is similar to the Johnson-Cook damage model and implies that fracture is a function of the tensile stresses and equivalent plastic strain. However, *if the maximum principal stress is compressive, fracture cannot occur*. Furthermore, neither stresses nor strains alone are sufficient to cause fracture. The critical value of W_{cr} is the area under the plastic true stress-strain curve in tension up to fracture and can be determined by simple uniaxial tensile tests. In FEM simulations, element failure occurs when $W = W_{cr}$. Cockroft-Latham damage evolution is defined as

$$\dot{D} = \frac{D_c}{W_{cr}} \langle \sigma_1 \rangle \dot{\bar{\varepsilon}}^{pl}$$

Eq. 2-24

$$D = \int_0^{\bar{\varepsilon}_f^{pl}} \frac{\langle \sigma_1 \rangle}{\bar{\sigma}^{pl}} d\bar{\varepsilon}^{pl} \leq D_C$$

where D_C is the critical damage parameter at fracture defined as unity for most materials. The damage in plastic deformation is defined by Cockroft and Latham as the amount of work that the ratio of maximum tensile stress σ_1 to effective plastic stress $\bar{\sigma}^{pl}$ carries out through the applied equivalent plastic strain $\bar{\varepsilon}^{pl}$.

2.5.4.6 Temperature Rise due to Adiabatic Heating

In studying the formation of ASBs under deformation at high strain rates and larges strains, it is important to be able to calculate the temperature rise for the purpose of understanding the microstructural evolution of metals during deformation. The temperature increment due to adiabatic heating is calculated by

$$\Delta T = \int_0^{\bar{\varepsilon}^{pl}} \chi \frac{\bar{\varepsilon}^{pl} d\bar{\varepsilon}^{pl}}{\rho C_p}$$

Eq. 2-25

where ρ is the material density, C_p the specific heat and χ the Tylor-Quinney coefficient that represents the proportion of plastic work converted into heat. Typically this value is

equal to 0.9 for adiabatic heating, first calculated for copper by Taylor and Quinney [105], and then universally used for all materials. The Taylor-Quinney coefficient varies with strain and strain rate for steel [106] but a value of 0.9 will be used for all simulations in this thesis.

Additionally, according to Lederman et al. [107] the specific heat of steel varies with temperature by the equation:

$$C_p = \begin{cases} A_1 + B_1 t + C_1 |t|^{-a} & if\ T < T_C \\ A_2 + B_2 t + C_2 t^{-a'} & if\ T > T_C \end{cases} \quad \textbf{Eq. 2-26}$$

where

$$t = \frac{T}{T_C} - 1$$

and T_c is the critical temperature at which the phase transformation from the α to the γ phase takes place, and A_1, A_2, B_1, B_2, α, and α' are constants. In this thesis a constant specific heat C_p = 465 [J/kg/K], equal to that of annealed AISI 4340 steel was used for all heat treatments [108].

A temperature based failure criterion for ASB formation can be adopted based on temperature rise in the material during deformation. In studying the deformation of spirl-strand steel cables subject to high velocity fragment impact, Judge, et al. [109] used a temperature based failure criterion in their simulations that assumed metal failed when T_c = $0.9T_m$, where T_m is the melting temperature of the steel. At this temperature the material becomes too soft and loses its strength carrying capacity.

2.5.5 Continuum Modeling Limitations

Macroscopic constitutive material models assume the material to be analyzed behaves in the continuous mass or that the object to be modeled is completely homogenous. A continuous physical body can be continually subdivided into infinitesimal elements with properties being those of the bulk material. In reality, a solid object's properties become heterogeneous as the length scale is reduced. On a nanoscopic scale, materials such as solids, liquids and gases, are composed of molecules separated by "empty space". On a microscopic scale solids such as metals are made up of grains which can contain multiple phases, impurities, discontinuities or even micro-cracks. When the length-scale is large the heterogeneity of materials becomes irrelevant and a continuum assumption can be made.

In general continuum modeling can be used to simulate metal deformation behavior in the elastic and plastic region accurately up to a certain deformation strain rate. Phenomena such as ASBs which form at particularly high strain rates and large strains in metals are discontinuous and form as severely localized deformation. This form of deformation cannot properly be modeled in continuum mechanics and assumptions must be made. The properties of ASBs have been found to be different than that of the bulk material.

2.5.6 Modeling ASB Formation

There have been many studies in the literature using macroscopic modeling to simulate ASB formation in metals [14, 30-37]. These models assume ASB formation is synonymous with material failure defined by a loss of load carrying capacity (stress collapse) using failure models. Metals contain a variety of characteristic defects and phase compositions induced though manufacturing and heat treatment processes. The formation of ASBs and the mechanisms behind them are strongly driven by microstructure. The mechanical behavior of metals at the microscopic level is strongly influenced by chemical composition, phase distribution, and microstructural geometry such as grain size, shape, and orientation [110]. Some authors have developed models for simulating ASB formation based on the importance of microstructure [111-113]. These models take into effect the heterogeneity of material properties and imperfections which exist in the microstructure.

Additionally, there have been models developed to define microscopic failure which combine the advantages of continuum mechanics and classic fracture mechanics [114]. They are based on the concept of ductile fracture through microvoid formation and coalescence during plastic deformation. The most prominent of such models was first proposed by Gurson [115] and extended by Tvergaard and Needleman [116], called the GTN model.

Gurson's model assumes that metallic materials can be considered porous on the microstructural level and is governed by the first and second stress invariant and the initial void volume fraction. Tvergaard and Needleman included void nucleation, growth and coalescence to Gurson's model in a phenomenological way. They showed that voids nucleate and grow until a local plastic fracture of the intervoid matrix occurs, which causes the coalescence of neighboring voids.

Xue [117] expanded the GTN model to incorporate the void shearing mechanism of damage by looking at the dependence of damage evolution on the third stress invariant. This model is based on work done by McClintock et al. [118] who proposed a damage model based on the void evolution in localized shear banding.

Several authors have also shown that ASB formation may be simulated on the microscopic scale by modeling dynamic recrystallization and kinematics of grain deformation. Hines et al. [30] developed a mechanical subgrain rotation model that accounts for the recrystallized grains which have been observed in adiabatic shear bands based on testing of copper hat shaped specimens under impact conditions using a split Hopkinson pressure bar. Hallberg et al. [38] developed a constitutive model for Aluminum 1050 for grain refinement due to continuous dynamic recrystallization on the micromechanical scale. Yazdipour et al. [39] modeled recrystallization and grain growth in austenitic stainless steel

304 during hot torsion using a 2D irregular cellular automata method. This method is popular in simulating initial microstructure and dynamic recrystallization.

There are a number of numerical models used for grain-level microstructural material simulations: (1) Multi-phase field models [119]—used in modeling solid state phase transformations, grain growth, recrystallization where microstructure is described by a set of order parameters, each of which is related to a specific crystallographic orientation; (2) the Monte-Carlo (Cellular Potts) model which is a lattice based model used to simulate the collective behavior of cellular structures such as grains and is thought of as a generalized version of the Cellular Automata method; (3) Voronoi Tessellation based models which is a mathematical model that tessellate a space with seeds that are encircled with shapes whose interior consist of all points closer to that particular seed than any other seed. Zhang et al. [120] developed a controlled Poisson Voronoi tessellation model for producing 2D virtual grain structures that are statistically equivalent to metallographic observations of polycrystalline materials in terms of grain size distributions. Fan et al. [121] proposed a Voronoi tessellated microstructure model for polycrystalline materials based on a random closed packing of spheres.

2.5.7 Meshing Techniques

Finite element analysis uses meshing to divide complex problems into smaller elements using a grid. Traditional grid-based meshing techniques, i.e. Lagrangian and Eulerian, have been commonly used to discretize areas or volumes of material for numerical and computational FE problems.

2.5.7.1 The Lagrangian Meshing Formulation

The Lagrangian meshing technique uses a grid which is fixed to or attached to the material throughout the entire computational process, and moves with the material. Any movement of the connecting nodes results in expansion, compression and deformation of a meshed cell (or element). When the material deforms, the mesh deforms accordingly. A Lagrangian mesh is represented in Fig. 22.

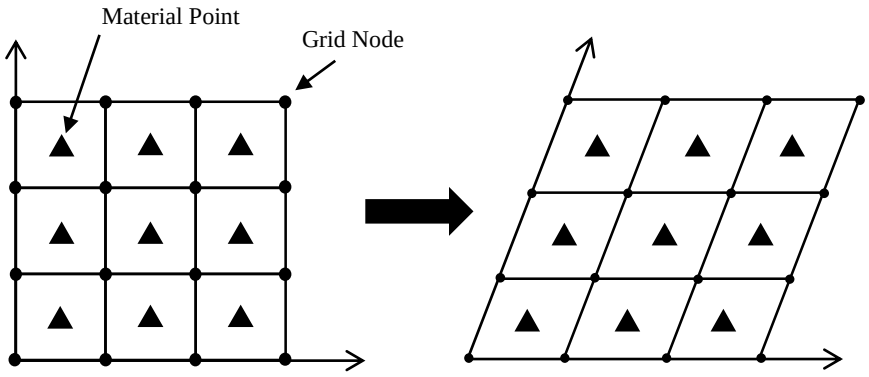

Fig. 22 Lagrangian mesh representation of a set of grid and material points (illustration by this author)

Mass, momentum, and energy are transported with the movement of the meshed cells. Because the mass within each cell remains fixed, no mass flux crosses the mesh cell boundaries [122]. Some advantages of using this method include:

1. Low computational cost and reduction in computation time due to lack of convective term in the related partial differential equations
2. Easy tracking of time history of field variables at material points due to a fixed grid on a moving material.
3. Irregular or complicated geometries can be meshed using an irregular mesh

This grid-based method fails when the mesh becomes extremely distorted, i.e. in large deformation applications or penetration simulations. When the mesh is heavily distorted, i.e. when the elements have extremely high aspect ratio, the accuracy of the formulation and

solution is affected greatly. Simulation fails when the boundaries of an element cross-over itself. Reducing element size by refinement can reduce the distortion. However, the time step, which is controlled by the smallest element size, can approach zero eventually breaking down the computation. Adaptive re-meshing techniques which dynamically re-mesh the model can be implemented at the expense of high computational costs to avoid these issues. The meshed Lagrangian method is a popular method used in simulating the deformation of solids.

2.5.7.2 The Eulerian Meshing Formulation

Unlike the Lagrangian meshing technique, the Eularian grid is fixed in space and the simulated area or volume moves across fixed meshed cells in the grid. The Eulerian grid nodes are fixed and do not change with time while the material flows across the mesh. The Eularian mesh representation can be seen in Fig. 23.

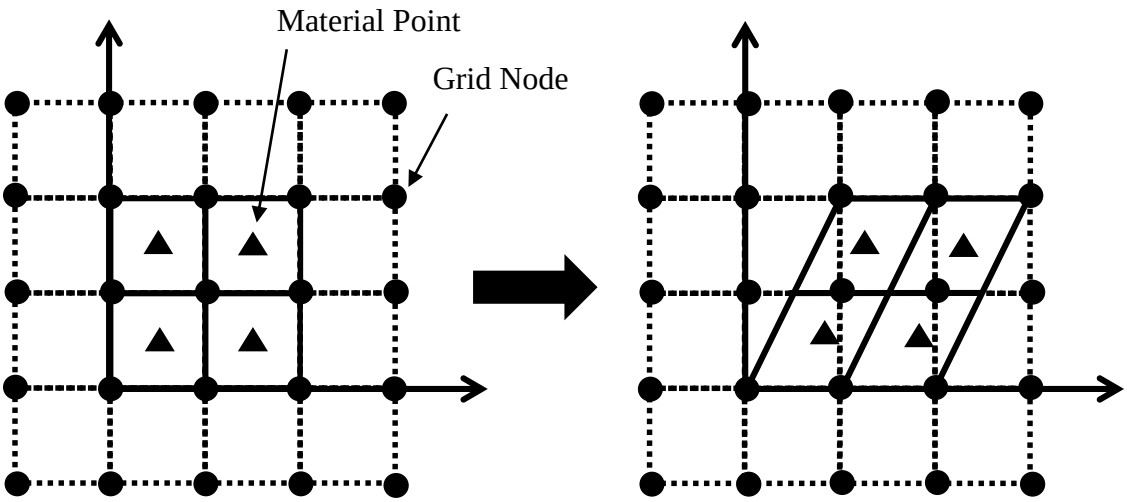

Fig. 23 Eularian mesh representation of a set of grid and material points (illustration by this author)

Mass flux, momentum and energy across mesh cell boundaries are simulated to compute the distribution of mass, velocity, energy, etc. in the problem domain. The shape and volume of the meshed cell remains unchanged during computation.

Large deformations in the object do not cause any deformations in the mesh itself and do not cause the same kind of numerical problems as in the Lagrangian method. As a result Eulerian methods are dominant in the area of computational fluid dynamics, where flow of the material is commonplace. However there are a number of disadvantages to the Eulerian method. Some include:

1. Difficulty in analyzing the time history of field variables at a fixed point on the material, because the movement of the material cannot be tracked.

2. Expensive numerical mapping is required to treat irregular or complicated geometries of material/media.
3. The position of free surfaces, deformable boundaries, and moving material interfaces are difficult to be determined accurately since Eulerian methods track the mass, momentum, and energy flux across the mesh cell boundaries.
4. A coarse grid is often needed for computational efficiency at the expense of resolution of domain discretization and accuracy of the solution in cases of large computational domains or areas where the material can possibly flow.

2.5.7.3 Arbitrary Lagrangian-Eulerian Method

To overcome many of the disadvantages of purely Lagrangian and Eulerian meshing techniques many simulation problems involving both liquids and solids use a combined meshing technique known as Arbitrary Lagranian-Eularian (ALE) finite element technique. Problems meshed with ALE have a mesh which is either fixed in space (Eularian) or attached to a material (Lagrangian) [123]. The mesh can also move arbitrarily to optimize the shapes of the elements, while the mesh on the boundaries and interfaces of the domains move along with the materials to track the boundaries and interfaces of a multi-material system. This arbitrary movement allows for greater distortion of the continuum compared with purely Lagrangian methods. The ALE method can be used in coupled multi-physics and multi-

material problems (moving boundary and interfaces); fluid-structure interaction, and manufacturing problems (metal forming/cutting, casting).

2.5.7.4 Meshless Modeling using Smoothed Particle Hydrodynamics (SPH)

The difficulties and limitations of grid-based methods are evident when simulating hydrodynamic phenomena such as explosion and high velocity impact, both of which involve large deformations, large in-homogeneities, moving material interfaces, deformable boundaries, free surfaces, and possibly penetration of one material into another. Some high velocity impacts involve shock waves propagating through colliding or impacting bodies that behave like fluids.

Grid-based numerical methods are also not suitable for situations where objects undergo localized discontinuous deformation or deformation outside of the continuum spectrum. This applies to materials which are better defined by a set of discrete physical particles rather than a continuum, e.g. movement of millions of atoms in equilibrium or non-equilibrium state, granular materials which flow like sand, etc. This lead to the development of mesh-free methods which provide an accurate and stable numerical solution for non-continuum problems.

A popular meshfree method is the Smoothed Particle Hydrodynamics (SPH) method first developed by Lucy [124] and Gingold and Monaghan [8] in 1977 to model astrophysical phenomena and then extended to applications of solid and fluid mechanics by Libersky and Petchek [9, 10] in 1990, and Randles and Libersky [125] in 1996; and then implemented into finite element software LS-DYNA [126]. SPH is a meshless Lagrangian method that can be used to simulate problem with large irregular geometry.

Mathematically, each SPH particle represents an interpolation point on which all the properties of the material are known. The solution of the entire domain is then calculated on all particles with a regular interpolation function, called the smoothing length, over which the properties of the material are smoothed. The equations of conservation are equivalent to the fluxes or inter-particlar forces. In finite elements, there is only one spatial discretization parameter: the characteristic length of the mesh. In SPH there is an additional parameter determine the spatial resolution: the smoothing length. Each SPH particle has a smoothing length which depends on the local number of particles. Due to the lack of a numerical grid SPH particles require the setting of initial masses and coordinates. The particle coordinates also needs to be sufficiently regularly distributed so that all particles in a given neighborhood have the same mass to ensure convergence and avoid instabilities. Consequently, the particles of the same material, need to have the same density and initial volume.

The main advantage of SPH is the ability to simulate large local distortions or deformations in solid mechanics, e.g. metal forming, impact, crack growth, fracture, fragmentation, etc. Mesh dependence problems are avoided.

One of the main disadvantages of the SPH meshless formulation is that it is considerably more computationally expensive to use than Lagrangian, Eulerian, or ALE meshed formulations.

In this thesis the SPH method is used to more accurately simulate large localized distortion and ASB formation.

This chapter gave an overview of the microstructure of metals, and steel and covered the effect of heat treatment and chemical composition on the mechanical properties of steels. A review of current experimental and theoretical procedures for predicting ASB formation in the literature was also presented. The next chapter outlines the experimental investigation performed in this thesis for analyzing the formation of ASBs in AISI 4340 steel under impact to map out the effect of microstructure and mechanical properties, as well as testing conditions on the formation of ASBs. The experimental investigation provides a basis for the development of a simulation model to simulate the kinetics of the microstructural based mechanism of ASB formation in steel.

3. EXPERIMENTAL INVESTIGATION

3.1 Experimental Set-up

It has been reported in the literature that the grain size of steel changes with heat treatment temperature [45, 127-128]. A proper simulation of the impact behavior of such a material, therefore, requires a good understanding of the microstructure of the material before and after impact. An experimental program was designed to determine (a) the effect heat treatment on the grain size of AISI 4340 steel, and (b) the conditions that lead to the formation of ASBs. The information obtained was used to determine the optimal heat treatment process for reducing ASB formation and to develop the simulation model. To meet the objectives of the experimental investigation, the following parametric variations were selected:

- Type of steel: AISI 4340
- Heat Treatments: 800°C, 900°C, 1000°C / 30mins, oil quenching, & tempering at 400°C/90mins and 550°C/90mins
- Impact momenta: 30kgm/s, 45kgm/s, 49kgm/s, 52kgm/s
- Testing Temperatures: 20°C, 428°C

Specimens were tested under impact using the Direct Impact Hopkinson Pressure Bar (DIHPB) shown in Fig. 20. Modifications were made to the existing DIHPB with the addition of a custom built furnace which could be used to heat specimens up to 1200°C as well as the addition of a specimen loading apparatus that minimizes the time between heating and impact. These modifications are shown in Fig. 24.

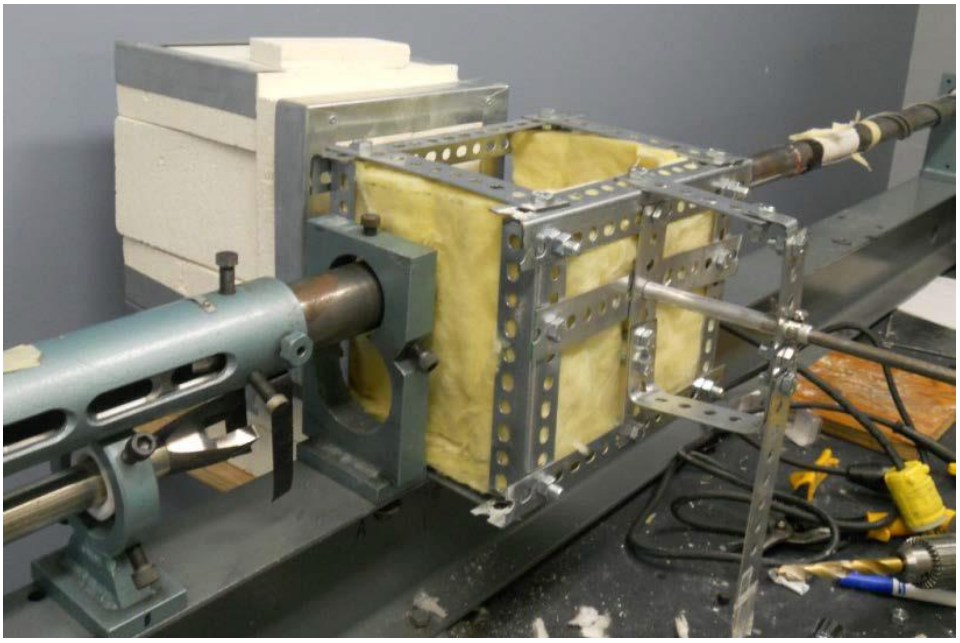

Fig. 24 Furnace and high temperature test chamber attachment to DIHPB showing interior and control box

The steel was supplied as an annealed 3/8 inch (9.525 mm) nominal diameter rod 4 feet in length (1219.2 mm) which was cut into 9.5 mm pieces, providing a one to one length to diameter ratio. The dimensions of the specimens are shown in Fig. 25.

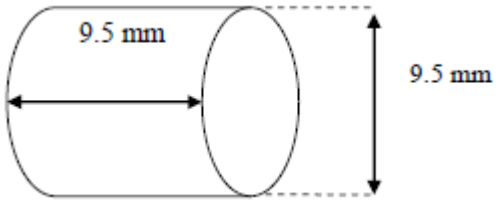

Fig. 25 Cylindrical test specimen geometry used in the DIHPB (illustration by this author)

Prior to heating, the cylindrical specimens were placed at the center of a circular piece of high temperature ceramic insulation. The ceramic insulation was then placed in a ring of steel screwed to a rod which was held close to the transmitter bar, as shown in Fig. 26.

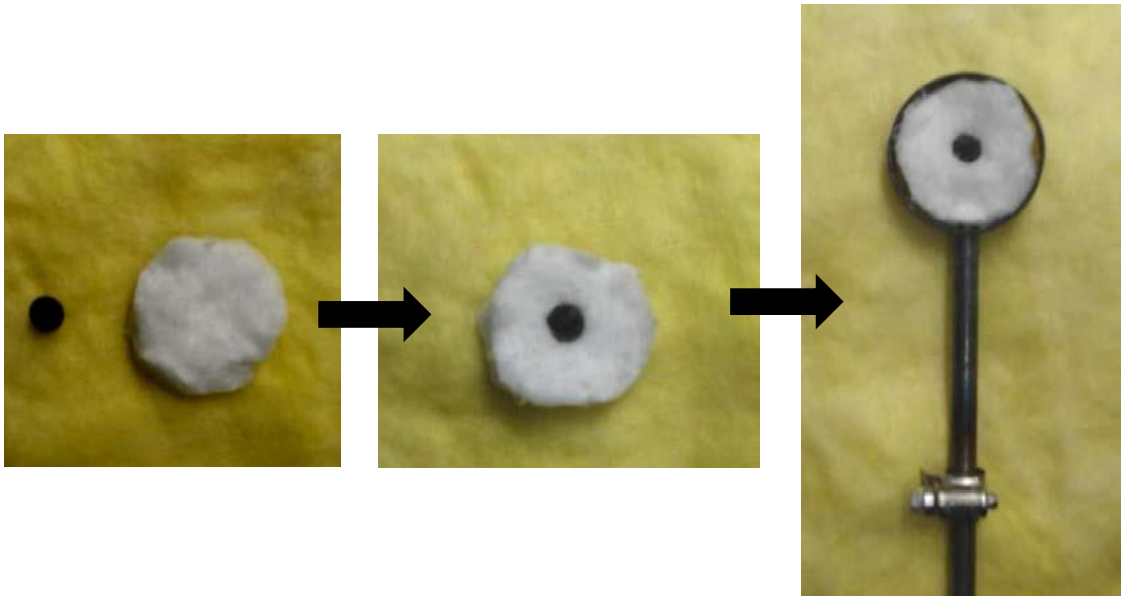

(a) (b) (c)

Fig. 26 Fixture arm for holding specimen

Prior to testing, the specimen was fed into the furnace through a hole and heated to the desired temperature, as shown in Fig. 27, and held there for two minutes to allow sufficient and uniform heating to take place. This length of time was an estimation of the total amount of time required to heat a specimen to a uniform stabile temperature based on the efficiency of the temperature controller (the degree at which if fluctuates to maintain a temperature) and effectiveness of insulation at the furnace door. The temperature in the furnace was monitored through a thermocouple attached to a temperature control device.

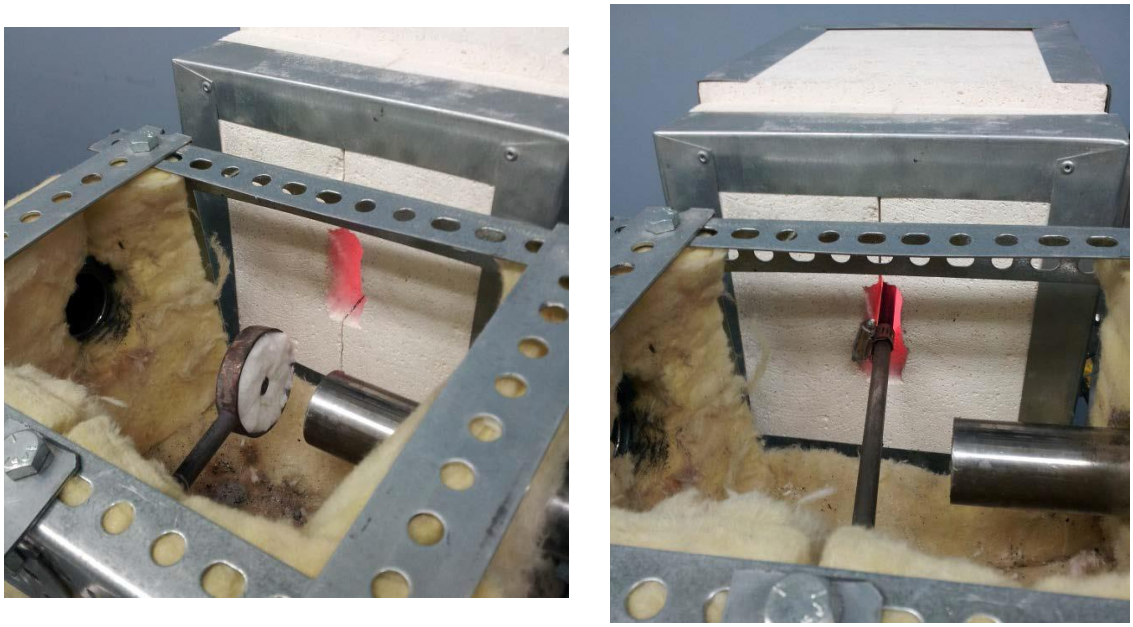

Fig. 27 Loading of specimen into furnace using specially designed loading arm

The specimen was then retracted, aligned with the transmitting bar and impacted. Preliminary testing with a thermo-coupled specimen showed a rate of cooling in air of 1°/s from a temperature of 450°C. Mounting of the thermocouple was achieved drilling a 0.0625 inch (1.5875 mm) diameter hole through the center of the specimen along the longitudinal axis, to a depth of approximately 6 mm to accept the end of a thermocouple probe. The twisted end of a K-type thermocouple was threaded into the specimen until it was held securely and the other ends of the thermocouple wires were attached to a digital multimeter with maximum resolution of 1mV. Time measurements were taken and voltage was converted to temperature based on a thermocouple Seebeck Coefficient of 41 μV/°C. The rate of cooling allowed for a large enough window of time between removal of the specimen

and impact for specimens tested at 428°C. This testing temperature was chosen as it is approximately 30% of the melting temperature of 4340 steel and below the austenization temperature. Air-cooling rate was also measured for each tempering process to be approximately 1.0°C/s from 550°C and 400°C to room temperature.

3.2 Materials

Specimens were cut from high strength low-alloy AISI 4340 steel rods with a diameter of 3/8 inch or 9.525 mm. This steel was selected since it is commercially available and may be heat-treated to achieve a wide range of mechanical properties. AISI 4340 steel is a medium-carbon, low-alloy martensitic steel whose principal alloying elements are nickel, chromium, and molybdenum.

3.3 Heat Treatment and Microstructure of AISI 4340 steel

Heat treatment (hardening) and tempering alters the mechanical properties of steel by controlling the rate of diffusion of carbon and alloying elements in the iron crystal structure when heated or cooled at extreme temperatures. To achieve the desirable range of

mechanical properties for testing, AISI 4340 steel cylindrical specimens, shown in Fig. 28, were rapidly heated to various temperatures above austenization (800°C,900°C,1000°C) for 30 minutes followed by oil quenching to produce a martensitic structure. The specimens were then tempered at two different tempering temperatures 400°C and 550°C for 90 minutes followed by air cooling. These temperatures were chosen as they maximize the range of tempering for testing, while avoiding the embrittlement ranges. Tempering below 375°C and above 600°C, causes the steel to suffer from temper embrittlement which is accompanied by a significant reduction in toughness [129].

Fig. 28 AISI 4340 Steel Specimen prior to heat treatment

Fig. 29 AISI 4340 steel specimen after heat treatment

A summary of the various heat treatment temperatures and testing parameters for all specimens is summarized in Table 1. A total of 48 specimens were tested.

Table 1. Summary of Experimental Investigation

HEAT TREATMENT PARAMETERS		TESTING PARAMETERS	
Austenization Temperature (°C)/Time	**Tempering Temperature (°C)/Time**	**Testing Temperature (°C)**	**Impact Momentum (kgm/s)**
800°C/30mins 900°C/30mins 1000°C/30mins	550°C/90mins	20	30
			45
			49
			52
		428	30
			45
			49
			52
	400°C/90mins	20	30
			45
			49
			52
		428	30
			45
			49
			52

The range of impact momenta was selected on the basis of the capabilities of the DIHPB which are directly related to the air pressure in the firing chamber. The heat treatment and tempering processes chosen for experimentation are shown in Fig. 30. Specimens were heat treated for 30 minutes, oil quenched, and then tempered with a controlled heating rate over 10 minutes followed by air cooling at 1°C/s.

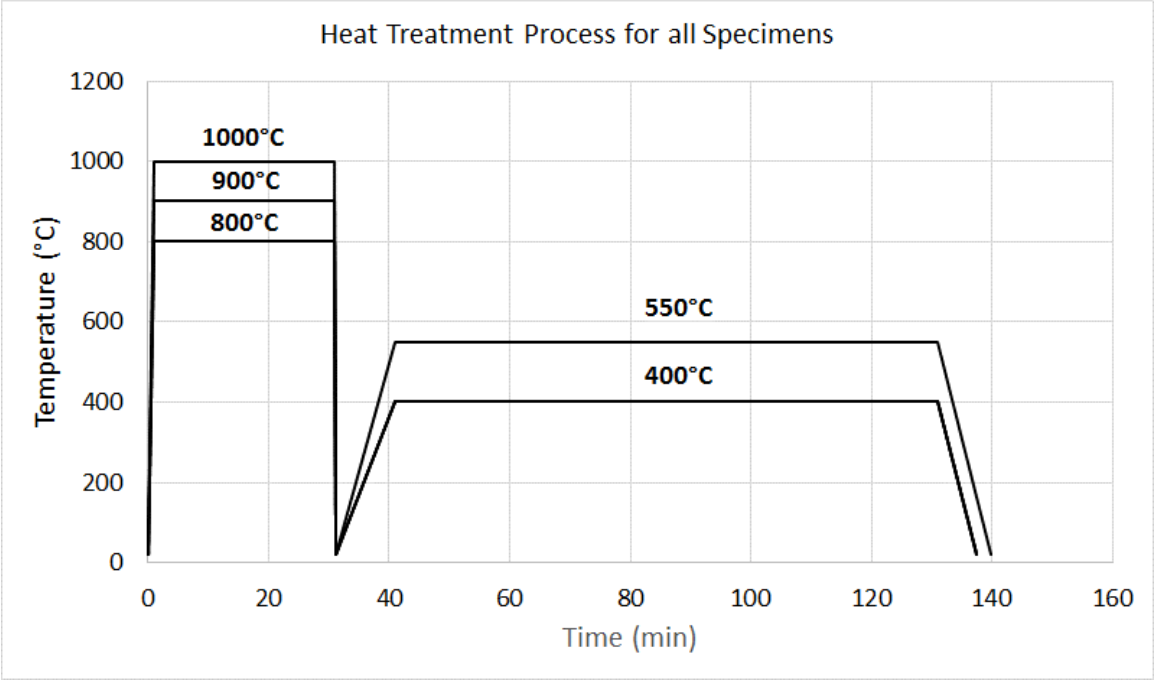

Fig. 30 Heat treatment processes for each tested specimen

Quench and tempered martensite takes on the appearance of a lath structure. Tempered lath martensite (α'-Fe) in steel is made up of a hierarchical microstructure consisting of packets, blocks, sub-blocks, and laths [130, 131]. The prior austenite grain is divided into packets which are groups of laths with the same habit plane (~{111}γ-Fe) that consist of blocks of laths with the same crystal orientation, as shown in Fig. 31.

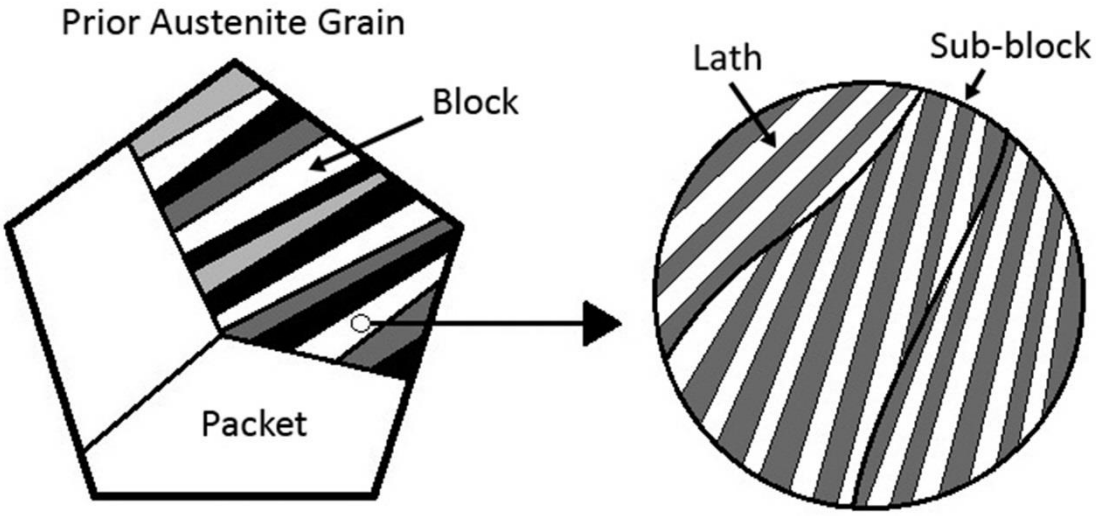

Fig. 31 Schematic of a prior austenite grain containing martensitic laths, packets, and blocks in steel (illustration by this author)

The size and density of the lath martensite structure affects the toughness and strength of high strength steel [132, 133]. The sub-block boundaries are low angle boundaries that act as barriers to dislocation gliding, which also increase the strength of the lath martensite steel [134].

3.3.1 Chemical Etching to Reveal Prior Austenite Grain Boundaries

In studying martensitic steel AISI 4340, the accepted measure of grain size is the size of the crystallographically coherent block or the prior austenite grain which is formed when the steel is austenized at elevated temperatures. One of the techniques that has been

successfully used to reveal prior austenite grain boundaries in heat treatable steel is through chemical etching using picric acid solutions [135]. The most common etchant (2% Nital) tends to reveal primarily the details of martensitic microstructures and gives no indication of grain boundaries.

One of the most effective prior-austenite grain boundary etchants is a saturated aqueous solution of picric acid containing a wetting agent with small additions of hydrochloric acid. This etch is sensitive to phosphorus segregated to the prior-austenite grain boundaries and will not work otherwise. It has been shown that saturated aqueous picric acid with a wetting agent (used at room temperature) reveals prior austenite grain boundaries (PaGBs) if phosphorus is present in the grain boundaries [136]. However, this type of etch is usually accompanied by substantial pitting.

In the current experimental investigation, a unique picric based etchant was developed particularly for the AISI 4340 steel specimens[1]. It is a modification of the original picric acid-based etchant developed by Bechet and Beaujard in 1955 [137] and studies performed by Vandervoot [135] on several grades of steel in the as-quenched condition and after tempering at 400, 800 and 1200°F.

[1] The picric acid used in this experimental procedure was obtained with the help of the Department of Chemistry at the University of Manitoba and the etchant was developed under the supervision of trained lab technicians.

A beaker of 100 ml of an aqueous solution of saturated picric acid was first mixed followed by the addition of 200µl of 1% hydrochloric acid and 3g of wetting agent (sodium dodecylbenzenesulfonate [$C_{18}H_{29}NaO_3S$]). These proportions were calculated based on studies by Vandervoort [135] who showed that additions of small amounts of HCl to the etchant solution produces remarkable better results in steels with low phosphorus content.

The solution was then filtered to remove excess picric acid solute crystals and brought to a near boiling temperature. Specimens were then submerged in the etchant for 20 seconds using a specially designed glass holder[2] to allow sufficient surface etching, shown in Fig. 32.

[2] Only glass or plastic tools can be used with picric acid since it can easily form metal salts when exposed to metals and become unstable corroding them. The holder used in this investigation was specially manufactured by the Chemistry Department at the University of Manitoba for this purpose.

Fig. 32 Glass holder for Bakelite mounted specimens during etching

This was followed by light polishing with 0.5 micron silica solution on a stationary cloth to remove intergranular microstructural features, then light swabbing with etchant for 20 seconds. This 3-step process was repeated until the grain boundaries were clearly revealed under optical microscopy.

3.4 Prior Austenite Grain Size Measurements

To study the grain growth and refinement due to deformation, average grain sizes were measured in each tested specimen for each temperature and impact momentum. In

specimens that contained shear bands, grain sizes inside, near, and away from shear bands were measured. Additionally, grain size measurements were taken of a specimen prior to impact to establish a basis for comparison with tested specimens.

The ASTM grain size number, G, was computed using image analysis software IQMaterials [138] marketed by Media Cybernetics and a modified Hyen Intercept Method. This method uses a randomly positioned circle of known circumference that is overlaid on the micrograph and the number of intersections of grain boundaries with the circumference is calculated. In the current study, multiple circles are used to cover the micrograph within a selected area. The number of grain boundaries that intercept the circles was meticulously counted and recorded and used to measure the mean intercept length, L, defined as 1/N, where N is the total grain boundary interception count. The ASTM grain size number, G, was then calculated based on ASTM E112-10 [139] using the equation:

$$G = [-6.6457 \log(L)] - 3.298 \qquad (L, mm) \qquad \textbf{Eq. 3-1}$$

The ASTM grain size number can be correlated to average grain diameter using the data found in ASTM E112 [139]. The finer the grain size the greater the number of grains per unit area or the smaller the intercept distance, the higher is the ASTM grain size number. Grain sizes in the steel specimens were determined at a magnification of 1000x within a 120

μm x 90 μm area via optical microscope. Fig. 33 shows an example of an examined area of steel heat treated to 800°C for 30 minutes, tempered at 400°C for 90 minutes, and tested at an impact momentum of 52 kg·m/s at 20°C. The area was selected randomly. The measured ASTM grain size was G = 9.6 which correlates to an average approximate grain diameter of 13 μm using the conversion table shown in Table 2, which correlates ASTM grain size to average grain diameter for uniform, randomly oriented, equiaxed grains.

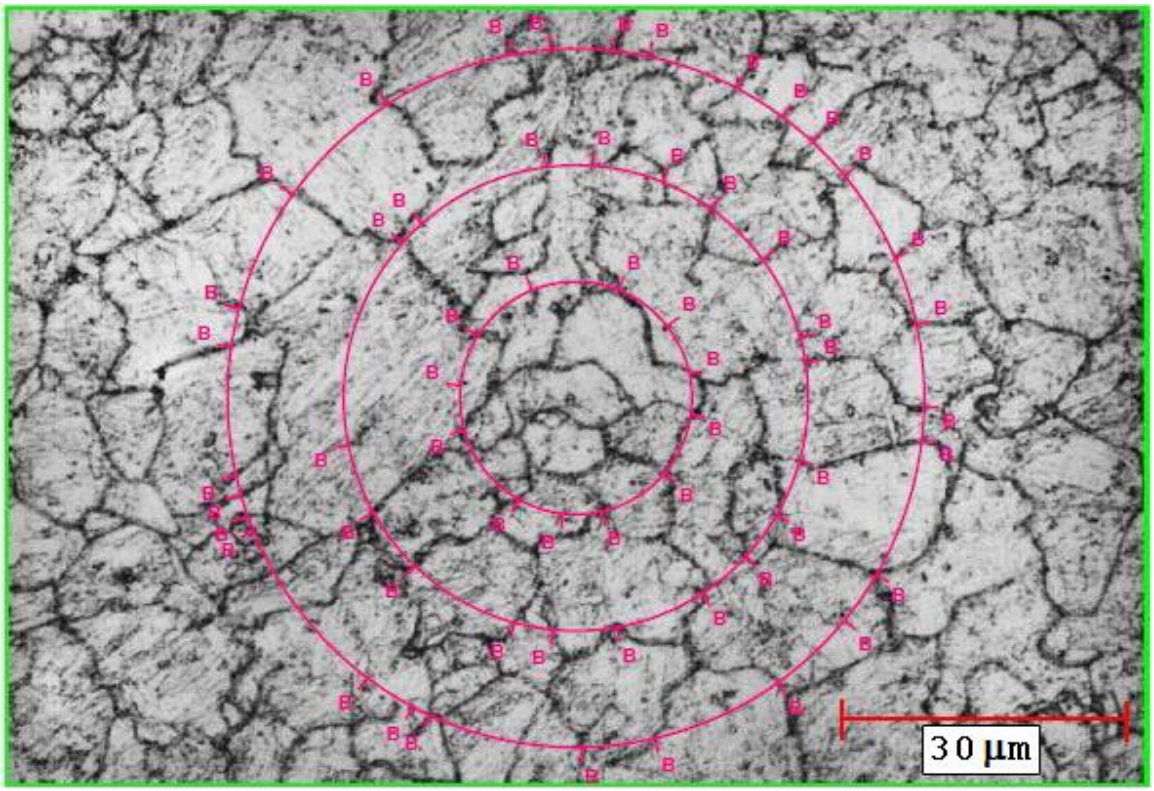

Fig. 33 Micrograph of AISI 4340 specimen heat treated at 800°C, tempered at 400°C and impacted at 52 kgm/s showing area used to calculate ASTM grain size (micrograph sharpened to enhance grain boundaries) (illustration by this author)

Table 2. Grain sizes for uniform, randomly, oriented, equiaxed grains

Grain Size No. G	$\bar{N}_A$ Grains/Unit Area		$\bar{A}$ Average Grain Area		$\bar{d}$ Average Diameter		$\bar{\ell}$ Mean Intercept		$\bar{N}_L$
	No./in.^{2} at 100X	No./mm^2 at 1X	mm^2	μm^2	mm	μm	mm	μm	No./mm
00	0.25	3.88	0.2581	258064	0.5080	508.0	0.4525	452.5	2.21
0	0.50	7.75	0.1290	129032	0.3592	359.2	0.3200	320.0	3.12
0.5	0.71	10.96	0.0912	91239	0.3021	302.1	0.2691	269.1	3.72
1.0	1.00	15.50	0.0645	64516	0.2540	254.0	0.2263	226.3	4.42
1.5	1.41	21.92	0.0456	45620	0.2136	213.6	0.1903	190.3	5.26
2.0	2.00	31.00	0.0323	32258	0.1796	179.6	0.1600	160.0	6.25
2.5	2.83	43.84	0.0228	22810	0.1510	151.0	0.1345	134.5	7.43
3.0	4.00	62.00	0.0161	16129	0.1270	127.0	0.1131	113.1	8.84
3.5	5.66	87.68	0.0114	11405	0.1068	106.8	0.0951	95.1	10.51
4.0	8.00	124.00	0.00806	8065	0.0898	89.8	0.0800	80.0	12.50
4.5	11.31	175.36	0.00570	5703	0.0755	75.5	0.0673	67.3	14.87
5.0	16.00	248.00	0.00403	4032	0.0635	63.5	0.0566	56.6	17.68
5.5	22.63	350.73	0.00285	2851	0.0534	53.4	0.0476	47.6	21.02
6.0	32.00	496.00	0.00202	2016	0.0449	44.9	0.0400	40.0	25.00
6.5	45.25	701.45	0.00143	1426	0.0378	37.8	0.0336	33.6	29.73
7.0	64.00	992.00	0.00101	1008	0.0318	31.8	0.0283	28.3	35.36
7.5	90.51	1402.9	0.00071	713	0.0267	26.7	0.0238	23.8	42.04
8.0	128.00	1984.0	0.00050	504	0.0225	22.5	0.0200	20.0	50.00
8.5	181.02	2805.8	0.00036	356	0.0189	18.9	0.0168	16.8	59.46
9.0	256.00	3968.0	0.00025	252	0.0159	15.9	0.0141	14.1	70.71
9.5	362.04	5611.6	0.00018	178	0.0133	13.3	0.0119	11.9	84.09
10.0	512.00	7936.0	0.00013	126	0.0112	11.2	0.0100	10.0	100.0
10.5	724.08	11223.2	0.000089	89.1	0.0094	9.4	0.0084	8.4	118.9
11.0	1024.00	15872.0	0.000063	63.0	0.0079	7.9	0.0071	7.1	141.4
11.5	1448.15	22446.4	0.000045	44.6	0.0067	6.7	0.0060	5.9	168.2
12.0	2048.00	31744.1	0.000032	31.5	0.0056	5.6	0.0050	5.0	200.0
12.5	2896.31	44892.9	0.000022	22.3	0.0047	4.7	0.0042	4.2	237.8
13.0	4096.00	63488.1	0.000016	15.8	0.0040	4.0	0.0035	3.5	282.8
13.5	5792.62	89785.8	0.000011	11.1	0.0033	3.3	0.0030	3.0	336.4
14.0	8192.00	126976.3	0.000008	7.9	0.0028	2.8	0.0025	2.5	400.0

A summary of the prior austenite grain sizes measured in all the specimens tested are shown in Table 3, Table 4, and Table 5. In cylindrical shaped specimens, ASBs form in an hourglass pattern along the path of maximum shear, as shown in Fig. 17. On the top and bottom faces of the specimen, ASBs appear as a ring, concentric with the outer edge. Grains farthest from the formation of shear bands were located at the centers of the top and bottom faces and were measured along with grain sizes inside the ASBs in order to establish the degree of grain refinement. Three measurements were taken for grain sizes at the center of each specimen and averaged using the grain measuring software IQMaterials [138]. The type of ASB formed was labeled as either deformed or transformed, as explained in Section 2.4. *Grain refinement was observed only in specimens which formed transformed ASBs*. *Deformed ASB formation was accompanied by a severe elongation of the grain structure with no measurable refinement*. Final refined grain sizes, in the ASBs, were measured manually using optical microscopy based on an average of 20 grain sizes measurements. The label '-F', in Table 3 and Table 4, denotes that some specimens which formed ASBs also fractured.

Table 3. Approximate Grain Sizes of steel hardened at 800°C

Austenizing	Tempering	Testing Temperature (°C)	Impact Momentum (kgm/s)	Matrix Grain Size (µm) [± 0.5]	ASB Formation and Type	Approx. Avg. ASB Grain Size (µm)
800°C/30mins & Oil Quench	550°C/90mins & Air Cool	20	0 (Pre-Impact)	16	None	--
			30	14	None	--
			45	16	Deformed	--
			49	15	Deformed	--
			52	14	Transformed	2 ± 0.05
		428	0 (Pre-Impact)	16	None	--
			30	15	None	--
			45	15	Deformed	--
			49	13	Deformed	--
			52	14	Deformed	--
	400°C/90mins & Air Cool	20	0 (Pre-Impact)	16	None	
			30	14	Transformed	2 ± 0.05
			45	13	Transformed	2 ± 0.05
			49	15	Transformed-F	2 ± 0.05
			52	13	Fracture	--
		428	0 (Pre-Impact)	16	None	--
			30	16	Deformed	--
			45	15	Deformed	--
			49	14	Deformed	--
			52	14	Transformed	3 ± 0.075

Table 4. Approximate Grain Sizes of steel hardened at 900°C

Austenizing	Tempering	Testing Temperature (°C)	Impact Momentum (kgm/s)	Matrix Grain Size (μm) [± 0.5]	ASB Formation and Type	Approx. Avg. ASB Grain Size (μm)
900°C/30mins & Oil Quench	550°C/90mins & Air Cool	20	0 (Pre-Impact)	23	None	--
			30	23	None	--
			45	22	None	--
			49	23	Deformed	--
			52	20	Deformed	--
		428	0 (Pre-Impact)	23	None	--
			30	22	None	--
			45	19	None	--
			49	20	None	--
			52	21	Deformed	--
	400°C/90mins & Air Cool	20	0 (Pre-Impact)	23	None	--
			30	22	None	--
			45	22	Deformed	--
			49	22	Transformed	2 ± 0.05
			52	20	Transformed-F	2 ± 0.05
		428	0 (Pre-Impact)	23	None	--
			30	22	None	--
			45	21	Deformed	--
			49	20	Deformed	--
			52	23	Deformed	--

Table 5. Approximate Grain Sizes of steel hardened at 1000°C

Austenizing	Tempering	Testing Temperature (°C)	Impact Momentum (kgm/s)	Matrix Grain Size (µm) [± 0.5]	ASB Formation and Type	Approx. Avg. ASB Grain Size (µm)
1000°C/30mins & Oil Quench	550°C/90mins & Air Cool	20	0 (Pre-Impact)	30	None	--
			30	32	None	--
			45	33	None	--
			49	31	None	--
			52	33	Deformed**	--
		428	0 (Pre-Impact)	30	None	--
			30	32	None	--
			45	32	None	--
			49	32	None	--
			52	31	None	--
	400°C/90mins & Air Cool	20	0 (Pre-Impact)	30	None	--
			30	31	None	--
			45	30	Deformed	--
			49	33	Deformed	--
			52	32	Deformed	--
		428	0 (Pre-Impact)	30	None	--
			30	32	None	--
			45	33	None	--
			49	32	Deformed	--
			52	33	Deformed	--

** No ASBs observed for this heat treatment on top and bottom faces of the specimen. A deformed ASB was observed through the cross-section of specimen at an impact momentum of 52kgm/s

3.4.1 Effect of Austenization Temperature on Prior Austenite Grain Size

Examination of the quenched microstructure prior to impact revealed a large increase in prior austenite grain size with increasing austenizing temperature, shown in Fig. 34. Specimens were repeatedly lightly etched and resurfaced to reveal the prior austenite grains while suppressing the appearance of the martensite substructure. The dark spots in Fig. 34 represent pitting from repeated etching.

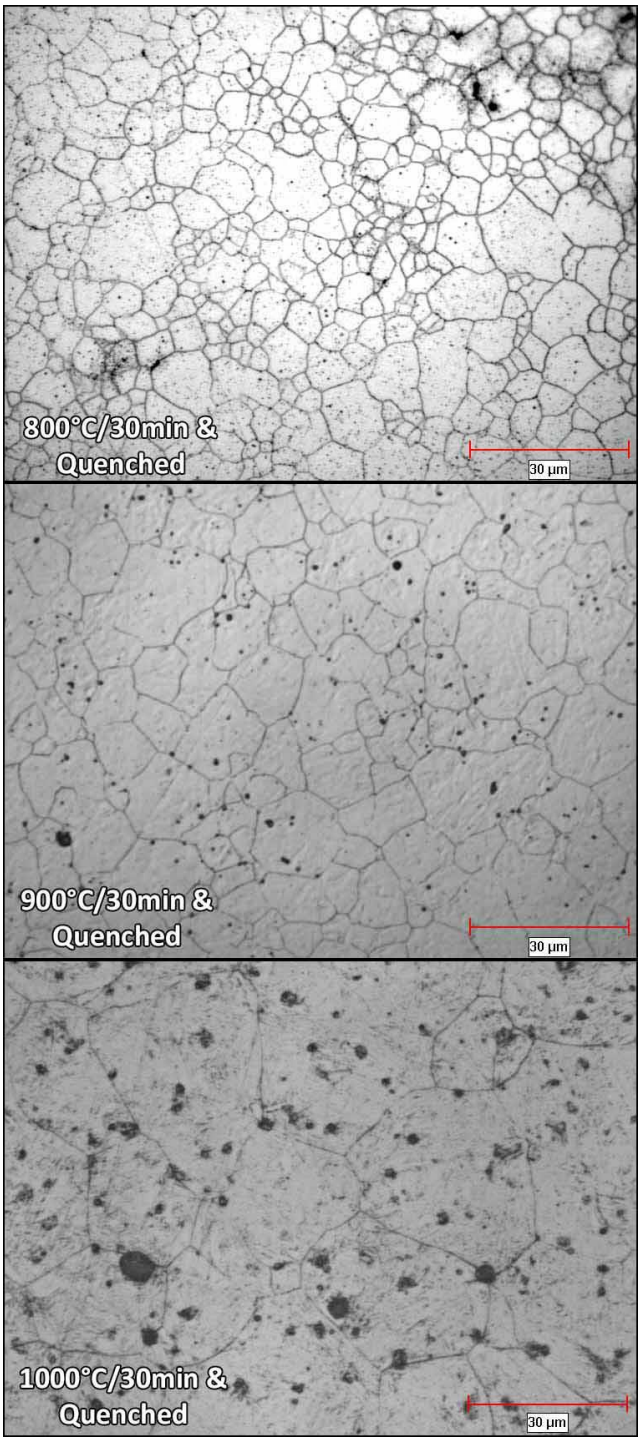

Fig. 34 Prior-austenite grain sizes in quench-hardened specimens austenized at 800°C, 900°C, 1000°C for 30 min and quenched in oil showing increase in prior austenite grain size (16µm→23µm→30µm) with increasing temperature

Higher temperatures translates to more energy driving the recovery and growth of the grains which push out dislocations, as discussed in Section 2.3.2. The grains will grow at a faster rate as temperature increases until the metal is quenched.

In studying heat treatments of AISI 4340, Lim et al. [140] found that quenched steel has a strong segregation of carbon atoms at the prior austenite grain boundaries, in addition to chromium and phosphorus. The prior austenite grain boundary is a high-angle grain boundary and is considered to be a more thermodynamically favorable site for segregation of impurities compared to low-angle martensite laths. This gives the prior austenite grains a darker appearance under the optical microscope.

3.4.1.1 Effect of Austenization Temperature on Martensite Lath Block Size

Average martensite lath sizes are in the range of a few nanometers and cannot be measured directly using an optical microscope. Instead, the lath blocks (groups of laths of the same orientation) are the smallest discretization of the microstructure which is visible under optical microscopy. The size of the blocks was based on both their lengths (equal to the average packet size or prior austenite grain size) and their widths. Martensite forms by a displacive transformation, as discussed in Section 2.3.3, whose growth is limited to within

the prior austenite grain. As a result the blocks grow in length to the edge of the prior austenite grain boundary.

Prior austenite grains are 3D and multi-sided, containing several martensite packets, blocks, and laths. The martensite blocks have a length, width, and depth. Within the same habit plane (packet) their largest dimension is equal in size to the size of the prior austenite grain, due to their displacive transformation.

Optical microscopic micrographs are 2D cross-sections of these 3D grains. Under this form of observation the martensite blocks appear as long slivers having high aspect ratios, where their lengths are several times larger than their widths. The lengths of the martensite blocks were observed to extend either to the packet boundary, or to the prior austenite boundary such that the martensite block length equaled to the size of the packet or the prior austenite grain, depending on the number of packets shown to form within each prior austenite grain.

Micrographs of specimens austenized at 800°C, 900°C, and 1000°C, shown in Fig. 35, Fig. 36, and Fig. 37 respectively, reveal an increase in block length with increasing austenization temperature, equal to the size of the prior austenite grain. Also, there is a noticeable increase in block width as austenization temperature is increased. The majority of blocks in steel austenized at 800°C appear as very thin slivers, measuring as thin as 1μm

and as long as the size of the prior austenite grain. At 1000°C the blocks are on average thicker by 2-4μm. This observation is consistent with theory [60] which states that for small austenite grains, produced from austenizing just above the austenization temperature for a particular steel, the martensite laths are so small that they cannot be observed in a micro-section and are usually called structureless. Martensite lath size, and by extension block size, decreases with decreasing austenization temperature.

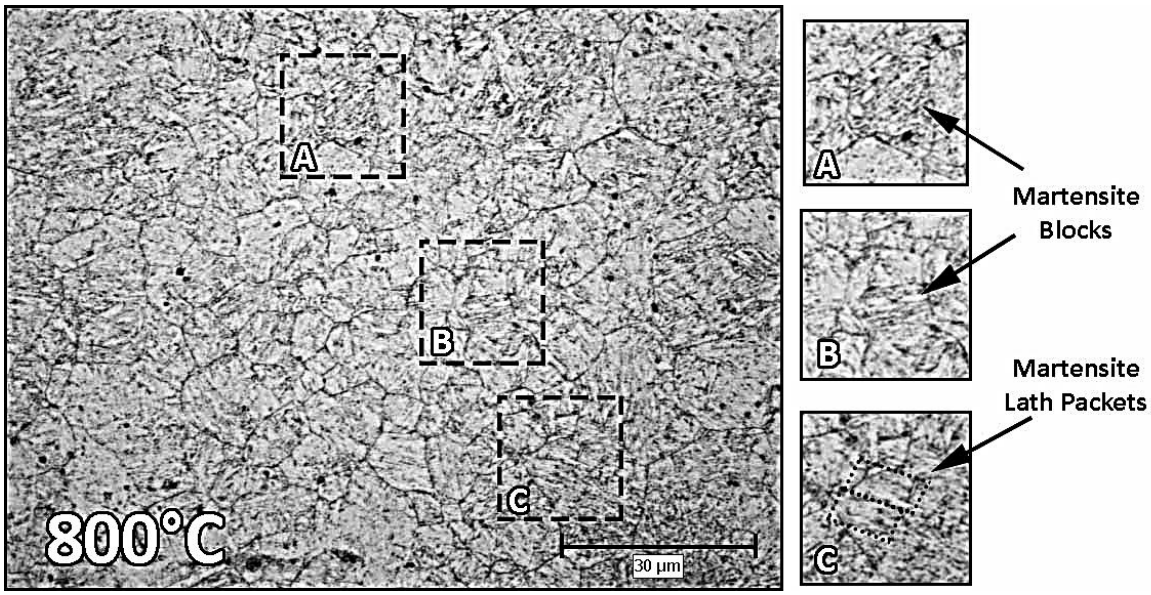

Fig. 35 Etched specimen of quenched steel austenized at 800°C to reveal martensite blocks within the prior austenite grains. The Lath block packets are outlined in section C

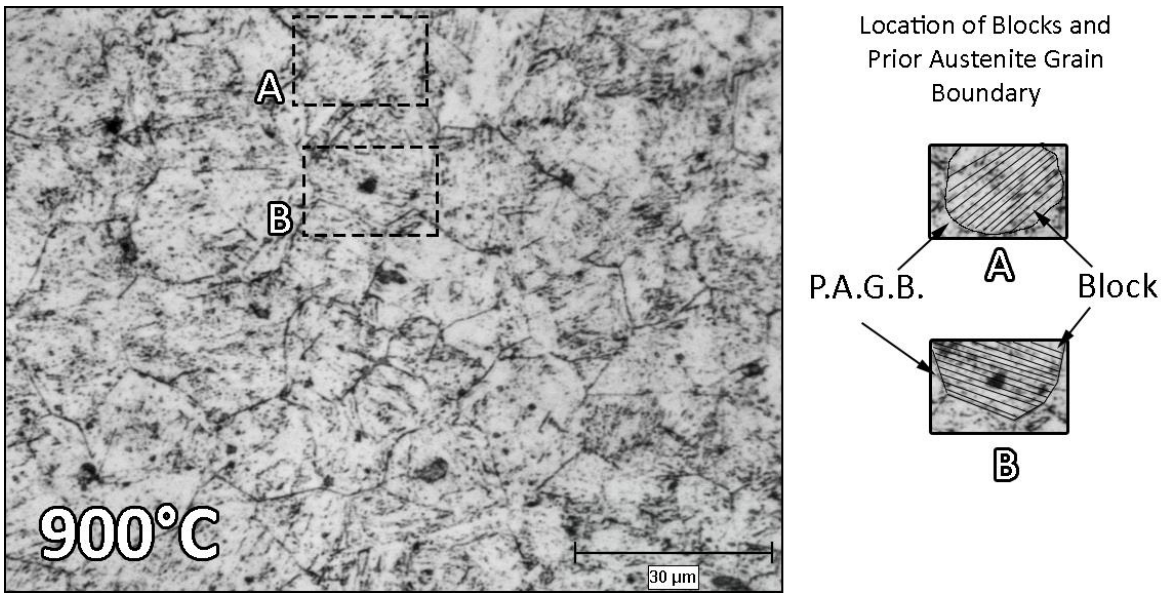

Fig. 36 Etched specimen of quenched steel austenized at 900°C to reveal martensite blocks within the prior austenite grains. Lines drawn in Sections A and B outline the locations of the blocks and prior austenite grain boundaries

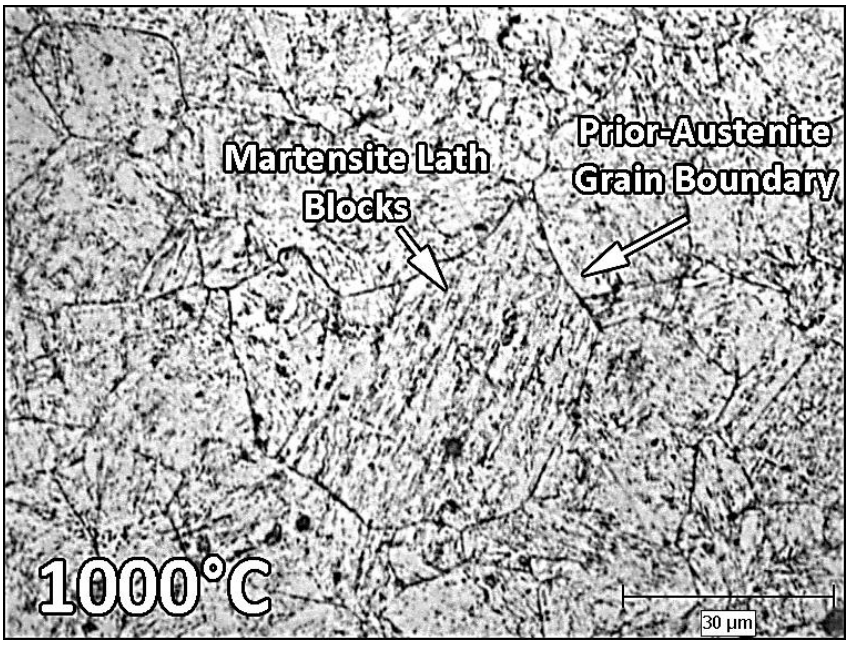

Fig. 37 Etched specimen of quenched steel austenized at 1000°C to reveal martensite blocks within the prior austenite grains

3.4.1.2 Effect of Austenization Temperature on Mechanical Properties of Steel

The larger martensite blocks and prior austenite grains associated with an increase in austenization temperature are expected to have a lower yield strength, according to the Hall-Petch theory of grain boundary strengthening discussed in Section 2.1.1. The theory states that yield strength is related to the smallest denomination of grains in the microstructure. At room temperature, the smallest denomination of grains that govern the yield strength are the martensite laths, while at austenization temperatures it is the austenite grains that govern the yield strength. The difference in widths of the laths and blocks between austenization temperatures is very small, so the difference in yield will be miniscule (in the order of 5-10 MPa). The experimental results of this investigation showed a greater tendency to form transformed or 'white-etched' type ASBs in steels austenized at lower temperatures, which form predominantly in stronger harder metals. The occurrence of ASBs decreased with increasing austenization temperature. The decrease in ASB formation is tied directly to the increase in toughness. The exact microstructural effects contributing to the toughening of the steel at higher austenization temperatures has been examined by several authors. In studying the effect of austenization temperature on toughness of quenched 4340 steel, Lai et al. [141] , and later confirmed by Ritchie et al. [142] and Khan and Wood [143], showed that specimens austenized at 1200°C, for 1hr, followed by quenching in oil to room

temperature produced a two-fold increase in fracture toughness compared with quenching from 870°C. These authors concluded that the increase in toughness is attributed to a greater dissolution of carbides at higher solution temperatures; and a higher amount of retained austenite which forms as thin films between the martensite laths. Retained austenite has a high toughness but is metastable and will decompose into ferrite, pearlite and cementite during tempering. Retained austenite hinders inter-lath fracture. Fracture tests, performed by Lai et al. [141] on 4340 steel quenched from 870°C showed trans-granular cleavage across the prior austenite grains due to a greater concentration of undissolved carbides in the laths, while fibrous fracture and inter-granular fracture was prominent in steel quenched from 1200°C due to a greater amount of retained austenite in the lath boundaries.

These findings were confirmed in the current research investigation where specimens austenized at 800°C showed a greater formation of ASBs under impact compared to than specimens austenized at 1000°C. Stress-strain and hardness measurements confirmed the mechanical properties of the microstructure.

3.4.2 Effect of Tempering Temperature on Grain Size

Quench hardened specimens, tempered at 400°C and 550°C, revealed no measurable change in the prior austenite grain size compared with the quenched state. The difference in martensite block size between the quenched state and tempering at 400°C was unnoticeable. Between tempering temperatures 400°C and 550°C, there was a significant increase in block size, due to dislocation annihilation between the low angle lath grains and blocks, which occurs when tempering steel above the recovery (static recrystallization) temperature of $0.30T_m = 428°C$, as dscussed in Section 2.3.2. As a result, the laths appear thicker within the prior austenite grain. Micrographs of specimens austenized at 800°C and 1000°C and tempered at 550°C, shown in Fig. 38 and Fig. 39, respectively, show the appearance of large rounded martensite blocks which form by dislocation annihilation. Additionally, the martensite block boundaries are more pronounced due to the precipitation of carbides. It is expected that the increase in tempered martensite block size from tempering at 550°C would result in a drop in strength and hardness and an increase in toughness.

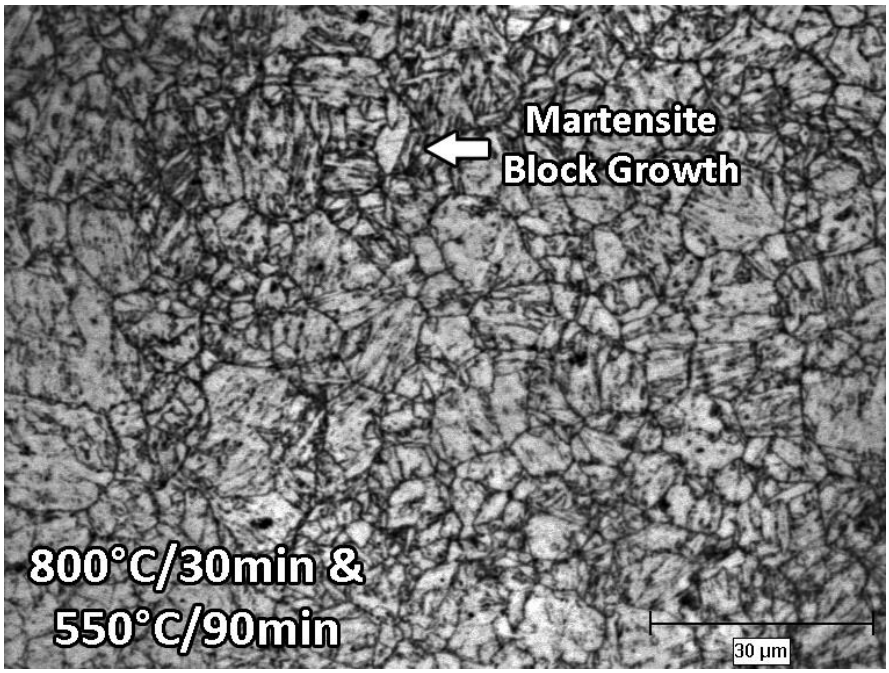

Fig. 38 Martensite block growth by dislocation annihilation at the grain boundary in a specimen austenized at 800°C and tempered at 550°C

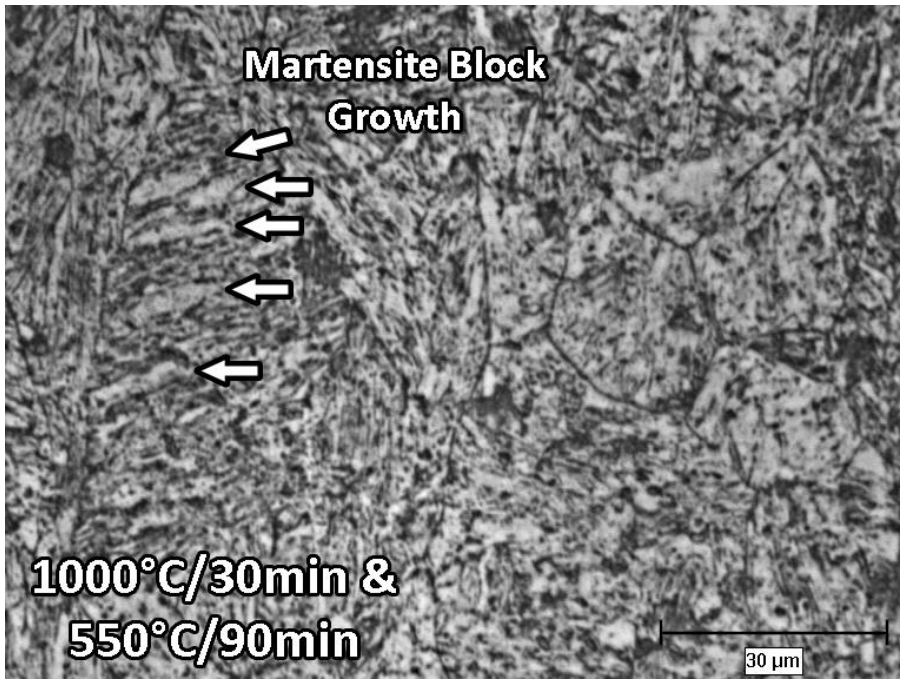

Fig. 39 Martensite block growth by dislocation annihilation at the grain boundary in a specimen austenized at 1000°C and tempered at 550°C

3.4.3 Effect of Impact Momentum on Grain Size and Formation of ASBs

Quench and tempered specimens were impacted at a range of momenta to determine the effects of heat treatment and testing conditions on the formation of ASBs. Deformed type ASBs formed more predominantly at higher austenization and tempering temperatures, reflecting steels having high toughness and low strength, while transformed or 'white-etched' ASBs formed at lower austenization and tempering temperatures--in steels with low toughness and higher strength. Additionally, the resistance to ASB formation increased with increasing austenization and tempering temperatures resulting in increased toughness but lower strength.

There were no ASBs observed on the top or bottom faces of the cylindrical specimens austenized at 1000°C and tempered at 550°C. This heat treatment resulted in steel having the lowest strength and highest toughness. However, a deformed ASB was observed in a specimen impacted at the highest momentum of 52kgm/s, represented by a collection of micrographs depicting the extent of the deformed ASB through the cross section of the specimen shown along with a schematic representation of the specimen in Fig. 41. Two close-ups show the extent of the microstructural reorientation towards the shear direction and the severe elongation of the grains in the center of the band.

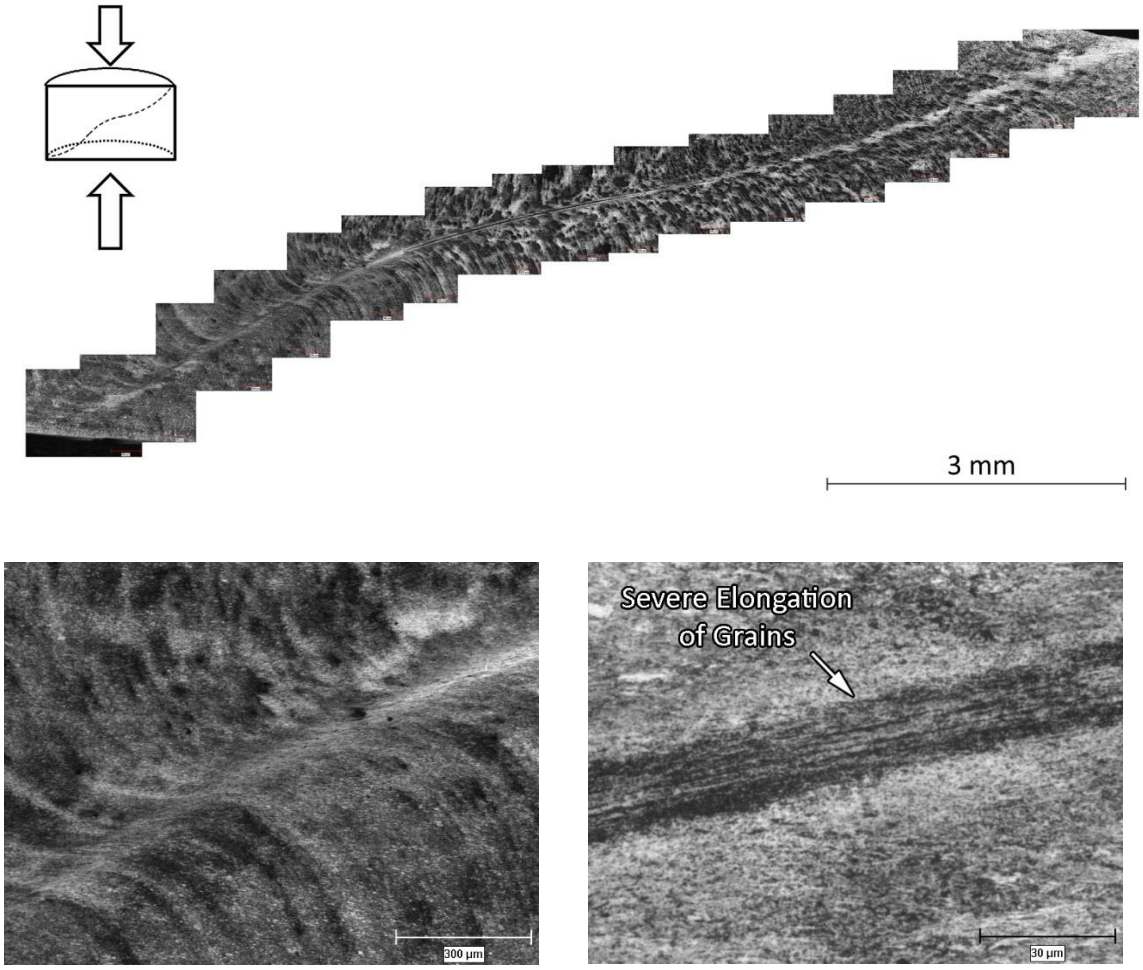

Fig. 40: Schematic showing a cross section of a cylindrical specimen impacted with a dotted line indicating the location of the ASB.

Note: Compiled micrographs show the extent of ASB formation through cross-section of specimen austenized at 1000°C & tempered at 550°C and impacted at 52 kg·m/s with a) showing the extent of microstructural reorientation towards the shear direction and b) the severe elongation of the grains in the center of the deformed ASB.

As austenization temperatures and tempering temperatures increase, strength decreases and toughness increases. Consequently, ASB formation in steels austenized and tempered at the lowest temperatures of 800°C and 400°C, respectively, were predominantly

transformed or ‘white-etched’ in appearance and even fractured at the highest impact momentum of 52 kgm/s.

Specimens which formed ‘white-etched’ ASBs showed little or no grain reorientation towards the ASB but instead showed a gradual refinement of the grains approaching the edge of the band followed by a severe refinement inside the band.

A compilation of micrographs in Fig. 41 shows the extent of a transformed ASB formation on the front face of the cylindrical specimen austenized at 800°C, tempered at 400°C and impacted at 49 kgm/s with a section showing a gradient of grain refinement approaching the center of the band. Over-etching of a specimen of steel, shown in Fig. 42, revealed a severely deformed prior austenite grain structure approaching the ASB followed by a severely refined grain structure inside the center of the band along with a micro-crack formation. The refinement of the grains due to severe localization results in a randomly oriented grain structure within the band and the crack formation appears to be intergranular. A close-up of the crack formation in the ASB from Fig. 41, shown in Fig. 43, reveals a crack surface resembling brittle transgranular fracture/cleavage. Grain sizes in the band are so refined that it is difficult to discern the exact type of fracture (intergranular or transgranular) in the ASB, using optical microscopy. The crack surfaces into the ASB are revealed using a variable magnification capture of the specimen.

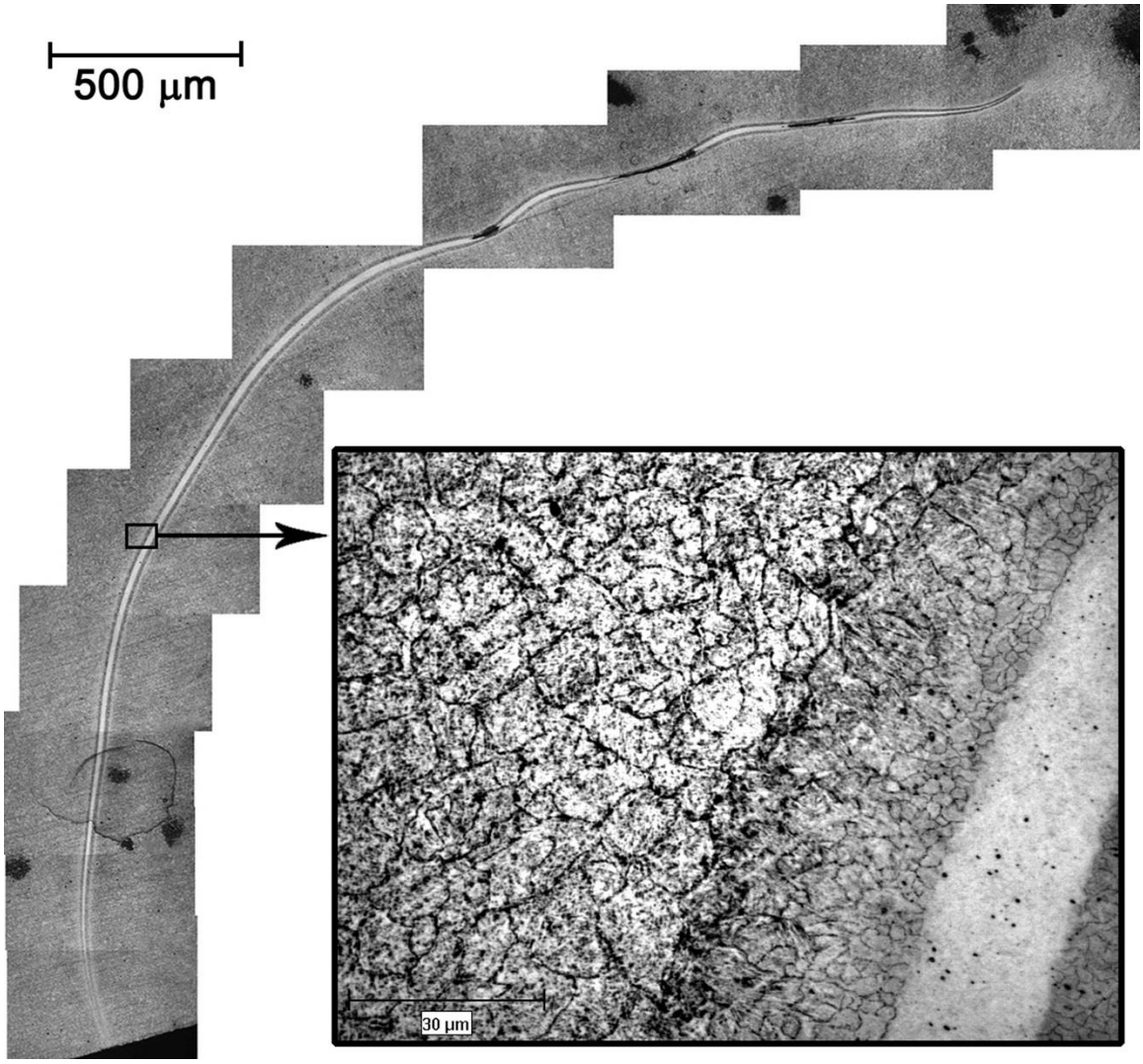

Fig. 41 Compiled micrographs of single ASB formed in a specimen of steel austenized at 800°C, tempered at 400°C and impacted at 49 kg·m/s with cutout showing degree of grain deformation and refinement close to the formation of the ASB (image is sharpened to reveal grain boundaries near ASB)

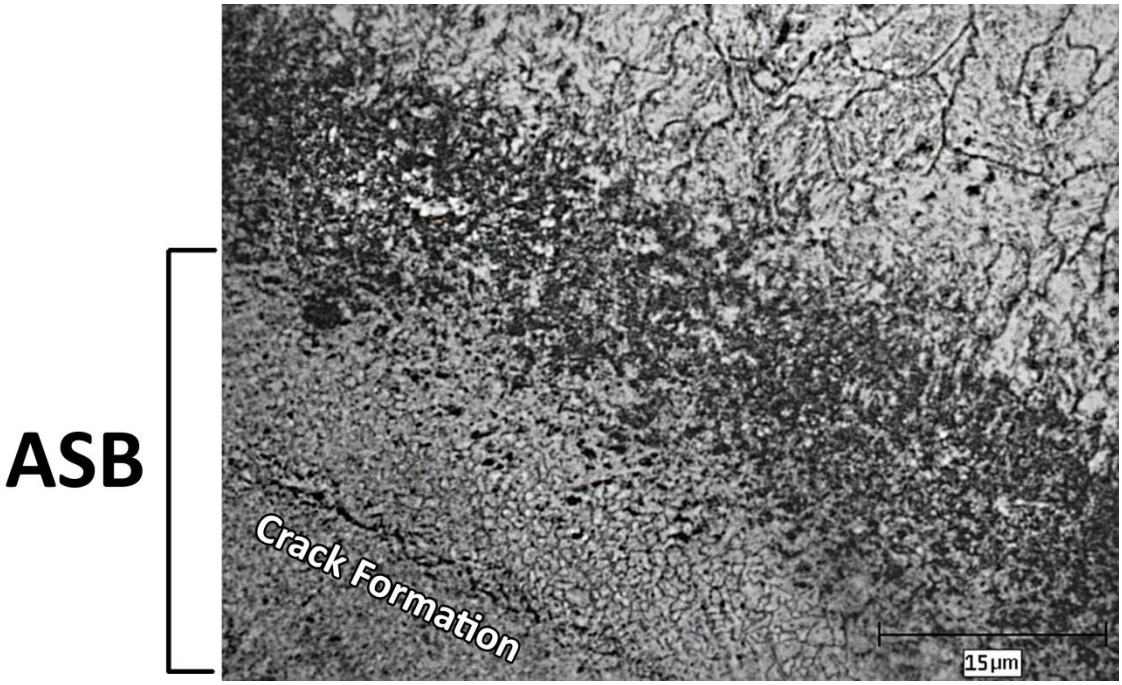

Fig. 42 Close up of an edge of an ASB in 4340 steel austenized at 800°C, tempered at 400°C and impacted at 49 kg·m/s showing grain refinement and microcrack formation in the middle of the ASB (image is sharpened to reveal grain boundaries)

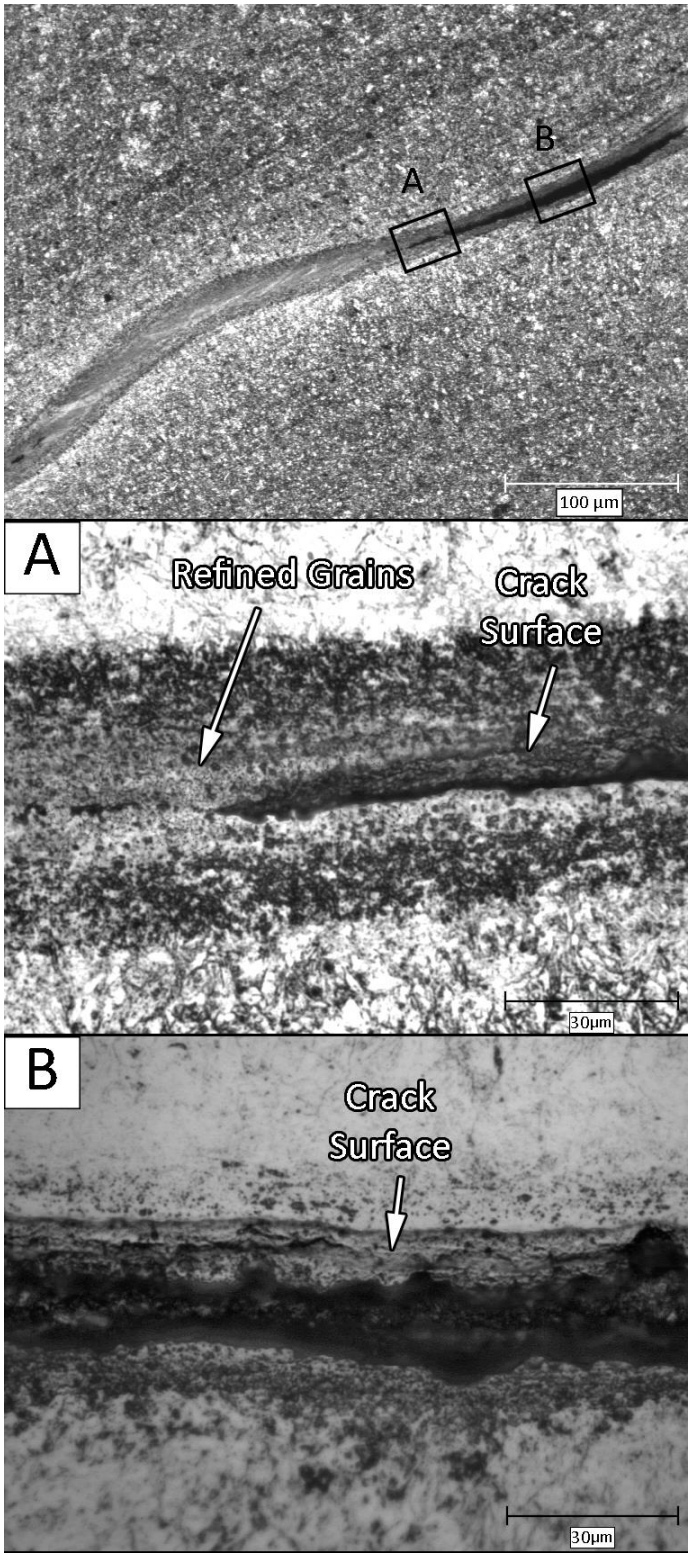

Fig. 43 Crack surface within a formation of a transformed ASB in a specimen of steel with heat treatment 800°C/30 min & 400°C/90 min and impacted at 49kgm/s showing inter/trans-granular fracture

The nature of the microstructure surrounding the ASBs changed with heat treatment. Heat treating and tempering at high temperatures produced softer steels which exhibited a large reorientation of the microstructure and elongation of the grains in the ASBs, while at lower heat treatment temperatures this reorientation zone decreased and there was a progressive refinement of the grains near the ASB followed by a severe refinement inside the ASB.

In specimens of steel heat treated at (900°C/30 min & 400°C/90 min) and tested at 20°C with an impact momentum of 52 kgm/s, there was a combination of grain reorientation, stretching, and refinement with an ASB formation. The reorientation of the microstructure was observed to occur very close to the ASB. This could be due to the decreased toughness of the steel, which increases the mechanically-driven force required to rotate the subgrain microstructure. This can be seen in Fig. 44. Refined grain boundaries are slightly visible inside the ASB.

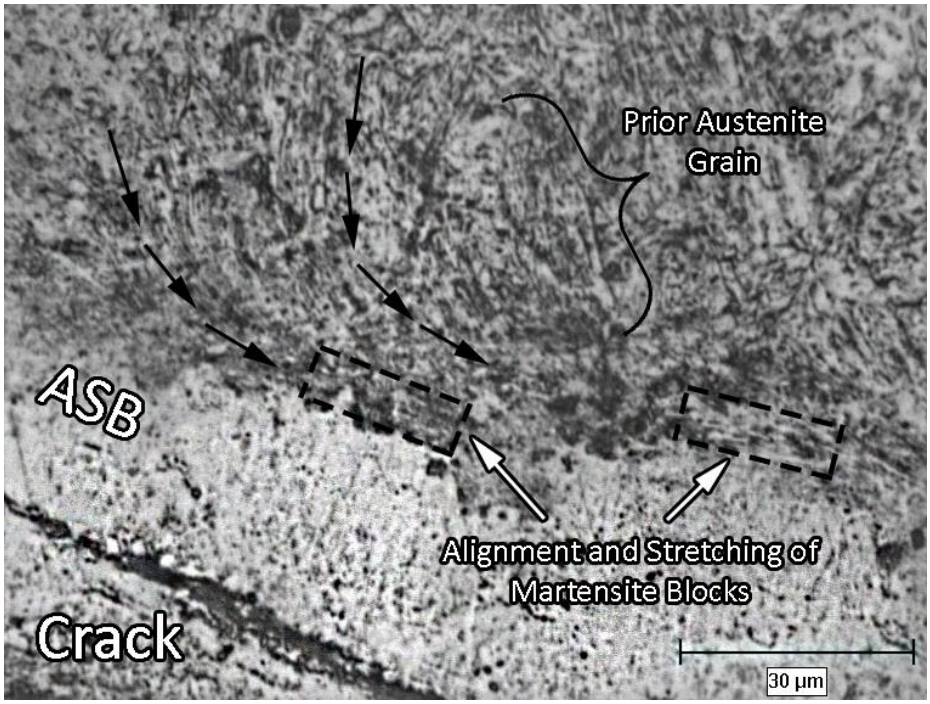

Fig. 44 Micrograph of a specimen with heat treatment (900°C/30 min & 400°C/90 min) impacted at 52 kgm/s at 20C showing grain realignment and stretching near the formation of an ASB

The microstructure in Fig. 44 reveals a reorientation of the grains in the direction of maximum shear which correlates well with the PriSM model discussed in Section 2.4.1.1. This mechanically-driven subgrain rotation in the direction of the ASB is followed by a break-up of the grain structure inside the ASB, indicated by visibly rounded grain boundaries.

3.4.4 Effect of Testing Temperature on Grain Size and Formation of ASBs

When testing at the higher temperature of 428°C, a reduced tendency for ASBs to form was observed. Softening of the material at this temperature allowed deformation to take place over a larger plastic zone. Elevated temperatures increase the mobility of atoms in the steel allowing for easier deformation at lower stresses. Prior austenite grain and martensite block sizes remained the same as those in specimens tested at room temperature. The testing temperature of 428°C is equal to the minimum temperature required for the material to initiate recovery of the crystalline structure, as discussed in Section 2.3.2. However, specimens were not held long at this temperature prior to impact for lath boundary annihilation which typically occurs after 1 hour.

The compilation of micrographs, in Fig. 45, of an area close to a deformed band in steel austenized at 800°C, tempered at 400°C and impacted at 428°C & 49 kgm/s show the extent of the microstructural reorientation towards the formed ASB due to high plasticity behavior of steel at the elevated testing temperature.

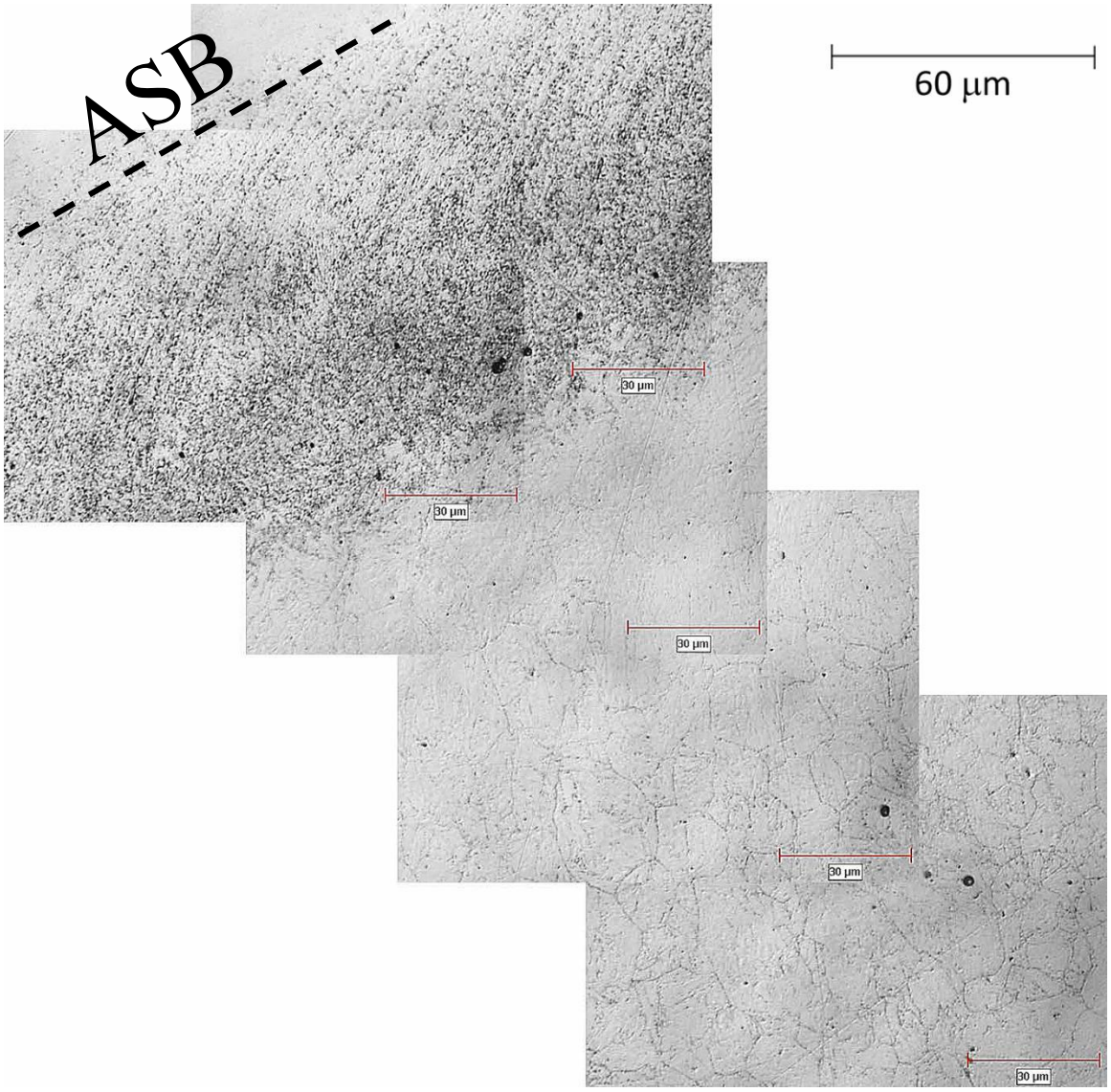

Fig. 45 Overlapping micrographs of area close to shear band formed on the top face of a specimen (800°C/30min & 400°C/90min) tested at 428°C at an impact momentum of 49 kg·m/s.

The micrograph in Fig. 46 shows a close-up of an ASB in a specimen austenized at 800°C and tempered at 400°C formed under impact at 428°C and 52 kgm/s revealing severe

grain refinement. Over-etching reveals the smaller grains. At room temperature these testing conditions caused complete fracture of the specimen.

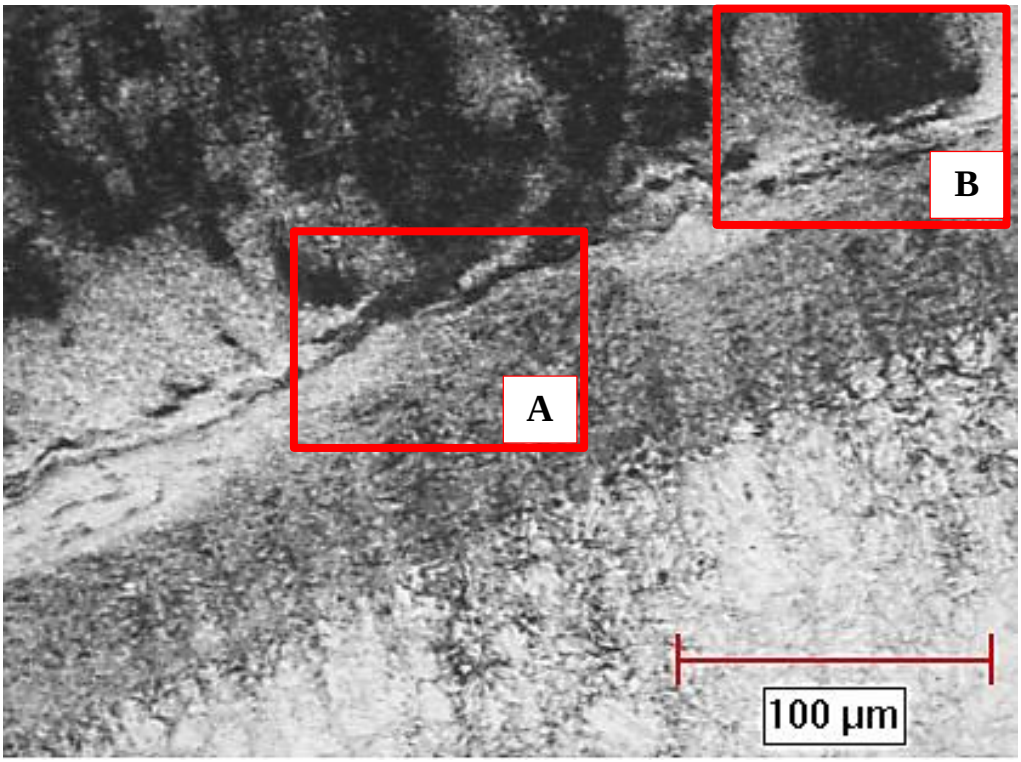

Fig. 46 Micrograph of over etched specimen of (800°C/30min & 400°C/90min) steel impacted at 52 kg·m/s at 428°C (Area A and B are shown in Fig. 47 and Fig. 48)

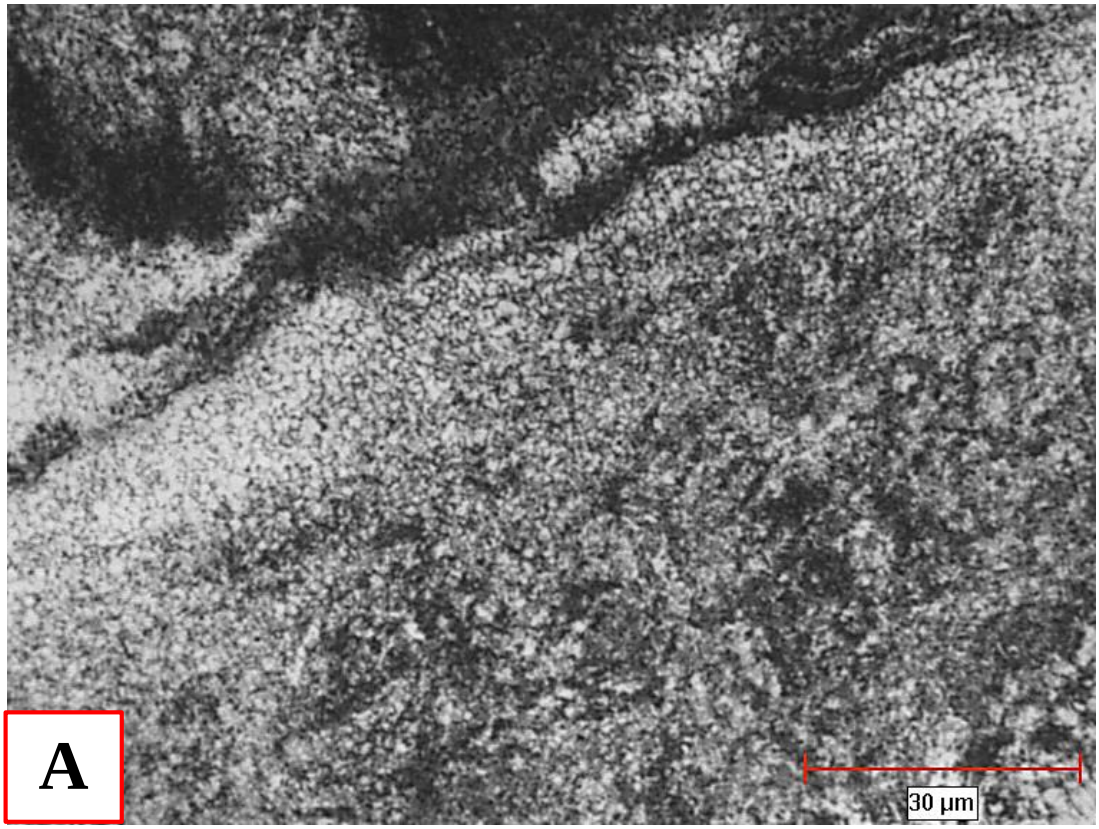

Fig. 47 Section A of the micrograph of a (800°C/30min & 400°C/90min) steel specimen impacted at 52 kg·m/s showing grain boundaries inside the ASB

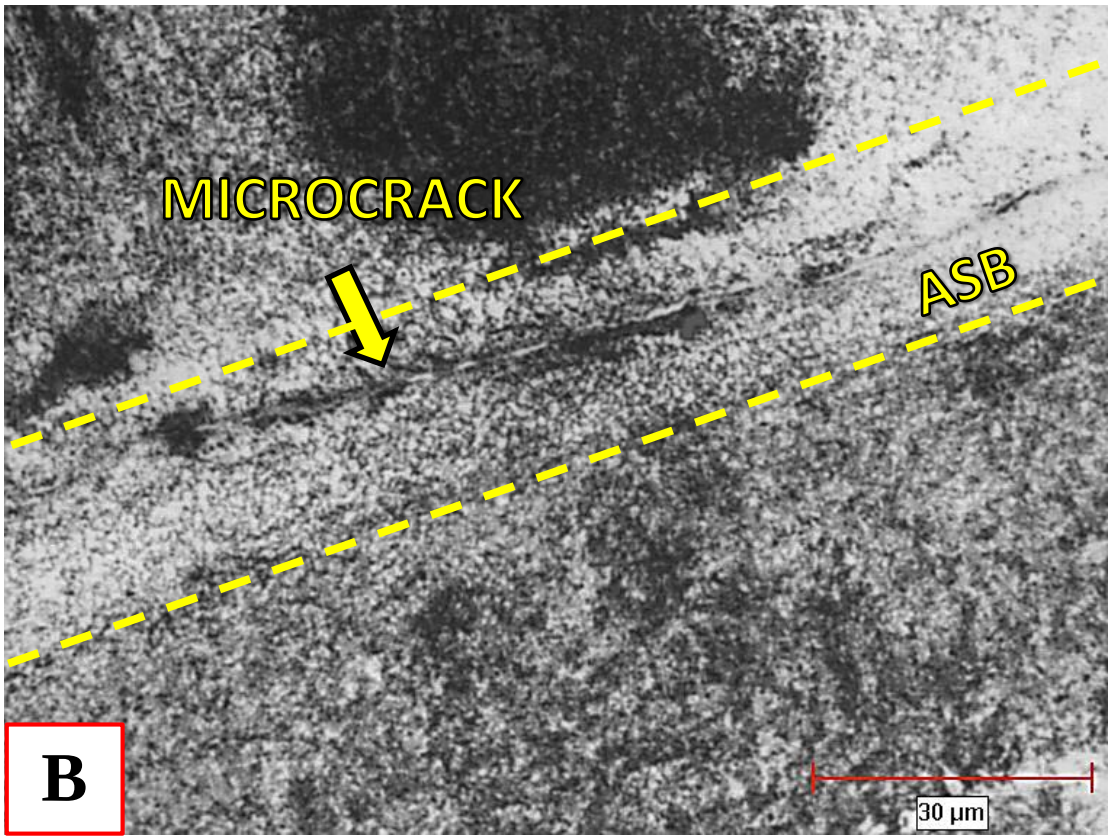

Fig. 48 Section B of the micrograph of the (800°C/30min & 400°C/90min) steel specimen impacted at 52 kg·m/s showing grain boundaries inside the ASB and the formation of a microcrack in the center of the band

The grain sizes inside the ASB, shown in Fig. 47 and Fig. 48, ranged from one to five micrometers in size. These were in general larger in size than those observed in specimens tested at room temperature.

In addition to grain size measurements, stress-strain and hardness data were also gathered for all tested specimens in order to correlate mechanical properties to grain size

and microstructure—information that was important in the development of the simultion model discussed in Chapter 4.

3.5 Dynamic Stress-Strain Response Data

Dynamic stress-strain responses of impacted specimens are useful for understanding the dynamic impact properties of the steel under various testing conditions and for relating them to microstructure. Material properties such as dynamic yield strength and maximum deformation stress and strain can be correlated to the heat treatment as well as contribute to the understanding of the mechanism of ASB formation.

The dynamic response of the tested specimens under impact was gathered as voltage-time data from strain gauges attached to the transmitter bar of the DIHPB. A full bridge strain gage configuration was selected to improve signal quality for experimentation. Four strain gages spaced equally around the perimeter of the bar, with adjacent gauges being perpendicular, allow for the rejection of bending strains and improved sensitivity to axial strains (by a factor of $2(1+\nu)$, where ν is the Poisson's ratio). The schematic showing the configuration of the strain gages is shown in Fig. 49, with axially oriented gages labeled "ε" and perpendicular gages labeled "$-\nu\varepsilon$".

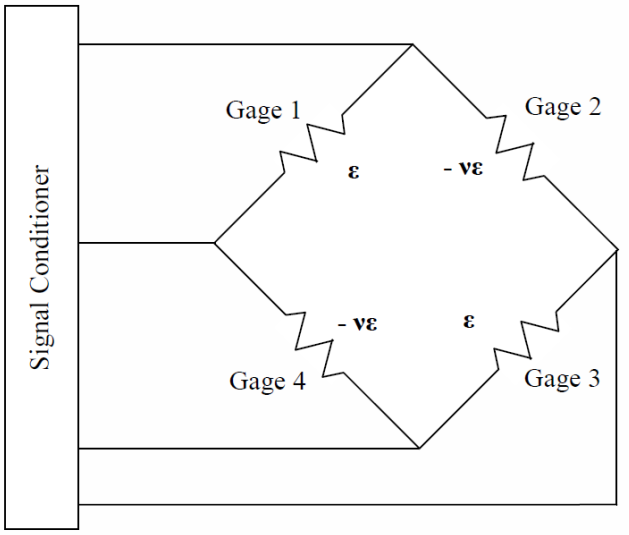

Fig. 49 Full bridge axial strain gage located on transmitter bar of DIHPB (illustration by this author)

3.5.1 Calibration of the DIHPB

Calibration of the DIHPB involves determining the strain-voltage relationship for the apparatus and the elastic properties of the transmitter bar (wave speed, elastic modulus). These calibrations ensure that the calculations of specimen stress/strain curves are as accurate as possible.

For a full bridge arrangement, the strain-voltage relationship, ε(Vr), is calculated as:

$$\varepsilon = -\frac{2V_r}{GF[(\nu+1) - V_r(\nu-1)]} \qquad \textbf{Eq. 3-2}$$

where V_r is the ratio of excitation voltage to output voltage, GF is the gage factor, and ν is the Poisson's ratio for the transmitter bar.

The strain-voltage relationship is simplified to:

$$\varepsilon(t) = k \cdot V(t) \qquad \textbf{Eq. 3-3}$$

where k is a constant (units of 1/mV) calculated from the gage factor, excitation voltage and Poisson's ratio of the transmitter bar.

Wave speed was measured by examining the time between successive reflections within the bar. A single reflection is shown in Fig. 50. The initial wave detected by the strain gages is in compression (negative voltage) and its reflection is in tension (positive voltage). The length of time between peaks is the time required to travel one lap of the bar, or twice the bar length.

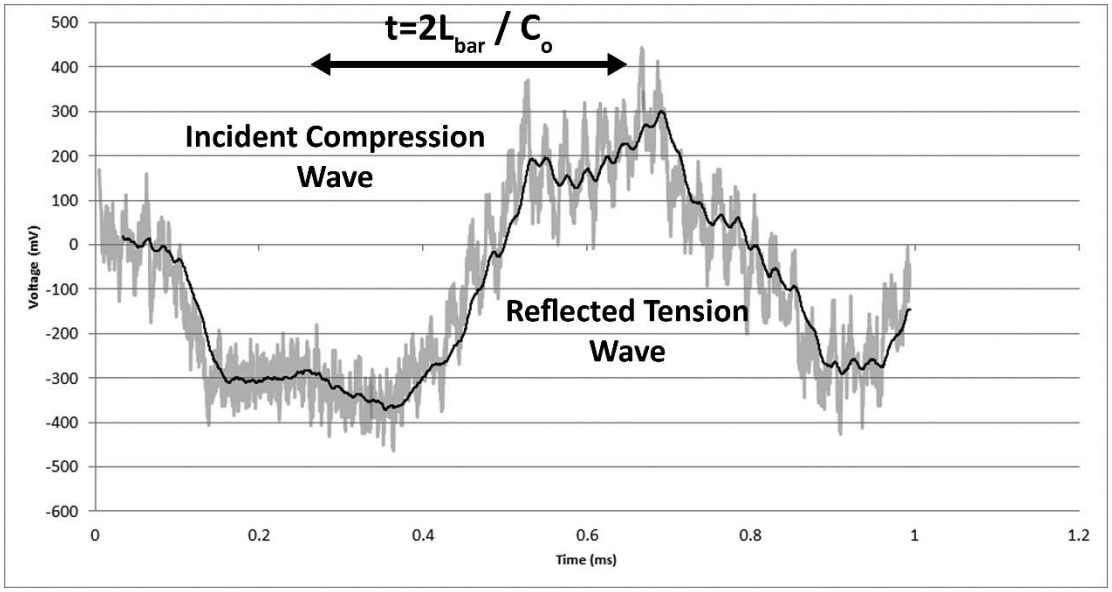

Fig. 50 Single Reflection of an elastic wave in the transmitter bar of the DIHPB

An accurate measurement of the time was obtained by recording the average distance over a very large number of reflections by taking the Discrete Fourier Transform (DFT) of a large number of reflections and extracting the primary frequency component shown in Fig. 51.

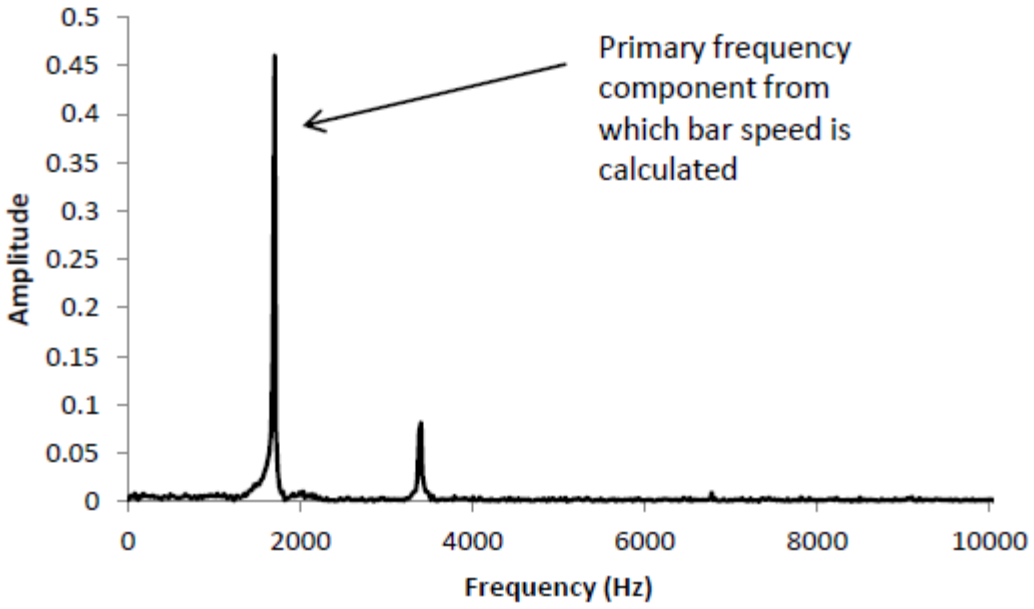

Fig. 51 Amplitude spectrum of voltage calculated using the Discrete Fourier Transform

The bar speed can then be calculated from the primary frequency component as:

$$C_0 = 2L_{bar}f \qquad \textbf{Eq. 3-4}$$

For the transmitter bar used in the DIHPB apparatus, C_0 was calculated to be approximately 5180 m/s,

The elastic modulus can then be calculated as

$$C_0 = \sqrt{\frac{E}{\rho}};\ E = C_0^2\rho \qquad \textbf{Eq. 3-5}$$

3.5.2 Stress-Strain Calculations

The strain-voltage relationship in Eq. 3-3 can be converted to force-time assuming that the stress in the elastic transmitter bar is purely longitudinal so that,

$$F(t) = \varepsilon(t) \cdot (EA)_{tbar} \quad \textbf{Eq. 3-6}$$

where F(t) is the force or load at any time *t*, ε(t) is the strain at any time *t* in the elastic transmitter bar, and $(EA)_{tbar}$ is the product of the elastic modulus and cross-sectional area for the transmitter bar. A force balance is taken at the bar-specimen interface, and the stress is calculated by assuming a uniaxial state of stress within the specimen. The stress within the specimen $\sigma_s(t)$ is defined as

$$\sigma_s(t) = \frac{F(t)}{A_s(t)} \quad \textbf{Eq. 3-7}$$

Where $A_s(t)$ is the cross sectional area of the specimen at any time *t*.

It is important to remember that in the DIHPB configuration, there is a mismatch in cross sectional area between the transmitter bar and the specimen as well as between the specimen and striker bar. The constant strain rate portion of the direct impact test is only up to the

point where the elastic compression wave has traveled from the impact end down the length of the striker bar, reflected from the free end, and returned to the impact face. Past this point, the strain rate is significantly diminished due to the mechanical impedance mismatch between the striker and specimen. The time where constant strain rate is valid was shown in Eq. 2-11. Also, if it is assumed that there is no volume change in the specimen during deformation,

$$A_s(t) \cdot L(t) = A_0 \cdot L_0 \qquad \textbf{Eq. 3-8}$$

where A_o and L_o are the initial cross-sectional area and length of the specimen prior to deformation. Assuming constant strain rate of deformation, the length L(t) of the specimen is assumed to be related to time linearly as,

$$L(t) = L_0 - \frac{L_0 - L_f}{t_f} \cdot t \qquad \textbf{Eq. 3-9}$$

where L_f is the final length of the specimen at time t_f which is equal to $t_{\dot{\varepsilon}}$ from Eq. 2-11. The final specimen true stress as a function of strain, assuming constant strain rate, is calculated as

$$\sigma_s(t) = \varepsilon_s(t) \cdot \left[\frac{EA\left[L_0 - \left(L_0 - L_f\right)\left(t/t_f\right)\right]}{A_0 L_0}\right] \qquad \textbf{Eq. 3-10}$$

where A_0 and L_0 are the original cross-sectional area and length of the specimen before deformation and E and A are the modulus of elasticity and cross-sectional area of the elastic transmitter bar. The true strain of deformation of the specimen, $\varepsilon_s(t)$ is calculated to be

$$\varepsilon_s(t) = ln\left(\frac{L_0}{L_0 - (L_0 - L_f)\left(\frac{t}{t_f}\right)}\right) \quad \textbf{Eq. 3-11}$$

Strain rate of deformation is constant up to $t_{\dot{\varepsilon}}$, after which it is diminished due to the mechanical impedance mismatch between the striker and specimen. The actual strain rate is difficult to measure. Thus stress-strain calculations are only valid up to where strain rate is measured to be constant. For a striker bar of length 0.2 m used in the DIHPB, the strain rate of deformation is constant up to $t_{\dot{\varepsilon}} \approx 77\ \mu s$, after which it diminishes, as discussed in Section 2.4.2.2.

3.5.3 Effect of Heat Treatment and Testing Conditions on Dynamic Stress-Strain Response of AISI 4340 Steel

In this thesis, the dynamic high strain rate impact stress-strain responses of all 48 tested specimens were calculated from voltage-time data. Based on this data, an estimation of the quasi-static yield strength in compression, for various heat treatments, as well as the quasi-static elastic modulus at various testing temperatures were determined by regression fitting

the dynamic values against strain rate and extrapolating to $\dot{\varepsilon} = 1\ s^{-1}$. The elastic moduli and yield strength are important physical properties used for defining the elastic behavior of various heat treatments of steel in FEA analysis.

The elastic modulus of a material is defined as its resistance to elastic deformation, or stiffness, and is determined by the binding forces between atoms. These forces cannot be changed without changing the basic nature of the material. It is affected by slight additions of alloying elements, heat treatment, cold work and testing temperature [144]. The modulus of elasticity also varies depending on the direction of deformation. For example, annealed AISI 4340 steel (heated to 810°C, furnace cooled 11°C/hr to 355°C, air cooled) has an elastic modulus of 205 GPa (compression and tension), a bulk modulus of 160 GPa, and a shear modulus of 80 GPa. It also has a yield strength of 470 MPa [145]. It is much stiffer in uniaxial deformation than in shear. For an isotropic material such as steel, the Young's modulus, defines the elastic stiffness of a material in tension or compression by the ratio of uniaxial stress divided by the uniaxial strain, as

$$E = \frac{\sigma}{\varepsilon}, \qquad \textbf{Eq. 3-12}$$

up to the yield stress of the material. When an isotropic material is subjected to hydrostatic pressure, all shear stresses are zero, and the normal stresses are uniform. A material's

resistance to volume change under a hydrostatic load is defined by the bulk modulus or the ratio of applied pressure divided by volume strain as

$$K = \frac{P}{(\Delta V)/V_0} = \frac{\sigma_{xx} + \sigma_{yy} + \sigma_{zz}}{\varepsilon_{xx} + \varepsilon_{yy} + \varepsilon_{zz}}. \quad \textbf{Eq. 3-13}$$

It is related to Young's modulus by the equation

$$K = \frac{E}{3(1 - 2\nu)}, \quad \textbf{Eq. 3-14}$$

where 'ν' is the Poisson's ratio. The shear modulus defines the stiffness of a material under pure shear and can be calculated from the Young's and bulk modulus, and Poisson's ratio by

$$G = \frac{3KE}{9K - E} = \frac{E}{2(1 + \upsilon)} \quad \textbf{Eq. 3-15}$$

Born's Theory [146] states that for any process leading to the distortion of a crystal lattice, e.g. from quenching, there is reduction in Young's Modulus. Conversely, heating the steel through tempering promotes recovery of the lattice, reduces distortion, and should thus increases the modulus of elasticity. Generally speaking, the value of Young's modulus, depends almost entirely on the energy of the inter-atomic bonds in metals and alloys. It is usually considered a microstructure insensitive property. Although heat treatment results,

such as martensite formation in steels, may affect the value to some extent due to lattice distortion, the nature behind the elastic constant should not change, i.e. the metallic or free electron bond in the material.

The Young's modulus is normally determined through acoustic techniques by the speed of sound through a material and its density [147]. In some accoustic techniques, the determination of the Young's modulus depends on the excitation of longitudinal waves in specimens by piezoelectric transducers.

Young's modulus is a thermodynamic quantity which is greatly affected by the ambient temperature of a material. Temperature affects both the speed of sound through a material and its density. According to ASME standard B31.1-1995 [148], the *Young's modulus decreases with increasing testing temperature for metals*. This phenomena is based on Born's theory of bulk melting [146] which states that as temperature is increased, the distances between the atoms of the meatal increases due to thermal expansion. As a result, the restoring forces between the atoms are reduced and the elastic modulus decreases. As temperature continues to increase, the distance between the atoms will increase until the crystal lattice collapses and the material melts. According to Tomlinson [149], "…when an iron or steel wire is thrown into longitudinal vibrations, so as to produce a musical note, the pitch of this note becomes lower as we raise the temperature". This was shown

experimentally by Nowacki & Kasprzyk [150]. Increasing temperature, decreases the speed of sound through a metal and decreases the modulus of elasticity according to Eq. 3-5.

In studying the effect of testing temperature on the poisson's ratio, Young's modulus and the shear modulus of various steels (SAE 1095, 1020, 3340, and 5140), Everett and Miklowitz [151] determined that *the elastic moduli decrease with increasing testing temperature (from 20°C to 537°C) while Poisson's ratio increases.* When comparing the moduli of hot rolled to cold rolled SAE 1020 steels, *the elastic moduli and Poisson's ratio all increased with decreasing hardness and strength at the same testing temperature.* In this thesis, Poisson's ratio was assumed constant at 0.29 for steel.

The quasi-static Young's moduli, in this thesis, were estimated from the dynamic stress-strain responses using a line of best fit on the observed elastic portions of the stress strain-curves. This method was used in the absence of quasi-static testing. This method is fast but had a high % error [1-3 GPa]. *As a result the relationship between elastic modulus and heat treatment temperature may not be accurate as the differences in elastic moduli between heat treatment temperatures fall within the margin of error.* However there is a noticeable drop in Young's modulus with increasing testing temperature

An example of a measurement of Young's modulus for steel with heat treatment (800°C/30 min & 550°C/90 min) impacted at 45 kgm/s and tested at 20°C is shown in Fig.

52, as the slope of the linear best fit curve of the elastic portion of the dynamic stress vs strain curve. The yield strength is calculated at the 0.2% offset.

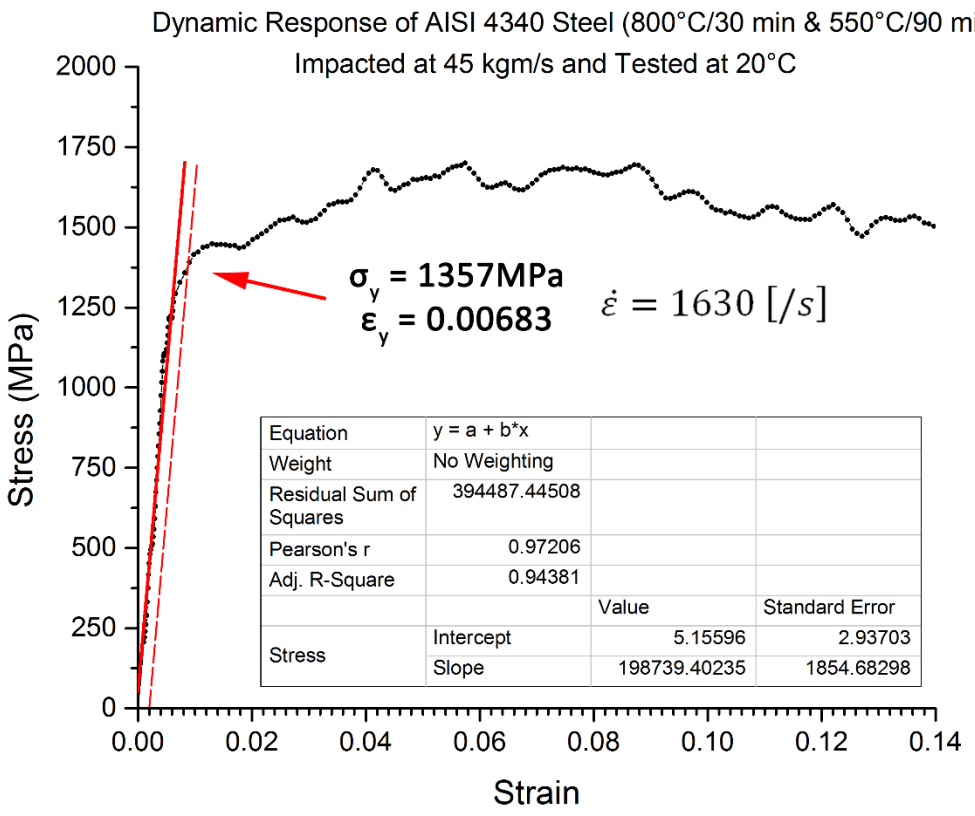

Fig. 52 Dynamic stress-strain response of a specimen heat treated at 800°C/30min & 550°C/90min and impacted at 45 kgm/s at 20°C showing calculated Young's modulus, yield strength at 0.2% offset, and yield strain

The elastic portion of the stress-strain curve was determined by linear regression fitting and shifting the curve fit until the y-intercept was closest to zero and the error was minimized. Strain rate was measured to be constant up to a deformation time of 77μs after

impact, as discussed in Section 3.5.2. after which it diminishes. The stress and strain calculations using Eq. 3-10 and Eq. 3-11, are only accurate up to this deformation time. The extent of the stress measurement up to this deformation time is shown in Fig. 53 of a plot of stress vs time.

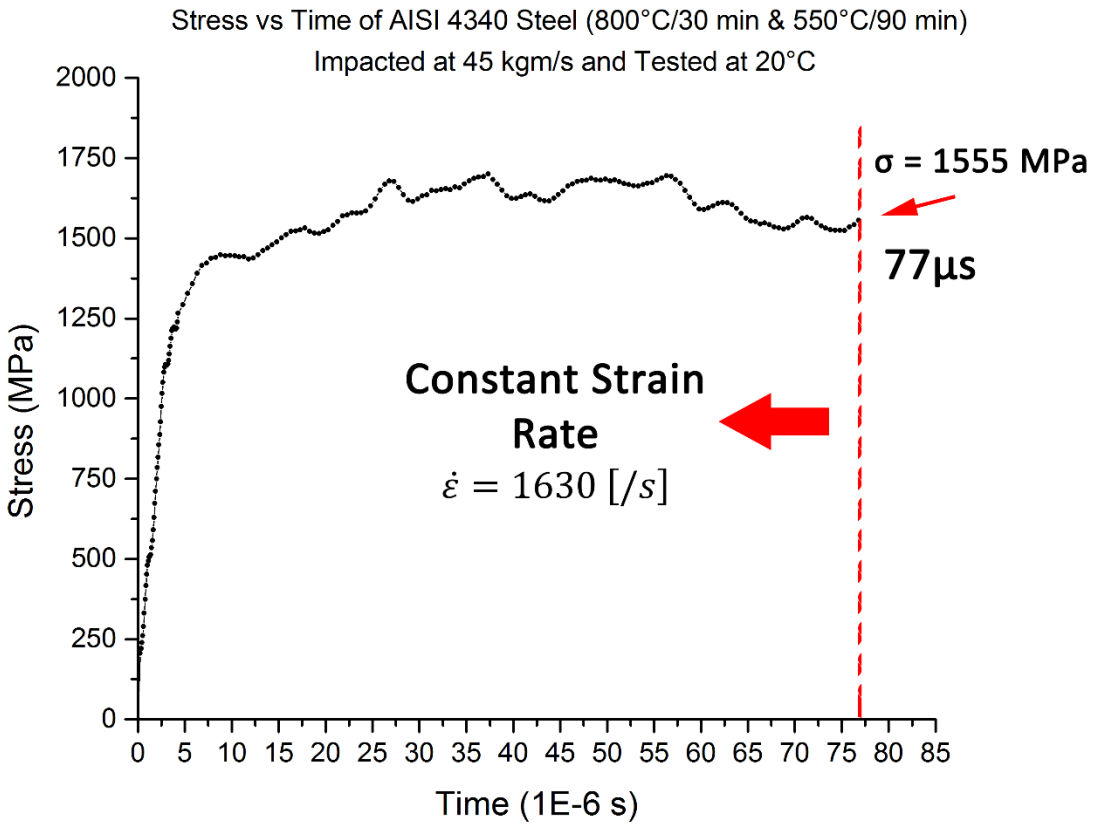

Fig. 53 Stress vs Time response of a specimen heat treated at 800°C/30min & 550°C/90min and impacted at 45 kgm/s at 20°C showing the measurement of constant strain rate up to 77µs of deformation time

As a comparison, a plot of the dynamic response calculated for the full deformation of a specimen of steel of this heat treatment and testing conditions, assuming constant strain rate, is shown in Fig. 54. A line is drawn showing the division between constant and variable strain rate measurement.

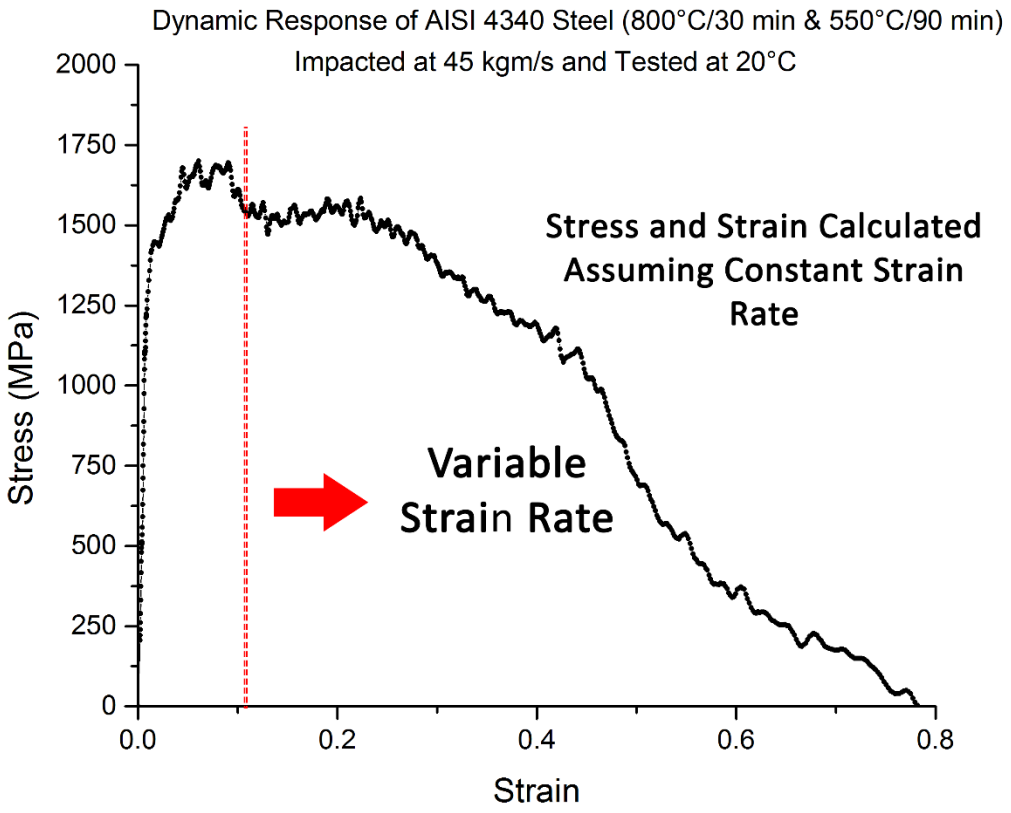

Fig. 54 Dynamic response of full deformation of a specimen of AISI 4340 steel heat treated at 800°C/30min & 550°C/90min and impacted at 45 kgm/s at 20°C showing the division between constant and variable strain rate measurement

A summary of the dynamic response data for this heat treatment and impact conditions is shown in Table 6.

Table 6 Summary of Estimated Elastic Properties of AISI 4340 steel with heat treatment (800°C/30 min & 550°C/90 min) tested at 45 kgm/s and 20°C.

Austenization Temperature [°C]	800
Tempering Temperature [°C]	550
Testing Temperature [°C]	20
Impact Momentum [kgm/s]	45
Strain Rate [/s]	1630
Yield Strength [MPa]	1357
Yield Strain	0.00683
Young's Modulus [GPa]	199 $\pm$ 2

3.5.3.1 Effect of Impact Momentum on Young's Modulus and Yield Strength

Increasing the impact momentum to 49 kgm/s has very little effect on the Young's modulus, but increases the dynamic yield strength and strain, as shown in Fig. 55, for the same heat treatment and impact conditions. The difference in the Young's moduli lies within the margin of error. Since the Young's modulus is an atomic property, *there is no change in modulus with impact momentum.* A comparison between the dynamic responses for all four impact momenta and under constant strain rate of deformation, are shown in Fig. 56. Increasing the impact momentum increases the yield strength.

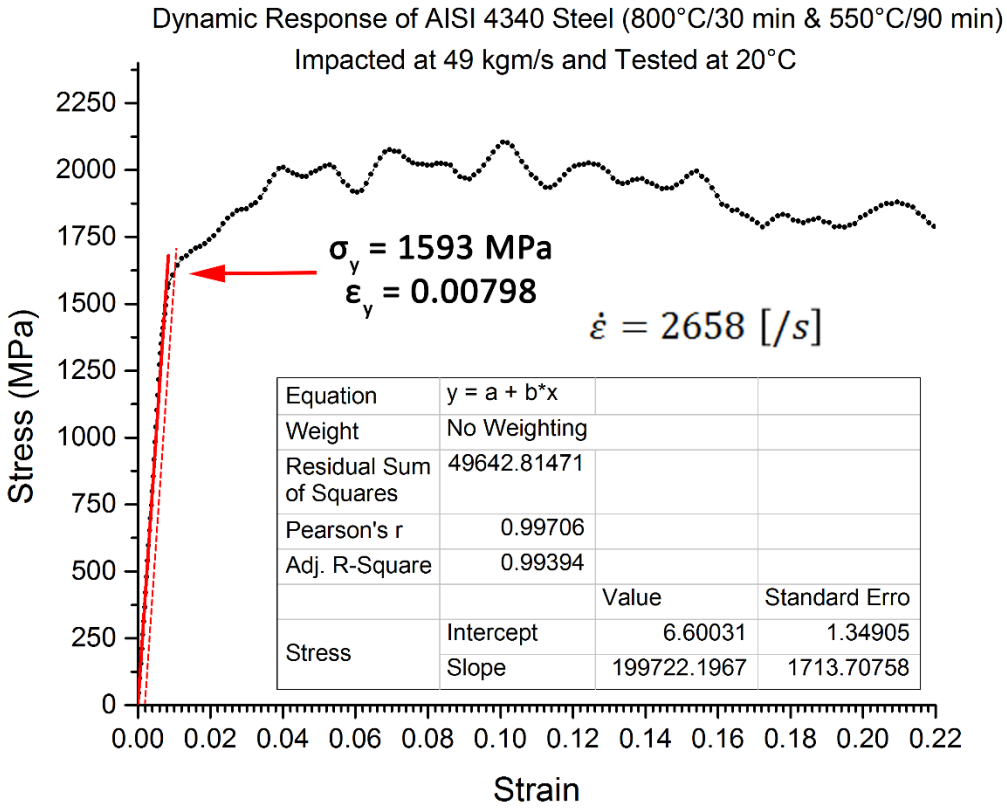

Fig. 55 Dynamic stress-strain response of a specimen heat treated at 800°C/30min & 550°C/90min and impacted at 49 kgm/s at 20°C showing calculated Young's modulus, yield strength at 0.2% offset, and yield strain

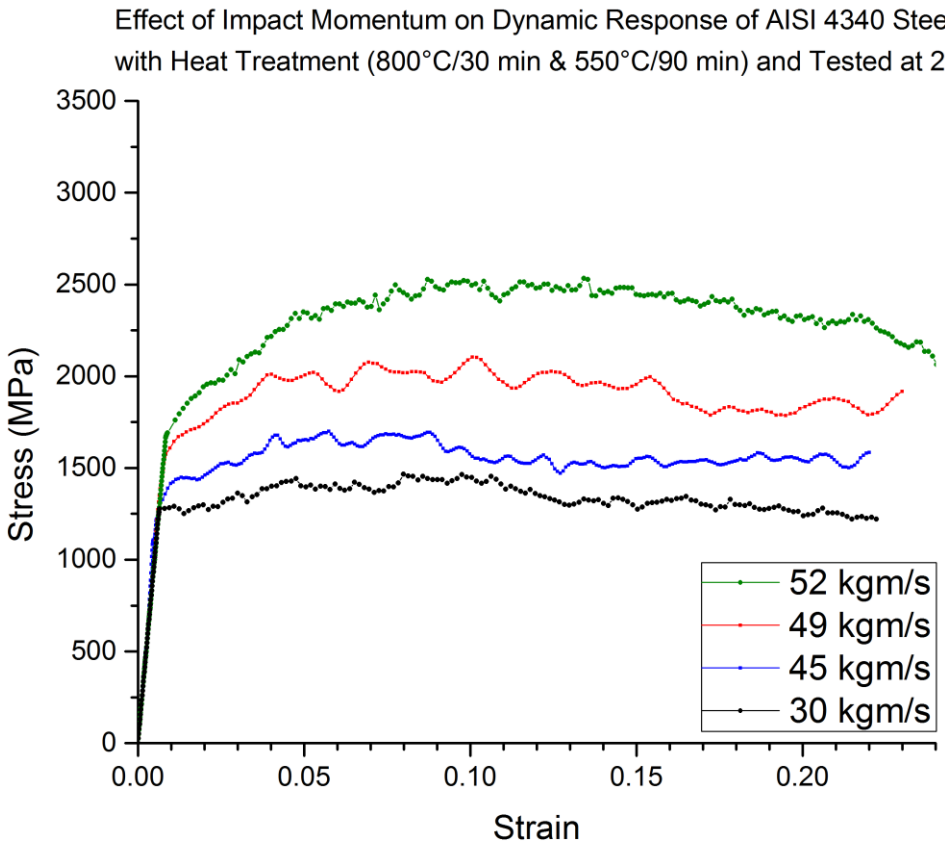

Fig. 56 Comparison of dynamic stress-strain responses of AISI 4340 steel heat treated at 800°C/30min & 550°C/90min and impacted at two momenta under constant strain rate of deformation

3.5.3.2 Effect of Tempering Temperature on Young's Modulus and Yield Strength

When tempering temperature was reduced from 550°C to 400°C, Young's modulus was shown to decrease by 3% and yield strength increase by 14%, as seen in Fig. 57 of a plot of dynamic stress vs strain for a specimen of AISI 4340 steel heat treated at 800°C/30 mins & 400°C/90 min and tested at 45 kgm/s and 20°C. There is also a reduction in the strain rate

of deformation despite being impacted at the same momentum. This can be attributed to the higher strength and hardness of the steel at a tempering temperature of 400°C which deforms over smaller strains.

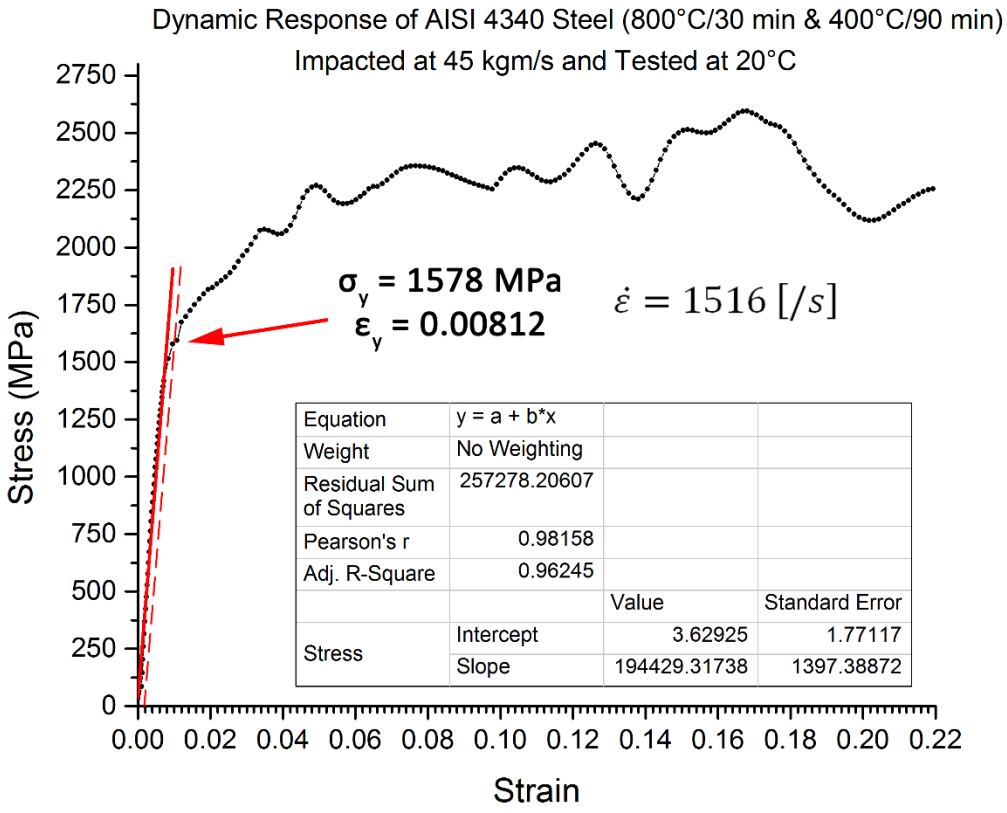

Fig. 57 Dynamic stress-strain response of a specimen heat treated at 800°C/30min & 400°C/90min and impacted at 45 kgm/s at 20°C showing calculated bulk modulus, yield strength at 0.2% offset, and yield strain

A plot comparing the stress-strain responses of specimens tempered at 400°C and 550°C, impacted at 45 kgm/s and tested at 20°C shown in Fig. 58, shows the magnitude of the yield

strength and ultimate strength difference. Decreasing the tempering temperature also increases the stress hardening effect after yield.

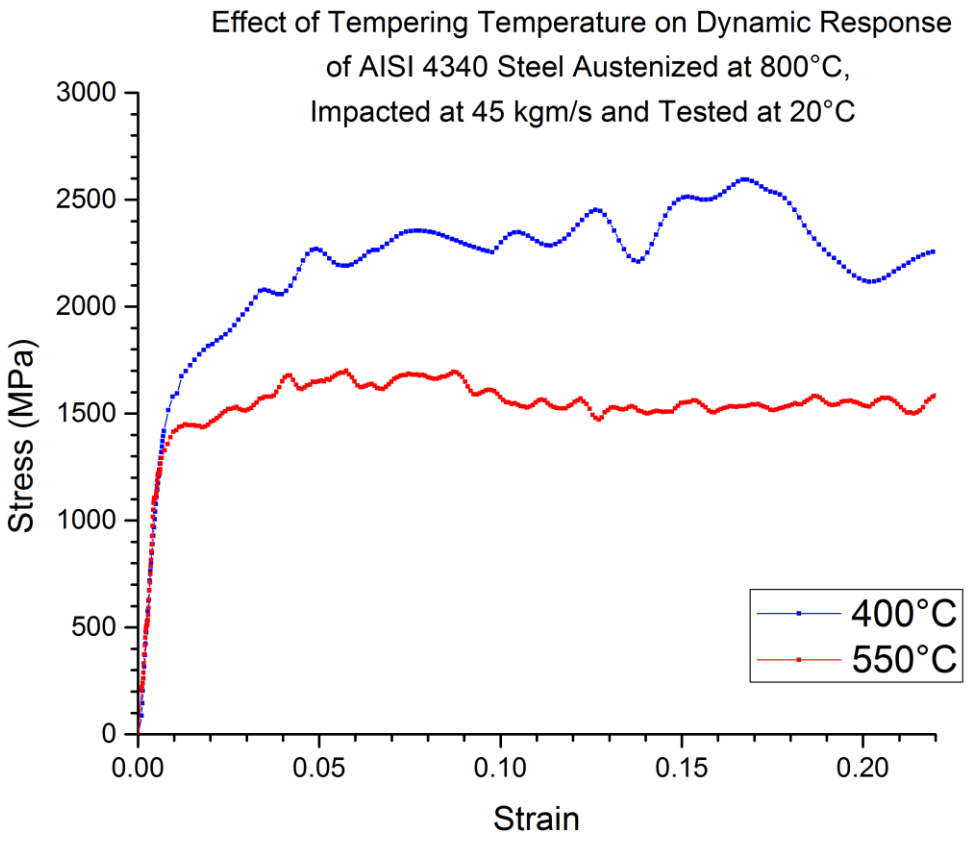

Fig. 58 Effect of tempering temperature on stress-strain response of AISI 4340 steel austenized at 800°C/30min and impacted at 45 kgm/s at 20°C

3.5.3.3 Effect of Testing Temperature on Young's Modulus and Yield Strength

Increasing the testing temperature decreases both the elastic modulus and yield strength of a material. According to the ASME B31.1 [148], the Young's modulus for an annealed AISI 4340 steel tested at 428°C is approximately 175.9 GPa. For specimen of steel austenized at 800°C and tempered at 400°C, increasing the testing temperature from ambient 20°C to 428°C resulted in a decrease in Young's modulus of 13% and a decrease in yield strength of 18%, as shown in Fig. 59 of a plot of the dynamic stress vs strain for specimen of AISI 4340 steel with this heat treatment, impacted at 45 kgm/s and tested at 428°C.

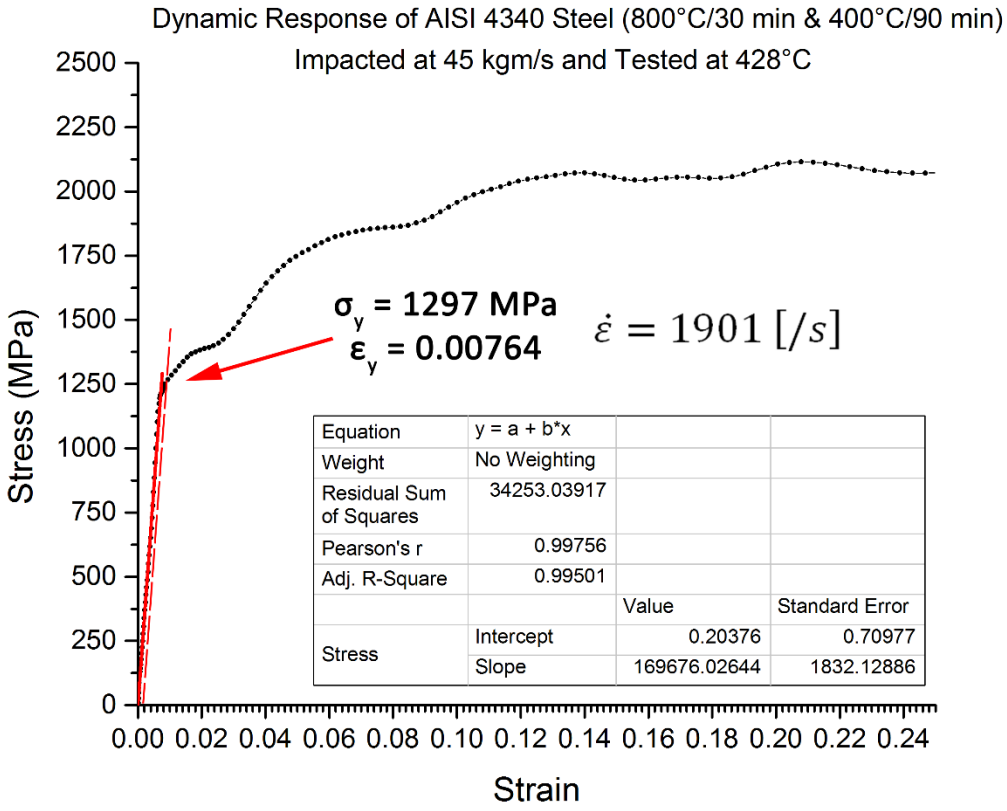

Fig. 59 Dynamic stress-strain response of a specimen heat treated at 800°C/30min & 400°C/90min and impacted at 45 kgm/s at 428°C showing calculated Young's modulus, yield strength at 0.2% offset, and yield strain

A comparison between the dynamic stress-strain responses of two AISI 4340 steel specimens with heat treatment (800°C/30min & 400°C/90min), tested at 20°C and 428°C is shown in Fig. 60. Increasing the testing temperature reduces the degree of stress and strain hardening.

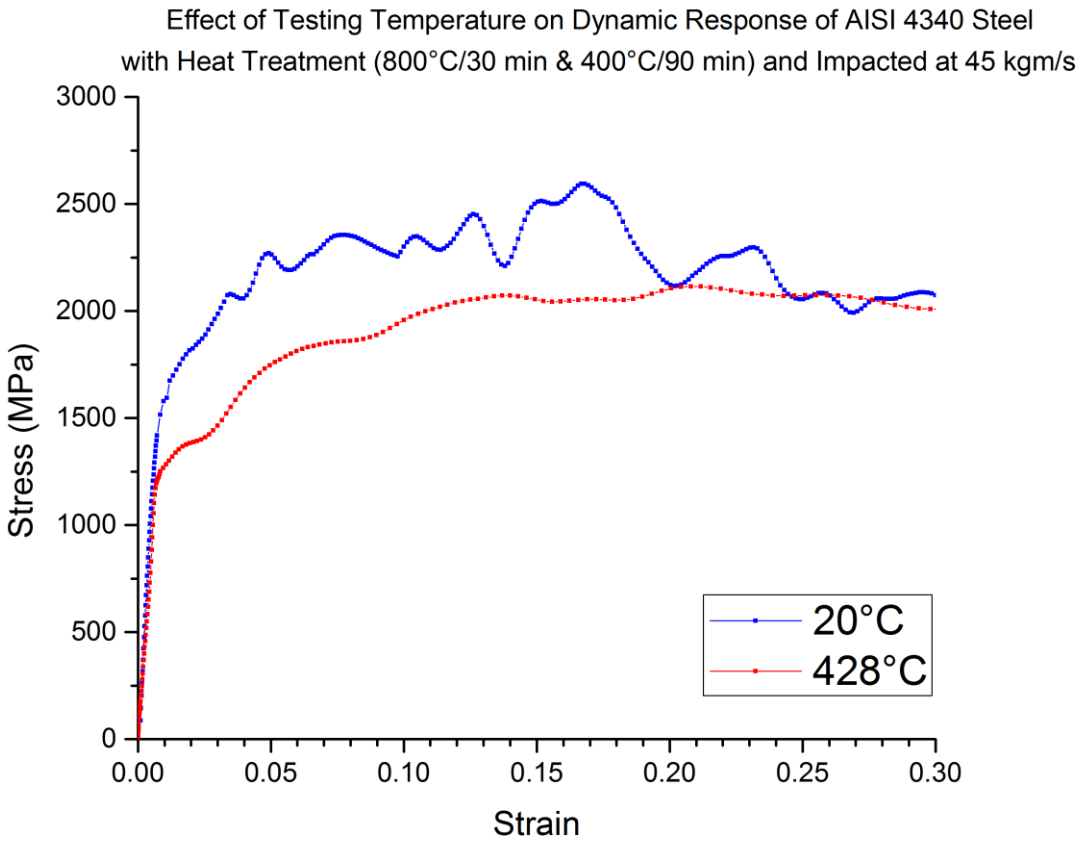

Fig. 60 Effect of testing temperature on stress-strain response of AISI 4340 steel austenized at 800°C/30min, tempered at 400°C, and impacted at 45 kgm/s

3.5.3.4 Effect of Austenization Temperature on Young's Modulus and Yield Strength

When the austenization temperature of steel is increased there is an increase in toughness and decrease in hardness, as discussed in Section 3.4.1.2, caused by the formation of retained austenite in the martensite lath grain boundaries [127, 152]. Also a decrease in hardness is accompanied by an increase in elastic modulus. Plots of the stress-strain responses of AISI

4340 steel specimens austenized at 900°C and 1000°C, shown in Fig. 61 and Fig. 62 respectively, under the same tempering temperature (550°C) and testing conditions (45 kgm/s at 20C), reveal an increase in Young's modulus of approximately 2% and a decrease in yield strength of 15% for every 100°C increase in austenization temperature.

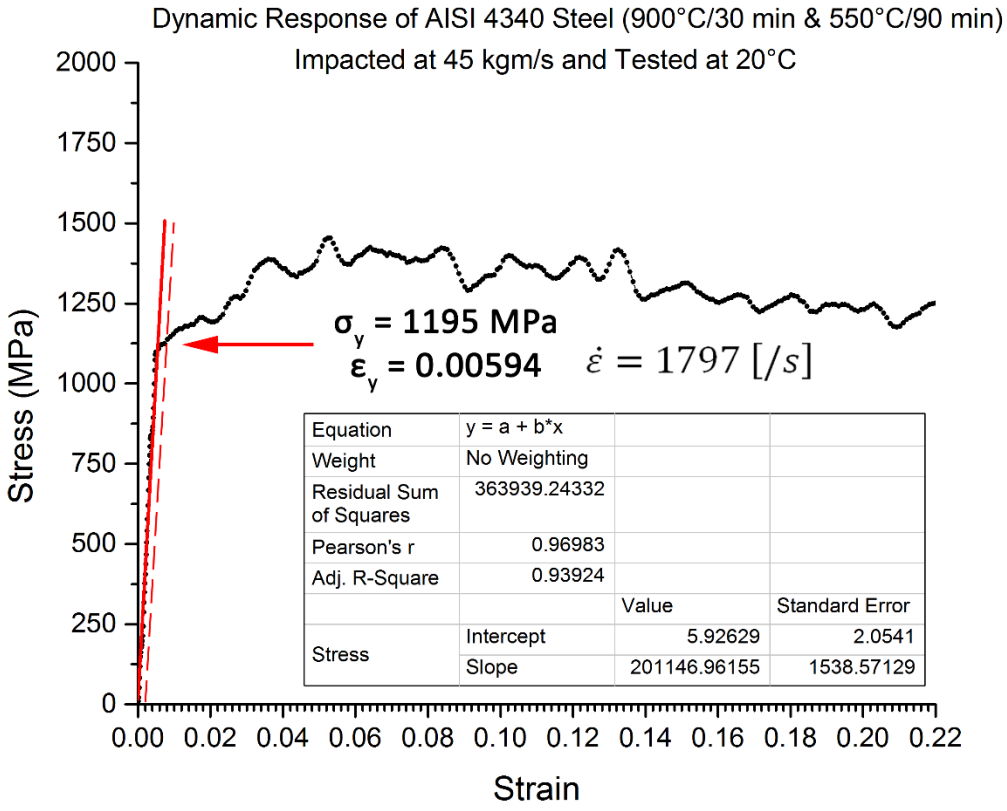

Fig. 61 Dynamic stress-strain response of a specimen heat treated at 900°C/30min & 550°C/90min and impacted at 45 kgm/s at 20°C showing calculated Young's modulus, yield strength at 0.2% offset, and yield strain

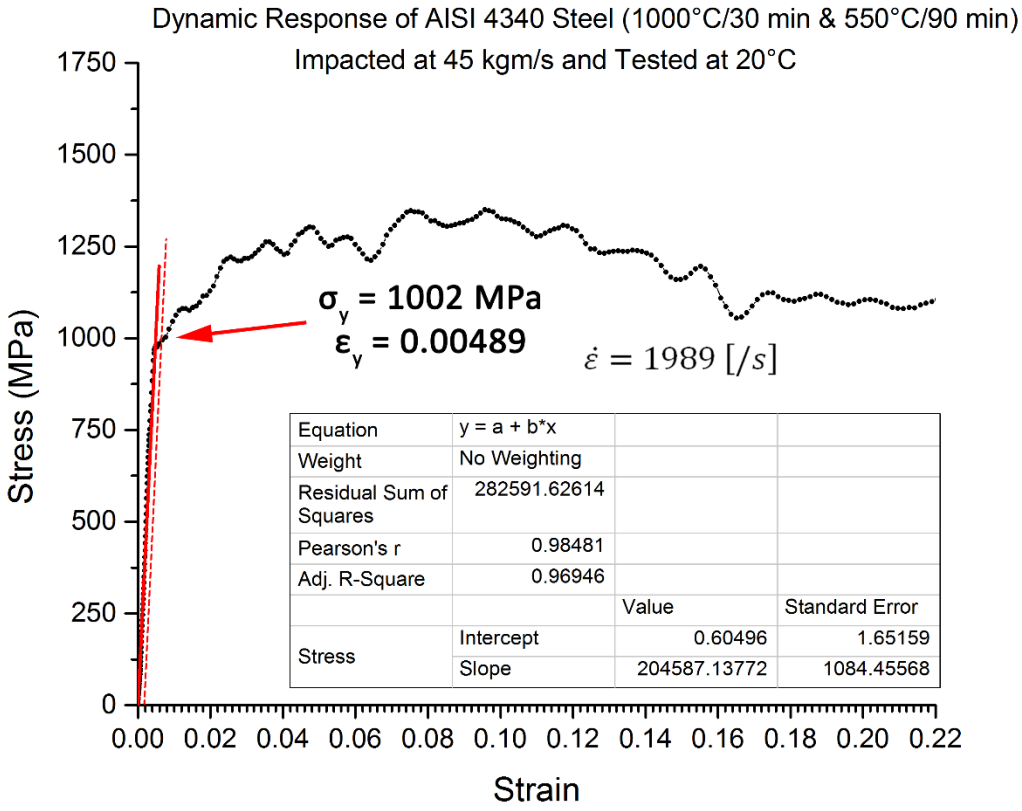

Fig. 62 Dynamic stress-strain response of a specimen heat treated at 1000°C/30min & 550°C/90min and impacted at 45 kgm/s at 20°C showing calculated Young's modulus, yield strength at 0.2% offset, and yield strain

The increase in Young's modulus and decrease in yield strength as austenization temperature increases is shown in Fig. 63, in a plot comparing the dynamic responses of all three austenization temperatures for AISI 4340 steel specimens tempered at 550°C and tested at 45 kgm/s and 20°C.

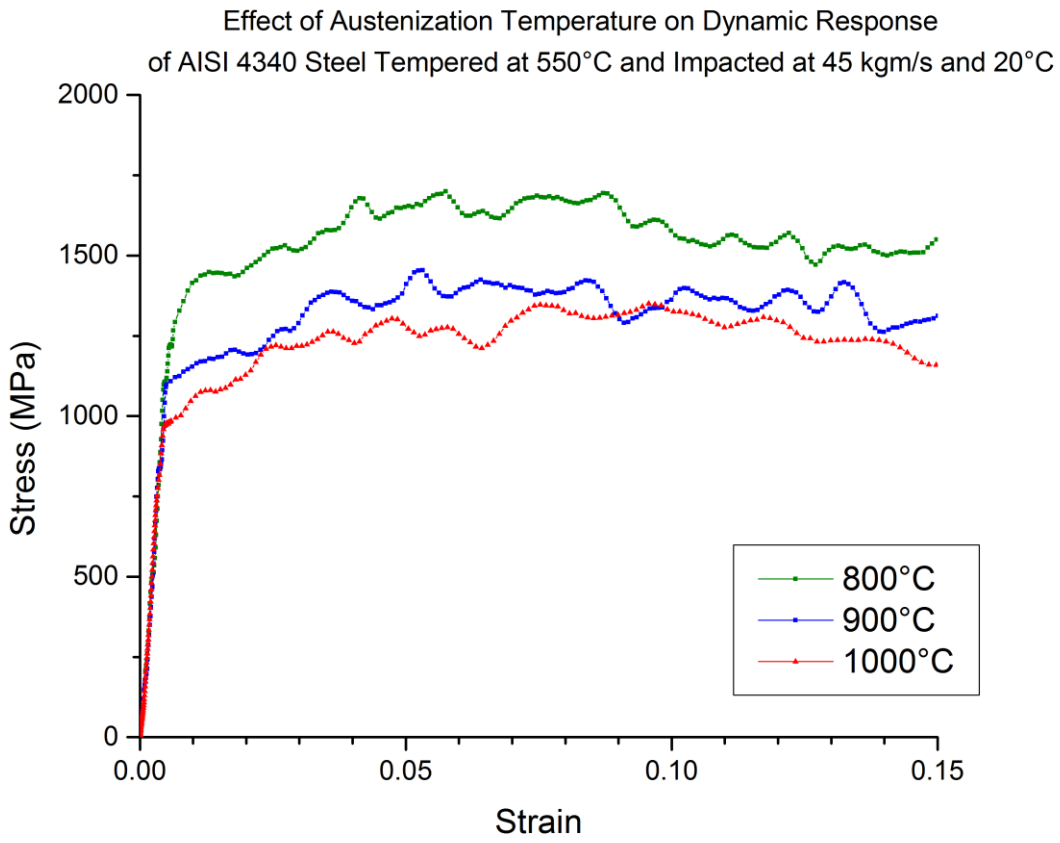

Fig. 63 Effect of austenization temperature on dynamic response of AISI 4340 steel tempered at 550°C and tested at 45 kgm/s and 20°C

3.5.3.5 Summary of Dynamic Stress-Strain Response Data and Discussion of Results

A summary of all calculated Young's moduli and yield strengths for all tested specimens is shown in Table 7, Table 8, and Table 9. A large margin of error of ±50 MPa was calculated for the measurements of yield strength due to the large fluctuations in the voltage-time readings from the oscilloscope.

Table 7 Calculation of Young's modulus for steel specimens hardened at 800°C

Austenizing	Tempering	Testing Temperature [°C]	Impact Momentum [kgm/s]	Strain Rate [s^{-1}]	Dynamic Yield Strength ± 50 [MPa] [1]	Dynamic Yield Strain	Young's Modulus [GPa]
800°C/30mins & Oil Quench	550°C/90mins & Air Cool	20	30	978	1298	0.00653364	198.664 ± 2
			45	1630	1357	0.00682805	198.739 ± 2
			49	2658	1593	0.00801211	198.824 ± 2
			52	3972	1784	0.00898166	198.627 ± 2
		428	30	1103	846	0.00493087	171.572 ± 2
			45	2132	1103	0.00643794	171.328 ± 2
			49	3046	1302	0.00758185	171.726 ± 2
			52	4025	1528	0.00891342	171.427 ± 2
	400°C/90mins & Air Cool	20	30	903	1502	0.00772944	194.322 ± 2
			45	1516	1578	0.00811607	194.429 ± 2
			49	2578	1723	0.00885297	194.624 ± 2
			52	3058	1869	0.0096093	194.499 ± 2
		428	30	987	957	0.00564775	169.448 ± 2
			45	1901	1297	0.0073493	169.676 ± 2
			49	2624	1472	0.00869673	169.259 ± 2
			52	3373	1686	0.00995812	169.309 ± 2

[1] Dynamic yield strength based on 0.2% offset through best fit line of elastic portion of curve

Table 8 Calculation of Young's modulus for steel specimens hardened at 900°C

Austenizing	Tempering	Testing Temperature [°C]	Impact Momentum [kgm/s]	Strain Rate [s^{-1}]	Dynamic Yield Strength ± 50 [MPa] [1]	Dynamic Yield Strain	Young's Modulus [GPa]
900°C/30mins & Oil Quench	550°C/90mins & Air Cool	20	30	1331	1105	0.00549008	201.272 ± 2
			45	1797	1195	0.00594093	201.147 ± 2
			49	2893	1326	0.00657898	201.551 ± 2
			52	4182	1529	0.00759457	201.328 ± 2
		428	30	1452	757	0.00436238	173.529 ± 2
			45	2305	877	0.00506582	173.121 ± 2
			49	3219	1023	0.00590013	173.386 ± 2
			52	4195	1265	0.00728489	173.647 ± 2
	400°C/90mins & Air Cool	20	30	1019	1322	0.00672339	196.627 ± 3
			45	1656	1437	0.00729727	196.923 ± 3
			49	2703	1532	0.00778119	196.885 ± 3
			52	3220	1655	0.00841276	196.725 ± 3
		428	30	1143	810	0.00471056	171.954 ± 3
			45	2082	1049	0.00610494	171.828 ± 3
			49	2752	1238	0.00721752	171.527 ± 3
			52	3506	1403	0.00816971	171.732 ± 3

[1] Dynamic yield strength based on 0.2% offset through best fit line of elastic portion of curve

Table 9 Calculation of Young's modulus for steel specimens hardened at 1000°C

Austenizing	Tempering	Testing Temperature [°C]	Impact Momentum [kgm/s]	Strain Rate [s^{-1}]	Dynamic Yield Strength ± 50 [MPa] [1]	Dynamic Yield Strain	Young's Modulus [GPa]
1000°C/30mins & Oil Quench	550°C/90mins & Air Cool	20	30	1514	993	0.00484672	204.881 ± 1
			45	1989	1002	0.00489767	204.587 ± 1
			49	3066	1067	0.00521075	204.769 ± 1
			52	4327	1126	0.00549952	204.745 ± 1
		428	30	1872	693	0.00395478	175.231 ± 2
			45	2809	814	0.00465334	174.928 ± 2
			49	3449	927	0.00529481	175.077 ± 2
			52	4526	1079	0.00616036	175.152 ± 2
	400°C/90mins & Air Cool	20	30	1354	1239	0.0062114	199.472 ± 3
			45	1768	1312	0.00656598	199.818 ± 3
			49	2822	1378	0.0069053	199.557 ± 3
			52	3576	1453	0.0072896	199.325 ± 3
		428	30	1587	730	0.00421938	173.011 ± 2
			45	2394	848	0.00490465	172.897 ± 2
			49	2931	935	0.00539455	173.323 ± 2
			52	4015	1106	0.00642273	172.201 ± 2

[1] Dynamic yield strength based on 0.2% offset through best fit line of elastic portion of curve

Based on the data, Young's modulus *increases* with increasing austenization and tempering temperatures but *decreases* with increasing testing temperature. However the changes in Young's modulus with heat treatment temperatures lie within the margin of error. It is difficult to discern the exact effect of heat treatment temperatures on Young's modulus. There is no significant change in Young's modulus with deformation strain rate. Any variation is within the calculated margin of error. These findings are consistent with the literature.

When testing temperature is increase to 428°C, Young's modulus is shown to decrease by as much as 15%, as shown in Fig. 64, in specimens austenized at 800°C, tempered at 550°C and impacted at various momenta. This drop in modulus is consistent across all austenization temperatures.

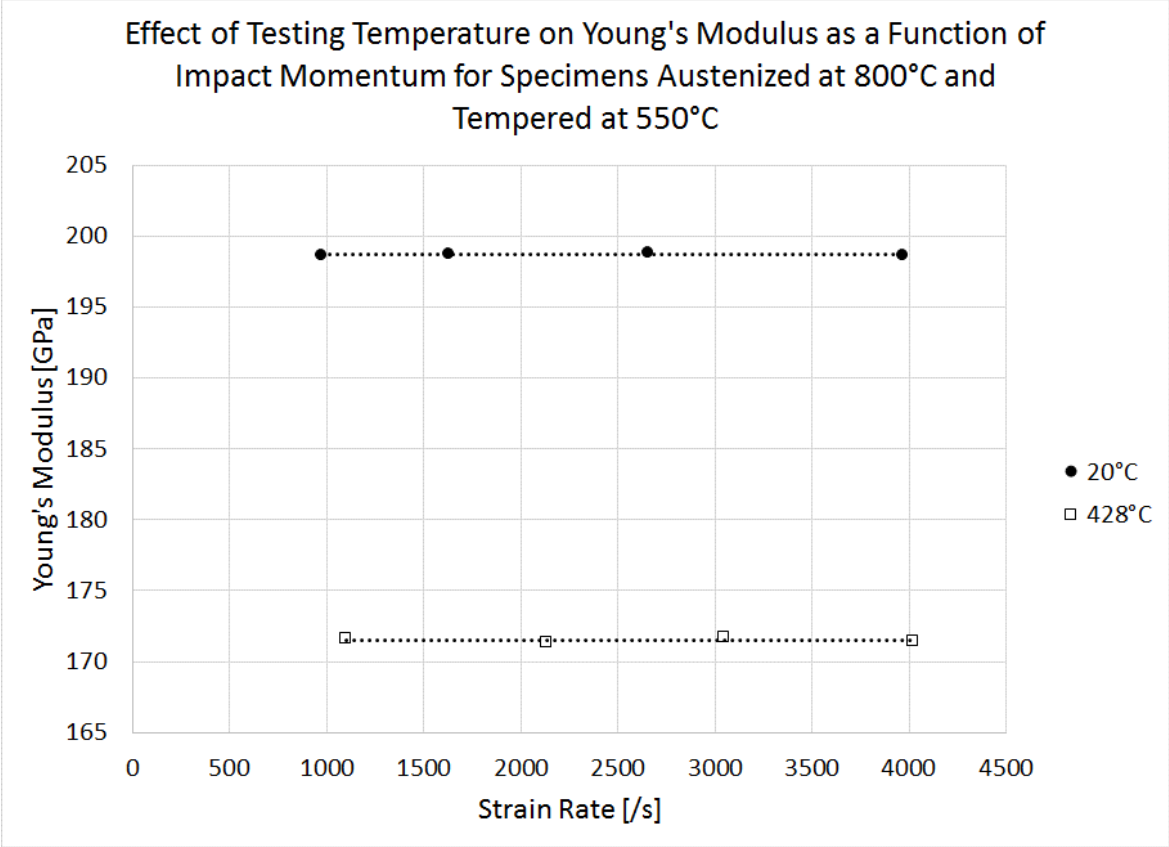

Fig. 64 Effect of testing temperature on Young's modulus as function of impact momentum for AISI 4340 steel specimens austenized at 800°C and tempered at 550°C

Since, any change in Young's modulus with strain rate is negligible within the margin of error, it can be assumed that the quasi-static Young's modulus for each heat treatment is the average of the moduli over all strain rates. A summary of the average Young's moduli calculated for each heat treatment and testing temperature is shown in Table 10.

Table 10 Summary of Young's modulus calculated for each heat treatment and testing temperature

Austenization Temperature [°C]	Tempering Temperature [°C]	Testing Temperature [°C]	Average Young's Modulus [GPa]
800	400	20	194.46 ± 2
		428	169.42 ± 2
	550	20	198.71 ± 2
		428	171.51 ± 2
900	400	20	196.79 ± 3
		428	171.76 ± 3
	550	20	201.32 ± 2
		428	173.42 ± 2
1000	400	20	199.53 ± 3
		428	172.85 ± 2
	550	20	204.74 ± 1
		428	175.09 ± 2

According to the data in Table 7, Table 8, and Table 9, the yield strength of AISI 4340 steel *increases* with increasing impact momentum (strain rate), and decreasing austenization and tempering temperatures. The quasi-static yield strength for all heat treatments can be estimated by regression fitting a plot of dynamic yield vs strain rate using a single term exponential function and extrapolating to a strain rate of 0.0001/s. Similarly, the value for the Johnson-Cook yield strength 'A', used in FEA simulations, is found by extrapolating the function to a strain rate of 1/s. The variation in yield strength with austenization temperature and strain rate is shown in Fig. 65, for specimens austenized at 800°C and tested at 20°C.

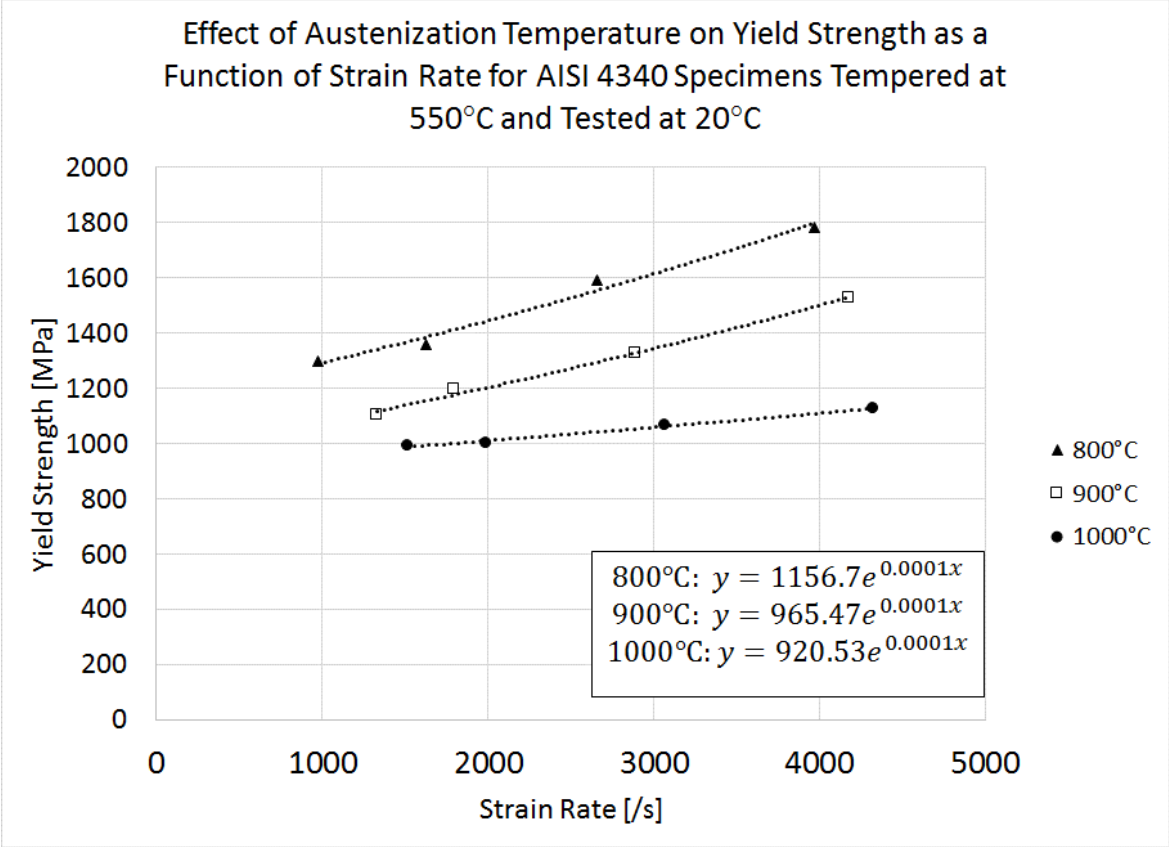

Fig. 65 Effect of austenization temperature and strain rate on yield strength of specimens tempered at 550°C and tested at 20°C

The quasi-static yield strengths, estimated at a strain rate of 1/s, are shown in Table 11 for each austenization temperature in specimens tempered at 550°C and tested at 20°C.

Table 11 Estimated quasi-static yield strengths of steel at various austenization temperatures tempered at 550°C and tested at 20°C

Austenization Temperature [°C]	Estimated Quasi-static Yield Strength [MPa]
800	1156.7
900	965.47
1000	920.53

There is an average increase in quasi-static yield strength of approximately 5-15% every 100°C decrease in austenization temperature for specimens tempered at 550°C. This increase is also consistent in specimens tempered at 400°C, as shown in Fig. 66 of a plot of dynamic yield strength as a function of strain rate for specimens tempered at 400°C.

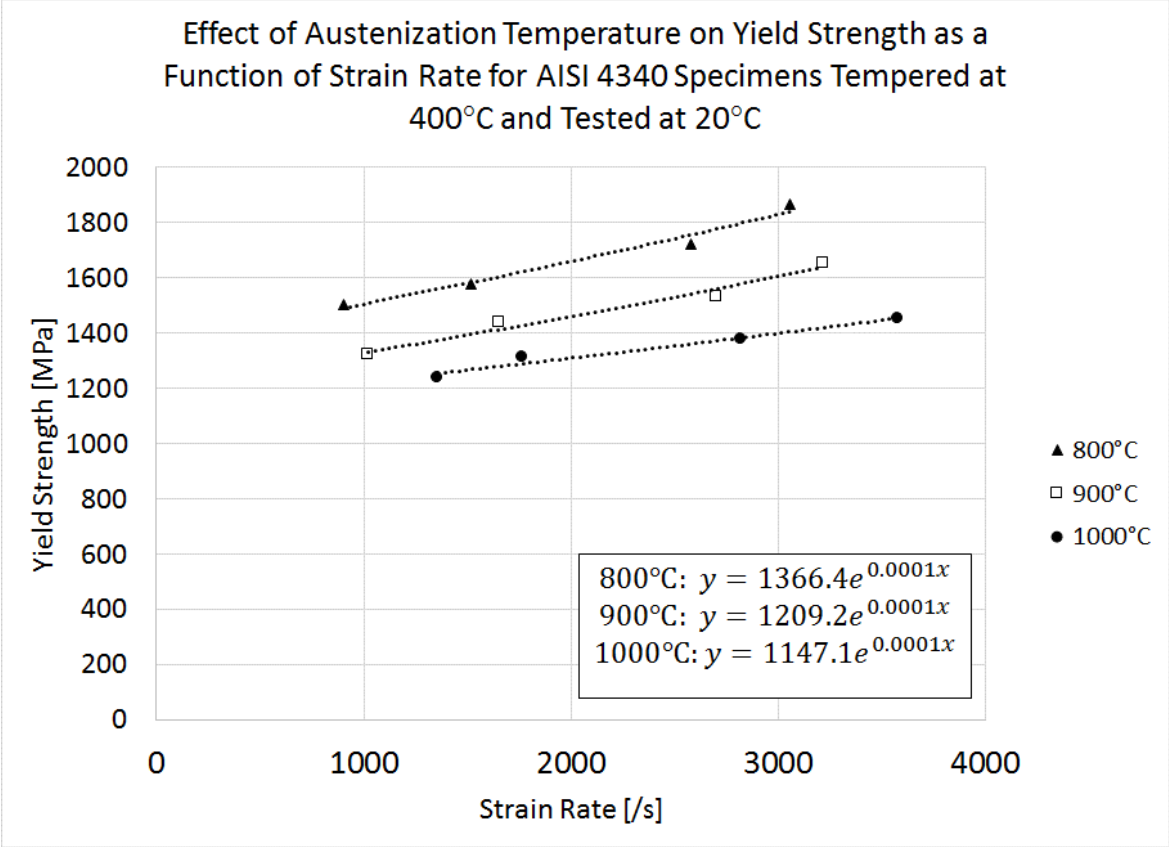

Fig. 66 Effect of austenization temperature and strain rate on yield strength of specimens tempered at 400°C and tested at 20°C

When tempering temperature was decreased from 550°C to 400°C, there was an average increase in quasi-static yield strength of 15-20% for all austenization temperatures, an example of which is shown in Fig. 67 of a plot of yield strength as a function of strain rate for AISI 4340 steel specimens austenized at 800°C and tested at 20°C.

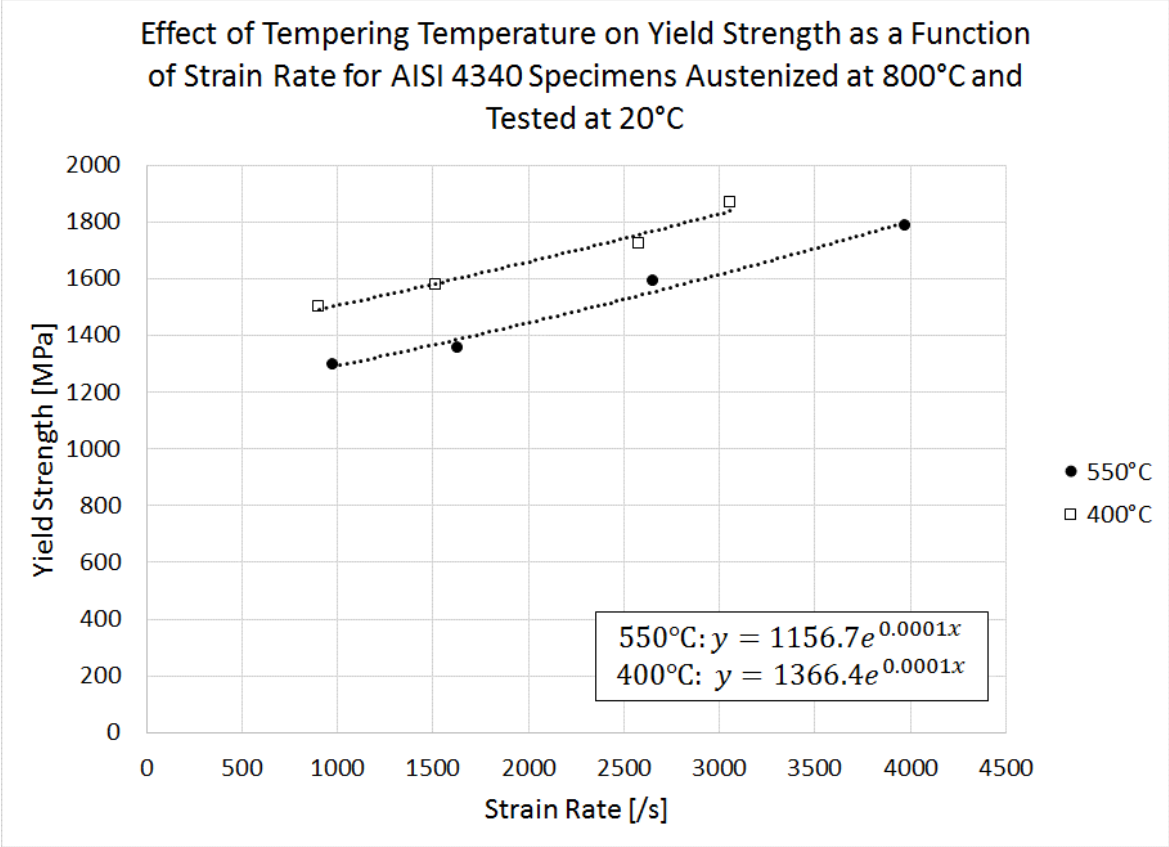

Fig. 67 Effect of tempering temperature and strain rate on yield strength of specimens austenized at 800°C and tested at 20°C

The yield strength measurements at each heat treatment in AISI 4340 steel is consistent with data collected in the ASM handbook for heat treatment of steels [145]. An increase in

yield strength with decreasing austenization and tempering temperatures can be explained by the Hall-Petch theory of grain boundary strengthening. A decrease in austenization and tempering temperatures results in a decrease in grain size. Decreasing the grain size decreases the amount of dislocations that form in each grain, which in turn increases the energy required to diffuse them. This increases the yield strength.

When tested at an elevated temperature of 428°C, the steel specimens exhibited a large drop in quasi-static yield strength (~40%) compared to the specimens tested at 20°C. This drop is twice as large as the effect from austenization and tempering temperatures. The increase in applied thermal energy to the metal from testing at elevated temperatures reduces the energy required from an applied stress to deform the material. This lowers the yield strength. The effect of testing temperature on yield strength is also related to the effect of temperature on the Peierls-Nabarro stress. As temperature increases, the vibration of atoms increases and the Peierls stress and yield strength decrease as a result of weaker atomic bond strength at higher temperatures. The drop in yield strength with increasing testing temperature is shown in Fig. 68, in a plot of yield strength as a function of strain rate for specimens of steel austenized at 800°C and tempered at 400°C.

Yield strength increases with increasing strain rate due to an increase in the dislocation density from dislocation pile-up in each grain. This occurs when the rate of dislocation generation exceeds the rate of diffusion to the grain boundary.

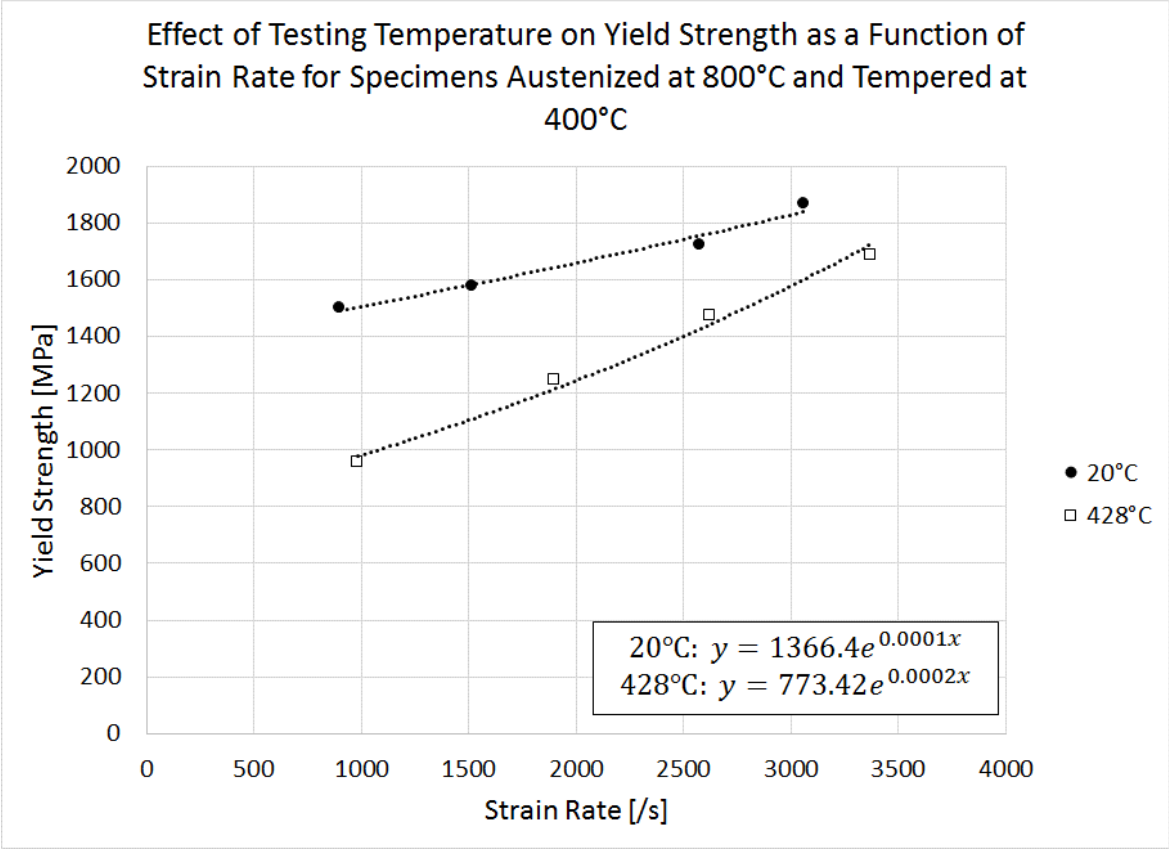

Fig. 68 Effect of testing temperature and strain rate on yield strength of specimens austenized at 800°C and tempered at 400°C

It is important to note that the testing temperature of 428°C, is equal to the static recovery temperature for steel which initiates dislocation annihilation, promotes grain growth, and softens the steel when it is held at this temperature for longer than 1 hour. However,

specimens were not held long enough under this temperature (1 minute) for recovery or any permanent microstructural changes to take place.

A summary of the estimated quasi-static yield strengths for all heat treatments and testing temperatures is shown in Table 12. Based on the regression fit curves, the Johnson-Cook yield strengths at a strain rate of 1/s matched closely (within 0.001 MPa) with the quasi-static yield strengths at 0.0001 /s.

Table 12 Summary of estimated quasi-static yield strengths for all heat treatments and testing temperatures of AISI 4340 steel

Austenization Temperature [°C]	Tempering Temperature [°C]	Testing Temperature [°C]	Estimated quasi-static Yield Strength [MPa]	Estimated quasi-static Yield Strain
800	400	20	1366.40	0.007027
		428	773.42	0.004565
	550	20	1156.7	0.005821
		428	695.94	0.004058
900	400	20	1209.20	0.006145
		428	632.47	0.003682
	550	20	965.47	0.004796
		428	573.28	0.003306
1000	400	20	1147.10	0.005749
		428	560.72	0.003244
	550	20	920.53	0.004496
		428	508.52	0.002904

3.5.4 Hardness Measurements

The hardness of a metal is measured by its surface resistance to plastic deformation, usually by indentation [153]. The greater the hardness, the greater the resistance to plastic

deformation. Hardness tests are often used as a simple and effective means of estimating the mechanical properties of materials. Various scales of hardness have been correlated to the ultimate tensile strength for a variety of metals and alloys [153-155]. In general, hardness increases with increasing strength.

Indentation hardness testing allows for selective measurements of hardness at specific locations on the surface of a metal. Hardness can measured on the macro-, micro-, or even nano-scale by adjusting the indentor size and applied force. For example, the hardness and strength of different phases in the complex microstructure of steel are measured using micro-indentors with a load of 15-1000 gf [154]. The indentations are so small that they must be measured using a microscope. Micro-hardness testing is invaluable for determining the microstructural variation in hardness and strength.

There are three main types of tests used to measure indentation hardness: the Brinell hardness test, the Rockwell hardness test, and the Vickers hardness test [153]. The three tests measure the metal's resistance to penetration by a non-deformable ball or cone. The tests determine the depth of penetration under a given load and within a period of time and are measured on different scales based on the shape of the indentor and load.

In this thesis, Vickers micro-hardness was measured in all tested specimens to determine the variation in material properties within the microstructure and inside the formation of

ASBs for the purpose of developing the material models for simulations. The hardness measurements were then correlated to the estimated yield strengths of each heat treatment as well as to the measured grain sizes.

Micro-hardness measurements were taken in all specimens, using a Buehler Micromet 5100 series micro-indentation machine, shown in Fig. 69. Specimen hardness values were measured using a diamond pyramid-shaped Vickers indenter with a test load of 300gf ≈ 2.94 N.

Fig. 69 Buehler Micromet 5100 Series micro-indentation machine for measuring Vickers hardness of specimens (image taken by this author)

To determine the variation in hardness in specimens which formed ASBs, a series of Vickers hardness (HV) measurements were taken inside, adjacent to, and just outside the ASBs. An example of the measurements taken around an ASB in a specimen of steel austenized at 900°C, tempered at 400°C, and impacted at 49 kgm/s at 20°C, is shown Fig. 70 of a micrograph of a transformed ASB.

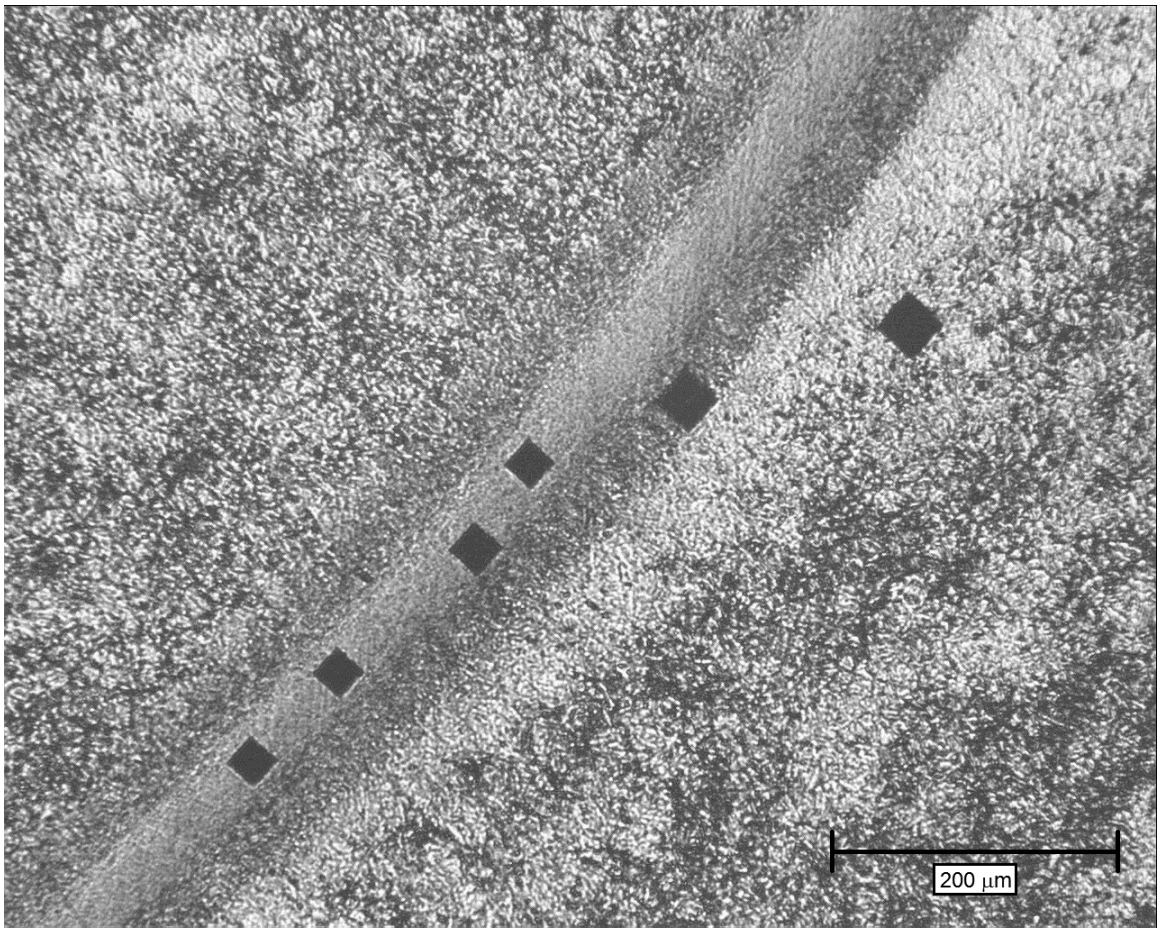

Fig. 70 Hardness indentations inside, near, and away from an ASB formed in a specimen with heat treatment 900°/30 mins & 400°/90 mins impacted at 49 kgm/s at 20°C

Similarly, Fig. 71 shows the indentation measurements in a specimen austenized at 800°C, tempered at 400°C, impacted at 52 kgm/s at a testing temperature of 428°C in and around a thick deformed band surrounded by a severe microstructure reorientation.

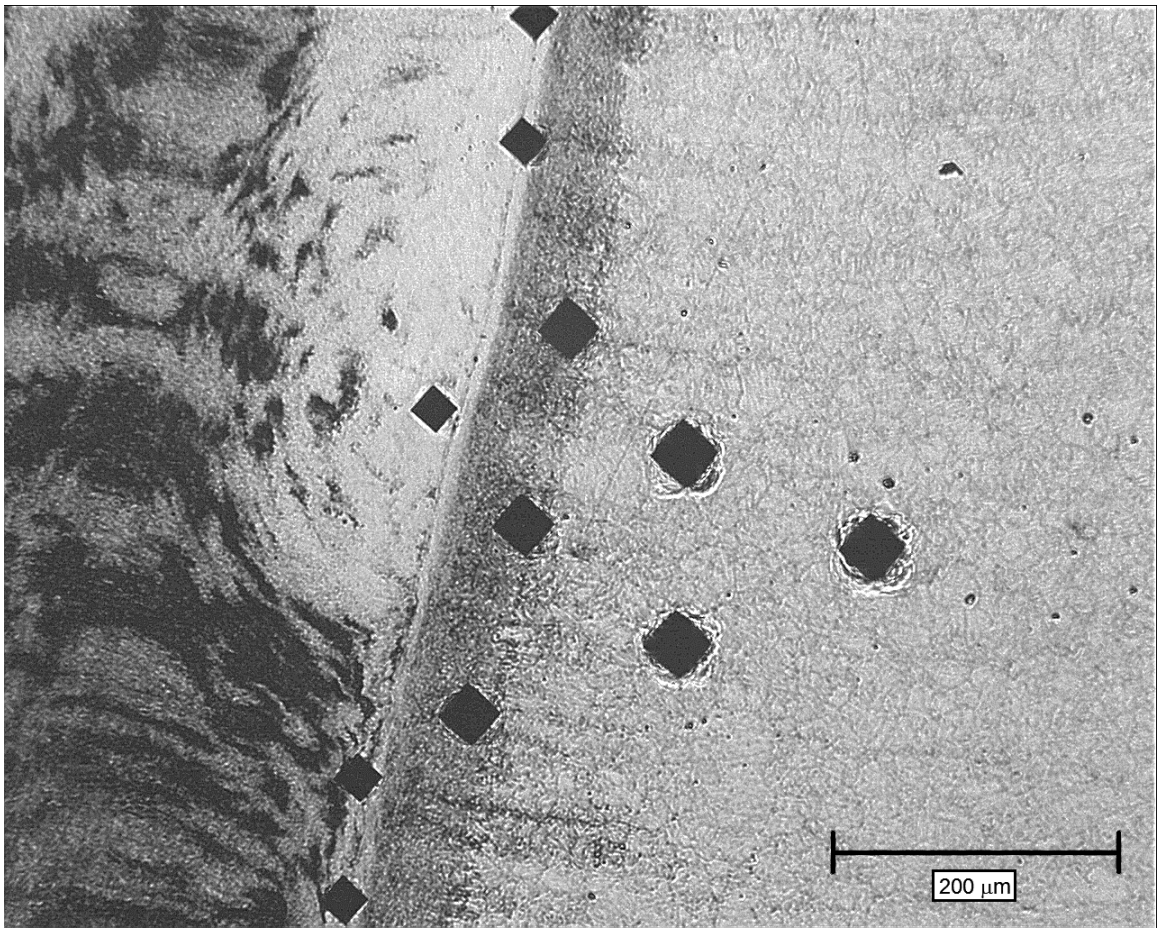

Fig. 71 Hardness indentations inside, near, and away from an ASB formed in a specimen with heat treatment 800°/30 mins & 400°/90 mins impacted at 52 kgm/s at 428°C

The variation in the size of the indentation at various locations around the ASBs indicate a variation in hardness. Smaller sized indentations indicate a harder microstructure, as seen

closer to the ASB. A close-up of an indentation, shown in a specimen of steel austenized at 800°C and tempered at 400°C in Fig. 72, reveals that the size of the indentation is larger than the average grain size in a specimen.

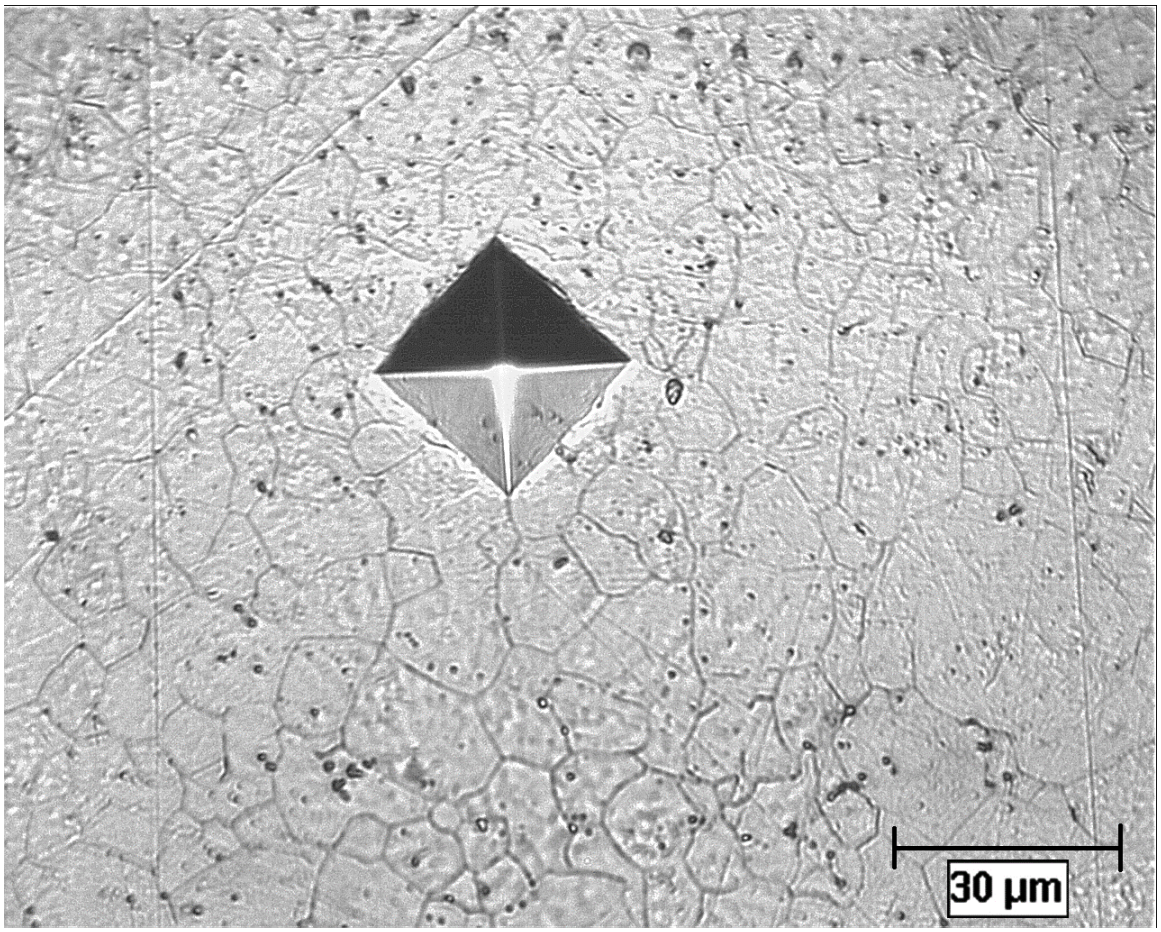

Fig. 72 Vickers hardness indentation in a specimen with heat treatment 800°/30 mins & 400°/90 min prior to impact

Measuring the hardness of individual grains was not possible with the smallest available indentor size. An average of ten measurements taken inside, and outside the ASBs for each impact momentum and heat treatment to minimize error, are reported here.

Vickers hardness number (HV) is determined by the ratio of *F/A* where *F* is the force applied to the diamond indentor in kg-f and *A* is the surface area of the resulting indentation in mm^2. The indentation has a square-based pyramid shape and the surface area A is determined by the formula

$$A = \frac{d^2}{2sin(136°/2)} \approx \frac{d^2}{1.8544} \qquad \textbf{Eq. 3-16}$$

where *d* is the average length of the diagonal left by the indenter in mm. The resulting HV hardness number is

$$HV = \frac{F}{A} \approx \frac{1.8544F}{d^2} \qquad \textbf{Eq. 3-17}$$

where *F* is in kgf and *d* is in mm.

For the specimen shown in Fig. 72, the indentor dimensions measured approximately 34 μm across the diagonals. This gives an HV hardness of

$$HV = \frac{1.8544(0.3)}{(0.0341)^2} = 478.4\ \frac{kg \cdot f}{mm^2} \qquad \textbf{Eq. 3-18}$$

The average HV hardness measurements for all tested specimens far from, near, and inside any formed ASBs are listed in Table 13, Table 14, and Table 15.

All hardness measurements were taken at room temperature, and consequently, the hardness values for specimens tested at 428ºC do not reflect well on the actual hardness of the steel when it is heated. There were no measureable differences in hardness in specimens tested at 20C and 428C far from, near, or inside the ASBs; for each heat treatment. As a result, no hardness measurements were recorded for specimens tested at 428ºC but instead were estimated from the values of yield strength using a regression fit of the yield strength vs hardness relationship and discussed later in Section 3.6.

Table 13 Summary of Vickers hardness measurements for specimens austenized at 800°C

Austenizing	Tempering	Testing Temperature (°C)	Impact Momentum (kgm/s)	Deformation Strain Rate (/s)	Average HV (kg-f/mm^2)		
					Far From ASB	Near ASB	Inside ASB
800°C/30mins & Oil Quench	550°C/90mins & Air Cool	20	0 Pre-Impact	0	**419**	--	--
			30	978	414	--	--
			45	1630	421	434	D-515
			49	2658	420	431	D-521
			52	3972	416	462	T-589
	400°C/90mins & Air Cool	20	0 Pre-Impact	0	**478**	--	--
			30	903	473	522	T-659
			45	1516	479	526	T-663
			49	2578	477	521	T-655
			52	3058	476	--	--

'D-' indicates deformed ASB; 'T-' indicates transformed ASB

Table 14 Summary of Vickers hardness measurements for specimens austenized at 900°C

Austenizing	Tempering	Testing Temperature (°C)	Impact Momentum (kgm/s)	Deformation Strain Rate (/s)	Average HV (kg-f/mm^2)		
					Far From ASB	Near ASB	Inside ASB
900°C/30mins & Oil Quench	550°C/90mins & Air Cool	20	0 Pre-Impact	0	**365**	--	--
			30	1331	364	--	--
			45	1797	365	--	--
			49	2893	366	381	D-454
			52	4182	365	378	D-457
	400°C/90mins & Air Cool	20	0 Pre-Impact	0	**433**	--	--
			30	1019	430	--	--
			45	1656	431	447	D-535
			49	2703	434	477	T-610
			52	3220	432	476	T-603

'D-' indicates deformed ASB; 'T-' indicates transformed ASB

Table 15 Summary of Vickers hardness measurements for specimens austenized at 1000°C

Austenizing	Tempering	Testing Temperature (°C)	Impact Momentum (kgm/s)	Deformation Strain Rate (/s)	Average HV (kg-f/mm^2)		
					Far From ASB	Near ASB	Inside ASB
1000°C/30mins & Oil Quench	550°C/90mins & Air Cool	20	0 Pre-Impact	0	**353**	--	--
			30	1514	355	--	--
			45	1989	352	--	--
			49	3066	354	--	--
			52	4327	351	369	D-437
	400°C/90mins & Air Cool	20	0 Pre-Impact	0	**415**	--	--
			30	1354	416	--	--
			45	1768	418	432	D-521
			49	2822	413	427	D-525
			52	3576	416	426	D-523

'D-' indicates deformed ASB; 'T-' indicates transformed ASB

The hardness values at locations away from ASBs were plotted in Fig. 73, Fig. 74, and Fig. 75, as a function of deformation strain rate for each austenization and tempering temperature. These figures show that the hardness of the steel was consistently lower in specimens tempered at 550ºC compared with those tempered at 400ºC.

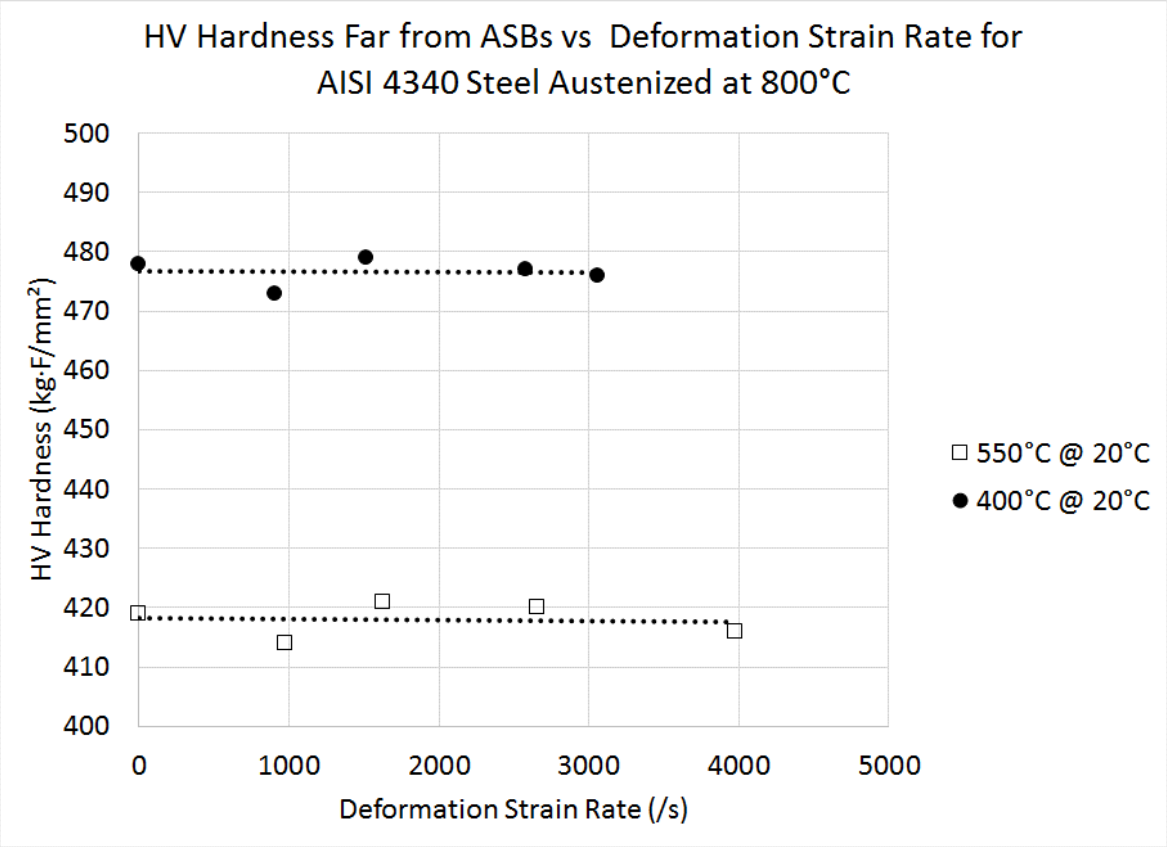

Fig. 73 Effect of tempering temperature on HV hardness away from the ASB as a function of deformation strain rate for specimens of AISI 4340 steel austenized at 800°C

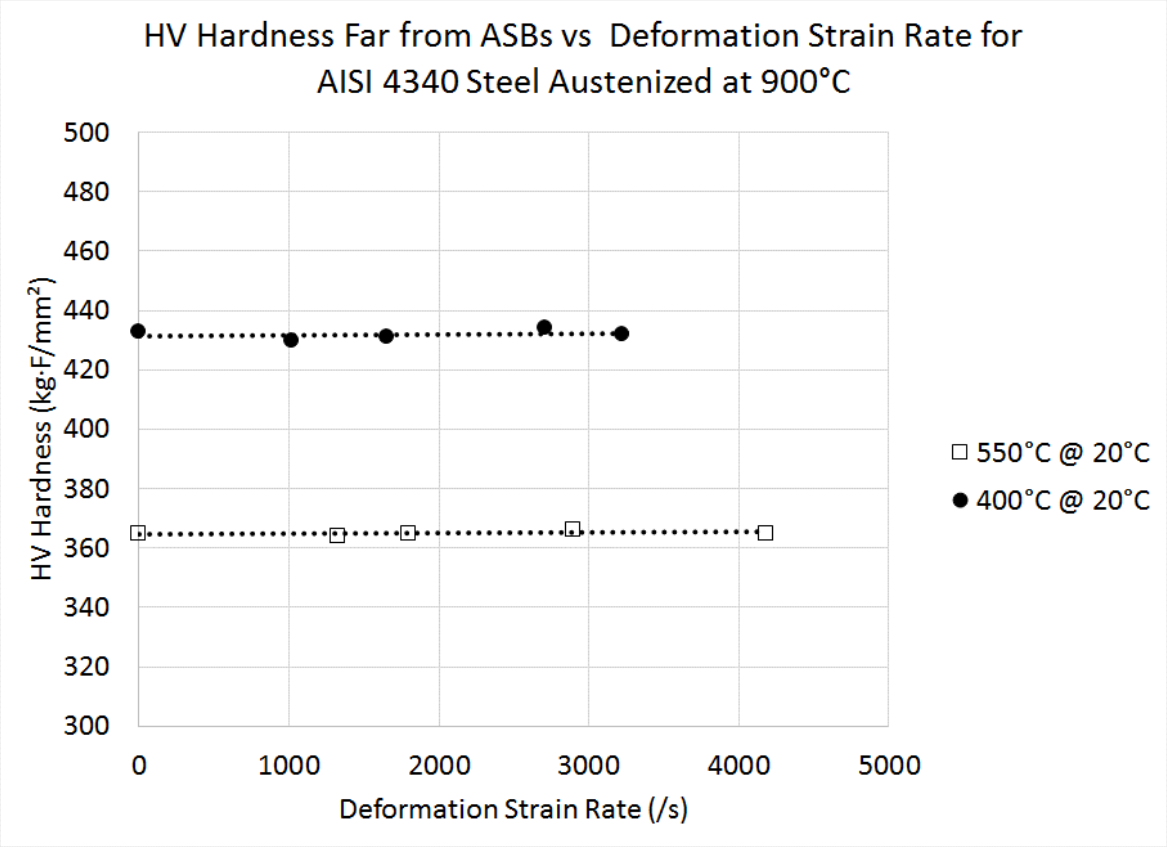

Fig. 74 Effect of tempering temperature on HV hardness away from the ASB as a function of deformation strain rate for specimens of AISI 4340 steel austenized at 900°C

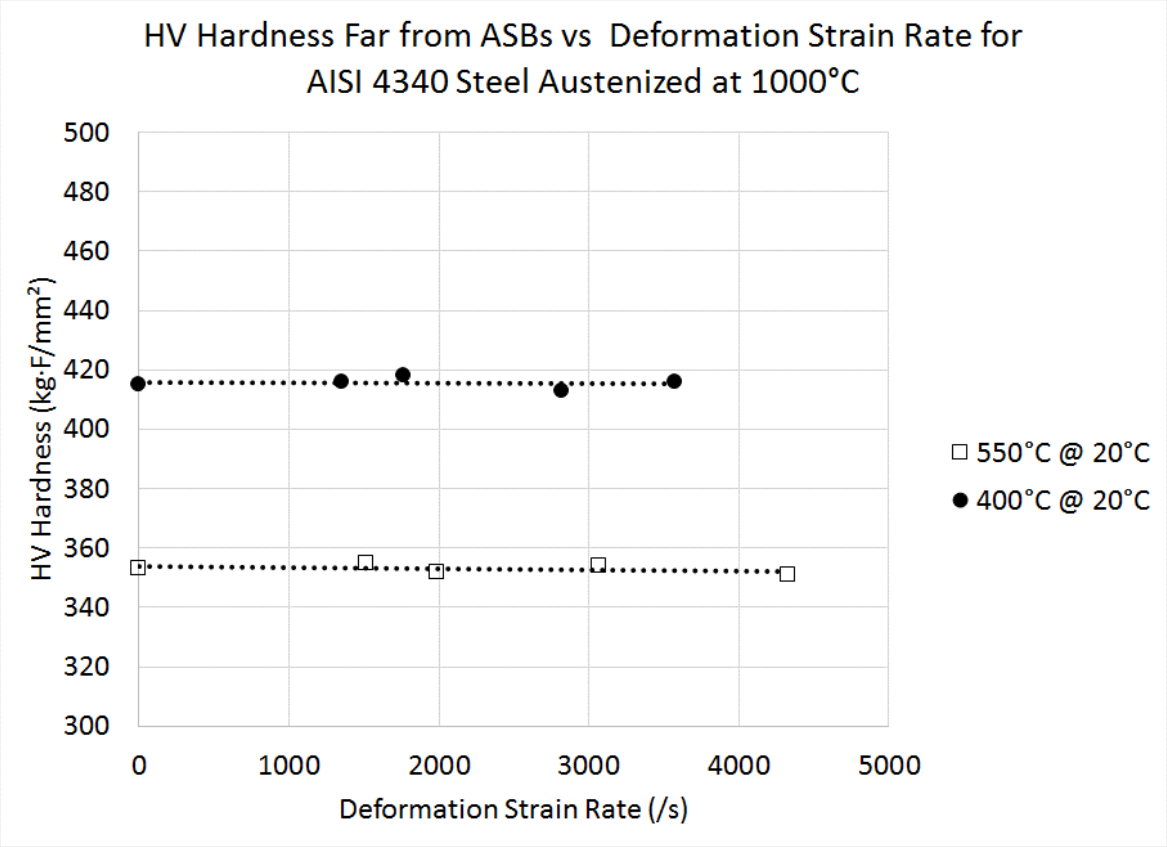

Fig. 75 Effect of tempering temperature on HV hardness away from the ASB as a function of deformation strain rate for specimens of AISI 4340 steel austenized at 1000°C

There also was a decrease in hardness with increasing austenization temperature. This reflects well on the changes in yield strength measured for each heat treatment. The change in hardness with austenization and tempering temperatures is shown in Fig. 76, for pre-impacted specimens. Hardness increased more dramatically when austenization temperature was decreased from 900ºC to 800ºC.

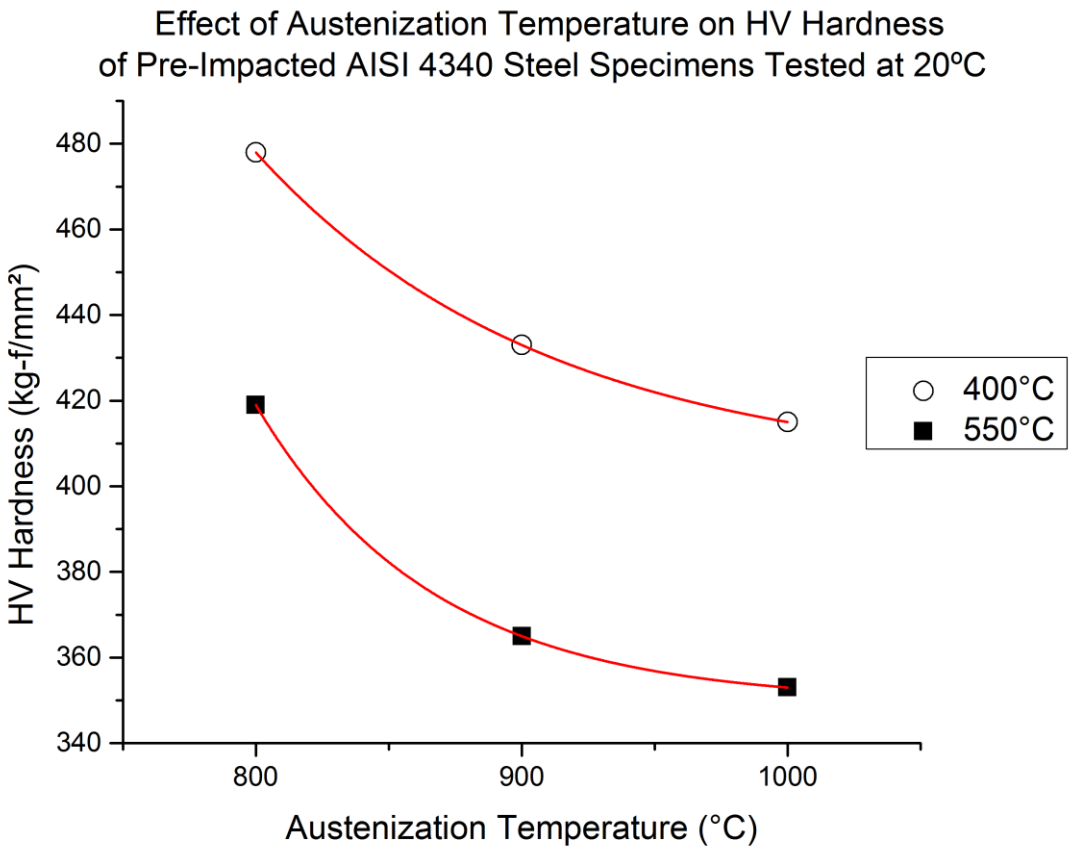

Fig. 76 Effect of austenization and tempering temperature on pre-impacted specimens of AISI 4340 steel.

This changes in hardness with heat treatment temperatures match closely to the changes in yield strength. However, there is no considerable change in hardness with deformation strain rate, despite results showing an increase in yield strength with increasing deformation strain rate. This is due to the fact that all hardness measurements were taken under quasi-static conditions at low strain rates of indentation.

Hardness measurements near the formation of deformed and transformed ASBs are plotted in Fig. 77, Fig. 78 and Fig. 79 against deformation strain rate for each austenization, tempering. Hardness data points in specimens which formed deformed ASBs are labeled by a ‘D’, while those which formed transformed ASBs are labeled with a ‘T’.

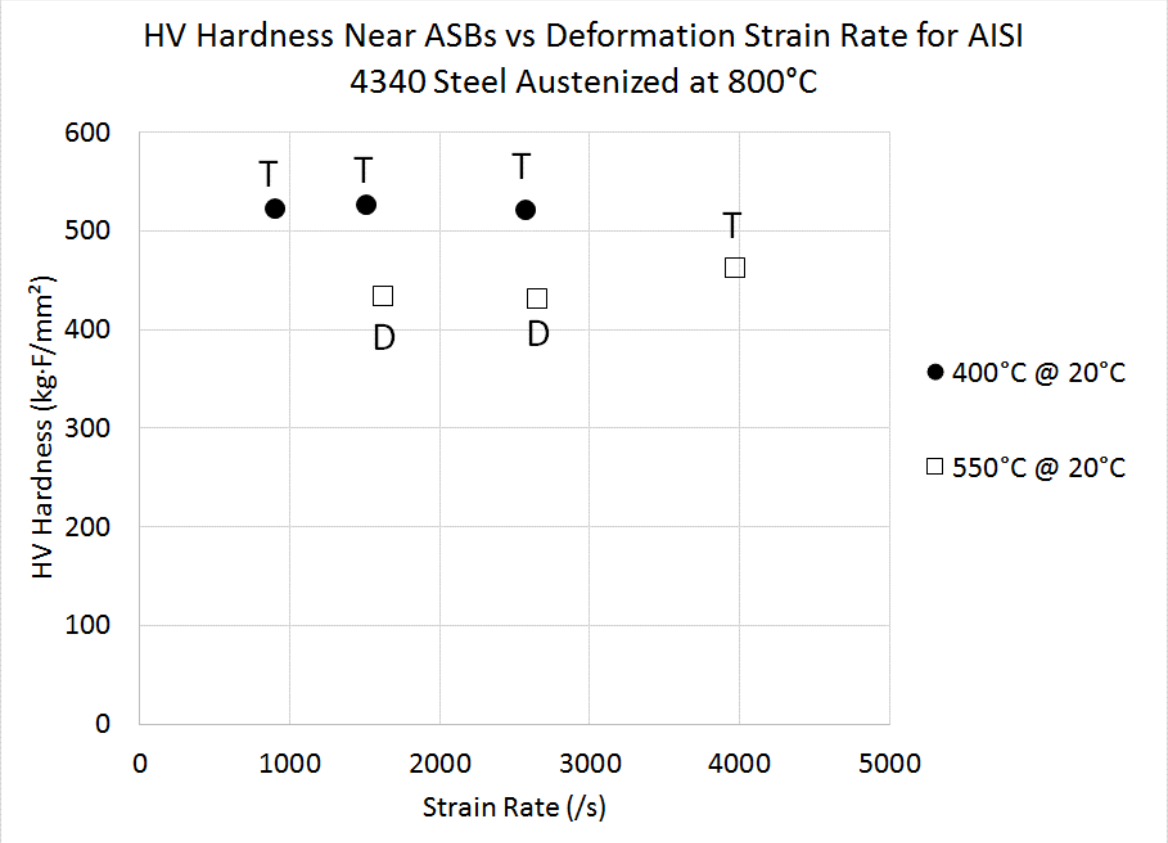

Fig. 77 Effect of tempering temperature on HV hardness near the ASB as a function of deformation strain rate for specimens of steel austenized at 800°C

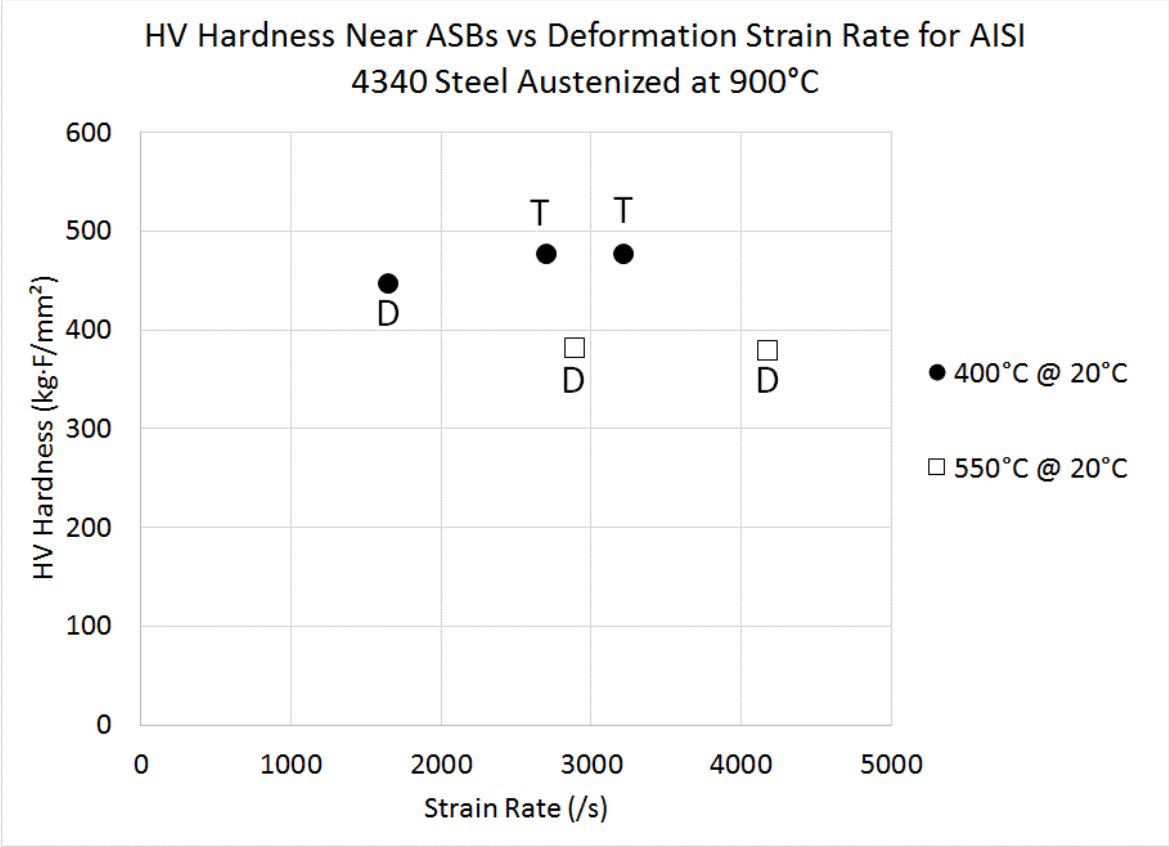

Fig. 78 Effect of tempering temperature on HV hardness near the ASB as a function of deformation strain rate for specimens of steel austenized at 900°C

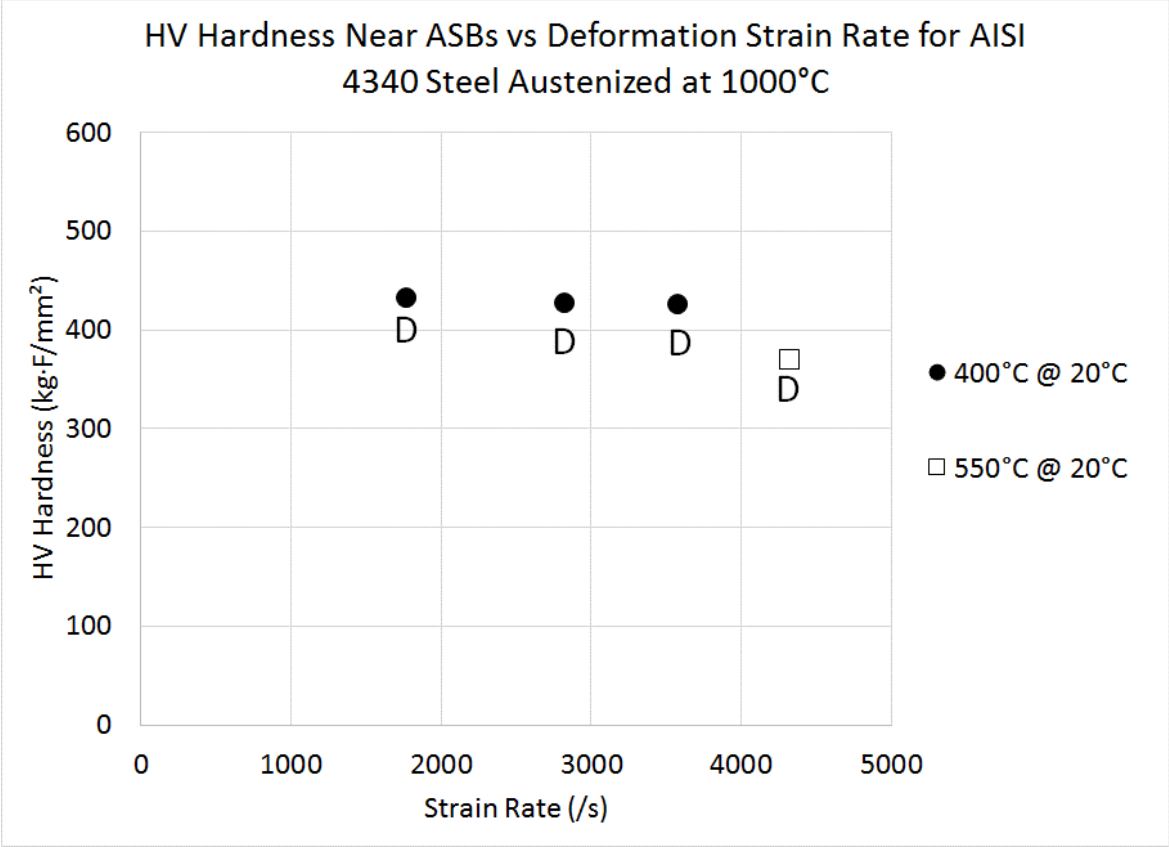

Fig. 79 Effect of tempering temperature on HV hardness near the ASB as a function of deformation strain rate for specimens of steel austenized at 1000°C

The results indicate that the hardness of the steel is higher near transformed ASBs than near deformed ASBs for all heat treatments. There is an average increase in hardness of 4% near deformed ASBs and an average increase in hardness of 10% near transformed ASBs. *The increase in hardness approaching ASBs is attributed to the gradual rotation and densification of grains as they align in the direction of shear and elongate severely*. This elongation reduces the width of the grains and increases the grain boundary area in a given location, increasing the hardness. The area near transformed ASBs contain gradually

refining grains which were observed to have a *higher grain boundary density* than rotated and elongated grains near deformed ASBs. The figures also indicate a consistent drop in hardness with increasing tempering and austenization temperatures.

Hardness was also shown to be consistently higher *inside* transformed bands compared to inside deformed bands for all heat treatments and testing temperatures, as shown in Fig. 80, Fig. 81, and Fig. 82. *This is attributed to the increase in grain boundary density by the severe refinement of the grains.*

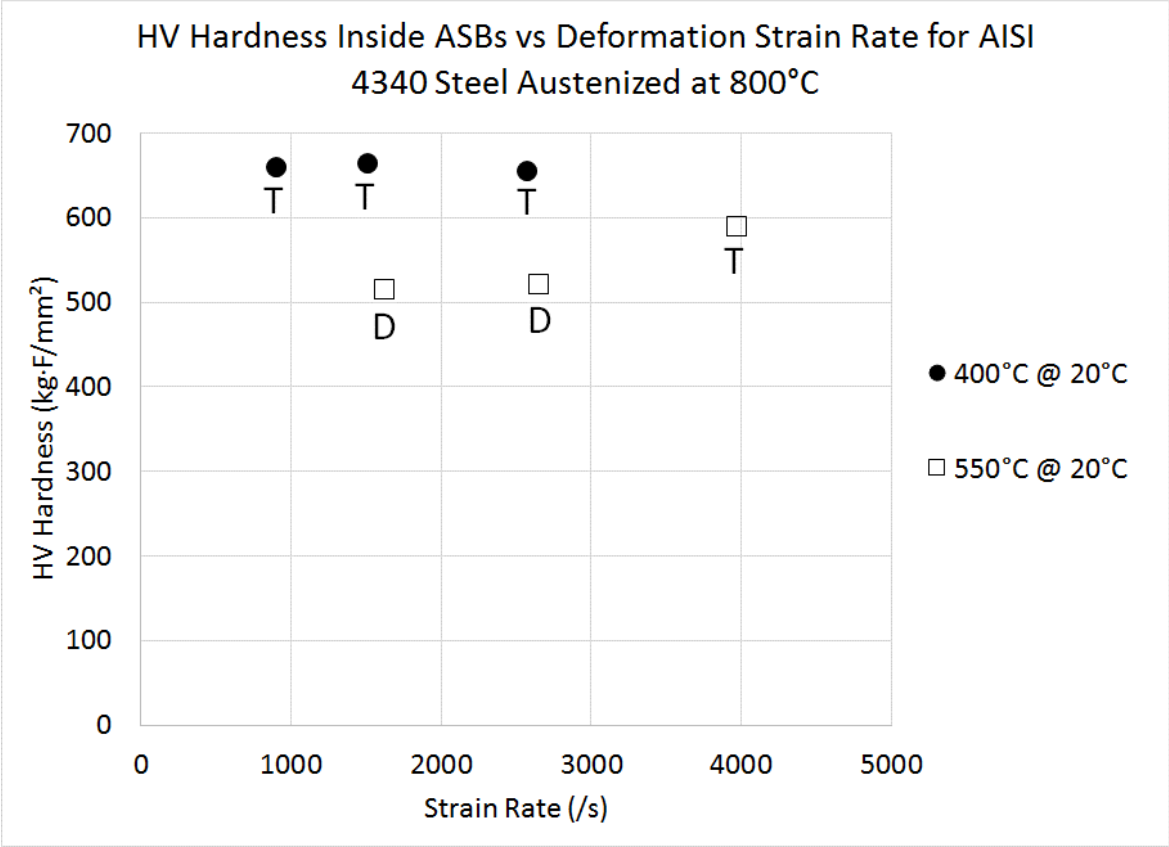

Fig. 80 Effect of tempering temperature on HV hardness inside the ASB as a function of deformation strain rate for specimens of steel austenized at 800°C

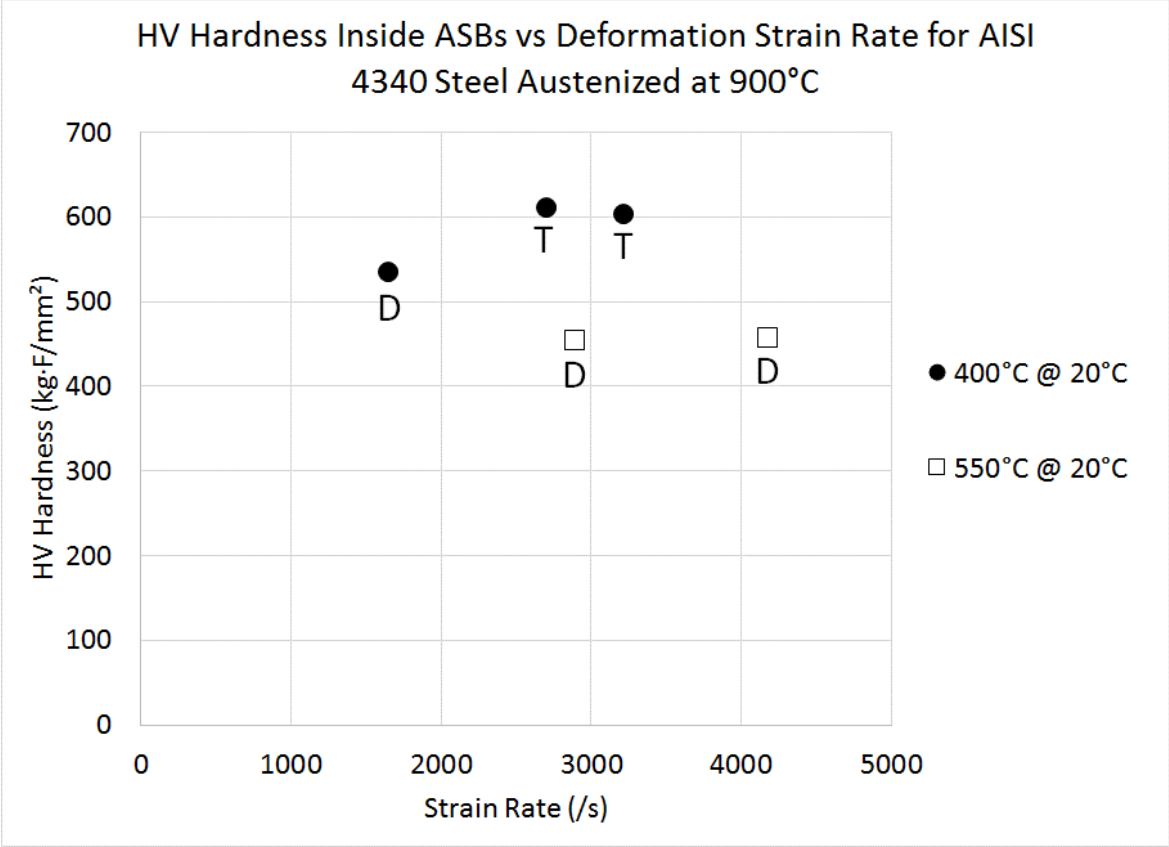

Fig. 81 Effect of tempering temperature on HV hardness inside the ASB as a function of deformation strain rate for specimens of steel austenized at 900°C

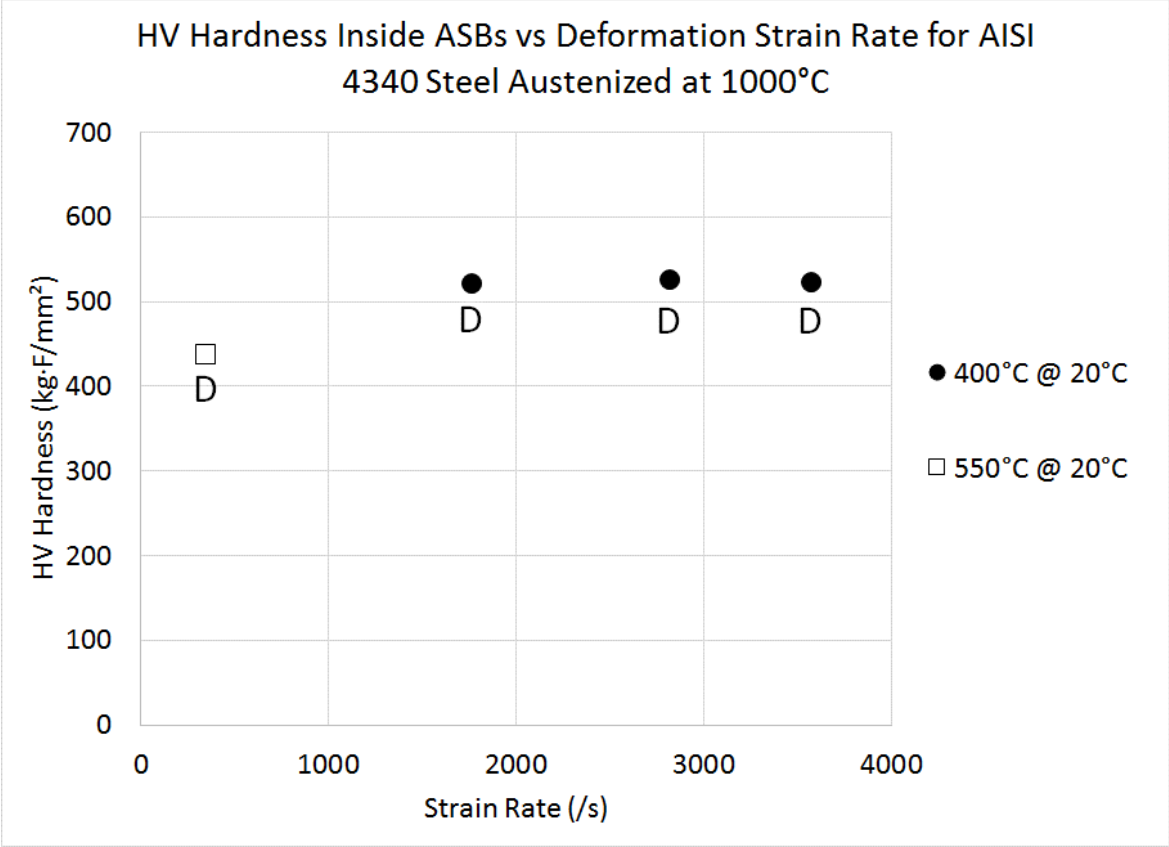

Fig. 82 Effect of tempering temperature on HV hardness inside the ASB as a function of deformation strain rate for specimens of steel austenized at 1000°C

Hardness was measured to increase by an average of 25% inside a deformed ASB and 40% inside a transformed ASB compared to measurements far from the ASB for all heat treatment temperatures. This consistent increase in hardness is shown in plots of hardness vs strain rate for AISI 4340 steel specimens austenized at 800ºC and tempered at 400ºC and 550ºC, shown in Fig. 83 and Fig. 84 respectively.

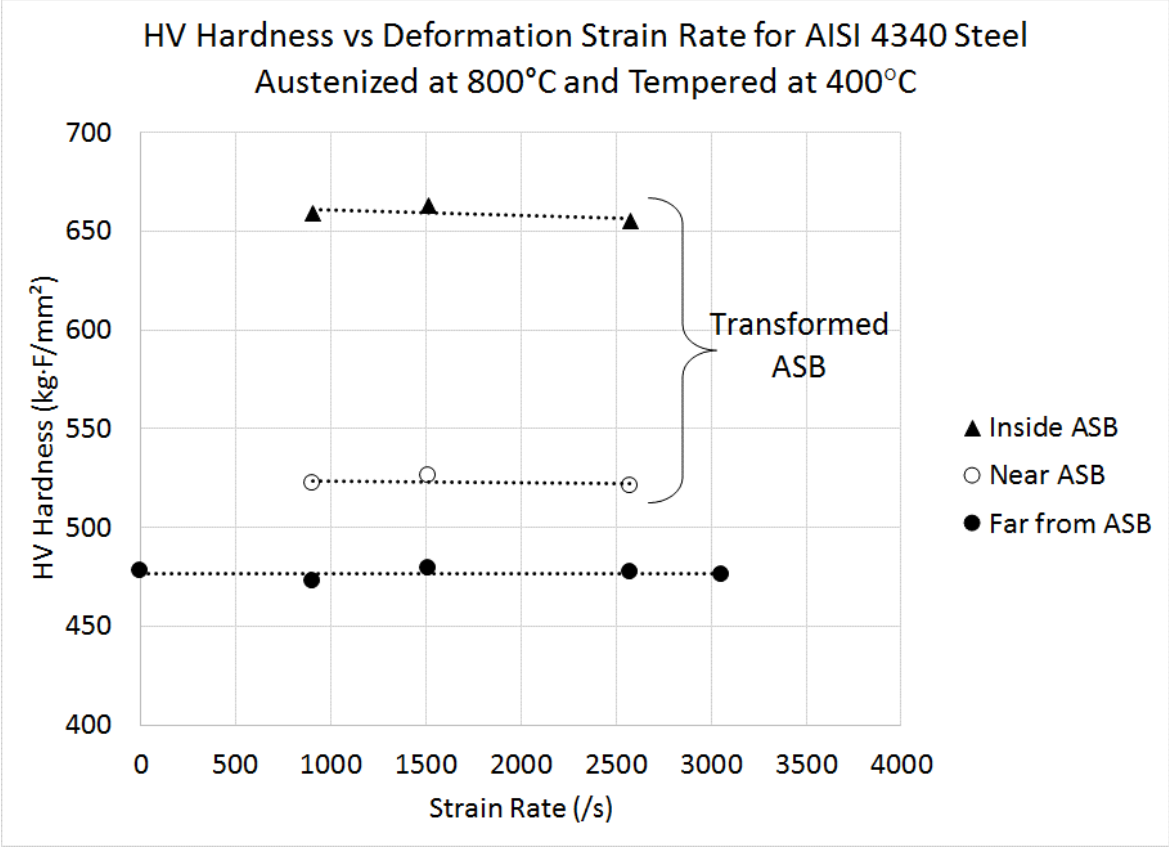

Fig. 83 Plot of hardness inside, near, and outside the formation of an ASB as a function of deformation strain rate for steel austenized at 800°C and tempered at 400°C

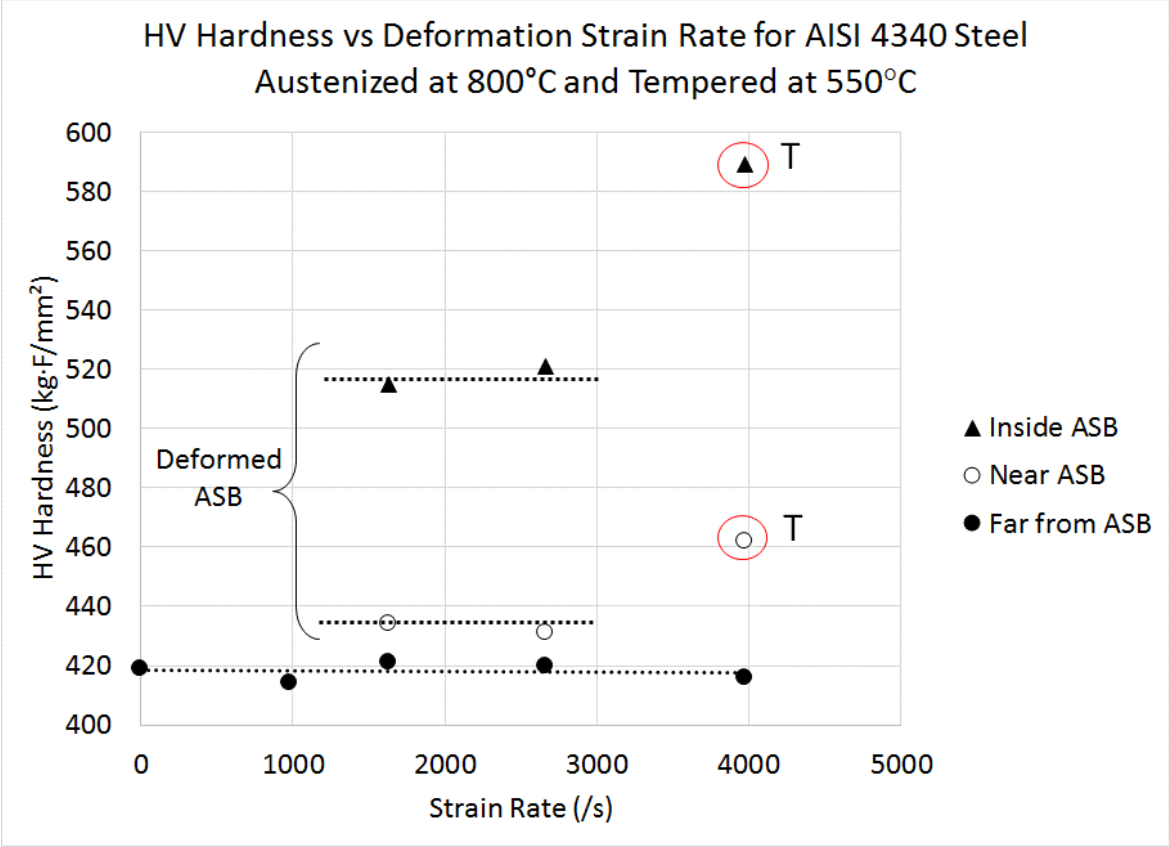

Fig. 84 Plot of hardness inside, near, and outside the formation of an ASB as a function of deformation strain rate for steel austenized at 800°C and tempered at 550°C

The increase in hardness from the increase in grain boundary density is related to the grain boundary strengthening mechanism or Hall-Petch strengthening mechanism where smaller grains increase the likelihood of dislocations running into grain boundaries which act as dislocation barriers increasing the hardness of the material. Dislocation density cannot be calculated using optical microscopy but based on evidence of gradual grain rotation and refinement under high stresses and strains, as well as the Hall-Petch grain boundary strengthening theory it can be inferred that there is a high dislocation density within the

deformed and refined grains due to the trapping effect of dislocations under severe deformation conditions.

3.6 Relationship between Yield Strength and Hardness for AISI 4340 Steel

The changes in hardness with deformation strain rate were shown to be proportional to the changes in yield strength. The exact relationship between these two properties is important because it can be used to establish the hardness of steel at elevated temperatures and define both the elastic and early-onset plastic/hardening properties of the constituents of the microstructure of steel at various heat treatments for the purpose of developing a simulation model to simulate microstructural deformation. This relationship was determined by plotting quasi-static yield strength as a function of pre-impact HV hardness for all heat treatments at 20ºC, as summarized in Table 16, and performing a regression fit of the curve, as shown in in Fig. 85.

Table 16 Yield strength and hardness measurements for AISI 4340 steel specimens prior to impact at 20ºC

Austenization Temperature [°C]	Tempering Temperature [°C]	Testing Temperature [°C]	Estimated quasi-static Yield Strength [MPa]	Pre-Impact HV Hardness [kg-f/mm^2]
800	400	20	1366.4	478
	550	20	1156.7	419
900	400	20	1209.2	433
	550	20	965.47	365
1000	400	20	1147.0	415
	550	20	920.53	353

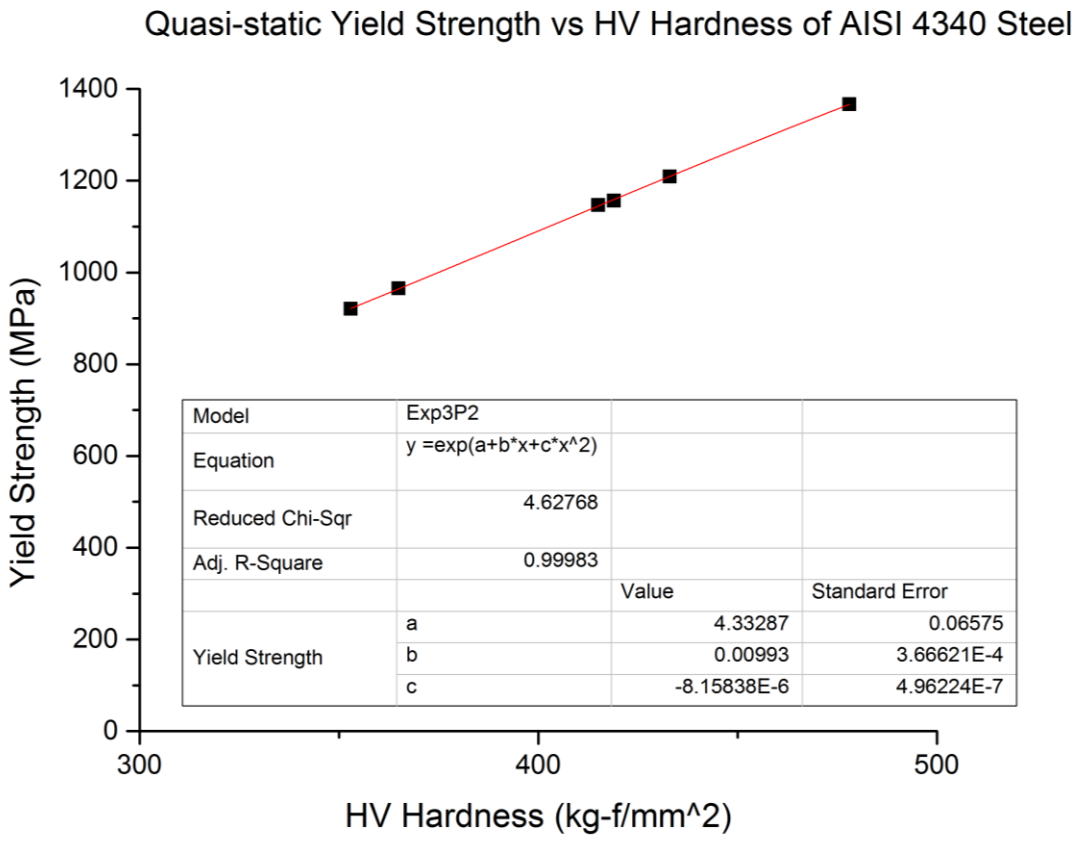

Fig. 85 Yield strength as a function of HV hardness for AISI 4340 Steel

The data was best fit using a three-parameter exponential function of the form:

$$\sigma_y = \exp[A + B * (HV) + C * (HV)^2] \quad \textbf{Eq. 3-19}$$

where A = 4.33287, and B = 0.00993, and C = -8.15838E-6. The function was tested against the documented yield strength and Vicker's hardness of annealed AISI 4340 steel [145, 154], which are 470 MPa and 228 kg-f/mm^2, respectively. For a hardness of 228, the best fit curve gives a yield strength of 479.529 MPa—an overestimation of 2%. The largest source of this error lies in the calculation of the quasi-static yield strength from experimentation and calculations of the stress-strain responses. In studying impact behavior of AISI 4340 steel, Banerjee [156] and Shivpuri et al. [157] used a two-parameter exponential fit of the hardness vs Rockwell-C hardness relationships for AISI 4340 steel in the ASM handbook [145]. This relationship was of the form:

$$A = \exp(A_1 R_C + A_2) \;\; MPa \quad \textbf{Eq. 3-20}$$

where A_1 = 0.0355, A_2 = 5.5312, and R_c is the Rockwell-C hardness of the steel. Annealed AISI 4340 steel has a Rockwell hardness of 17 using the conversion charts in ASTM E140-07 [158]. For this hardness value, the resulting yield strength is calculated to be 462; an underestimation of 2%. The approximation calculated in this thesis is within acceptable error for the purpose of simulation.

Using the regression relationship in Eq. 3-19, the hardness values of specimens tested at an elevated temperature of 428ºC were estimated. It was assumed that the hardness measurements near and inside the formation of ASBs in specimens tested at 428ºC followed the increase in hardness for specimens tested at 20ºC. A summary of the values of hardness and yield strength for all heat treatments and testing temperatures is shown in Table 17.

Table 17 Estimation of Hardness for all heat treatments and testing temperatures prior to impact

Austenization Temperature [°C]	Tempering Temperature [°C]	Testing Temperature [°C]	Estimated quasi-static Yield Strength [MPa]	Pre-Impact HV Hardness [kg-f/mm^2]
800	400	20	1366.4	478
		428	773.42	313
	550	20	1156.7	419
		428	695.94	292
900	400	20	1209.2	433
		428	632.47	275
	550	20	965.47	365
		428	573.28	259
1000	400	20	1147	415
		428	560.72	255
	550	20	920.53	353
		428	508.52	242

3.7 Experimental Conclusions and Microstructural Mechanism of ASB Formation

Results reported in this chapter show that the mechanical properties of steel are a function of the grain sizes in the microstructure which are directly affected by austenization and tempering temperatures. The results also showed that there is a distinct change in the size and orientation of grains near and inside ASBs which affects the mechanical properties of the steel. An attempt to simulate the behavior of steel using finite element analysis, must take into account grain size.

In the next section, it will be shown that the kinematics of the microstructural mechanism for ASB formation can be simulated using a simulation model based on grain size and variation in the material properties of the microstructure. Microstructural observations and experimental stress-strain and hardness measurements contribute to the development of this model and are used to compare with simulated results.

4. THEORETICAL INVESTIGATION

4.1 Introduction

The experimental investigation has shown that the formation of ASBs in steel can be described, on the microscopic level, through the behavior of grains as they deform under severe shear stresses. The type of ASB depends on the size and properties of the individual grains which are controlled directly by the heat treatment of the steel. It was shown that ASBs form by a mechanically-driven combination of grain elongation, reorientation and grain break-up in the direction of maximum shear, resulting in a localized band of severely deformed and refined grains. The theoretical investigation involves the development of an simulation model that can simulate grain deformation behavior and ASB formation in AISI 4340 steel at a microscopic level using continuum mechanics FEA methods and constitutive equations. The model accounts for the complex geometry of the grains and grain boundary structures and material inhomogeneity in the microstructure.

4.2 Simulation Model Set-Up

The simulation problem was set-up to recreate the experimental conditions of deformation under direct impact using the DIHPB. As discussed in Section 2.4.2.2, the DIHPB consists of three main components: a cylindrical striker bar measuring 0.2m and 0.038m in diameter with a mass of 1.781 kg; a cylindrical specimen measuring 0.01m in length and 0.0095m in diameter; and, a transmitter bar measuring 1.5m in length with a diameter of 0.038m.

A simulation model was developed using explicit FEA software LS-DYNA [5]. The striker bar and transmitter bar were modeled as infinite rigid walls whose normals are in the direction of impact. The striker rigid wall was given a mass of 1.781 kg and assigned initial velocities matching that of experimental impact momenta, while the transmitter bar was modeled as a fixed rigid wall. The specimen was modeled by a 2D axi-symmetric rectangle measuring 5 mm in width and 10 mm in length reflected about the vertical y-axis. Symmetric modeling reduces the computational cost of simulation which is normally very high for fully 3D modeling. A schematic of this setup is shown in Fig. 86.

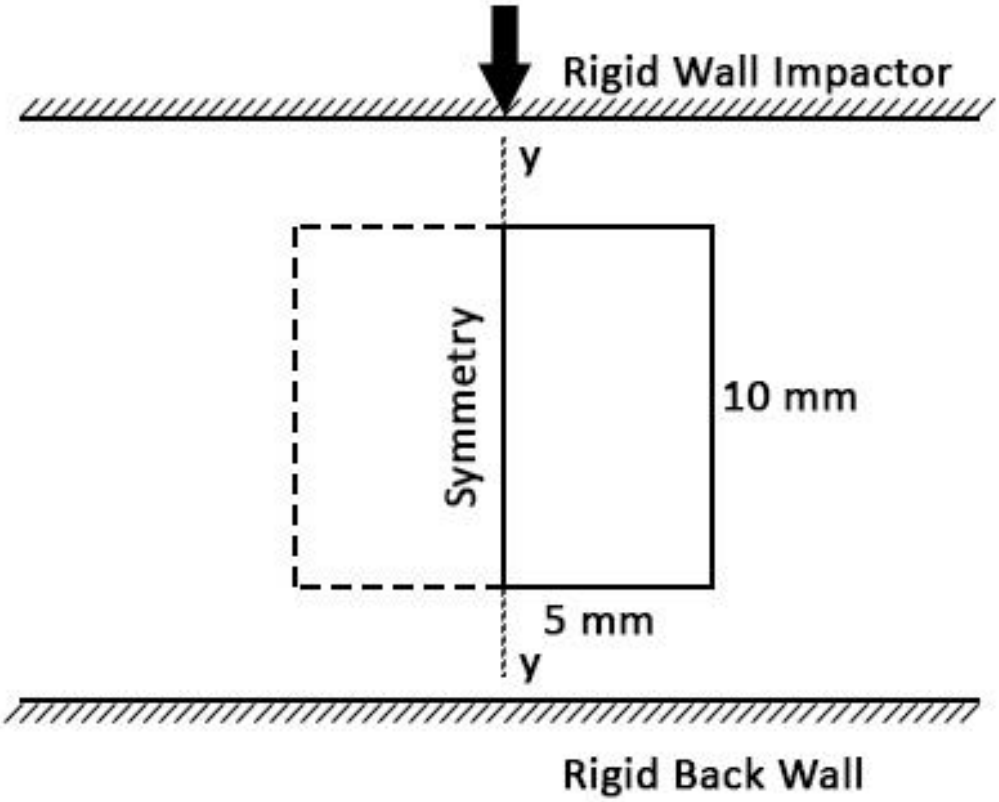

Fig. 86 Schematic of simulation model under direct impact (illustration by this author)

In the experimental investigation, optical micrographs of ASB formation were taken from the top and bottom faces of the specimens. The model, however, shows the deformation of the cross-section of a specimen. It can provide an indication of localization and the formation of cracks within the specimen which compromise it as a whole.

In this chapter, the material models for each heat treatment of steel were developed using the Johnson-Cook plasticity model, discussed in Section 2.5.3, and a failure criterion that

simulates shear failure. These material models were validated against experimental results by simulating impact at various momenta using simple geometry and meshing techniques. Later, a model based on grain size was developed using the Voronoi tessellation technique [6, 7], and utilizes multiple material assignments to simulate the heterogeneity observed in the microstructure of steel. The resulting simulated grain deformation and formation of ASBs were analyzed.

4.2.1 The Johnson-Cook Material Model and Determination of Material Parameters for Various Heat Treatments of 4340 Steel

The well documented Johnson-Cook material model [12, 13] defines the dynamic flow stress of a material by empirically curve fitting the dynamic stress strain response. It is dependent on both the strain rate and temperature and is defined as:

$$\sigma_o = [A + B(\bar{\varepsilon}^{pl})^n]\left[1 + Cln\left(\frac{\dot{\bar{\varepsilon}}^{pl}}{\dot{\varepsilon}_o}\right)\right]\left(1 - \hat{T}^m\right) \qquad \textbf{Eq. 4-1}$$

as discussed previously in Section 2.5.3. A visual representation of the Johnson-Cook stress-strain curve is shown in Fig. 87 for both Johnson-Cook quasi-static ($\dot{\varepsilon} = 1/s$) and high strain rate dynamic responses.

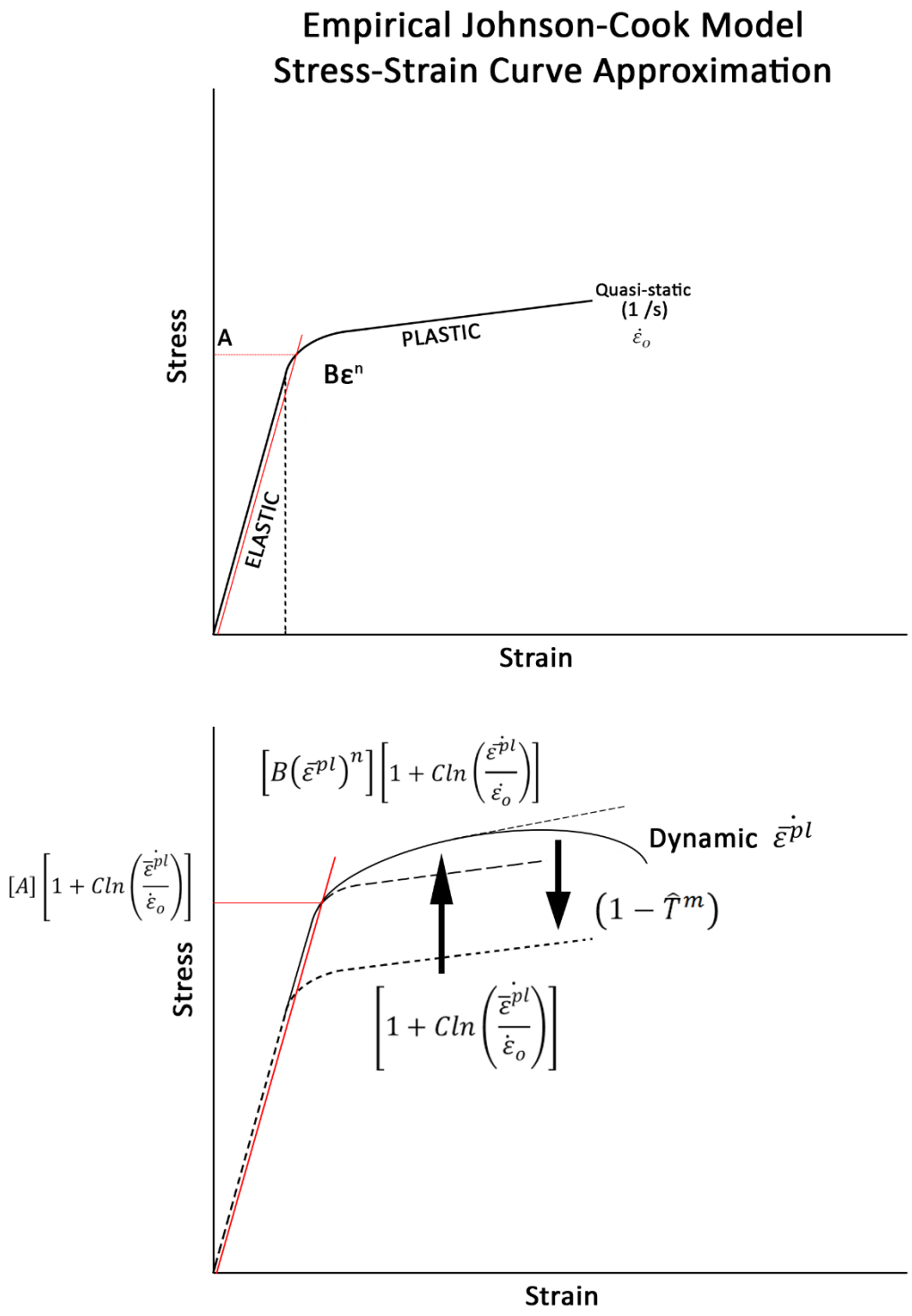

Fig. 87 Visual representation of the Johnson-Cook model for quasi-static and dynamic stress-strain curves (illustration by this author)

The physical properties of annealed AISI 4340 steel [11, 108] along with the established Johnson-Cook material parameters were used as a baseline to validate the calculated material parameters for the various heat treatments of the steel. The Johnson-Cook damage parameters ($D_1 – D_5$) were not directly employed but were used as a basis for comparison with other damage models. The model parameters are outlined in Table 18.

Table 18 Mechanical properties and Johnson-Cook Parameters for annealed AISI 4340 steel

Parameter	**Value**
Density	7850 [kg/m^3]
Young's Modulus	205 [GPa]
Poisson's Ratio	0.29
Taylor-Quinney coefficient	0.9
Specific Heat	465 [J/kg/K]
Thermal Expansion Coefficient	0.000013 [m/m/K]
Normalized Strain Rate: $\dot{\varepsilon}_o$	1 [/s]
Room Temperature: T_R	293 [K]
Melting Temperature: T_m	1793 [K]
Initial Temperature: T_0	293 [K]
Tensile Yield Strength @0.001s^{-1}	470 [MPa]
Ultimate Tensile Strength @ 0.001s^{-1}	745 [MPa]
A @ 1s^{-1}	792 [MPa]
B	510 [MPa]
n	0.26
C	0.014
m	1.03
D_1	0.05
D_2	3.44
D_3	-2.1199999
D_4	0.002
D_5	0.61

The Johnson-Cook material parameters for various heat treatments of AISI 4340 steel were determined using the experimental measurements of stress and strain at various impact momenta and testing temperatures.

4.2.1.1 Determination of the Johnson-Cook Hardening Parameters 'B' and 'n', and Strain Rate Sensitivity Parameter 'C' at $\dot{\varepsilon} = 1/s$

In the Johnson-Cook material definition of flow stress, the yield strength of AISI 4340 steel at $\dot{\varepsilon} = 1/s$, *A*, was determined in the experimental investigation for all tested heat treatments. The parameters 'B' and 'n' describe the quasi-static plastic isotropic hardening behavior of the metal as a power-law relationship between effective plastic stress and effective plastic strain, and are defined as the hardening coefficient, and hardening sensitivity factor respectively, measured at a strain rate of $1s^{-1}$. They are determined empirically using a three term power-law regression fit of the plastic portion of the quasi-static stress-strain curve from the yield strength up to the maximum stress within a deformation time of 77 μs. This was to ensure that the measurement of stress and strain were accurate, as discussed in Section 3.5.2. This equation is of the form:

$$\sigma_{QS}^{pl} = A + B(\bar{\varepsilon}^{pl})^n \qquad \textbf{Eq. 4-2}$$

The hardening sensitivity parameter ‘n’ represents the shape of the hardening curve or its slope, and is usually in the range of 0 < n < 1. At (n=0) there is no hardening and stress remains constant as strain increases. At (n=1) the stress increases linearly with strain and the magnitude of the increase is directly proportional to the strain. The hardening coefficient, ‘B’, is the magnitude of the stress amplification. It multiplies the total stress increase from strain.

In the absence of quasi-static stress-strain data, the hardening parameters were estimated from the high-strain rate tests. According to the Johnson-Cook model, the plastic portion of the stress-strain curve at elevated strain rates, under isothermal conditions, is defined as:

$$[A_1 + B_1(\bar{\varepsilon}^{pl})^{n_1}] = [A_0 + B_0(\bar{\varepsilon}^{pl})^{n_0}]\left[1 + Cln\left(\frac{\dot{\bar{\varepsilon}^{pl}}_1}{\dot{\bar{\varepsilon}^{pl}}_0}\right)\right] \qquad \textbf{Eq. 4-3}$$

Where A_1, B_1, n_1, are the yield strength and hardening parameters at an elevated strain rate of $\bar{\varepsilon}^{pl}{}_1$; and A_0, B_0, n_0 are the yield strength and hardening parameters at a strain rate of $\dot{\bar{\varepsilon}^{pl}}_0 = 1/s$. The dynamic and low strain rate yield strength values, ‘A’, were calculated in Section 3.5.3.5. The strain rate sensitivity parameter, ‘C’ defines the “average amplification” of the stress-strain response at higher strain rates and is the slope of the linear logarithmic strain rate dependence of flow stress.

The calculated hardening parameters B and n for a specimen of steel austenized at 800°C, tempered at 550°C, impacted at 45 kgm/s and tested at 20°C is shown in Fig. 88. A three-term power-law regression curve,

$$y = a + bx^c, \qquad \textbf{Eq. 4-4}$$

was fit around the data until the coefficient 'a' matched closely, and within error, to the dynamic yield strength, under these impact conditions.

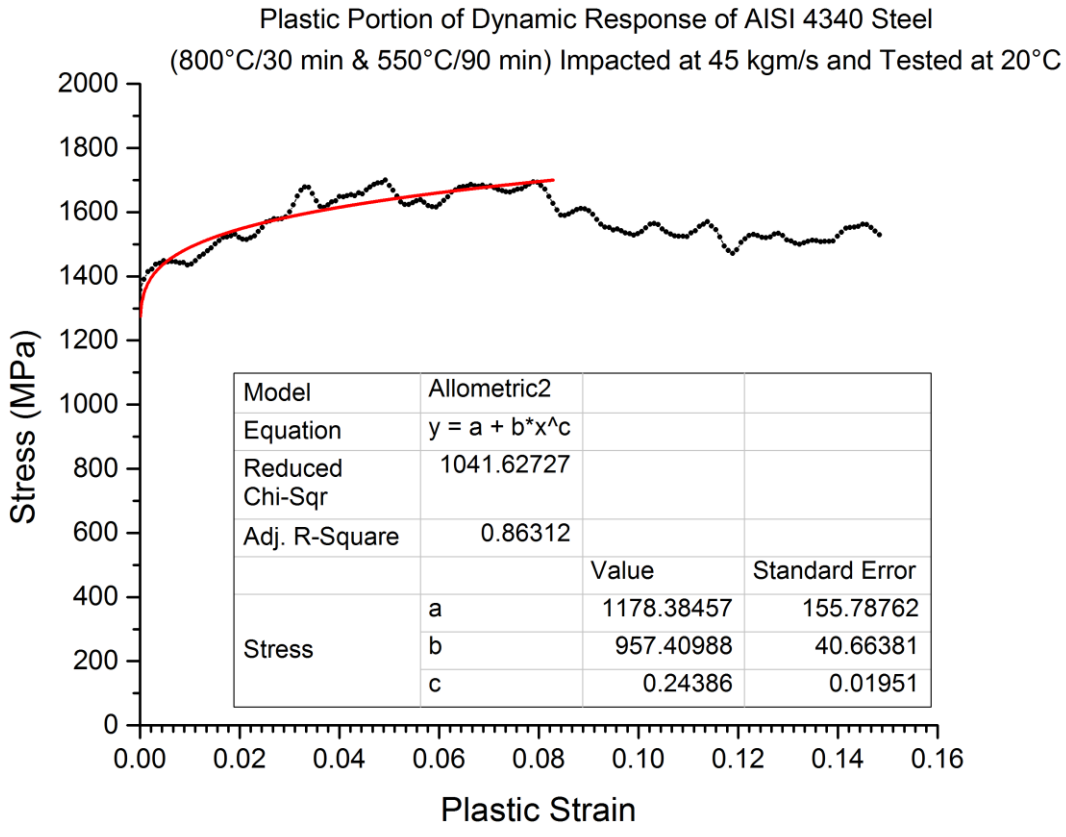

Fig. 88 Power-law regression fit of the plastic portion of the stress-strain curve of a specimen of AISI 4340 steel austenized at 800°C, tempered at 550°C, impacted at 45 kgm/s and tested at 20°C used to determine the Johnson-Cook hardening parameters B and n.

At this impact momentum, A = 1178 $\pm$ 155 MPa which under-predicts the experimentally measured yield strength, σ_y = 1356 $\pm$ 50 MPa, but lies within the estimated error. The Johnson-Cook hardening parameters are B = 957 $\pm$ 41 MPa and n = 0.24386 $\pm$ 0.01951.

When impact momentum was increased to 49 kgm/s, for the same heat treatment, as shown in Fig. 89, the Johnson-Cook dynamic yield strength was estimated to be 'a' = 1418 $\pm$ 134 MPa, which again under-predicts the experimentally determined yield strength, σ_y = 1593 $\pm$ 50 MPa, but lies within the margin of error. The hardening parameters also increase to 'B' = 1483 $\pm$ 88 MPa, and 'n' = 0.28712 $\pm$ 0.01544. Increasing the strain rate results in deformation at a slightly higher maximum stress with a larger hardening effect represented by a slightly steeper, faster hardening rate.

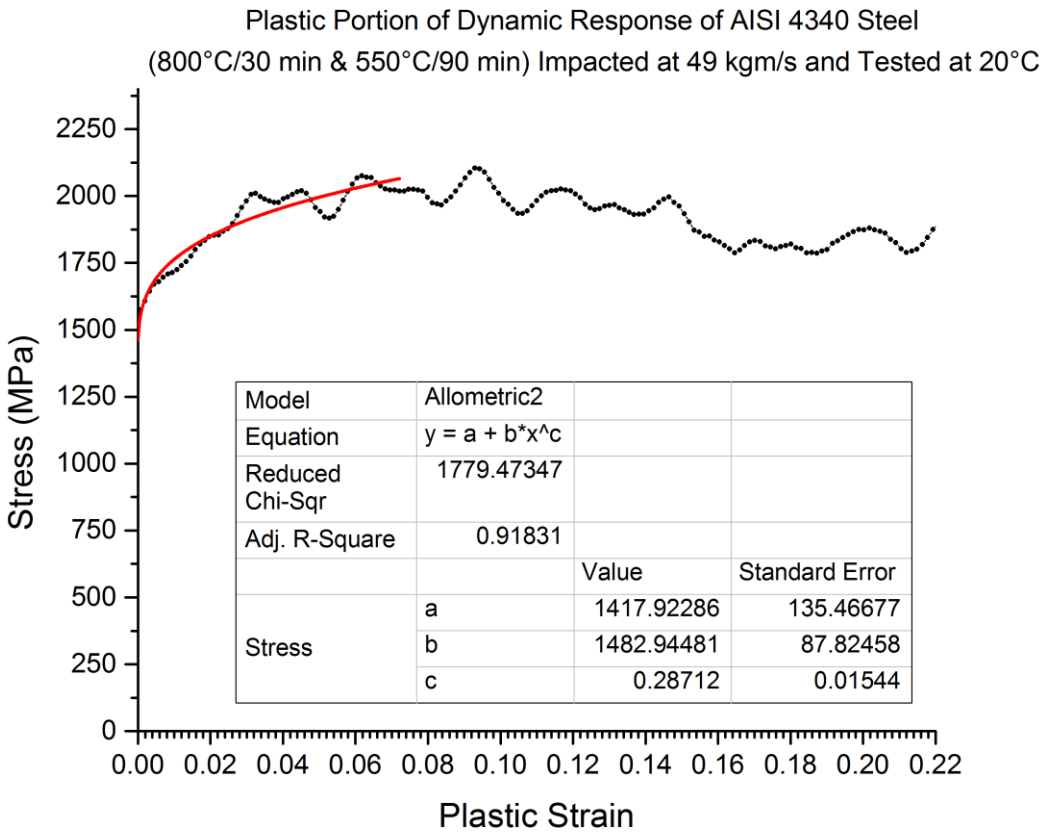

Fig. 89 Power-law regression fit of the plastic portion of the stress-strain curve of a specimen of AISI 4340 steel austenized at 800°C, tempered at 550°C, impacted at 49 kgm/s and tested at 20°C used to determine the Johnson-Cook hardening parameters B and n.

Hardening parameters B and n were calculated for all impact momenta for steel austenized at 800°C, tempered at 550°C and tested at 20°C and are summarized in Table 19. The predicted Johnson-Cook values for dynamic yield strength 'A' were consistently under-predicting the experimentally measured values. These observations match that of Schwer [100], who showed that the Johnson-Cook model consistently under-predicted the yield strength of A36 steel.

Table 19 Summary of estimated Johnson-Cook hardening parameters at elevated strain rates for AISI 4340 steel specimens austenized at 800°C

Aust. Temp. [°C]	Temper. Temp [°C]	Test Temp. [°C]	Imp. Mmtm [kgm/s]	$\dot{\bar{\varepsilon}}^{pl}$ [s^{-1}]	A [MPa	B [MPa]	n ± 0.02
800	550	20	30	978	1037 ± 92	869 ± 22	0.22874
			45	1630	1178 ± 155	957 ± 41	0.24386
			49	2658	1418 ± 134	1483 ± 88	0.28712
			52	3972	1635 ± 125	2940 ± 95	0.36213

The hardening parameters, B_0 and n_0, at a strain rate of $\dot{\bar{\varepsilon}}^{pl} = 1/s$ were determined by regression fitting plots of dynamic 'B' and 'n' vs strain rate, shown in Fig. 90 and Fig. 91, using a three-term exponential curve fitting to minimize the error. The Johnson-Cook quasi-static hardening parameters were determined to be B_0 = 733.8742 MPa and n_0 = 0.20731.

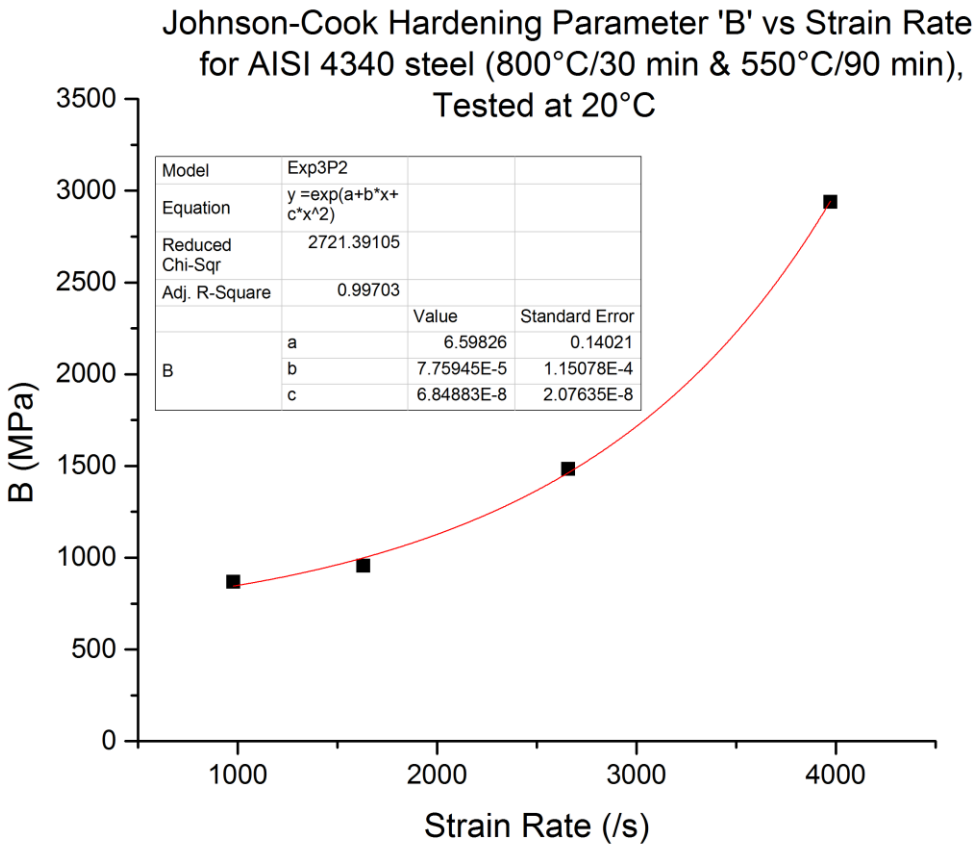

Fig. 90 Johnson-Cook hardening coefficient, 'B', as a function of strain rate for AISI 4340 steel austenized at 800°C, tempered at 550°C, and tested at 20°C.

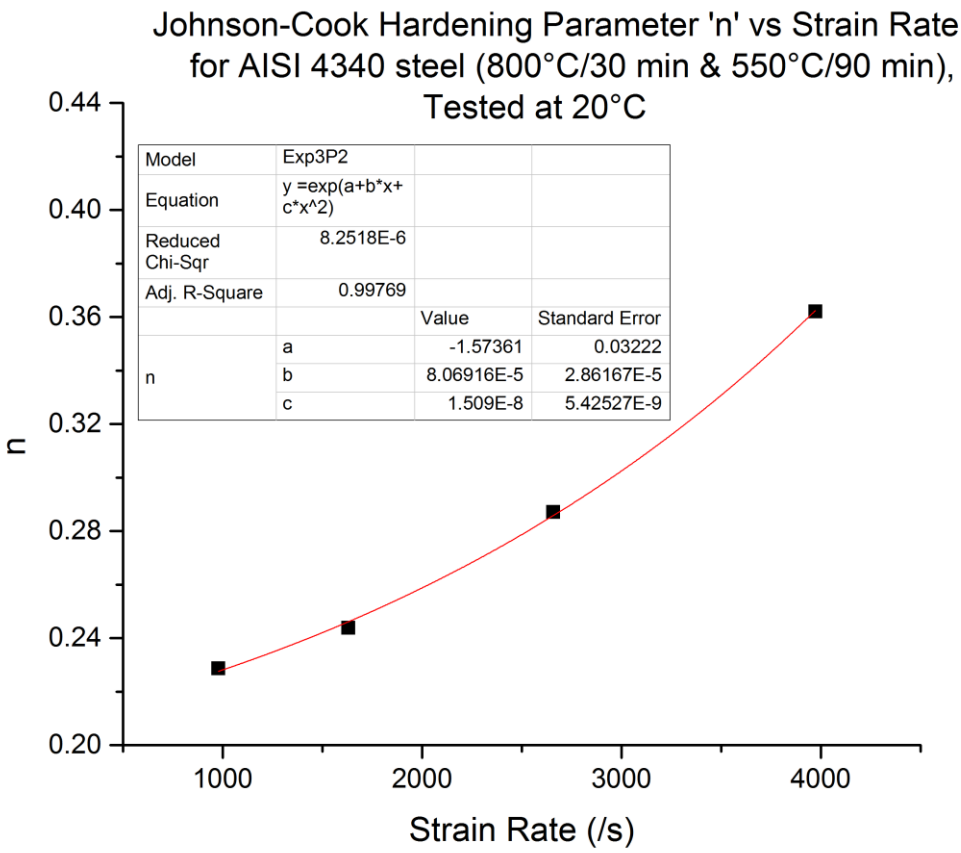

Fig. 91 Johnson-Cook hardening sensitivity parameter, 'n', as a function of strain rate for AISI 4340 steel austenized at 800°C, tempered at 550°C, and tested at 20°C.

According to the Johnson-Cook model, the quasi-static plastic portion of the stress-strain curve is proportional to the dynamic response by a linear logarithmic relationship, shown in Eq. 4-3. The strain rate sensitivity parameter 'C', is determined by plotting the stress ratio, $\frac{\left[A_1+B_1\left(\bar{\varepsilon}^{pl}\right)^{n_1}\right]}{\left[A_0+B_0\left(\bar{\varepsilon}^{pl}\right)^{n_0}\right]}$, of the dynamic stress at various strain rates over the quasi-static stress, at a

specific value of strain, against the natural log of the corresponding strain rate ratio, defined as $ln\left(\frac{\bar{\varepsilon}^{\dot{p}l}{}_1}{\bar{\varepsilon}^{\dot{p}l}{}_0}\right)$ and then regression fitting the curve using a linear relationship of the form:

$$y = a + bx \qquad \textbf{Eq. 4-5}$$

where

$$y = \frac{[A_1 + B_1(\bar{\varepsilon}^{pl})^{n_1}]}{[A_0 + B_0(\bar{\varepsilon}^{pl})^{n_0}]};\ \ a = 1; \qquad \textbf{Eq. 4-6}$$

$$b = C\ ;\quad x = \ ln\left(\frac{\bar{\varepsilon}^{\dot{p}l}{}_1}{\bar{\varepsilon}^{\dot{p}l}{}_0}\right);\qquad \bar{\varepsilon}^{\dot{p}l}{}_0 = 1 \qquad \textbf{Eq. 4-7}$$

The value of the plastic strain $\bar{\varepsilon}^{pl}$ is normally chosen at the minimum difference between the Johnson-Cook approximated quasi-static stress $A_0 + B_0(\bar{\varepsilon}^{pl})^{n_0}$ at a strain rate of 1/s, and the experimentally measured quasi-static stress, when the two stress-strain curves are compared. In the absence of experimental quasi-static stress-strain data, $\bar{\varepsilon}^{pl}$ was chosen to be the predicted quasi-static yield strain, summarized for each heat treatment, in Table 12. For AISI 4340 steel austenized at 800°C, tempered at 550ºC, and tested at 20°C, $\bar{\varepsilon}^{pl} = 0.00582$.

A summary of the calculated stress and strain rate ratios for AISI 4340 steel with heat treatment (800°C/30 min & 550°C/90 min) is shown in Table 20.

Table 20 Summary of dynamic stress and strain rate ratios for AISI 4340 steel (800°C/30 min & 550°C/90 min) tested at 20°C, for the determination of the Johnson-Cook strain rate sensitivity parameter 'C'

Impact Momentum [kg·m/s]	$\dot{\bar{\varepsilon}}^{pl}$ **[s^{-1}]**	$ln\left(\frac{\dot{\bar{\varepsilon}}^{pl}_{1}}{\dot{\bar{\varepsilon}}^{pl}_{0}}\right)$	$\frac{[A_1 + B_1(\bar{\varepsilon}^{pl})^{n_1}]}{[A_0 + B_0(\bar{\varepsilon}^{pl})^{n_0}]}$
REFERENCE	1	0	1
30	978	6.88550967	0.98481581
45	1630	7.39633529	1.0250945
49	2658	7.88532924	1.21476953
52	3972	8.28702503	1.40887599

A plot of the stress ratio vs logarithmic strain rate ratio for this heat treatment, shown in Fig. 92, gives a strain rate sensitivity parameter of 'C' = 0.02216 $\pm$ 0.01035. This value is 60% greater than the sensitivity parameter for annealed 4340 steel, shown in Table 18. This means that strain rate sensitivity increases with increasing strength and hardness.

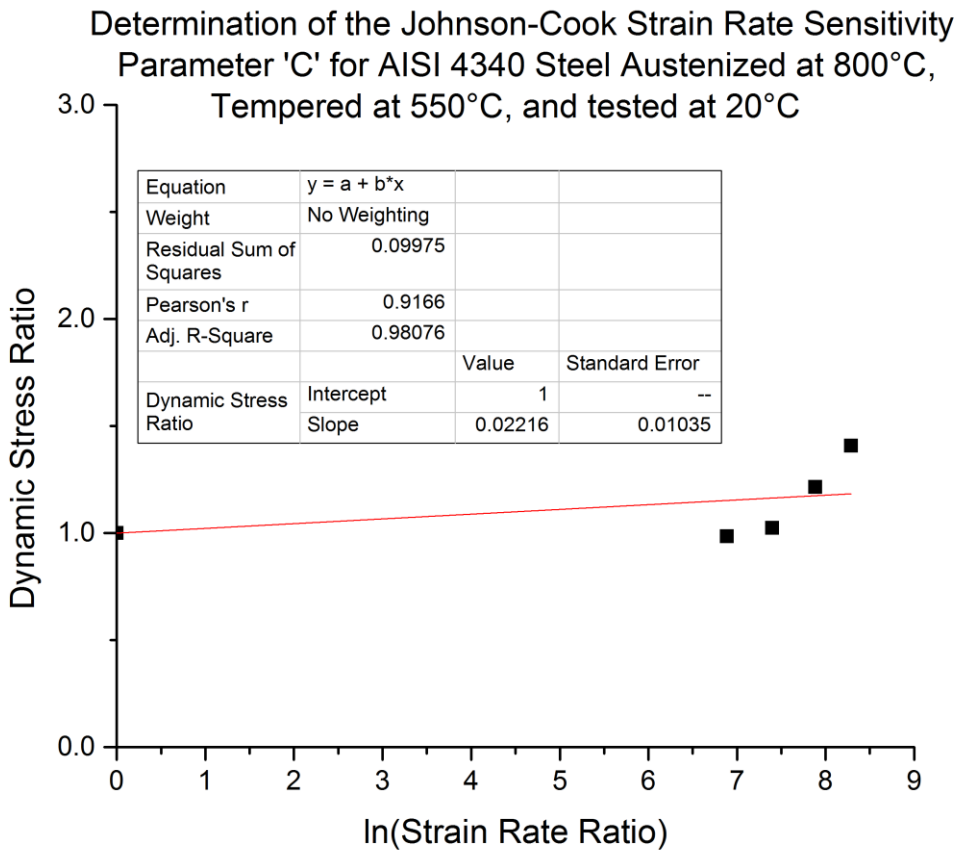

Fig. 92 Determination of the Johnson-Cook strain rate sensitivity parameter 'C' using a linear logarithmic relationship

4.2.1.2 Alternative Strain Rate Dependence Models

The predicted Johnson-Cook sensitivity parameter 'C', determined for AISI 4340 steel (800°C/30 min & 550°C/90 min) had a nearly 50% error margin. In Section 2.5.4, alternative strain rate forms were reviewed that could be used improve the accuracy of the strain rate dependence prediction depending on the material being analyzed, and the

deformation conditions. For example, the modified Johnson-Cook model [13], removes the logarithmic dependence on strain rate and defines the dynamic stress as a power law relationship with strain rate as

$$[A_1 + B_1(\bar{\varepsilon}^{pl})^{n_1}] = [A_0 + B_0(\bar{\varepsilon}^{pl})^{n_0}]\left[1 + \frac{\dot{\bar{\varepsilon}}^{pl}}{\dot{\varepsilon}_o}\right]^C. \qquad \textbf{Eq. 4-8}$$

This relationship is a modification of the Allen-Rule-Jones rate form [102], which states that the dynamic stress is exponentially dependent on strain rate, as discussed in Section 2.5.4.2. Allen et al. [102] showed that this relationship improves the accuracy of strain rate dependence for steels at very low strain rates of deformation ($\dot{\bar{\varepsilon}}^{pl} = 10^{-4}/s$). Also, the modified Johnson-Cook strain rate sensitivity parameter, 'C', is best predicted when strain rate data is gathered from very low to very high strain rates ($10^{-4}/s \leq \dot{\bar{\varepsilon}}^{pl} \leq 10^{4}/s$), where the metal exhibits a bi-linear dependence on strain rate [100]. For the limited strain rate range of ($1/s \leq \dot{\bar{\varepsilon}}^{pl} \leq 10^{3}/s$), used in this thesis, a three-term power law relationship of the form:

$$y = a + bx^c \qquad \textbf{Eq. 4-9}$$

where

$$y = \frac{[A_1 + B_1(\bar{\varepsilon}^{pl})^{n_1}]}{[A_0 + B_0(\bar{\varepsilon}^{pl})^{n_0}]}; \quad x = \left(\frac{\dot{\bar{\varepsilon}}^{pl}}{\dot{\varepsilon}_o}\right);$$

$$a = 1; \quad b = 1; \quad c = \boldsymbol{C}$$

was used to fit the stress ratio vs strain rate ratio data from Table 20 and is shown in Fig. 93. It is clear from the plot that the data cannot be fit accurately using this regression curve.

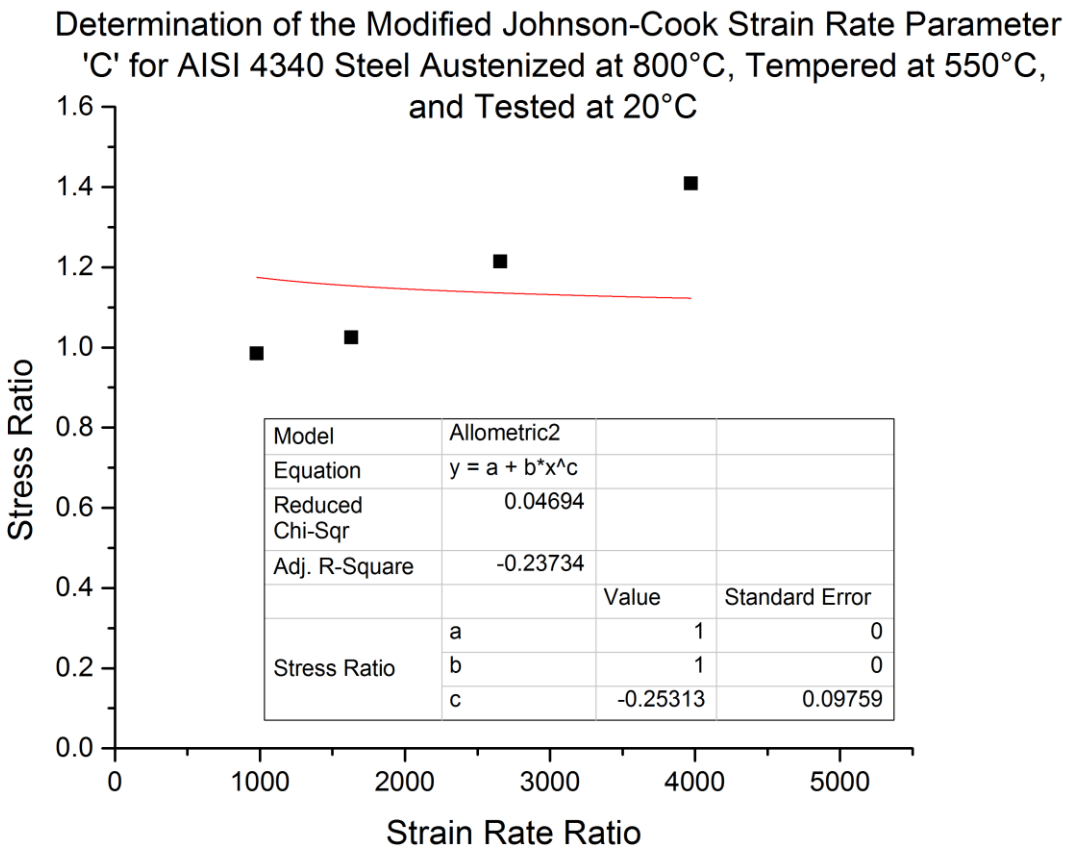

Fig. 93 Prediction of the modified Johnson-Cook strain rate sensitivity parameter 'C' using a power law regression fit

The modified Johnson-Cook model poorly predicts the strain rate dependence for this heat treatment based on the limited strain rate range. In the literature, the strain rate sensitivity parameters are always positive [11], such that increasing the strain rate of deformation increases the stress response, and typical values of the modified Johnson-Cook

strain rate sensitivity parameter are similar to those predicted using the standard Johnson-Cook model [100].

Alternatively, the Huh-Kang strain rate form replaces the linear logarithmic dependence on strain rate with a quadratic relationship, as discussed in Section 2.5.4.1. A quadratic regression fit of the stress ratio vs ln(strain rate ratio), shown in Fig. 94, incorrectly predicts a negative value for the first of two strain rate constants. Huh and Kang showed that the strain rate parameters C1 and C2 are always positive [101]. Thus, the Huh-Kang strain rate form poorly predicts the strain rate sensitivity for this heat treatment and strain rate range.

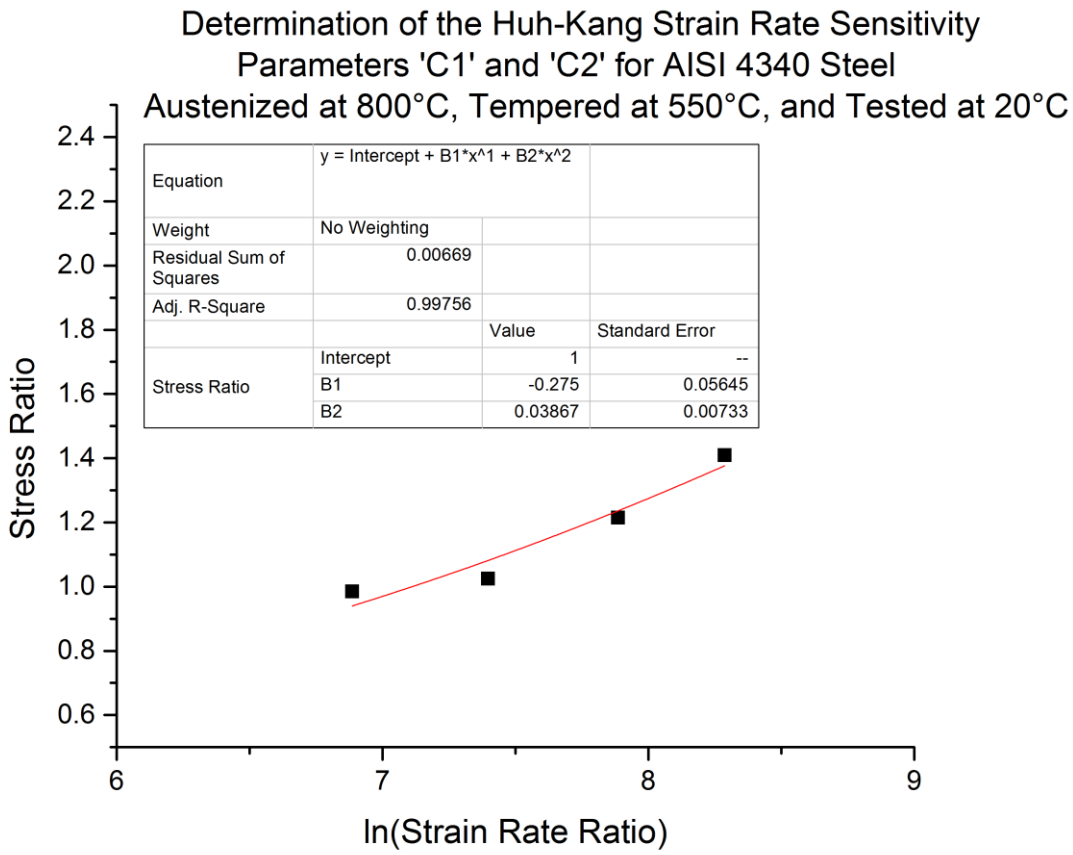

Fig. 94 Prediction of the Huh-Kang strain rate sensitivity parameters, 'C1' and 'C2' using a quadratic logarithmic relationship

The Cowper-Symonds strain rate form [103], discussed in Section 2.5.4.3, defines the strain rate dependence on flow stress as

$$[A_1 + B_1(\bar{\varepsilon}^{pl})^{n_1}] = [A_0 + B_0(\bar{\varepsilon}^{pl})^{n_0}]\left[1 + \left(\frac{\dot{\bar{\varepsilon}}^{pl}_1}{C}\right)^{\frac{1}{P}}\right] \qquad \textbf{Eq. 4-10}$$

where the Cowper-Symonds strain rate parameters ‘C’ and ‘P’ are found by plotting the stress ratio $\frac{\left[A_1+B_1\left(\bar{\varepsilon}^{pl}\right)^{n_1}\right]}{\left[A_0+B_0\left(\bar{\varepsilon}^{pl}\right)^{n_0}\right]}$ against the dynamic strain rate $\dot{\bar{\varepsilon}^{pl}}_1$ and regression fitting using a three term power-law regression fit of the form:

$$y = a + bx^c \qquad \textbf{Eq. 4-11}$$

where

$$a = 1; \quad b = \frac{1}{\boldsymbol{C}^{1/P}}; \qquad c = \frac{1}{\boldsymbol{P}}$$

The Cowper-Symonds parameters C and P can then be determined from:

$$\boldsymbol{C} = \left(\frac{1}{b}\right)^{P}; \qquad \boldsymbol{P} = \frac{1}{c} \qquad \textbf{Eq. 4-12}$$

A plot of the stress ratio against dynamic strain rate for AISI 4340 steel heat treated at (800°C/30 min & 550°C/90 min) is shown in Fig. 95.

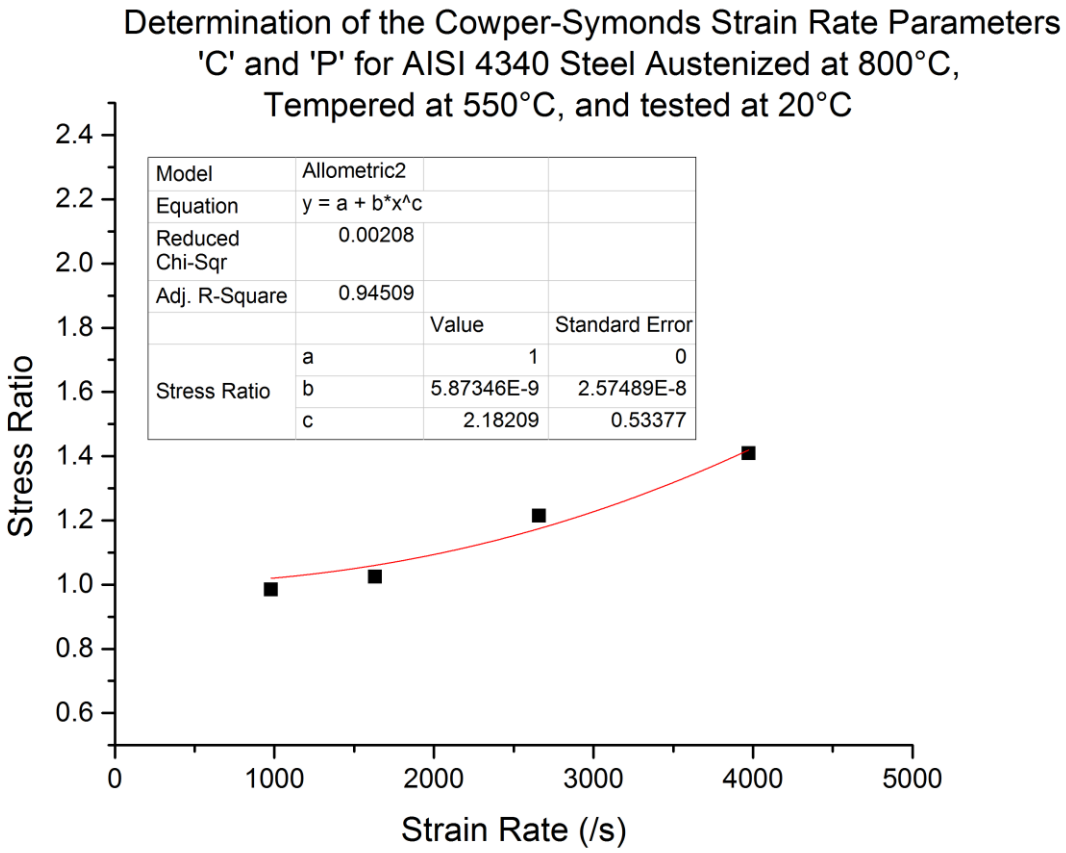

Fig. 95 Prediction of the Cowper-Symonds strain rate sensitivity parameters, 'C' and 'P' using a three-term power law relationship

The Cowper-Symonds strain rate parameters are determined to be C = 5917.255 s^{-1} and P = 0.45827. Typical values for annealed AISI 4340 steel are C = 200000 s^{-1} and P = 3.3 [103]. Also, according to the data gathered by Cowper and Symonds, the strain rate parameter C decreases while P increases as strength of the material decreases. A softer weaker steel will exhibit a lower stress increase over a larger strain rate compared to a harder steel, resulting in a flatter curve. Experimental results showed that annealed steel has a lower

strength than that of steel heat treated to (800ºC/30 min & 550ºC/90 min) and, therefore, should have a lower strain rate parameter C. Based on this observation, it can be concluded that the Cowper-Symonds prediction of strain rate dependence is not accurate for the data gathered.

The alternative strain rate forms discussed have been found to poorly predict the strain rate dependence of AISI 4340 steel based on the experimental data. The literature shows that these models are best used when data is gathered over a large strain rate range ($10^{-4}/s \leq \dot{\bar{\varepsilon}}^{pl} \leq 10^{4}/s$), while the standard Johnson-Cook model is typically used for strain rates $\geq$ 1 /s [100]. The standard Johnson-Cook prediction for strain rate sensitivity was found to have the smallest error compared with the alternative strain rate forms and was used to determine the parameters for all heat treatments.

A summary of the estimated Johnson-Cook hardening and strain rate sensitivity parameters for AISI 4340 steel austenized at 800°C, tempered at 550°C, and tested at 20°C, is shown in Table 21.

Table 21 Summary of Johnson-Cook hardening and strain rate sensitivity parameters for AISI 4340 steel (800°C/30 min & 550°C/90 min) tested at 20°C at a strain rate of $\dot{\varepsilon} = 1/s$

Parameter	Value
A [MPa]	1156.7
B [MPa]	733.87
n	0.20731
C	0.02216

4.2.1.3 Determination of the Johnson-Cook Thermal Softening Sensitivity Parameter 'm'

Normally, the deformation of a metal under high strain rates and large strains is not isotropic. In fact it undergoes thermal strain softening which is reflected on the stress strain curve as a gradual stress collapse. In other words, the temperature rise inside the steel due to the high strain rate deformation, defined in Section 2.5.4.6 by Eq. 2-25, induces a loss of stress carrying capacity. According to the Johnson-Cook definition of flow stress, the decrease in flow stress by thermal softening is defined as

$$\sigma = \sigma_{isotropic}\left(1 - \hat{T}^{m}\right) \qquad \textbf{Eq. 4-13}$$

where

$$\hat{T} = \frac{\left(T - T_{ref}\right)}{\left(T_{melt} - T_{ref}\right)} \qquad \textbf{Eq. 4-14}$$

and is observable immediately around the peak stress after hardening. According to Lee and Yeh [159], thermal softening is assumed to be constant for temperatures less than 298K and the thermal softening parameter takes the value of 1. Above 298K and lower than 1040K, 'm' is assumed to be 1.03, and beyond 1040 K, 'm' is assumed to be equal to 0.5. The reference temperature T_{ref} is equal to 298K and the melting temperature T_m is fixed at 1793K for AISI 4340 steel [160]. In this thesis, the thermal softening parameter 'm' is taken to be 1.03 for all heat treatments and strain rates.

4.2.1.4 Summary of Calculated Johnson-Cook Parameters for all Tested Heat Treatments

The Johnson-Cook parameters were calculated for all heat treatments and testing temperatures, a summary of which is shown in Table 22. The thermal sensitivity parameter 'm' is assumed to be constant at 1.03 for all heat treatments and testing temperatures.

Table 22 Estimated Johnson-Cook hardening parameters 'B' and 'n', and strain rate sensitivity parameter 'C', for all tested heat treatments and testing temperatures for AISI 4340 steel at $\dot{\varepsilon} = 1/s$

Austenization Temperature [°C]	Tempering Temperature [°C]	Testing Temperature [°C]	A [MPa]	B [MPa]	n	C
800	400	20	1366.4	867.37	0.1529	0.02581
		428	773.42	491.42	0.2594	0.01157
	550	20	1156.7	733.87	0.2073	0.02216
		428	695.94	439.69	0.2698	0.01013
900	400	20	1209.2	765.82	0.1838	0.02183
		428	632.47	402.13	0.2631	0.00967
	550	20	965.47	614.61	0.2374	0.01691
		428	573.28	364.79	0.2722	0.00894
1000	400	20	1147	728.11	0.2287	0.01999
		428	560.72	353.96	0.2767	0.00853
	550	20	920.53	582.77	0.2585	0.01586
		428	508.52	322.75	0.2824	0.00787

The estimated values of the quasi-static hardening coefficient 'B' are directly proportional to the quasi-static yield strength by an average factor of 0.634367. This matches closely to the estimated proportionality constant found by Banerjee [156] and Shivpuri et al. [157], for AISI 4340 steel and SAE 1070 steel respectively, to be 0.6339— a difference of only 0.074%. Plots of the variation in Johnson Cook parameters, n and C, with yield

strength, A, are shown in Fig. 96 and Fig. 97. The estimation of the Johnson-Cook parameters for all heat treatments is in good agreement with the documented values for annealed AISI 4340 steel. A regression fit of the curves shows that for the yield strength of A = 792 MPa at $\dot{\varepsilon} = 1/s$ for annealed AISI 4340 steel [11], the corresponding hardening exponent n = 0.26214 and strain rate sensitivity C = 0.0139740. These values vary from the documented parameters, in Table 18, by only 0.8% and 0.2% respectively.

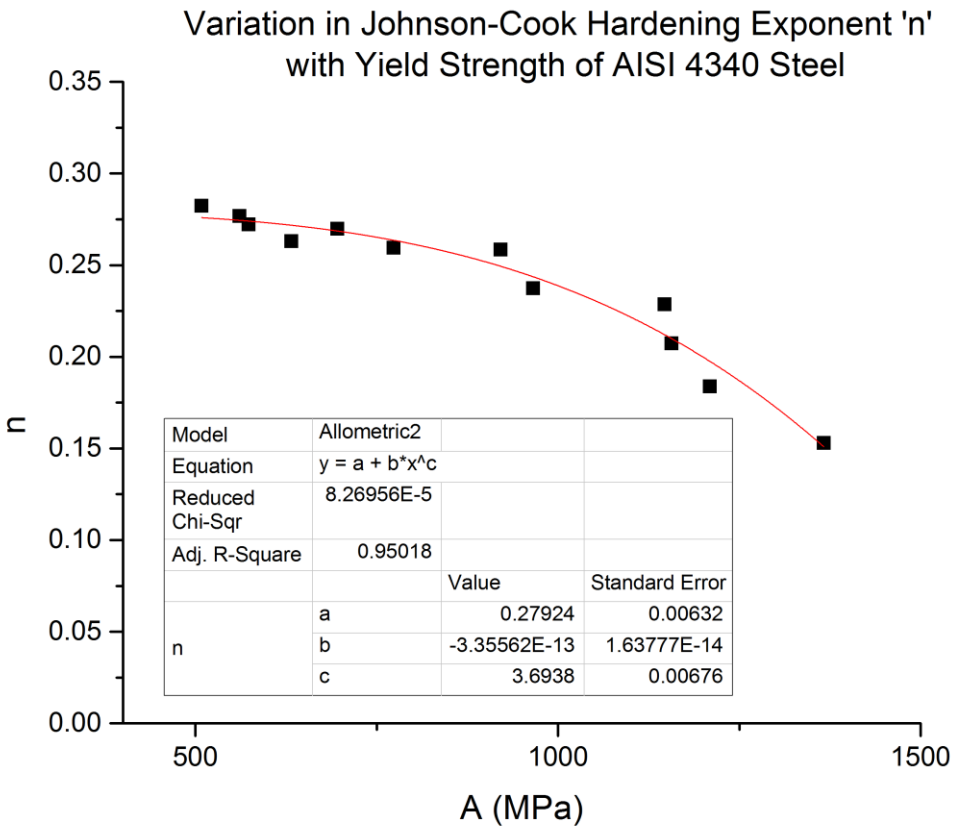

Fig. 96 Johnson Cook hardening exponent 'n' as a function of yield strength for AISI 4340 steel

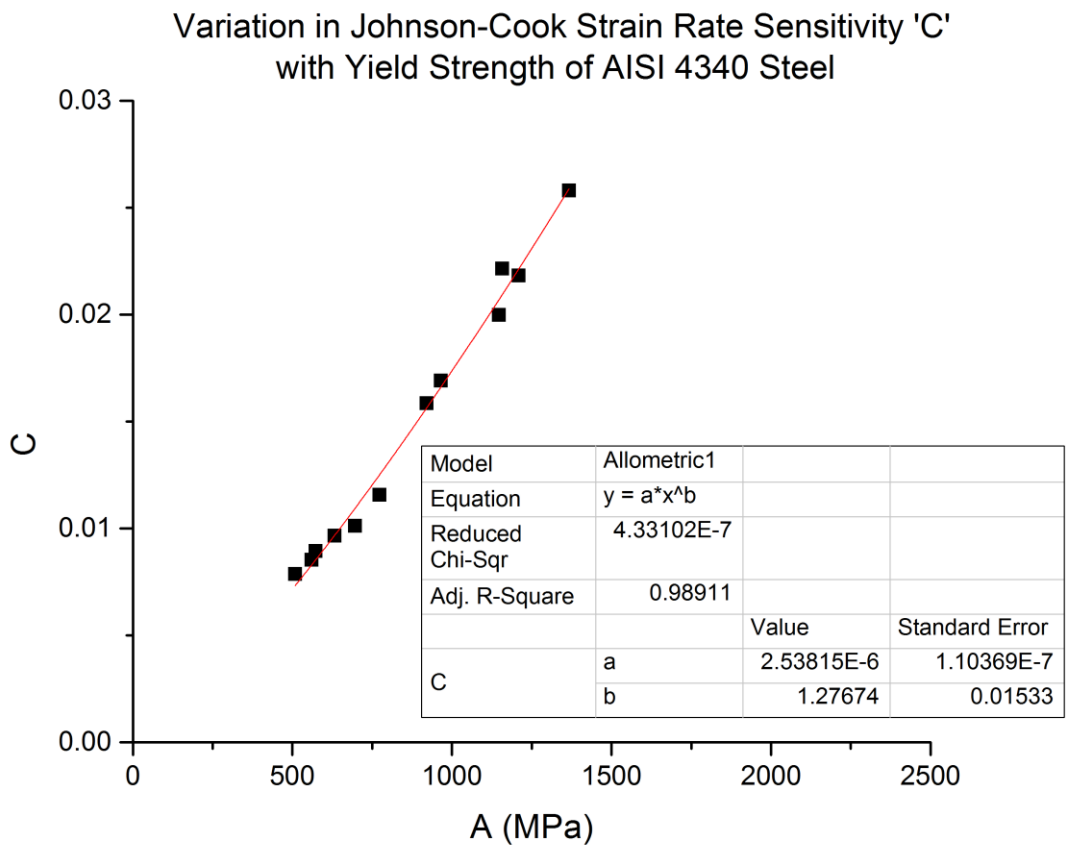

Fig. 97 Johnson Cook strain rate sensitivity parameter 'C' as a function of yield strength for AISI 4340 steel

In addition to the Johnson-Cook material parameters that define material plasticity, it was necessary to determine the failure parameters for each heat treatment, which simulate fracture and failure of steels. This criteria allows for better identification of localization and

ASB formation in the steel through the formation of microracks. The procedure used to obtain these parameters is described in the next section.

4.2.1.5 Determination of the Fracture and Failure Criteria for AISI 4340 Steel

A number of researchers, in the literature, use the Johnson-Cook failure model for simulating progressive damage of metals. Very few, however, determine their own damage parameters while considering the effectiveness of the Johnson Cook damage model under different modes of failure. Kay [161], Weirzbicki et al. [162], Bao and Weirzbicki [163], and Johnson and Holmquist [164] provide a complete description on the process of obtaining the Johnson-Cook damage parameters from negative to positive stress triaxiality (-1/3 $\leq \sigma_{TRI} \leq$ 0.5). The Johnson-Cook failure model defines the effective plastic strain to failure as a function of stress triaxiality, strain rate and homologous temperature. Stress triaxiliaty is defined as the mean stress divided by the equivalent Von Mises stress. That is,

$$\sigma_{TRI} = \frac{\left(\frac{\sigma_1 + \sigma_2 + \sigma_3}{3}\right)}{\sigma_{EVM}} \qquad \textbf{Eq. 4-15}$$

where

$$\sigma_{EVM} = \frac{1}{\sqrt{2}}\sqrt{(\sigma_1 - \sigma_2)^2 + (\sigma_2 - \sigma_3)^2 + (\sigma_3 - \sigma_1)^2} \qquad \textbf{Eq. 4-16}$$

In 2-D applications:

$$\sigma_{TRI} = \frac{\left(\frac{\sigma_1 + \sigma_2}{2}\right)}{\sigma_{EVM}} \qquad \textbf{Eq. 4-17}$$

where

$$\sigma_1 = \left(\frac{\sigma_{xx} + \sigma_{yy}}{2}\right) + \sqrt{\left(\frac{\sigma_{xx} - \sigma_{yy}}{2}\right)^2 + \left(\tau_{xy}\right)^2} \quad \textbf{Eq. 4-18}$$

$$\sigma_2 = \left(\frac{\sigma_{xx} + \sigma_{yy}}{2}\right) - \sqrt{\left(\frac{\sigma_{xx} - \sigma_{yy}}{2}\right)^2 + \left(\tau_{xy}\right)^2} \quad \textbf{Eq. 4-19}$$

$$\sigma_{EVM} = \frac{1}{\sqrt{2}}\sqrt{\sigma_{xx}^2 + \sigma_{yy}^2 - \sigma_{xx}\sigma_{yy} + 3\tau_{xy}^2} \quad \textbf{Eq. 4-20}$$

In studying the dependency of the strain to fracture on stress triaxiality in 2024 T351 Aluminum, Bao and Wierzbicki [163] found that the first bracket of the Johnson-Cook damage model in Eq. 2-22 considers only the fracture due to void growth under tension at high stress triaxiality (σ_{TRI} > 1/3) with no consideration for pure shear failure (trixiality = 0). Bao and Wierzbicki even demonstrated the presence of a cut-off value of ($\sigma_{TRI} = -1/3$) (compression) for fracture of different metals under which *no failure mode is possible using this failure model*. These authors concluded that the Johnson-Cook damage model is only valid for defining tensile ductile void growth failure and cannot properly simulate shear failure.

An alternative approach to define shear failure would be to modify the existing Johnson-Cook damage model, discussed in Section 2.5.4.4 and given by Eq. 2-21, by simply changing the direction of deformation from tension to shear so that the equivalent plastic shear strain at failure is dependent on shear strain rate and is defined as

$$\bar{\gamma}_f^{pl} = [d_1 + d_2 \exp(d_3 \sigma_{TRI})]\left[1 + d_4 ln\left(\frac{\dot{\bar{\gamma}}^{pl}}{\dot{\gamma}_o}\right)\right]\left[1 + d_5 \hat{T}\right] \quad \textbf{Eq. 4-21}$$

where $\sigma_{TRI} = 0\ for\ shear;\ \ \dot{\gamma}_o = 1/s\ (reference\ strain\ rate)$

Thus for this case,

$$\bar{\gamma}_f^{pl} = [d_1 + d_2][1 + d_4 ln(\dot{\bar{\gamma}}^{pl})]\left[1 + d_5 \hat{T}\right] \quad \textbf{Eq. 4-22}$$

The effective shear failure strain, $\bar{\gamma}_f^{pl}$, can be determined by performing characteristic torsion tests at room temperature ($\hat{T} = 0$) to determine the failure strain at various shear strain rates, $\dot{\bar{\gamma}}^{pl}$. The damage parameter d_4 would then be the slope of a linear regression fit of the form ($y = d_4 x + 1$) on a plot of $\bar{\gamma}_f^{pl} / [d_1 + d_2]$ vs $ln(\dot{\bar{\gamma}}^{pl})$.

Damage parameters d_1 and d_2 could be determined through quasi-static torsion tests where $\dot{\bar{\gamma}}^{pl} = 1/s$. When this is the case, the parameter d_4 has very little effect on the shear failure strain; and $\bar{\gamma}_f^{pl}$ is simply a constant = $[d_1 + d_2]$. To this end, it can be shown that the shear failure strain is simply dependent on strain rate and homologous temperature as,

$$\bar{\gamma}_f^{pl} = [D][1 + \dot{\bar{\gamma}}^{pl}]^{d_4}\left[1 + d_5 \hat{T}\right] \quad \textbf{Eq. 4-23}$$

where

$$D = \bar{\gamma}_f^{pl}\ at\ quasi - static$$

Very little data exist in the literature defining the shear strength and shear strain at failure for AISI 4340 steel especially at various heat treatments. Extensive experimentation using

a torsional Hopkinson bar or modified specimen geometry to achieve pure shear deformation under direct impact is required to obtain the Johnson Cook shear damage constants.

A simpler approach, proposed by Børvik et al. [13] and Nahshon et al. [165], is to use the damage rupture criterion, which is similar to the Johnson-Cook damage parameter D used for tensile failure, shown in Eq. 2-20, but defines the dynamic localized shear rupture of metals under high strain rate deformation, such as blast damage. The rupture criterion is based on a critical value of the equivalent plastic strain at failure ε_f, which is assumed to be independent of strain rate and stress triaxiality and is expressed in terms of a damage parameter, ω as,

$$\omega = \int \frac{d\varepsilon_e^{pl}}{\varepsilon_f} \qquad \textbf{Eq. 4-24}$$

Failure is predicted when ω reaches unity and the failure strain is calculated under quasi-static conditions. When simulating damage, the stress state of a failed element to set to zero and completely removing from computation, resulting in the formation of a crack. In simulations of impact and penetration, Nahshon et al. [165] showed that complete element deletion removed excess amounts of material leading to unrealistic relaxation of the material around the localized crack zone. Instead, shear failure was more accurately simulated by modifying the properties of the failed element so that only compressive stresses could be

supported. Under compressive loading this creates a mode II (shear) crack in the model along lines of maximum shear, because the elements cannot transmit shear.

Due to the absence of a material length scale in the failure criterion, simulation results of failure are inherently mesh-size dependent [166-167]. Mesh size and failure strain both dictate the severity and size of the localization and the distribution of strain and stress adjacent to the localization. A large mesh discretization will result in large cracks with poor strain and stress distribution, while a fine mesh will ensure a more accurate depiction of localization and stress-strain distribution.

When using the SPH meshless discretization, the resolution of stress and strain distribution in the model is defined by the number of SPH nodes in the model. However, the dependency of localization on SPH resolution is not as high as that of meshed techniques. SPH nodes are free to move within a radius defined by the critical failure strain and are not limited by element warping [10]. If stretched beyond this radius the bonds will break and the stress state in the nodes are set to zero. The bond radius, defined by the failure strain, allows for localized failure in all directions between shear and tension ($\sigma_{TRI} \geq 0$). After failure, the freely moving nodes continue to be in contact with each other during simulation and act as free particles with zero bond stiffness. Thus, *localization is simulated by the progressive failure of SPH bonds*. The effectiveness of using ε_f as a consistent failure

criterion for each heat treatment of AISI 4340 steel was assessed by comparing simulation results with experimental observations.

In the absence of fracture data from testing, the equivalent plastic strains at failure for the tested heat treatments of AISI 4340 steel were approximated from tensile data from similar heat treatments of AISI 4340 steel in the literature. In studying the effect of austeniation temperature on fracture strength of AISI 4340 steel, Ritchie et al. [142] found that AISI 4340 steel two-stepped quenched from 1200°C to 870°C to 20°C had an effective fracture strain of $\varepsilon_f = 0.07$ compared to steel directly quenched from 870ºC, whose fracture strain was $\varepsilon_f = 0.18$. Ritchie et al. [142] showed that increasing the austenization temperature from 870°C to 1200°C decreased the fracture strain of as-quenched steel by 60%, but also increased its fracture toughness.

In studying the fractography of AISI 4340 steel under tension, for specimens austenized at 840°C and tempered at various temperatures, Avyle [168] found that tensile fracture strain remained constant at $\varepsilon_f = 0.78$ for all tempering temperatures up to 427°C and then increased to $\varepsilon_f = 0.82$ for specimens tempered at 510°C. This jump in failure strain was attributed to the increase in toughness from tempering.

In this thesis, the values of tensile failure strain were chosen to be independent of austenization temperature, varying only with tempering temperature according to [168]. For

specimens tested at an elevated temperature of 428ºC, failure strains were estimated, for various heat treatments, from the failure strains at 20ºC using the Johnson-Cook damage model's thermal softening temperature dependence defined as

$$\bar{\varepsilon}_f^{pl}@\ 428°C = \left[\bar{\varepsilon}_f^{pl}@\ 20°C\right]\left[1 + d_5\hat{T}\right] \quad \textbf{Eq. 4-25}$$

where 'd_5' is a damage paramater and $\hat{T} = \frac{(T - T_{ref})}{(T_m - T_{ref})} = 0.272$ at 428ºC. The parameter d_5 was chosen to be that of annealed AISI 4340 steel (d_5 = 0.61), shown in Table 18, such that $\left[1 + d_5\hat{T}\right] = 1.16592$. A summary of the estimated tensile plastic strains at failure, are shown in Table 23, along with the specific heat treatment and reference from which they were recorded.

Table 23 Summary of failure strains for each heat treatment of AISI 4340 steel at 20ºC

Austenization Temperature	**800°C**		**900°C**		**1000°C**	
Tempering Temperature	**400°C**	**550°C**	**400°C**	**550°C**	**400°C**	**550°C**
ε_f @ 20ºC	0.78	0.82	0.78	0.82	0.78	0.82
ε_f @ 428ºC	0.91	0.96	0.91	0.96	0.91	0.96
References	1) Austenized at 870C/1 hr & oil quenched to 22°C; 2) Austenized at 1200°C/1 hr & salt quenched to 870°C for 30 min, then oil quenched to 22°C [142] Austenized at 840°C/1 hr in 80% $BaCl_2$-20% NaCl salt bath & oil quenched; Tempered at (270°C, 316°C, 427°C, 510°C) /1 hr in 50% $NaNO_3$-50% KNO_3 salt bath [168]					

A summary of the calculated physical properties of AISI 4340 steel including the elastic, Johnson-Cook plasticity, and failure parameters which vary with heat treatment and testing temperatures, are shown in Table 24. The physical properties which were chosen not to, or do not vary with heat treatment are shown in Table 25. The shear modulus, G, was calculated from the Young's modulus and Poisson's ratio using Eq. 3-15.

The material parameters for each heat treatment were then implemented into FEA software LS-DYNA [5] to simulate impact under various momenta and predict the formation of ASBs. An extensive look into the development of a microstructural based multi-material simulation model is discussed in the next section.

Table 24 Summary of elastic properties, and Johnson-Cook plasticity and failure parameters for AISI 4340 steel for all tested heat treatments

Austenization Temperature (°C)	Tempering Temperature (°C)	Testing Temperature (°C)	E [GPa]	G [GPa]	σ_y (A) [MPa]	B [MPa]	n	C	m	ε_f
800	400	20	194.46	75.372	1366.4	867.37	0.1529	0.02581	1.03	0.78
		428	169.42	65.667	773.42	491.42	0.2594	0.01157	1.03	0.91
	550	20	198.71	77.019	1156.7	733.87	0.2073	0.02216	1.03	0.82
		428	171.51	66.477	695.94	439.69	0.2698	0.01013	1.03	0.96
900	400	20	196.79	76.275	1209.2	765.82	0.1838	0.02183	1.03	0.78
		428	171.76	66.574	632.47	402.13	0.2631	0.00967	1.03	0.91
	550	20	201.32	78.031	965.47	614.61	0.2374	0.01691	1.03	0.82
		428	173.42	67.217	573.28	364.79	0.2722	0.00894	1.03	0.96
1000	400	20	199.53	77.337	1147.1	728.11	0.2287	0.01999	1.03	0.78
		428	172.85	66.996	560.72	353.96	0.2767	0.00853	1.03	0.91
	550	20	204.74	79.357	920.53	582.77	0.2585	0.01586	1.03	0.82
		428	175.09	67.864	508.52	322.75	0.2824	0.00787	1.03	0.96

Table 25 Physical properties of AISI 4340 steel, constant for all heat treatments

Density, ρ [kg/m^3]	7850
Poisson's Ratio, ν	0.29
Specific Heat, C_p [J/kg/K]	465
Taylor-Quinney Coefficient, χ	0.9
Thermal Expansion Coefficient [m/m/K]	0.000013
Melting Temperature, T_m [K]	1793
Reference Temperature, T_{ref} [K]	293

4.3 Homogenous Macroscopic Material Modeling

To test the stability of the estimated Johnson-Cook parameters during simulation, AISI 4340 steel specimens were modeled using simple geometry, shown in Fig. 86, and assigned the properties of each heat treatment. Modelled specimens were then impacted at various momenta to analyze the resulting macroscopic deformation and formation of ASBs and compare to experimental observations. Both Lagrange meshing and SPH meshless discretization techniques were implemented and compared.

4.3.1 Homogenous Impact Simulation of Various Heat Treatments of AISI 4340 Steel

To simulate impact, specimens were modeled in LS-DYNA by a 2D axisymmetric rectangle measuring half the size of a cross section of a specimen, shown in Fig. 86. The rigid wall striker was assigned an initial velocity matching the impact momentum in experimentation, and contact was defined using a coefficient of friction for lubricated steel on steel of 0.16 [169]. The elastic and Johnson-Cook plasticity parameters were implemented along with the rupture failure criterion defined by a tensile failure strain.

An example of the material parameters input into LS-DYNA for steel with heat treatment (800°C/30 min & 400°C/90 min), is shown in Fig. 98 and Fig. 99. The elastic and Johnson-Cook plasticity parameters were defined along with the rupture failure criterion. The Johnson-Cook damage model was replaced with a cumulative damage model that simulates element erosion and failure through tension and shear, based on the rupture criterion and defined by the failure strain. A consistency of units was chosen based on the length scale of the model (mass [g], length [mm], time [ms], force [N], stress [MPa], energy [N-mm]).

The reduced input file used in LS-DYNA for a model of AISI 4340 steel with heat treatment (800ºC/30 min and 400ºC/90 min), discretized into 31125 SPH nodes and impacted at 52 kgm/s is shown in Appendix A.

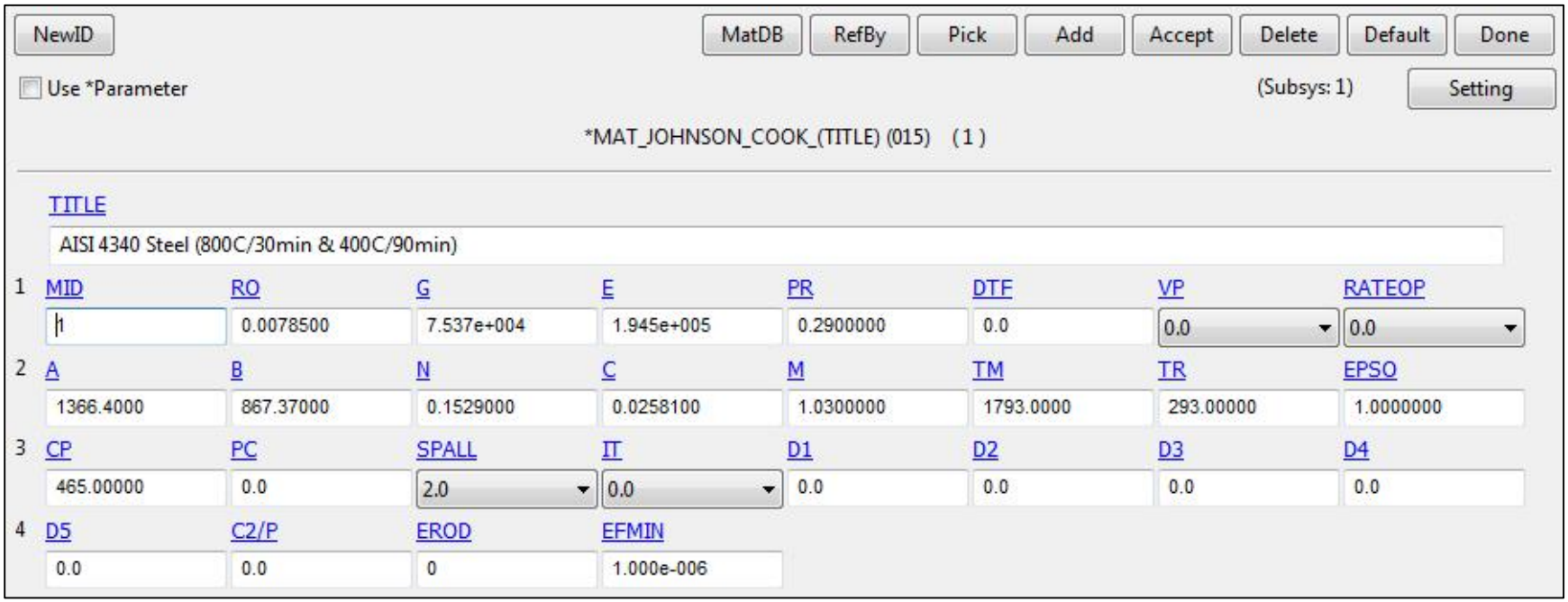

Fig. 98 Material input parameters the elastic and Johnson-Cook plastic model of AISI 4340 steel with heat treatment (800°C/30min & 400°C/90min)

Note: The Johnson-Cook failure model was not used but instead a separate rupture criterion, that defines element erosion, was implemented and is shown in Fig. 99.

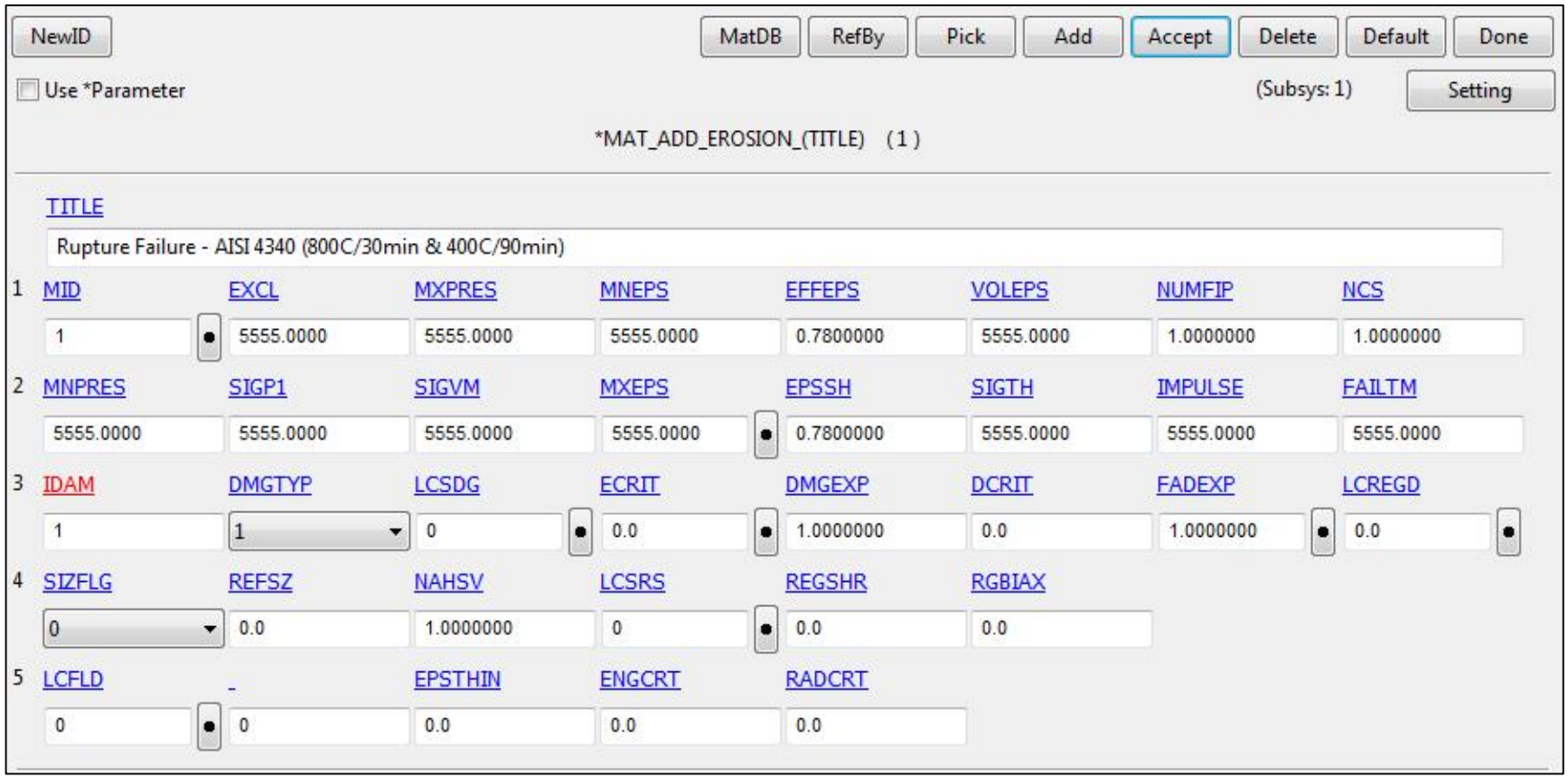

Fig. 99 Rupture failure criterion implemented for AISI 4340 steel with heat treatment (800°C/30min & 400°C/90min)

Note: Erosion can be defined by stress or strain failure in any direction. The exclusion number [EXCL] allows for bypassing of associated failure criteria calculations and is usually set to an unusual value. For example, to control failure to be in the tensile and shear directions alone, the maximum effective strain at failure [EFFEPS] and maximum effective shear strain at failure [EPSSH] are defined while all other parameters are set to the exclusion number. The damage model is then set by [IDAM] and [DMGTYP] to be cumulative, where element failure occurs for D=1 and damage is coupled to flow stress. *It is assumed that both shear and tensile failure strains are equal*.

The model was first meshed with 30750 2D shell elements using the Lagrangian formulation and then impacted by a rigid wall striker with a mass of 1.781 kg and an initial velocity of 29.2 m/s to give an impact momentum of 52 kgm/s. The resulting deformation, shown in Fig. 100, shows a crack formation along lines of maximum shear. This observation matches closely with experimental observation for the same impact conditions where specimens were shown to fracture completely when impacted at the highest momenta of 52 kgm/s.

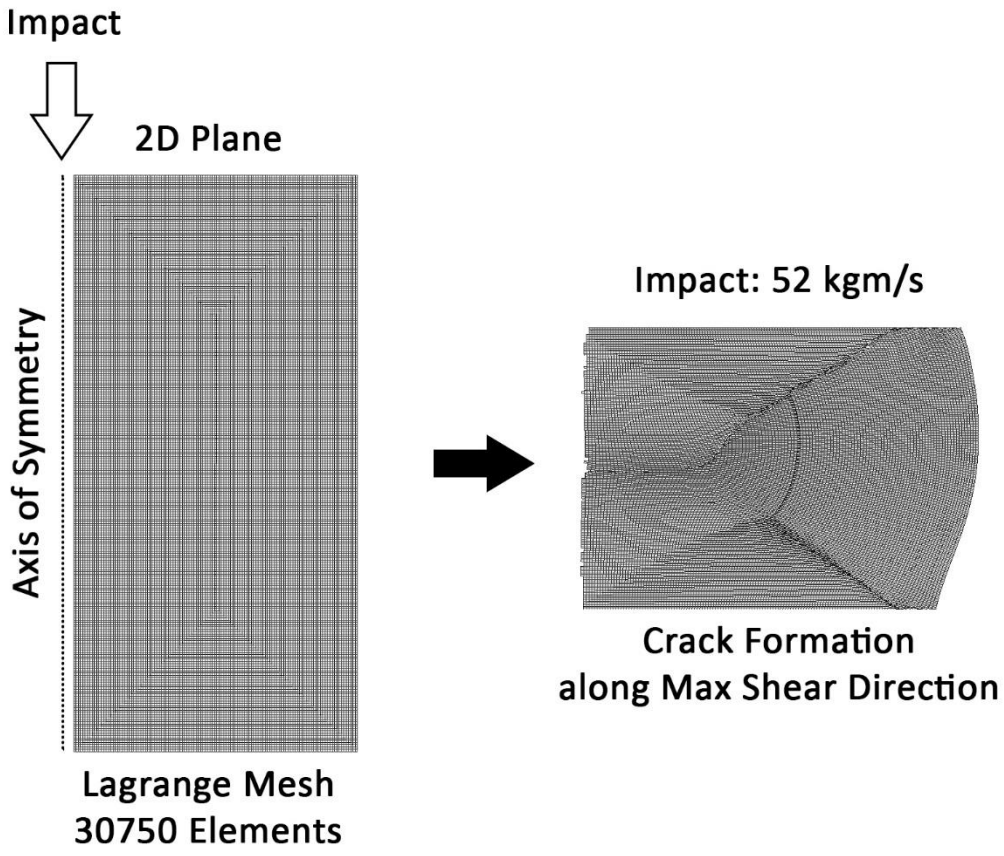

Fig. 100 Impacted Model of AISI 4340 Steel meshed using Lagrangian Formulation with heat treatment (800°C/30 & 400°C/90) impacted at 52 kgm/s showing the formation of cracks and failure along maximum shear direction

Similarly, a model discretized with mesh-less SPH nodes and impacted at the same momentum is shown in Fig. 101. Crack formation is not as clearly distinguished but there is greater model stability at the edge of the model closest to the axis of symmetry. In order to prevent negative area/volume errors, the model had be offset from the axis of symmetry so that nodes were not assigned on the axis. Consequently, a small offset creates unstable

deformation and failure near the axis of symmetry during deformation. This is evident in the resulting deformation shown in Fig. 100, where elements along the left-most wall erode and a crack forms through the center of the specimen. This instability is not seen when using SPH formulation.

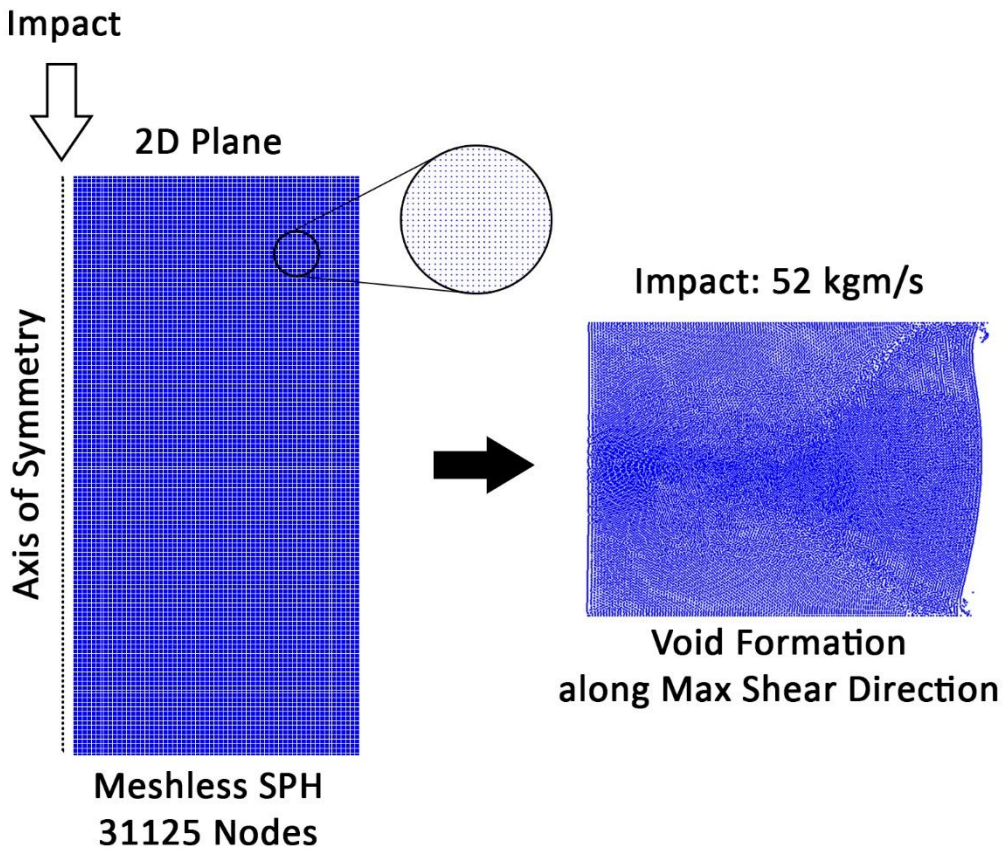

Fig. 101 Impacted Model of AISI 4340 Steel meshed using SPH formulation with heat treatment (800°C/30 & 400°C/90) impacted at 52 kgm/s showing the formation of cracks and failure along maximum shear direction

A comparison between the effective stress and strain responses of deformation between finite element and mesh-less formulation, in Fig. 102 and Fig. 103, show a clear difference in the distribution through the cross-section. Firstly, the stress and strain distribution using finite elements is not as symmetrical as the meshless SPH nodes. This is due to the instability of the elements near the reflected axis of symmetry, resulting in unstable crack formation. Secondly, the SPH meshless formulated model shows a noticeable gradient of effective shear strain in the vicinity of the crack tip in the direction of the crack propagation, as shown in Fig. 103, not present in the meshed finite element formulation. This is due to the excessive material stiffness relaxation surrounding the crack when using finite elements due to the removal of distorted elements from formulation. The severity of strain localization, is therefore represented by the size and thickness of the crack with no indication of the stress or strain distribution inside the localization.

The SPH meshless formulation, can better simulate severe localized deformation and distortion simply due to the lack of elemental boundaries. SPH nodes can distort freely between themselves within a radius defined by the effective plastic failure strain. Failure occurs when the nodes stretch beyond this radius at which time the nodes are considered freely moving with a zero stress state but remain in contact with their neighbors and continue to affect deformation. In meshed formulations, elemental distortion is limited up to a specific aspect ratio at which the simulation time-step will approach infinite and stop or the element

is removed from formulation and the stress is set to zero, indicating a crack formation. The surrounding elements continue to deform without the affected failed element.

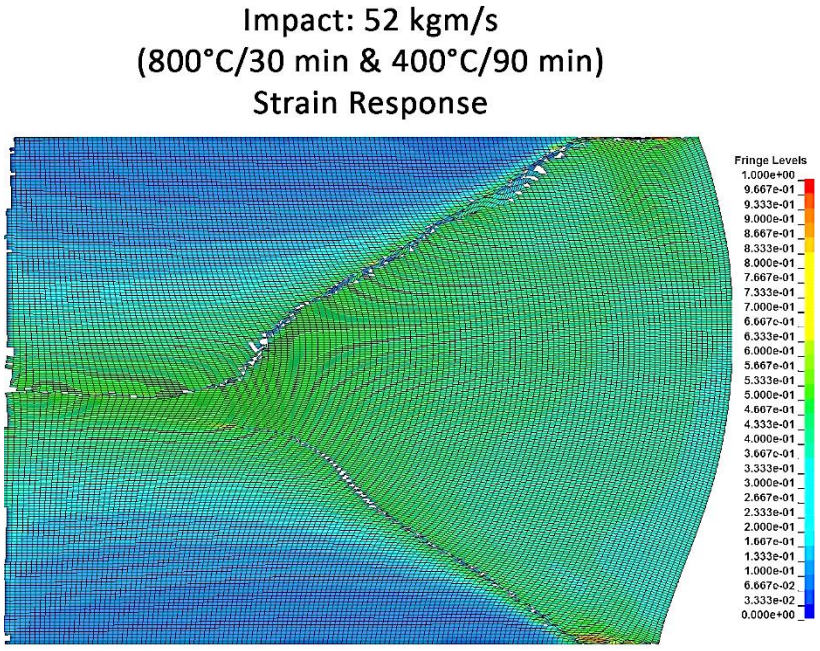

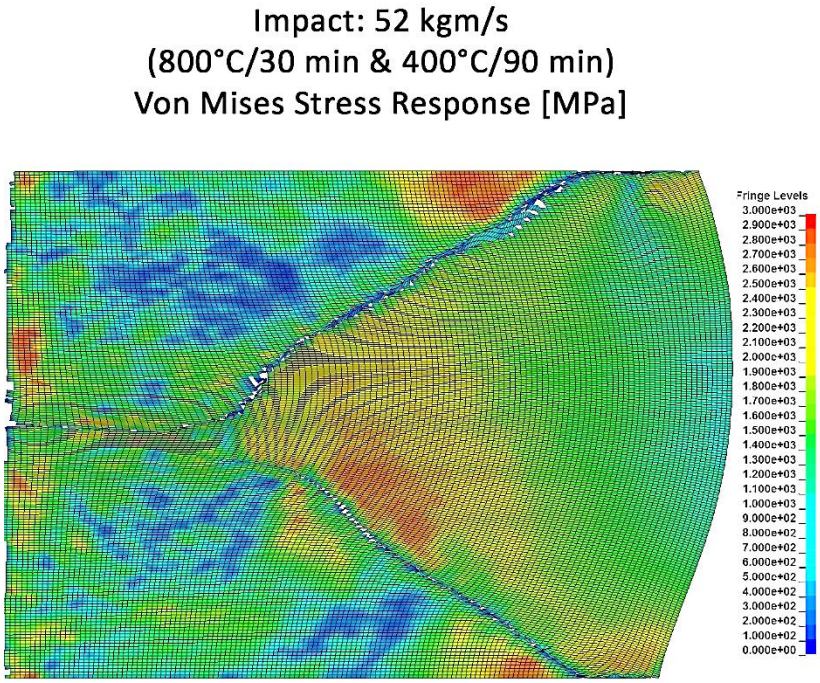

Fig. 102 Effective strain and Von Mises stress distribution of a model of AISI 4340 steel with heat treatment (800°C/30 & 400°C/90) meshed with Lagrangian finite elements and impacted at 52 kgm/s

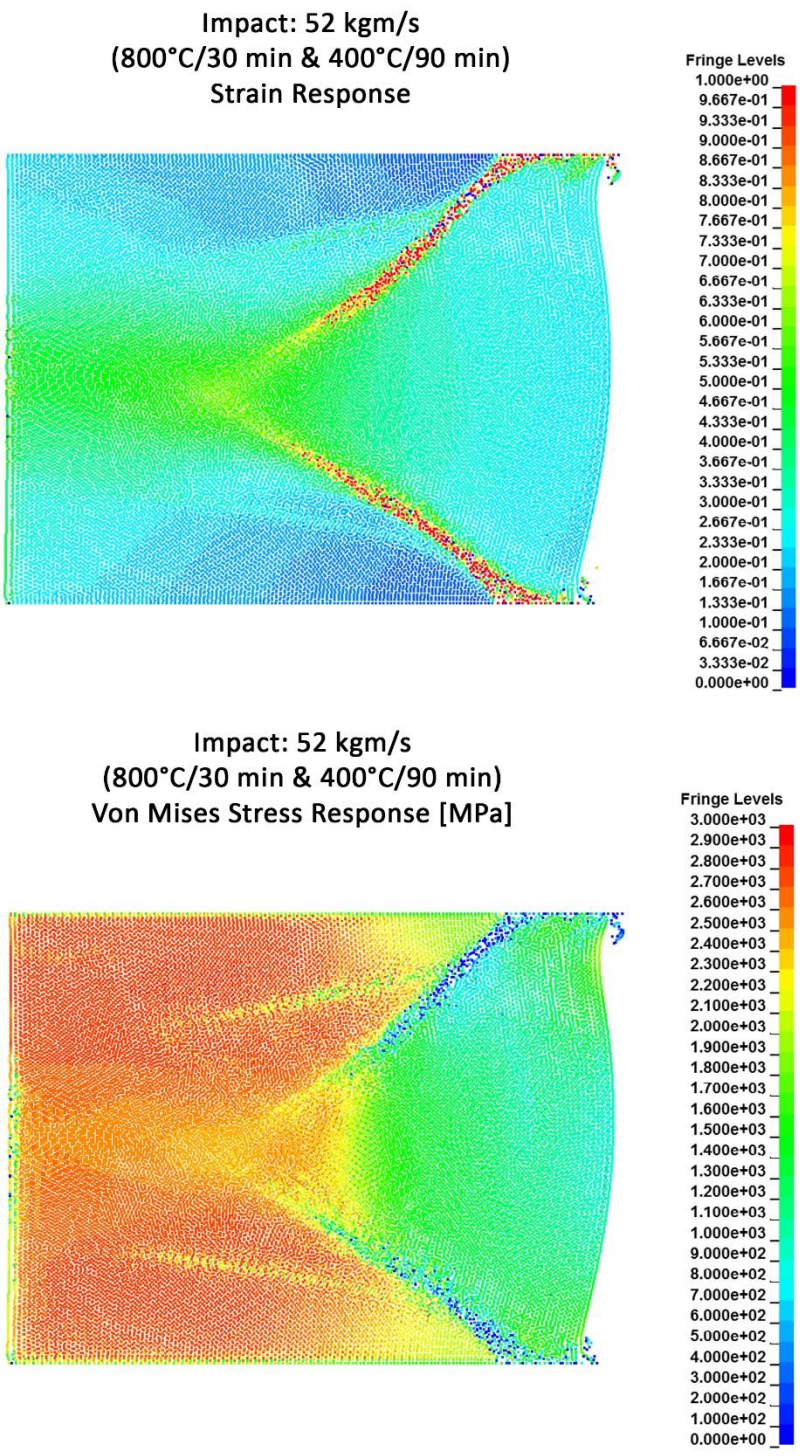

Fig. 103 Effective strain and Von Mises stress distribution of a model of AISI 4340 steel with heat treatment (800°C/30 & 400°C/90) using meshless SPH formulation and impacted at 52 kgm/s

In contrast, the stress and strain profile of a model of steel whose properties are that of the softest heat treatment (1000°C/30 min & 550°C/90 min), impacted at 52 kgm/s and discretized with SPH nodes are shown in Fig. 104.

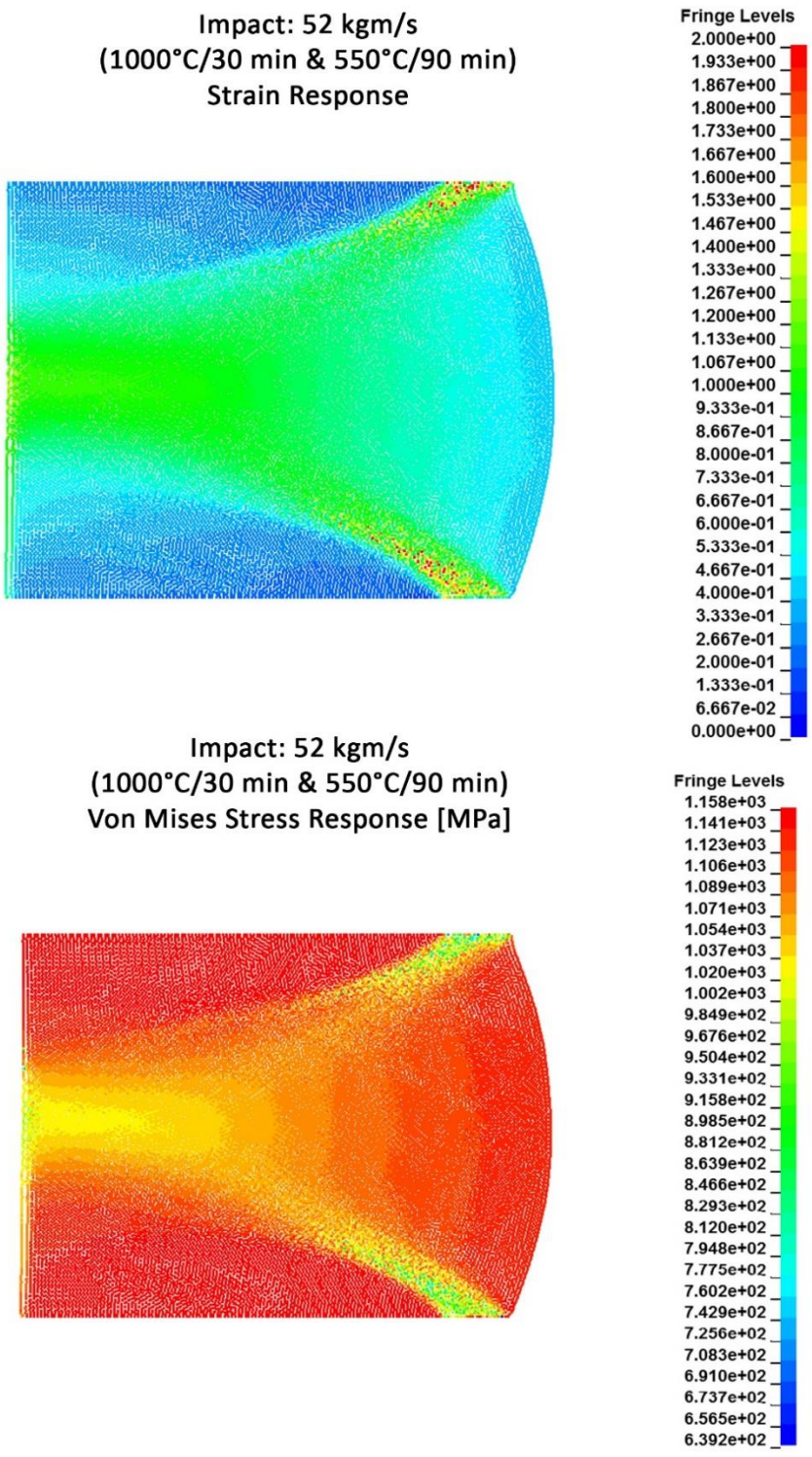

Fig. 104 Effective strain and Von Mises stress distribution of a model of AISI 4340 steel with heat treatment (1000°C/30 & 550°C/90) using SPH formulation and impacted at 52 kgm/s

There is no crack formation as indicated by the lack of a stress collapse in the nodes. However there is still a severe strain localization starting at the far corners of the model and leading partly inwards towards the center along lines of maximum shear. These zones are thicker than those found in the harder heat treatments and may be indicative of the formation of a deformed ASB. Additionally, there is large strain zone leading from the edge of the localization into the center of the model. This is due to a combination of the effective compressive and shear strains similar to the large plastic zone observed through the cross-section of a specimen of the same heat treatment which formed a deformed band, shown in Fig. 40.

The stress-strain responses of the model using the predicted Johnson-Cook parameters under various impact momenta matched closely with experimental results. Fig. 105 and Fig. 106 show a comparison between the modeled stress strain response taken from SPH nodes at the center of the model, and the experimental response for the two heat treatments (800ºC/30 min & 400ºC/90 min) and (1000ºC/30 min & 550ºC/90 min) at an impact momentum of 45 kgm/s. The figures show the stress-strain responses for the full deformation of the specimen. The Johnson-Cook approximation under-predicts the hardening portion of the response for both heat treatments and impact conditions. The stress

collapse in the model of AISI 4340 steel with heat treatment (800ºC/30 min & 400ºC/90 min) resulting from the defined failure criteria is evident around a strain of 0.78. This matches closely to experimental stress collapse around this value of strain.

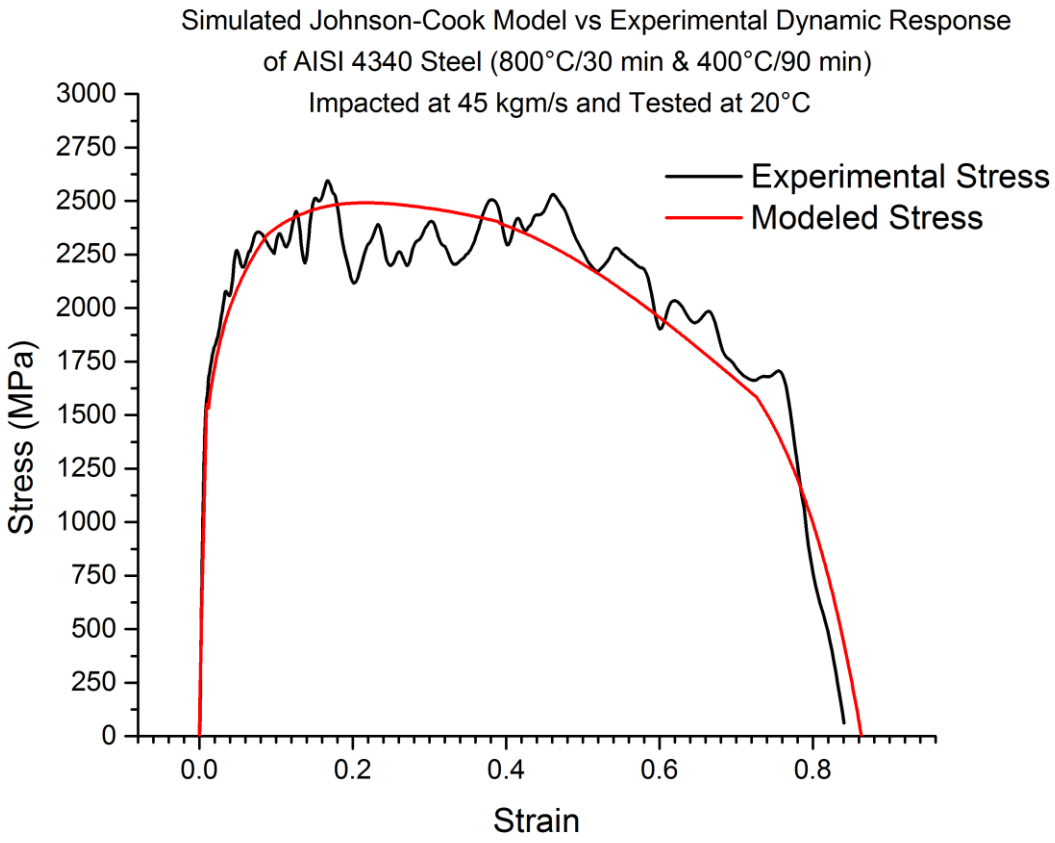

Fig. 105 Comparison between simulated stress-strain response and experimental response of AISI 4340 steel with heat treatment (800ºC/30 min & 400ºC/90 min) impacted at 45 kgm/s and tested at 20ºC

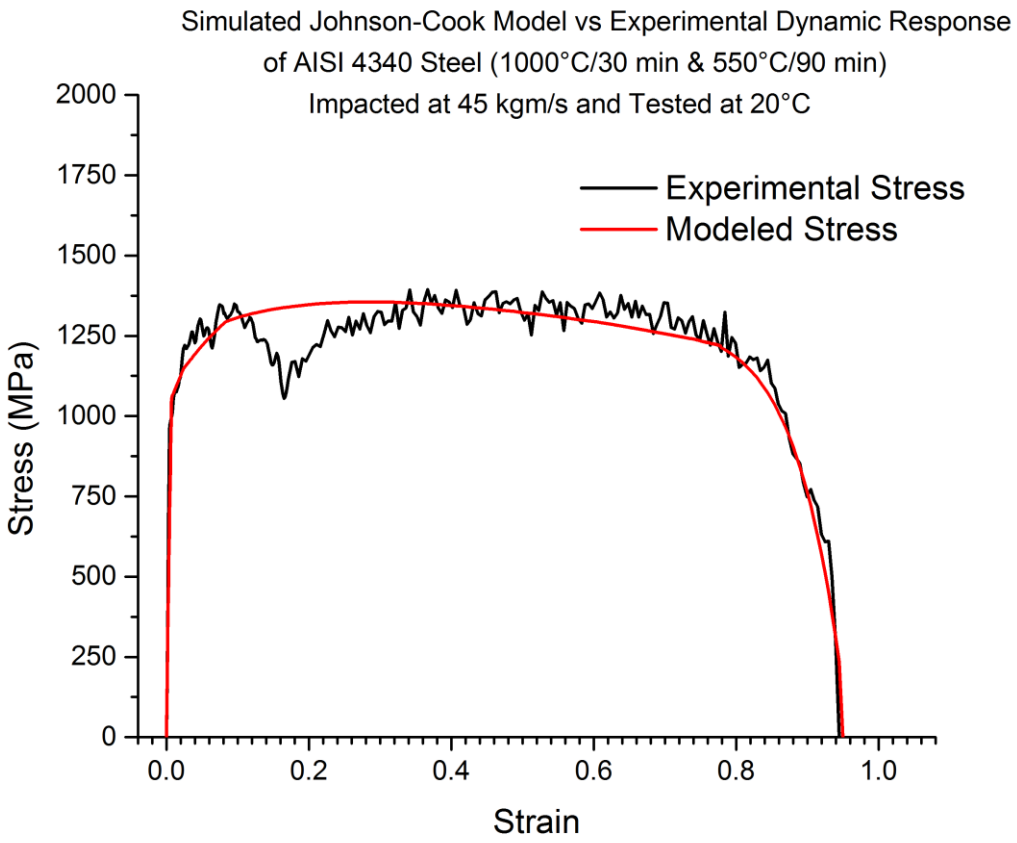

Fig. 106 Comparison between simulated stress-strain response and experimental response of AISI 4340 steel with heat treatment (1000ºC/30 min & 550ºC/90 min) impacted at 45 kgm/s and tested at 20ºC

Similarly for the heat treatment (1000ºC/30 min & 550ºC/90 min), the Johnson-Cook model under-predicts the strain hardening effect but matches closely to the stress collapse around the defined failure strain.

Simulation results based on the predicted Johnson-Cook material parameters and estimated failure criteria match closely with experimental microscopic observation. Deformed type ASBs are identified by a strain localization of SPH nodes along lines of maximum shear while transformed ASBs are identified by a stress collapse in the SPH nodes indicating microcrack formation. Also, deformed type ASBs appear thicker and are surrounded by a large zone of plastic strain while transformed type ASBs are much thinner.

In the next section, the microstructural dependence on the formation of ASBs will be explored by modeling grains and taking into account their size, shape, and orientation, as well as their material property heterogeneity.

4.4 Grain Boundary Modeling

In the experimental investigation, ASB formation was shown to be a microstructural phenomenon which depends on microstructural properties such as grain size, shape, orientation, and distribution of phases and hard particles—all controlled by the heat treatment process. Each grain is unique and its material properties are heterogeneous (based on its size, shape, and the complexity of the microstructure within the grain). Modeling grains requires the use of complex geometry and multiple material constitutive assignments

to ensure accuracy in simulation. However, assumptions must be made to maintain a balance between accuracy and computational cost/time. For the current model a level of microstructural complexity was chosen based on optical microscopic observation in the experimental investigation. ASB formation was shown to be dependent on the size, shape, and orientation of the prior austenite grains and tempered martensite blocks—both of which were incorporated into the model.

The grain model, developed in this thesis, is a 2D axi-symmetric geometrical representation of an area of prior-austenite grains in quenched and tempered AISI 4340 steel which are divided into randomly oriented blocks of tempered lath martensite. The initial size of grains is controlled by the heat treatment.

The grains themselves were modeled using the Johnson-Cook plasticity parameters for each heat treatment. They are separated by a grain boundary, which was found to contain a higher concentration of solute atoms and carbon giving it a higher strength and hardness compared with the surrounding material. Since these properties are difficult to measure directly, they were assigned to have the same properties as the grains but with a 5% increase in hardness. The corresponding yield strength and Johnson-Cook hardening parameters were then estimated based on the relationship between yield strength and hardness in Eq. 3-19.

Due to the relative size of the model (5mm x 10 mm) and the actual size of the grains, the length scale of the model was reduced to measure (50μm x 100 μm) which reflects the maximum magnification under optical microscopy observed in experimentation. Impact velocities and striker mass were also reduced to accommodate this length scale reduction.

The final grain model was developed in three parts:

(1) Generation of an evenly distributed prior austenite grain geometry in a $100\mu m^2$ area using a Voronoi Tessellation algorithm [6, 7] in MATLAB [4], given an initial grain size in μm. This area is equivalent to an optical micrograph at 1000x magnification.

(2) Generation of the grain boundary area and martensite lath block structure in each prior austenite grain using APDL (Ansys Parametric Design Language) code written in ANSYS [170]. A sample of this code can be found in Appendix A.

(3) Meshing and simulation in explicit dynamics FEA software LSDYNA [5] using the meshless Smooth Particle Hydrodynamics (SPH) formulation [8-10, 124], and the Johnson Cook constitutive equations for various heat treatments of AISI 4340 steel. Simulated grain deformation was then compared with experimental observation.

4.4.1 The Voronoi Tessellation

A Voronoi Tessellation [6. 7] resembles the natural geometry of a grain structure that originates from a homogeneous crystallization process. A given area is completely tessellated by grains. Grain shapes are usually non-uniform and exhibit large variability. The shape, orientation, and size of the grains is governed largely by the distribution of "seeds" and the proximity of adjacent "seeds", or site points p_i.

For a set of points p_i in a Euclidian space, the Voronoi tessellation of this set is the subdivision of the plane into *n* cells, one for each site. This is shown in Fig. 107.

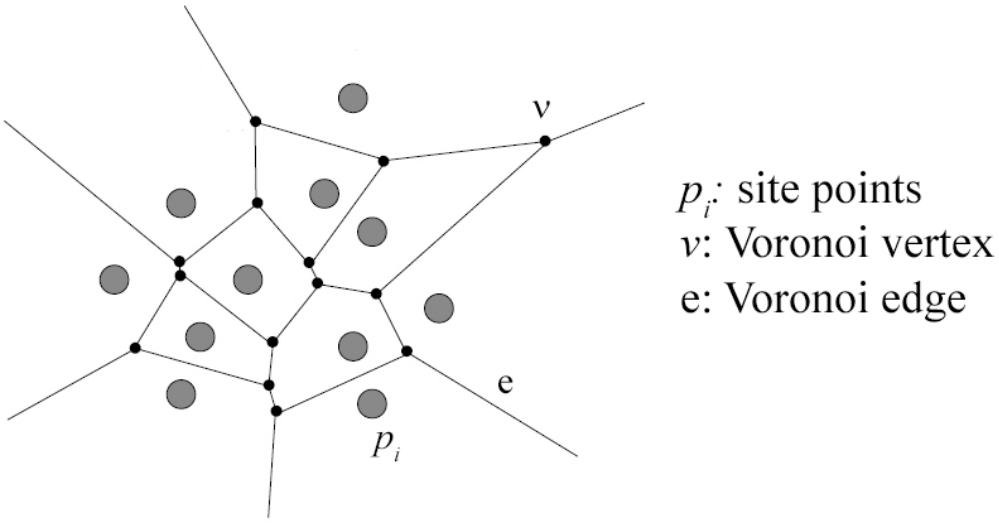

Fig. 107 Voronoi tessellation of a set of points p_i (illustration by this author)

A Voronoi vertex is defined as the center of an *empty* circle touching three or more points, shown in Fig. 108. A vertex has a degree ≥ 3. Four or more non-collinear sites are necessary to create a bounded cell.

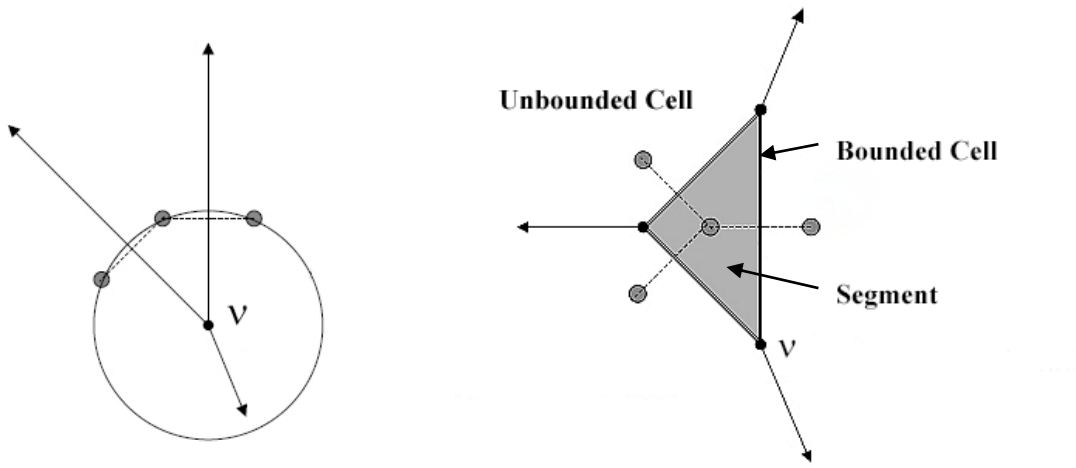

Fig. 108 Voronoi vertex and bounded cell (illustration by this author)

To generate the grain geometries, a function was written in MATLAB of the form [cells_total]=Grains2D(Gsize) that inputs a given grain size (Gsize) (average diameter) in μm and creates a random distribution of points representing the number of grains of that size which fit in a space measuring $100\mu m^2$ termed "cells_total". A $100\mu m^2$ area reflects an optical magnification of approximately 1000x. A Voronoi tessellation of those points is then generated whose average bounded areas corresponds to input grain size. The function also writes the Vornoi vertices and cells to a file which can be read by FEA software to generate geometry. The

MATLAB code for the function Grains2D is shown in Appendix A. Examples of output of grain distributions for various input grain sizes are shown in Fig. 109.

.

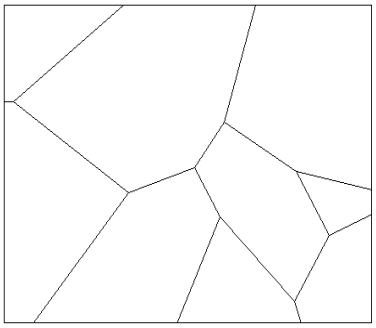

[9]=Grains2D(30)

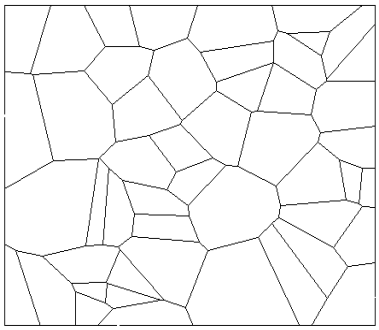

[49]=Grains2D(15)

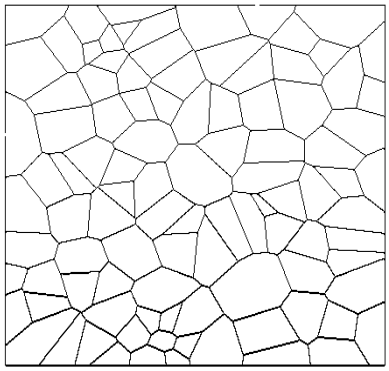

[100]=Grains2D(10)

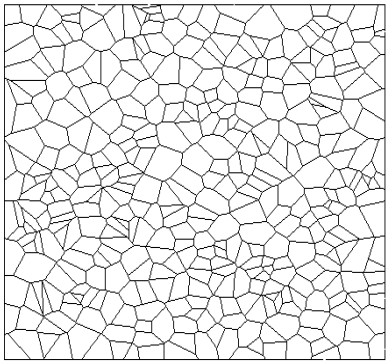

[400]=Grains2D(5)

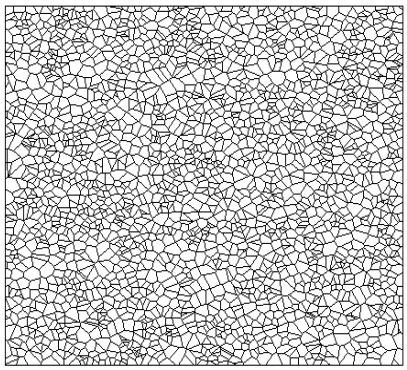

[2500]=Grains2D(2)

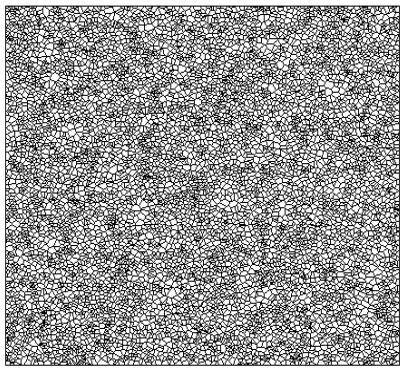

[10000]=Grains2D(1)

Fig. 109 Output of Matlab function Grains2D for various input grain sizes

4.4.2 Subgrain Lath Block Geometry Generation

Optical microscopy of the tested specimens reveals that the prior grains contain several packets and blocks of lath martensite, created by the heat treatment process. The number and orientation of the packets and blocks are random. To reduce computational time it is assumed that each grain contains a single packet of parallel martensite blocks which vary in orientation between grains.

In the experimental investigation, AISI 4340 steel with heat treatment 800°C/30 mins & tempering at 400°C/90 mins was shown to have the most ASB formation for all impact momenta. It also had the highest strength and hardness and the smallest initial prior austenite grain size which measured on average 16 μm in diameter. Fig. 110 shows a randomly generated Voronoi tessellation of grains of size 16 μm in a 100μm^2 area which was modeled into individual grain areas in ANSYS using ANSYS Parametric Design Language (APDL). A sample of this code is shown in Appendix A.

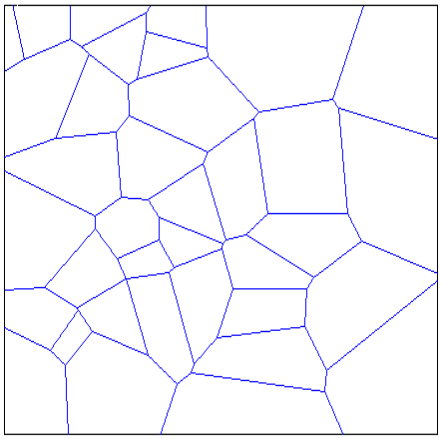

[36]=Grains2D(16)

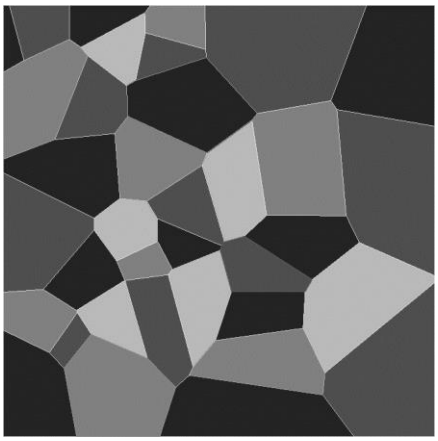

Area generation in ANSYS

Fig. 110 Model of a 100 μm^2 sample of AISI 4340 steel with heat treatment 800°C/30mins & 400°C/90mins and average grain size of 16μm

Microstructural observation of heat treated steel showed that upon quenching, martensite block size ranged approximately between 1-2 μm for austenization at 800°C, shown in Fig. 35. There was no measurable change in block size between the quenched state and 400ºC tempered steel. However, block boundry dislocation annihilation and block growth was observed during tempering at 550°C, resulting in an increase in block size. APDL code was written to generate a martensite block structure of a given size in each grain which varied in orientation between grains. Block sizes were calculated based on an average block size per prior austenite grain observed from experimentation. Additionally, the blocks were assumed parallel and identical in size to reduce computation time. In experimentation the martensite block size varied and were near-parallel, varying minimally in orientation. For the heat

treatment (800°C/30min & 400°C/90min) the martensite blocks modeled to be 1.5 μm in width. A generation of this block structure in the grain model is shown in Fig. 111.

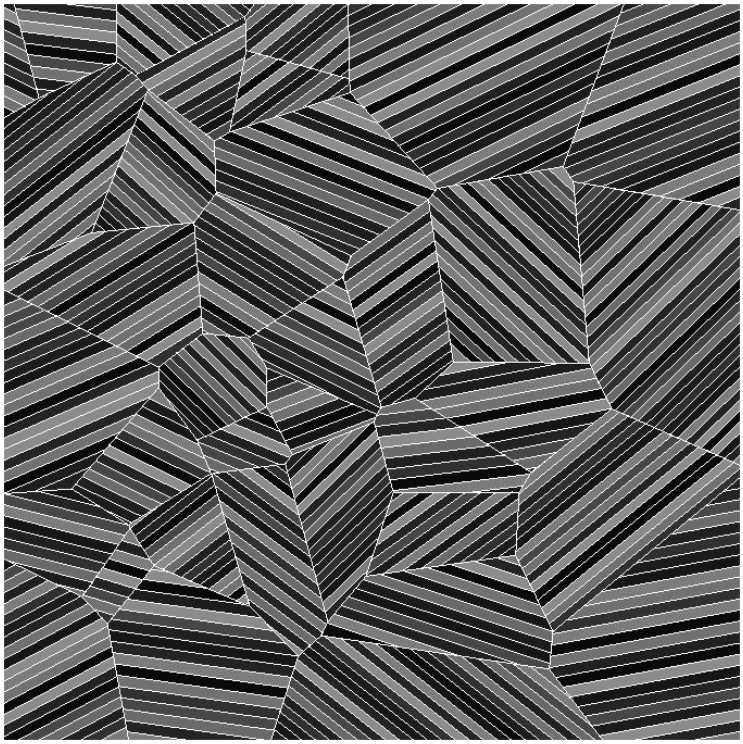

Fig. 111 Simulated microstructure of a specimen with heat treatment 800°C/30min & 400°C/90min with martensite blocks of size 1.5μm generated inside 16μm average sized prior austenite grains in an area of 100μm^2.

In the literature it was discussed how each lath block contains a varied amount of laths with a random amount of carbides and solute particles. As a result the physical properties of each block varies. In FEA analysis, each block can be assigned to have a separate material model whose properties varies slightly from block to block. This imparts a level of heterogeneity in the prior austenite grain and also gives the grain a form of material property

directionality so that the deformation of the grain depends on the shape, size, and orientation of the lath blocks. In the following sections, the effect of lath block geometry and physical properties on the formation of ASBs will be examined.

4.4.3 Grain Boundary Generation

The micro-mechanical properties of steel depend highly on the quantity and distribution of hard particles in the grain in the grain boundaries between prior austenite grains and martensitic lath grains. These grain boundaries typically contain a high concentration of dislocations, hard solute particles and carbides which segregate during heat treatment. Upon quenching there is a considerable amount of carbon atoms which segregate to the prior austenite grain boundaries, hardening them and can measure as thick as 5 nm [140]. At low austenization temperatures (i.e. 800°C) there is an even distribution of hard particles in the prior austenite grain boundaries and in the martensite block boundaries. As austenization temperature increases, the number of hard particles between the laths reduces as soft, tough retained austenite films form between the martensite laths. The lath grain boundaries are several times thinner than the prior austenite grain boundaries and were not modeled explicitly, but rather included in the material modeling of the lath blocks themselves. This reduced computation time by reducing the complexity of the geometry.

The prior austenite grain boundaries were modeled as thin layers separating the prior austenite grains and were assigned a material model which had a higher hardness than the surrounding prior austenite grains. The prior austenite grain boundary was also bonded to the grains so that no sliding was allowed ($f = 1$) and no separation.

In experimentation the grain boundary was not a physically separate entity but rather an zone of low energy separating the grains, to which solute particles and carbon atoms would segregate. The grain boundaries acted in such a way that when prior austenite grains were crushed, new grain boundaries would form between the refined grains. In the simulation model, no new grain boundaries formed between refined grains and the modeled prior austenite grain boundary only acts to define the initial position of the hard particles, to track their movement during deformation, and observe their effect on the formation of ASBs.

In order to obtain meaningful results and to reduce computation time and instabilities from complex geometry, the prior austenite grain boundary layer was assigned to have a thickness of 5% of the average size of the surrounding grain. This allowed for sufficient SPH discretization across the thickness of the grain boundary. The grain boundary layers were generated in APDL. Fig. 112 shows the model setup for a steel with heat treatment 800°C/30min & 400°C/90min. Since the model is axisymmetric, half of the generated grains, shown in Fig. 111, were used. The geometry measures 50 μm x 100 μm—a reduction

in scale of 1000 from original dimensions of the specimen. The time scale of deformation was reduced in order to achieve meaningful results.

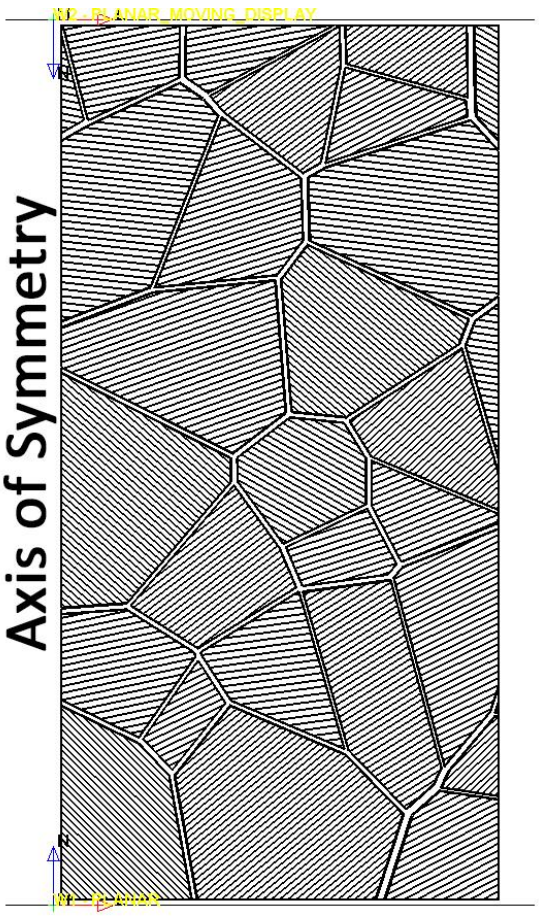

Fig. 112 Lath grain model with prior austenite grain boundary for a steel with heat treatment 800°C/30min & 400°C/90min and average initial grain size of 16µm and lath size of 1.5 µm

4.4.4 Impact Simulations of the Lath Grain Model

Experimental observation and analysis showed that at the microscopic scale, the properties of the lath blocks are not homogenous and the grain boundaries tend to be harder

than the parent prior austenite grain due to the presence of hard particles which segregates during heat treatment. To simulate a level of heterogeneity in the microstructure, while keeping the overall properties of the steel relatively the same, the prior austenite grain boundaries were assigned material properties which were 5% harder than the Johnson-Cook parameters for that heat treatment. Additionally, every lath block was assigned material properties which alternated between being 2.5% harder and 2.5% softer than the Johnson-Cook parameters for that heat treatment so that no two adjacent blocks shared the same properties.

The yield strength was determined from the relationship in Eq. 3-19, and the corresponding Johnson-Cook parameters, B n, and C were calculated using Table 24, and the relationships established in Fig. 96 and Fig. 97. The failure strain was assumed constant. These hardness properties were chosen as a preliminary assumption to test the effect of heterogeneity on the deformation and localization without affecting the overall properties of the material to a large degree. The actual degree of material heterogeneity was not measurable due to the limited resolution of the micro-hardness machine. A summary of the newly calculated material properties are shown in Table 26.

Table 26 Johnson-Cook parameters for heterogeneous Lath Grain Model based on AISI 4340 steel with heat treatment (800°C/30min & 400°C/90min)

Modification to Hardness	**Original**	**-2.5%**	**+2.5%**	**+5%**
Austenization Temperature	**800°C**	**800°C**	**800°C**	**800°C**
Tempering Temperature	**400°C**	**400°C**	**400°C**	**400°C**
HV [kgf/mm^2]	478	466	490	502
A [MPa]	1366.4	1324.3	1393.73	1424.8
B [MPa]	867.37	840.07	884.14	903.85
n	0.1529	0.1532	0.1413	0.1296
C	0.02581	0.02543	0.02623	0.02698
ε_f	0.78	0.78	0.78	0.78

To test the stability of the model, two simulations were performed. The first simulation involved changing the properties of the prior austenite grain boundary to be 5% harder than the parent prior austenite grain while keeping the grains themselves homogenous. The second simulation introduces a level of heterogeneity in the lath blocks by varying the hardness of the properties by $\pm$ 2.5% as summarized in Table 26. Both models are subject to an impact of 52 kgm/s.

In the first simulation, the model was discretized using 30220 SPH nodes. The resulting deformation after 1 μs is shown in Fig. 113. Full deformation after 2 μs resulted in the complete crushing of the model after which the projectile wall separated from the impact face indicating the end of deformation.

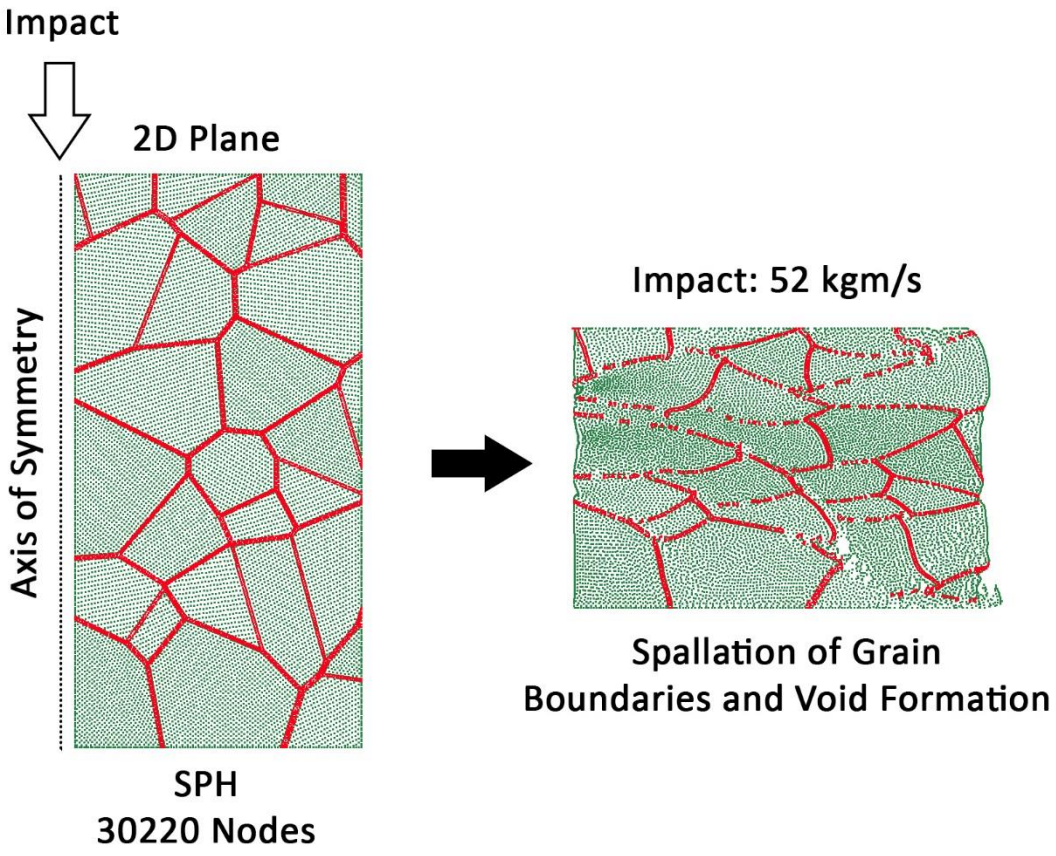

Fig. 113 Deformation of the bi-material lath grain model after 50μs at 52 kgm/s using the Johnson-Cook parameters for steel with heat treatment (800°C/30min & 400°C/90min)

The experimental investigation showed that the width of an ASB, which formed in the steel, was several times larger than the grains themselves. A complete crushing of the model under the given initial conditions indicates that the grain model is small enough to be contained within an ASB and the crushed grains can represent the final grain size inside that ASB. However a very fine SPH discretization is needed to calculate final grain size accurately, which is represented by the smallest cluster of SPH nodes after deformation.

Therefore, the simulated deformation process of the grain model gives a good indication of the source of ASB formation and its direction of propagation through the microstructure, which continues to grow under applied severe shear stresses, eventually consuming the grains.

After 0.6 μs of impact, the deformed model shows an elongation of the grains in the direction of maximum shear through the cross section. This is due to a combination of both compressive and shear forces. Additionally the harder grain boundary spalls and breaks up, pulling apart the surrounding softer grains and creating voids. Examining the progressive stress and strain responses, in Fig. 114, shows the propagation of a localization through the cross section which forms more favorably along the edges of the grain boundaries and is followed closely by the formation of microcracks (indicated by stress collapse) and void formation. The localization shears the bond between the hard grain boundary and soft surrounding grains. The overall direction of localization is along lines of maximum shear but is shown to also branch out along the grain boundaries as deformation progresses. Examining the stress and strain response during deformation, in Fig. 115, shows the extent of the branching effect of localization more clearly.

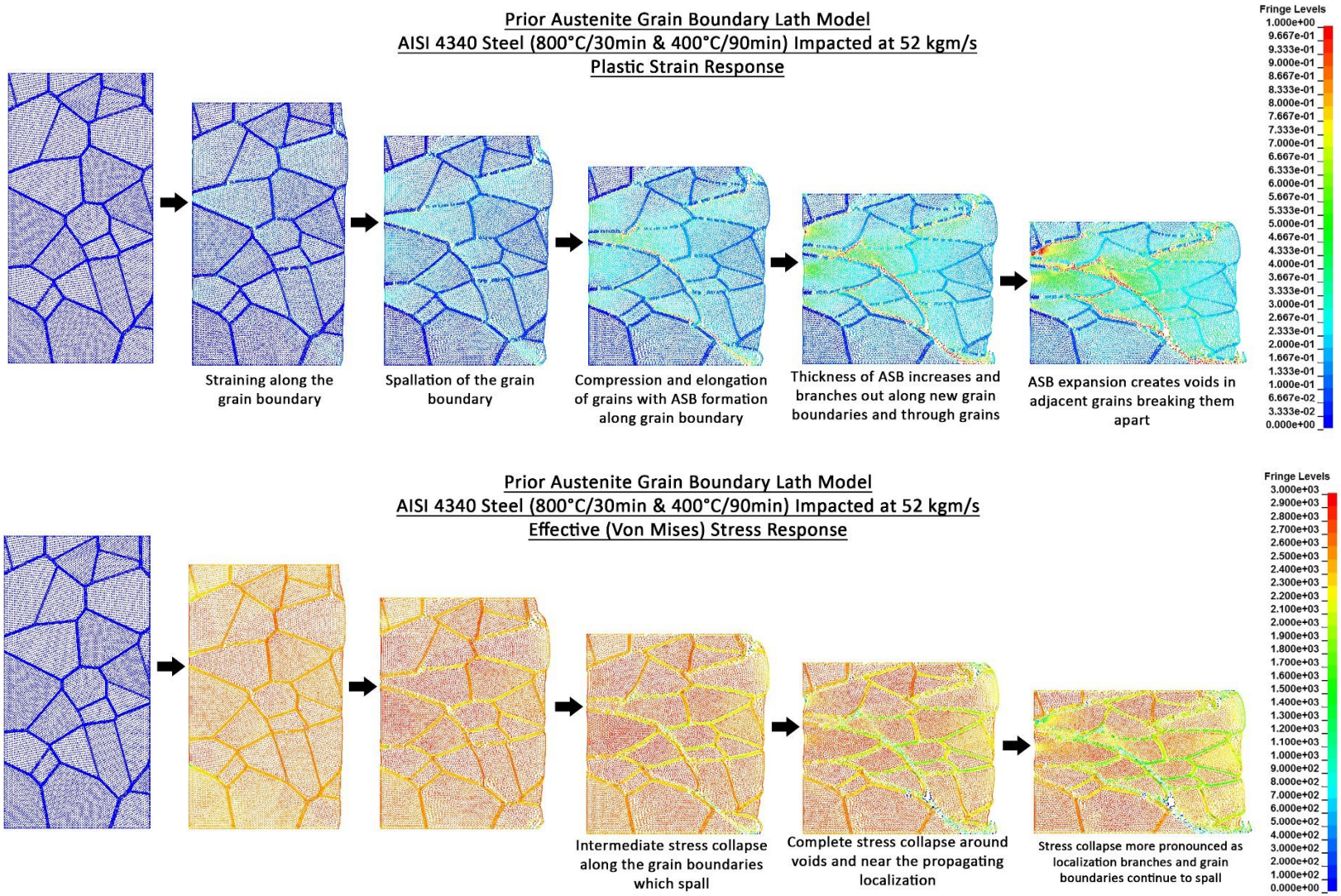

Fig. 114 Plastic strain and effective (Von Mises) stress deformation in a grain model of steel with heat treatment (800°C/30min & 400°C/90min)

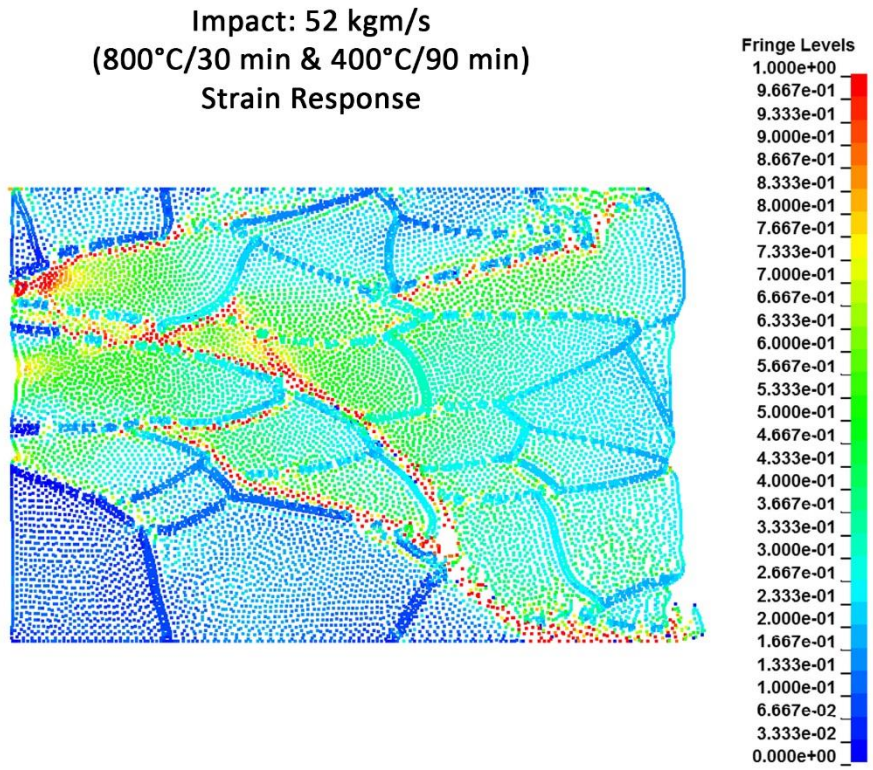

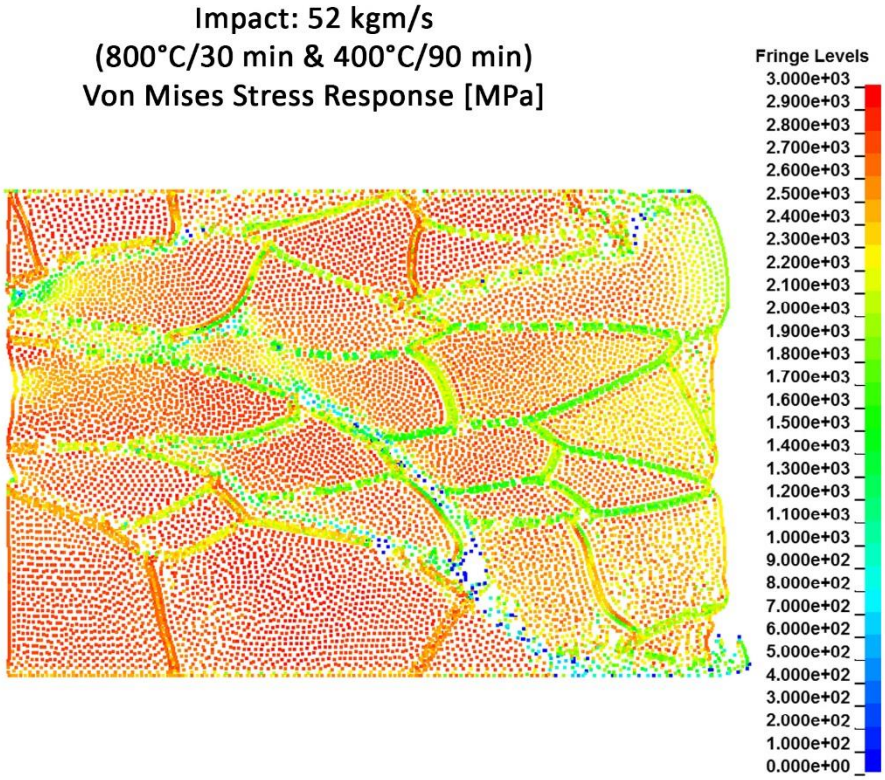

Fig. 115 Von Mises stress and plastic strain response in a model of AISI 4340 steel with heat treatment (800°C/30min & 400°C/90min) impacted at 52 kgm/s

The second simulation introduces a heterogeneity in material properties of the lath blocks. This gives the grains' properties directionality in that their deformation behavior not only depends on their size and shape but also the orientation of the lath blocks contained within. This increased geometrical and material complexity as well as the overall cost of simulation. The small size and high aspect ratio of the lath blocks required a certain degree of SPH discretization across the width of each block to give meaningful results. Consequently, the size of the model had to be reduced due to limited memory capacity of the computer. The final size of the model was reduced to 25% the original size and is shown in Fig. 116. The deformation time step was further reduced to accommodate the reduced model size.

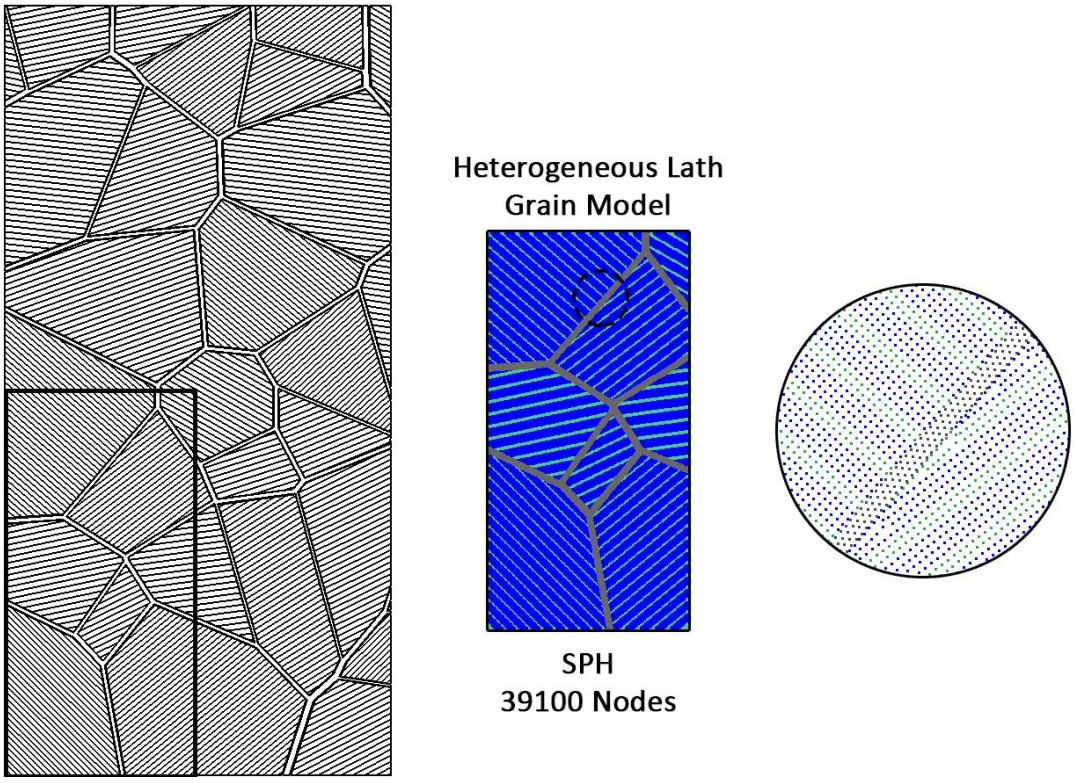

Fig. 116 Setup of heterogeneous lath grain model discretized with 39100 SPH nodes

The model was impacted at 52 kgm/s for a total deformation time of 0.5μs. The resulting deformation after 0.25μs, shown in Fig. 117, reveals a reorientation of the lath blocks towards the localization followed by a spallation of the grain boundary and void formation along lines of maximum shear.

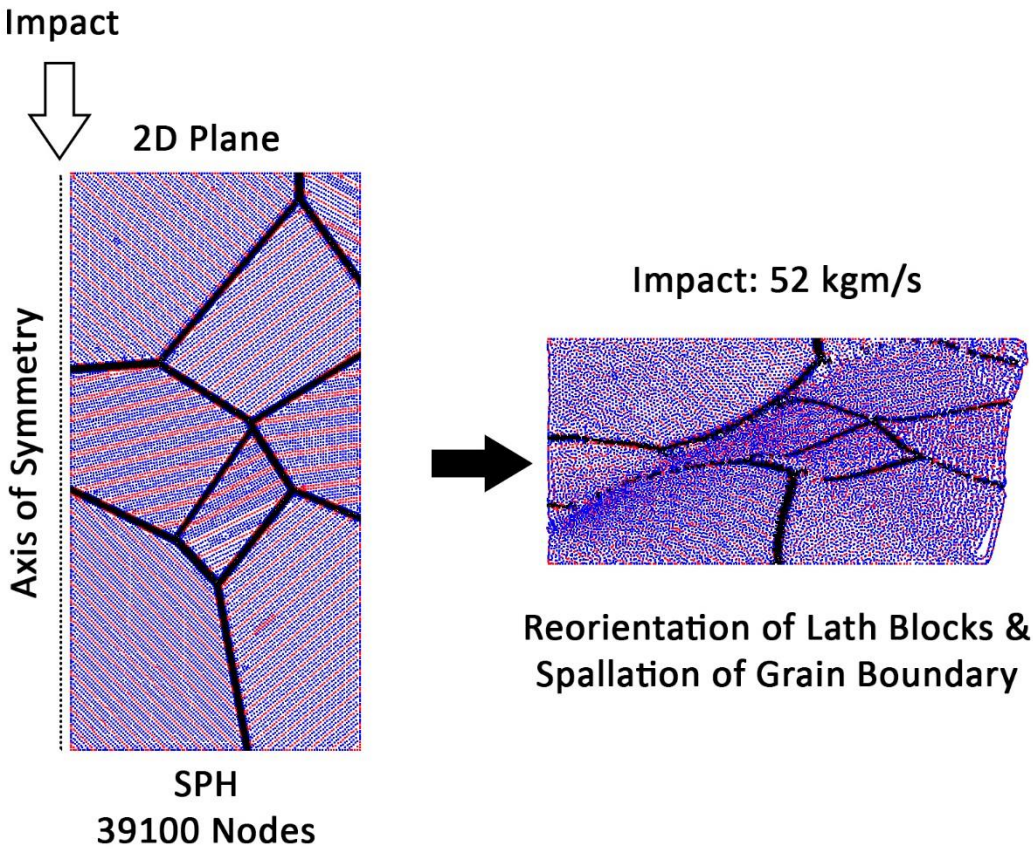

Fig. 117 Deformation of the lath grain model after 0.25 μs of deformation at an impact momentum of 52 kgm/s showing reorientation of the lath blocks and spallation of the grain boundary

A progression in the strain and stress response, in Fig. 118, shows ASB localization form predominantly close to the prior austenite grain boundary which lies closest to the lines of maximum shear. This localization forms most readily by shearing the bonds between the hard grain boundary and the softer grain. When a grain boundary is not present near the maximum shear direction, localization will occur through the grain but to a lesser extent.

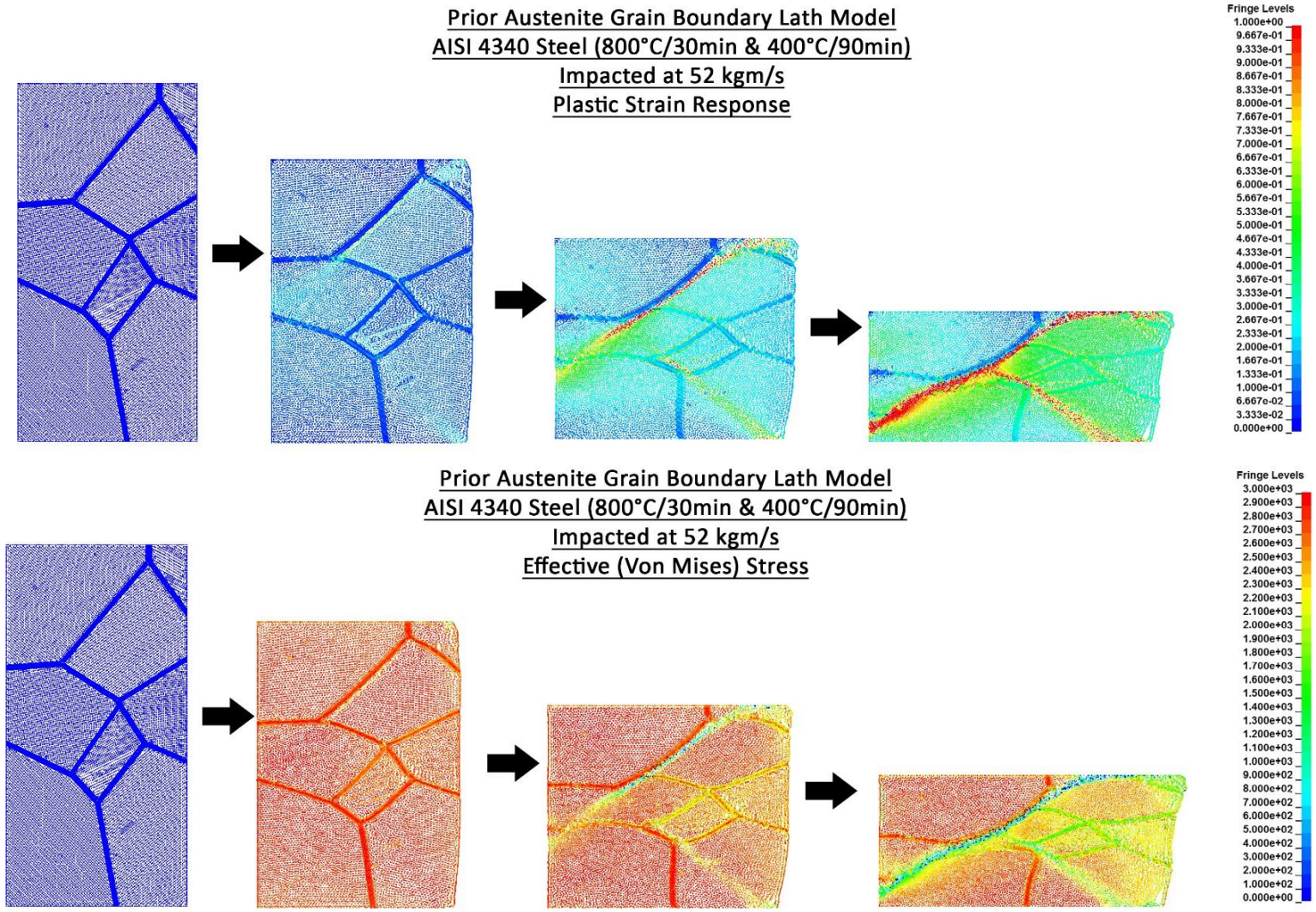

Fig. 118 Progressive effective plastic strain and effective Von Mises stress response of heterogeneous lath grain model of AISI 4340 steel with heat treatment (800°C/30 min & 400°C/90 min) impacted at 52 kgm/s

Based on this simulation, it can be said that strain localization initiates at high concentrations of hard particles—i.e. at the grain boundaries, and propagates outwards in the shear direction. Multiple initiation sites are possible during deformation. This is shown in Fig. 119 of a close-up of the progressive effective strain response of this model impacted at 52 kgm/s.

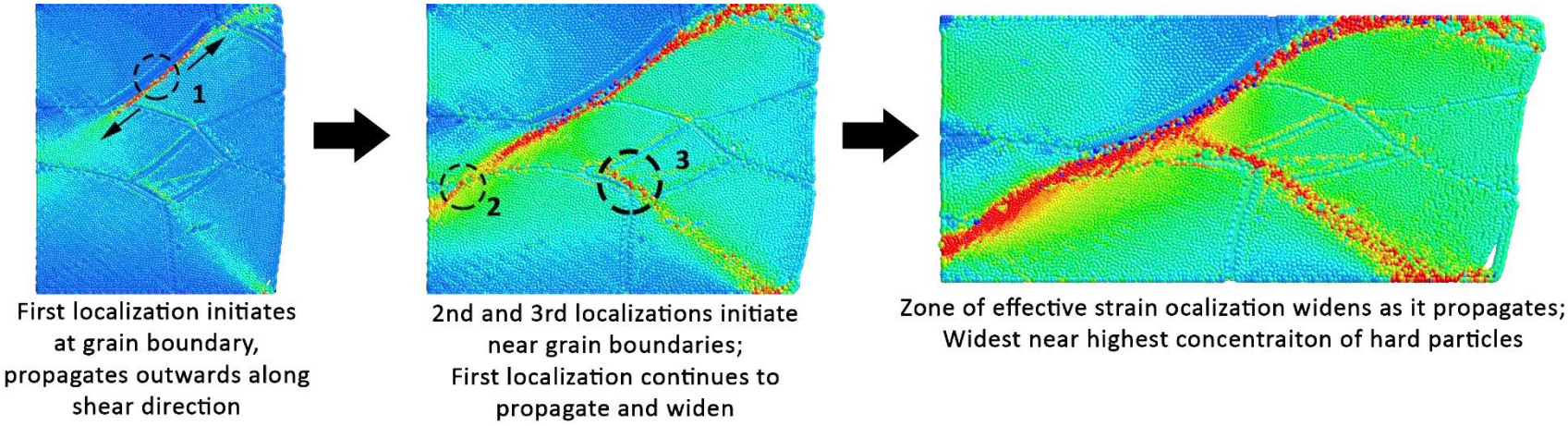

Fig. 119 Progression of ASB formation shown in the effective strain response of the grain model

A close-up of the effective stress and strain distribution after 0.25μs of deformation, shown in Fig. 120, shows the extent of the localization. Micro cracks represented by failed SPH nodes with zero stress capacity are more prominent along the sheared section between the prior austenite grain boundary and the surrounding grain. This may be an indication of the formation of a transformed ASB while the localization which propagates through the grains, shown to be wider but less severe, by the lack of failed SPH nodes, may be indicative of a deformed type ASB.

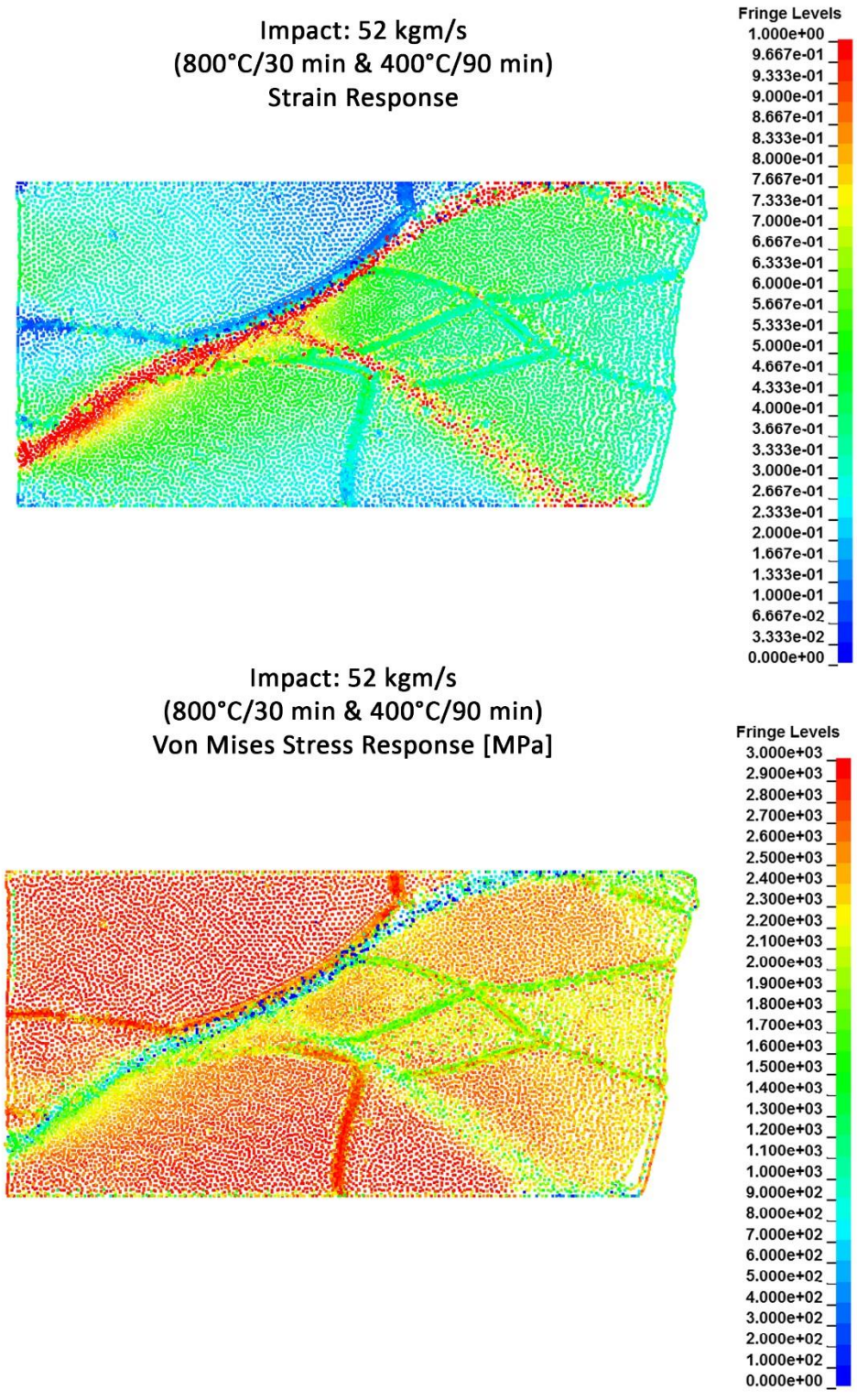

Fig. 120 Effective plastic strain and effective Von Mises stress distribution through lath grain model of AISI 4340 steel with heat treatment (800°C/30 min & 400°C/90 min) impacted at 52 kgm/s after 0.25μs of deformation

4.5 Determination of the Mechanism of ASB Formation Based on Simulation

Based on simulation results of the grain model it was shown that strain localization initiated at high concentrations of hard material in the maximum shear direction. This can include solutes, precipitates, carbides, or second phase particles which exist in the grains or grain boundaries. Additionally, multiple initiation sites can form at any time during deformation. An illustration of this concept is shown in Fig. 121 on the simulation grain model shown in the previous section.

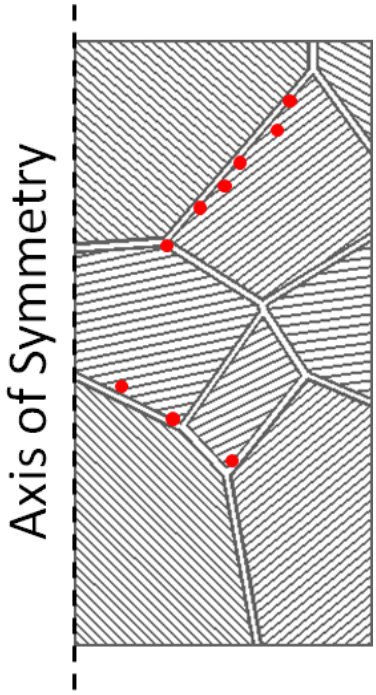

Fig. 121 Illustration of multiple ASB initiation sites indicated by red dots along the shear direction in areas of high concentration of hard particles—i.e. grain boundaries

During deformation the ASBs propagate outward from their initiation points in the direction of shear, as shown in Fig. 122. Two or more propagating ASBs which meet, coalesce to form a larger ASB.

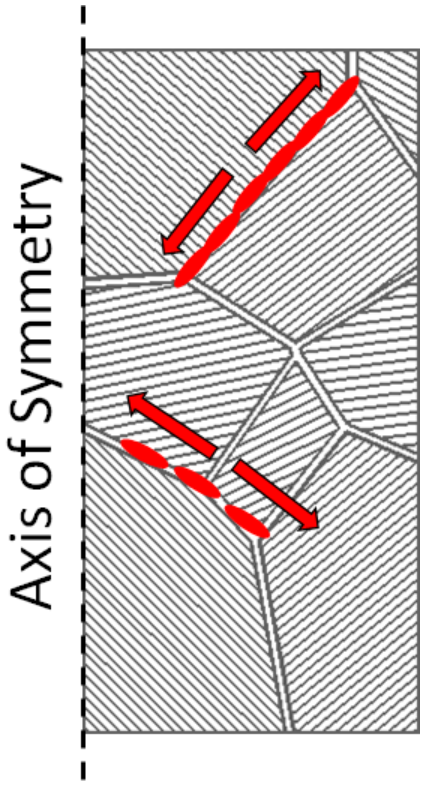

Fig. 122 Illustration of ASBs propagating outward from their initiation sites along the lines of maximum shear. ASBs coalesce to form a larger ASB

Under compressive loads the internally increasing shear forces increase and the ASBs coalesce and widen, as shown in Fig. 123. The zone inside the final ASB is characterized by a severely distorted structure with a higher density of nodes. The grains surrounding the ASB rotate and elongate in the direction of shear.

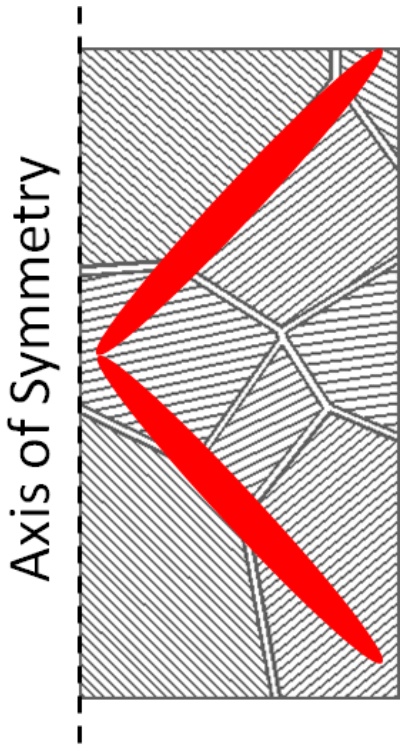

Fig. 123 Illustration of ASB widening from increasing shear forces

In the experimental investigation, the size and width of the ASBs were much larger than the size of the grains. The concept illustrated here can be extended to simulate with a smaller initial grain size and a higher number of SPH nodes. It is expected that ASBs would form under the proposed mechanism.

4.6 Theoretical Investigation Conclusions

The simulation models developed in this chapter are a good representation of the kinematics of deformation and the mechanism of ASB formation on both the macroscopic and microscopic scale. The predicted Johnson-Cook parameters for each heat treatment of AISI 4340 steel were shown to match closely the stress-strain response in the experimental investigation and analysis of the deformed models reflected the observed deformation of the specimens.

Simulation results using the multi-material Lath Grain Model have shown that ASBs formation is controlled by the size, shape, and orientation of the grains as well as the material property heterogeneity of the modeled microstructure. In this model, deformed ASBs were characterized by a thick localized zone of severe strain found to nucleate from the impact face and propagate through the grains while transformed ASBs were characterized by a thinner more prominent zone of severe localization propagating along the prior austenite grain boundary. This zone contained failed SPH elements indicative of the formation of micro-cracks. The final refined grain size upon complete compression of the lath grain model can be determined by the smallest cluster of SPH particles, which have not failed, after deformation.

5. SUMMARY AND CONCLUSIONS

High-strength low-alloy (HSLA) steels are commonly used in structures, such as military vehicles and armor plates, designed to resist high impact loads. However, HSLA steels are predisposed to forming adiabatic shear bands (ASBs), zones of severe shear localization, which form under deformation at high- strain rates and large strains and are a precursor to shear failure in metals.

To date, the formation mechanism of ASBs in metals has been primarily studied through experimentation; a process that is both labour intensive and expensive. As the experimental data continue to provide a rich depository of information, researchers have begun to assemble sophisticated simulation programs that will enhance the understanding of the formation of ASBs and provide stakeholders with the tools for analyzing the behaviour of metals under a wide range of testing conditions, *without the high cost of experimentation*.

The main objective of the present research project was to develop a simulation model that could be used to simulate the formation of ASBs in steel and to describe the microstructural mechanism of their formation based on grain size, shape, orientation, and the inhomogeneous distribution of material properties on the microstructural scale. To

accomplish this objective, a number of steps were taken. These included: (a) an extensive review of the related literature; (b) the undertaking of a thorough experimental investigation in order to map out the microstructural evolution, such as grain size, shape, and orientation and formation of ASBs at various heat treatments and testing conditions—information critical in the development of the simulation model; and (c) the development of a simulation model which can be used to simulate the microstructural mechanism of ASB formation and the evolution of the microstructure of steel under various heat treatments and testing conditions.

Based on both the experimental and the theoretical components of the research program, a number of conclusions were drawn and are summarized below.

5.1 Summary of Results from the Experimental Program

It has been reported in the literature that the grain size of steel changes with heat treatment temperature. A proper simulation of the impact behavior of such a material, therefore, requires a good understanding of the microstructure of the material before and after impact. The experimental program was designed to determine the effect heat treatment on the grain size of the steel investigated, as well as the conditions that lead to the formation

of ASBs. Experimental results were used to determine the optimal heat treatment process for reducing ASB formation and to develop the simulation model. The key findings are summarized below.

1) Grain Size

a) Effect of **austenization temperature** on grain size:

- Prior austenite grain size increased by an average of 7μm per 100ºC increase in austenization temperature.
- Martensitic block length increased proportionally to prior austenite grain size extending to the prior austenite grain boundary.

b) Effect of **tempering temperature** on grain size:

- Prior austenite grain size did not change with tempering temperature
- Martensitic block size increased with increasing tempering temperature from 400ºC to 550ºC by the mechanism of grain boundary dislocation annihilation when tempered above a temperature of 428ºC for longer than 1 hour.

c) Effect of **impact momentum** on grain size

- Prior austenite and martensitic block grain sizes away from the location of ASBs did not change with impact momentum.
- Under deformation, grains reoriented themselves and elongated in the direction of maximum shear.
- ASBs formed more readily at higher impact momenta.
    - Deformed ASBs are characterized by the reorientation and severe elongation of grains in the direction of maximum shear.
    - Transformed ASBs are characterized by the reorientation, elongation, and sudden refinement of grains inside the band.

d) Effect of **testing temperature** on grain size

- Prior austenite and martensitic block grain sizes did not change with testing temperature.

2) Mechanical Properties of Steel

a) Effect of **austenization temperature** on Young's modulus and yield strength

- Young's modulus increased with increasing austenization temperature by an average of 1% per 100ºC, however changes were within error.
- Yield strength decreases with increasing austenization temperature by an average of 10% per 100ºC.

b) Effect of **tempering temperature** on Young's modulus and yield strength

- Young's modulus increased with increasing tempering temperature by an average of 2% from 400ºC to 550ºC, however changes were within error.
- Yield strength decreased with increasing tempering temperature by an average of 20% from 400ºC to 550ºC.

c) Effect of **impact momentum** on Young's modulus and yield strength

- There was no change in Young's modulus with impact momentum.
- Yield strength increased exponentially with impact momentum.

d) Effect of **testing temperature** on Young's modulus and yield strength

- Young's modulus decreased with increasing testing temperature by an average of 15% from 20ºC to 428ºC.
- Yield strength decreased with increasing testing temperature by an average of 40% from 20ºC to 428ºC.

e) Hardness was shown to increase exponentially with yield strength.

f) Hardness increased when approaching the location of ASBs and was higher inside transformed ASBs than inside deformed ASBs:

- Hardness increased by 4% at the edge of deformed ASBs and 25% inside.
- Hardness increased by 10% at the edge of transformed ASBs, and 40% inside. This is attributed to the refined grain structure and increase in grain.

The results from the experimental component of the current research project showed that it is possible to simulate the kinematics of the microstructural mechanism for ASB formation using a simulation model based on grain size and the variation in the material properties of the microstructure. Microstructural observations and experimental stress-strain and hardness measurements were used to validate the simulated results. The conclusions from the theoretical investigation are summarized below.

5.2 Summary of Results from the Theoretical Program

The experimental investigation showed that the formation of ASBs in steel can be described, on the microscopic level, through the behavior of grains as they deform under severe shear stresses. The theoretical investigation focused on the development of a simulation model that could simulate grain deformation behavior and ASB formation in AISI 4340 steel at a microscopic level using existing continuum mechanics FEA methods and constitutive equations. The model developed considers the complex geometry of the grains and grain boundary structures as well as the material inhomogeneity in the microstructure.

Modeling grains requires the use of complex geometry and multiple material constitutive assignments. For the currently developed simulation model, a level of microstructural complexity was chosen based on optical microscopic observation in the experimental investigation. ASB formation was shown to be dependent on the size, shape and orientation of the prior austenite grains and tempered martensite blocks—both of which were incorporated into the model. The model uses the Voronoi tessellation to generate prior austenite grains, and generates geometry for the martensite sub-grain lath blocks and a grain boundary geometry in a 2D axi-symmetric area representative of the cross section of the specimens. The model was discretized using the meshless Smooth Particle Hydrodynamics

(SPH) method. The Johnson-Cook plasticity model and failure parameters were calculated for all the tested heat treatments and simulated against experimental results at various impact momenta. Simulated stress-strain responses matched closely with experimental responses.

Due to computational limitations, and the need for a balance between accuracy of simulation and computational costs, only the prior austenite grains, the sub-grain martensitic blocks and the prior austenite grain boundary were modeled. The grains themselves were modeled using the Johnson-Cook plasticity parameters for each heat treatment. They were separated by a grain boundary, which was found in the experimental investigation to contain a higher concentration of solute atoms and carbon, thereby giving it a higher strength and hardness compared to the surrounding material. Since these properties were difficult to measure directly, they were assigned to have the same properties as the grains but with a 5% increase in hardness. The corresponding yield strength and Johnson-Cook hardening parameters were estimated based on the relationship between yield strength and hardness.

The main results from the theoretical investigation are summarized below.

- The simulation models developed are a good representation of the kinematics of deformation and the mechanism of ASB formation on both the macroscopic and microscopic scale.

- The Voronoi Tessellation technique provides a fast and effective method for generating randomly oriented grain geometries, of a controlled size, in a given space.
- The predicted Johnson-Cook parameters for each heat treatment of AISI 4340 steel were shown to match closely to the stress-strain response in the experimental investigation and analysis of the deformed models reflected the observed deformation of the specimens.
- Simulation results using the multi-material Lath Grain Model showed that ASBs formation is controlled by the size, shape, and orientation of the grains as well as the material property heterogeneity of the modeled microstructure.
- Simulated grains were shown to rotate and elongate in the direction of shear
- In the simulation model, deformed ASBs were characterized by a thick localized zone of severe strain found to nucleate from the impact face and propagate through the grains while transformed ASBs were characterized by a thinner more prominent zone of severe localization propagating along the prior austenite grain boundary. The zone of severe localization contained failed SPH elements indicative of the formation of micro-cracks.

- The final simulated grain size, upon complete compression of the lath grain model, can be determined by the smallest cluster of SPH particles, which have not failed after deformation.

5.3 Uniqueness of the Current Research Program and Contribution to Knowledge

Adiabatic shear bands in metals are known to form under deformation at very high strain rates and at large strains and are a precursor to shear failure. Considerable effort has been expended to improve the strength and reliability of metals and alloys for applications ranging from aerospace and military, to medicine and commercial use and to reduce or eliminate the formation of ASBs. The formation of ASBs in metals has been extensively studied by researchers, mostly through experimentation, and a complete review of the related literature is provided in Chapter 2.

Based on experimental observations, researchers in this area have developed various models to simulate the formation of ASBs in metals. Many of these models have been based on the mechanics of deformation, using homogenous material models with no regard to the

actual composition of the material. These studies are also limited in that they cannot properly simulate strain localization due to the meshing technique used. They can only predict ASB formation under a limited set of variables by implementing material defects from which ASBs can form or define their formation by the nucleation and propagation of a crack. The removal of failed elements in the models results in an unrealistic relaxation of the surrounding material and gives a poor indication of the stress and strain distribution through the material.

The inability to properly simulate localization is due to the use of grid-based meshing techniques which have been shown to fail when the mesh becomes extremely distorted. Reducing element size by refinement can reduce the distortion. However, the time step, which is controlled by the smallest element size, can approach zero eventually breaking down the computation. Adaptive re-meshing techniques which dynamically re-mesh the model can be implemented to avoid this problem but at the expense of high computational costs.

To avoid this problem, researchers have begun using mesh-free methods which provide an accurate and stable numerical solution for non-continuum problems. A popular mesh-free method is the Smoothed Particle Hydrodynamics (SPH) method. In the present research

project, the SPH method was used to more accurately simulate large localized distortion and ASB formation.

More recently, researchers have begun to develop models to describe the experimentally observed mechanism of grain growth and dynamic recrystallization and grain refinement for metals. These models, however, are simple mathematical models that describe these processes schematically and account for only a limited number of variables.

In the current experimental investigation, ASB formation was shown to be a microstructural phenomenon which depends on microstructural properties such as grain size, shape, orientation, and distribution of phases and hard particles—all controlled by the heat treatment process. Each grain is unique and its material properties are heterogeneous (based on its size, shape, and the complexity of the microstructure within the grain). Modeling grains requires the use of complex geometry and multiple material constitutive assignments to ensure accuracy in simulation.

The Grain Model, developed by this author, provides a superior representation of the kinematics of ASB formation on the microstructural level, based on grain size, shape and orientation. It is able to simulate the microstructural mechanism of ASB formation and grain refinement in AISI 4340 steel, more accurately and realistically, for a wide range of heat treatment and testing conditions. The simulation results obtained using this model showed

that it can also be used for a complete mapping of the behavior of all high-strength low alloy steels with a similar composition to that of AISI 4340 steel and it can be also be used to design a steel that leads to the reduction of ASBs while maintaining good mechanical properties. This is an important contribution to the field of materials engineering.

The simulation model developed in the current study, and verified through comparison with extensive experimental data is an effective tool for simulating the microstructural mechanism of ASB formation and the evolution of the microstructure of steel under various heat treatments and testing conditions. An additional strength of the model is its utility in the examination of a wide array of parameters for metals subject to impact loading—without the high cost associated with multiple experimentations of a series of testing parameters.

Beneficiaries of this research include Civil and Military Defense Departments involved in Research and Development in security science and technology, material scientists who examine the microstructural behaviour of materials under impact conditions, and mechanical, structural, and aerospace engineers whose area of interest include simulation of structures under high strain rate deformation.

5.4 Recommendations for Future Work

Provided that there is sufficient computation capability to handle a large number of elements, the theoretical model developed in the current research program can easily be expanded to accommodate much smaller grain sizes over a larger area to simulate ASB on a larger scale, as shown in Fig. 124 of a grain model tessellated with 10000 grains in an area measuring $1mm^2$. Additionally, a more evenly distributed grain size can be modeled containing multiple packets per prior austenite grain and variably-sized near-parallel martensite blocks to increase the level of heterogeneity.

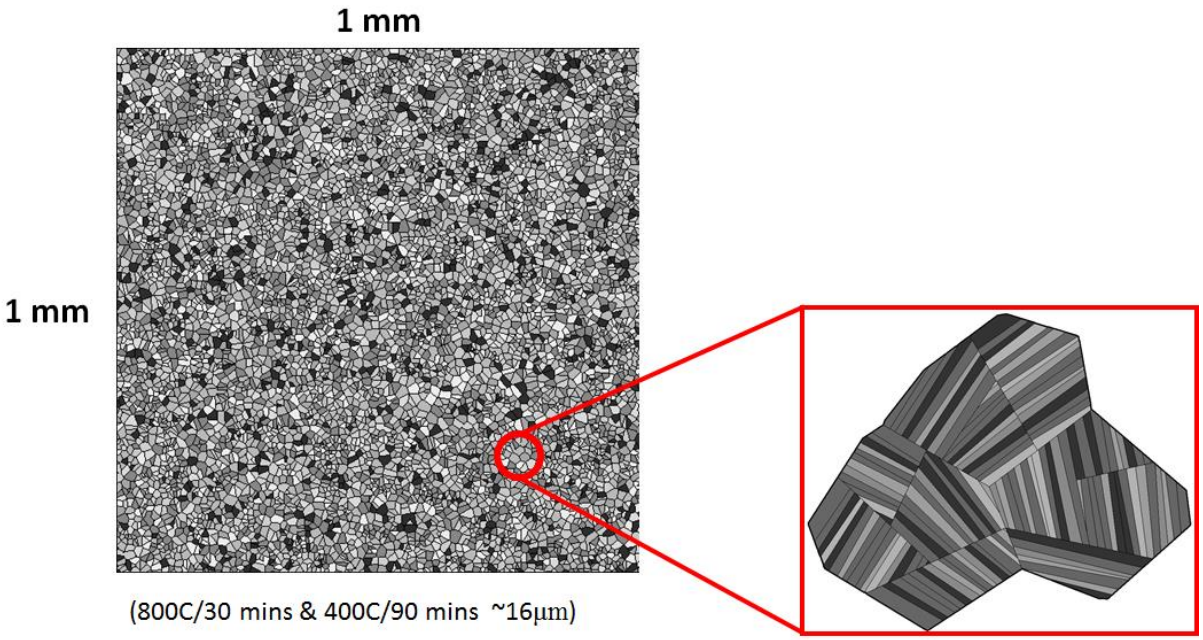

Fig. 124 Voronoi Tesselation of 10000 grains in a 2D area (illustration by this author)

The model can also be expanded to include 3D simulations, using the 3D Voronoi tessellation to generate grains for various geometries, providing a more realistic characterization of material behavior, as shown in Fig. 125 for rectangular and cylindrical geometries. The code used for generating the 3D Voronoi tessellated grains is shown in Appendix B.

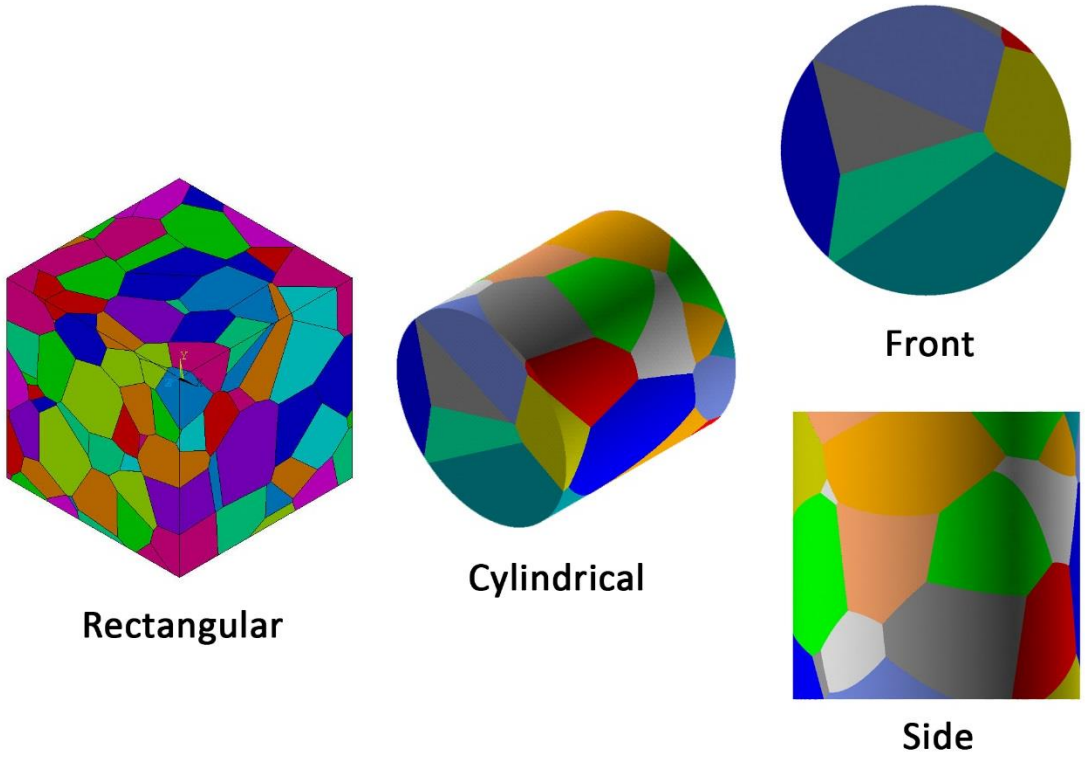

Fig. 125 3D Voronoi tessellated grain geometries (illustrations by this author)

While the current study focused on a specific steel alloy, AISI 4340 steel, the theoretical model can be used to simulate the behaviour of other materials as well, provided the mechanical properties of those material are known.

Further examination of the microstructure by the use of transmission electron microscopy, can improve the complexity of the simulation model by including more microstructural features.

High strain rate torsional experimentation using a Torsional Hopkinson Pressure Bar can improve the shear property definitions of the steel to implement an improved failure criteria that considers strain rate and cumulative damage.

Finally, nano-hardness testing of the grains and grain boundaries would improve material property definitions of individual microstructural features and increase the accuracy of the grain simulation model results.

APPENDIX A

SAMPLE CODE FOR 2D GRAIN TESSELATION IN MATLAB, GENERATION OF LATH GRAIN STRUCTURE IN ANSYS APDL, IMPLEMENTATION OF MODEL IN LS-DYNA AND COMPUTER HARDWARE SPECIFICATIONS

Reduced Input LS-DYNA Keyword File (No elemental/nodal data)

```
$# LS-DYNA Keyword file created by LS-PrePost 4.1 (Beta) -
29Sep2013(13:00)
$# Created on Mar-25-2014 (11:29:13)
*KEYWORD
*CONTROL_CONTACT
$#  slsfac    rwpnal    islchk    shlthk    penopt    thkchg
orien    enmass
  0.100000     0.000         2         2         0         0
1         2
$#  usrstr    usrfrc     nsbcs    interm     xpene     ssthk
ecdt   tiedprj
         0         0        10         1  4.000000         0
0         0
$#   sfric     dfric       edc       vfc        th     th_sf
pen_sf
  0.160000  0.160000     0.000     0.000     0.000     0.000
0.000
$#  ignore    frceng   skiprwg    outseg   spotstp   spotdel
spothin
         0         0         0         0         0         0
0.000
$#    isym    nserod    rwgaps    rwgdth     rwksf      icov
swradf    ithoff
         0         0         0     0.000  1.000000         0
0.000         0
$#  shledg    pstiff    ithcnt    tdcnof     ftall    unused
shltrw
         1         0         0         0         0
0.000
*CONTROL_CPU
$#  cputim
     0.000
*CONTROL_ENERGY
$#    hgen      rwen    slnten     rylen
         1         2         1         1
*CONTROL_HOURGLASS
$#     ihq        qh
         1  0.100000
*CONTROL_BULK_VISCOSITY
$#      q1        q2      type     btype
  1.500000 6.0000E-2         1         0
*CONTROL_RIGID
$#     lmf      jntf    orthmd     partm    sparse    metalf
plotel     rbsms
         0         0         0         0         0         0
0         0
*CONTROL_SOLUTION
$#    soln       nlq     isnan     lcint
         0         0         0       100
*CONTROL_SPH
$#    ncbs     boxid        dt      idim    memory      form
start      maxv
```

```
         5         0     0.000        -2      1000         1
0.000     0.000
$#    cont     deriv       ini     ishow     ierod     icont
iavis
         0         0         0         0         1         1
0
*CONTROL_CONTACT
$#  slsfac    rwpnal    islchk    shlthk    penopt    thkchg
orien    enmass
  0.100000     0.000         2         2         0         0
1         2
$#  usrstr    usrfrc     nsbcs    interm     xpene     ssthk
ecdt   tiedprj
         0         0        10         1  4.000000         0
0         0
$#   sfric     dfric       edc       vfc        th     th_sf
pen_sf
  0.160000  0.160000     0.000     0.000     0.000     0.000
0.000
$#  ignore    frceng   skiprwg    outseg   spotstp   spotdel
spothin
         0         0         0         0         0         0
0.000
$#    isym    nserod    rwgaps    rwgdth     rwksf      icov
swradf    ithoff
         0         0         0     0.000  1.000000         0
0.000         0
$#  shledg    pstiff    ithcnt    tdcnof     ftall    unused
shltrw
         1         0         0         0         0
0.000
*CONTROL_TIMESTEP
$#  dtinit    tssfac      isdo    tslimt     dt2ms      lctm
erode     ms1st
     0.000  0.500000         0     0.000     0.000         0
1         0
$#  dt2msf   dt2mslc     imscl    unused    unused     rmscl
     0.000         0         0                       0.000
*CONTROL_TERMINATION
$#  endtim    endcyc     dtmin    endeng    endmas
  0.500000         0  0.900000     0.000     0.000
*DATABASE_ELOUT
$#      dt    binary      lcur     ioopt   option1   option2
option3   option4
 1.0000E-2         1         0         1         0         0
0         0
*DATABASE_GLSTAT
$#      dt    binary      lcur     ioopt
 1.0000E-2         1         0         1
*DATABASE_MATSUM
$#      dt    binary      lcur     ioopt
 1.0000E-2         1         0         1
*DATABASE_SPHOUT
$#      dt    binary      lcur     ioopt
```

```
 1.0000E-2         1         0         1
*DATABASE_BINARY_D3PLOT
$#      dt      lcdt      beam     npltc    psetid
 1.0000E-2         0         0         0         0
$#   ioopt
         0
*ELEMENT_SPH
*NODE
*PART
$# title
SphNode
$#     pid     secid       mid     eosid      hgid      grav
adpopt      tmid
         2         1         1         1         0         0
0         0
*SECTION_SPH_TITLE
SPH
$#   secid      cslh      hmin      hmax    sphini     death
start
         1  1.200000     0.000     0.000     0.000     0.000
0.000
*MAT_JOHNSON_COOK_TITLE
AISI 4340 Steel (800C/30min & 400C/90min)
$#     mid        ro         g         e        pr       dtf
vp    rateop
         1 7.8500E-3 75370.000 1.9450E+5  0.290000     0.000
0.000     0.000
$#       a         b         n         c         m        tm
tr      epso
 1366.4000 867.37000  0.152900 2.5810E-2  1.030000 1793.0000
293.00000  1.000000
$#      cp        pc     spall        it        d1        d2
d3        d4
 465.00000     0.000  2.000000     0.000     0.000     0.000
0.000     0.000
$#      d5      c2/p      erod     efmin
     0.000     0.000         0 1.0000E-6
*EOS_LINEAR_POLYNOMIAL_TITLE
EOS-LP
$#   eosid        c0        c1        c2        c3        c4
c5        c6
         1     0.000 1.9450E+5     0.000     0.000     0.000
0.000     0.000
$#      e0        v0
     0.000     0.000
*RIGIDWALL_PLANAR_MOVING_DISPLAY
$#    nsid    nsidex     boxid    offset     birth     death
rwksf
         0         0         0     0.000     0.0001.0000E+20
1.000000
$#      xt        yt        zt        xh        yh        zh
fric      wvel
     0.000 10.100000     0.000     0.000 10.000000     0.000
0.160000     0.000
```

```
$#     mass         v0
 1781.0000 29.200001
*END
```

```
%-------------------------------------------------------------------------------------------------------
% Grain Model using Voronoi Tessellation in MATLAB
% by Ian Polyzois (C)
% March 2012
%-------------------------------------------------------------------------------------------------------


function [cells_total]=Grains2D(Gsize)

% Defines the number of grains, G, within a 0.0001 m^2 area
% where Gsize is the average size of the grains in micro meters

G=round(100/Gsize)^2;

% From a uniform distribution, create a 1xGsize matrix filled with
% random numbers, and choose from round(rand(1)*100) different combinations

[a,b] = gallery('uniformdata',[1 G],round(rand(1)*100));

%Determine Voronoi tessellation of x and y from 'grains' function
%which modifies built in 'voronoi' function to hide the appearance of the site
%points by changing their color to white

grains(a,b);

[v,c] = voronoin([a(:) b(:)]); % find Voronoi vertices and cells

vert=[];
cell_count=[];

for i=1:length(c),            %increment rows

   d=c{i};

   for j=1:length(d),         %increment columns


   % a{j}=n
   % go to row n in v --> v(a{j},1), get value x,y
   % x=v(a{j},1)
   % y=v(a{j},2)
   % vert=[x,y]=[v(a{j},1),v(a{j},2)]

   vert=[vert; v(d(j),1),v(d(j),2)];
   cell_count=[cell_count; i];
```

```
   end

end


for k=1:length(vert),
   vert_count=[vert_count; k];
end

% write the vertices coordinates and cell numbers to XLS for import by
% FEM software
% Note: Must convert ‘xlsx’ to ‘CSV’ format to be read by ANSYS

xlswrite('2D_Cell_Data.xlsx',vert_count,'2D_Cell_Data','A1');
xlswrite('2D_Cell_Data.xlsx',vert,'2D_Cell_Data','B1');
xlswrite('2D_Cell_Count.xlsx', cell_count, '2D_Cell_Count', 'A1');

cells_total=cell_count(size(cell_count,1),1);
end
```

```
!*************************************************************************
! ANSYS 13.0 APDL Code
! Prior Austenite Grain Model
!
! -Prior Austenite Grain Geometry Generation, March 2012
! -Grain Boundary Geometry Generation, November 2013
! -Lath Block Geometry Generation, January 2014
!
! by Ian Polyzois (C)
!
! This model reads the Voronoi vertices and cell numbers
! from MATLAB output code Grains2D and generates prior austenite
! grain geometry, subgrain lath blocks, and a grain boundary
! It outputs the geometry into an IGES file
!*************************************************************************

!-------------------------------------------------------------------------------------------------------
!PART 1: PRIOR AUSTENITE GRAIN GEOMETRY GENERATION
!-------------------------------------------------------------------------------------------------------

/PREP7
/UIS, MSGPOP, 4

! Speed up input reading by turning off graphics and output
!-------------------------------------------------------------------------------------------------------
/NOPR
IMMED,0
/SHOW,OFF

! Read nodal data from file
!-------------------------------------------------------------------------------------------------------
NRRANG,1,99999999,1,
NREAD,'2D_CELL_DATA','csv',' '


! Remove labels
/PNUM,KP,0
/PNUM,LINE,0
/PNUM,AREA,0
/PNUM,VOLU,0
/PNUM,NODE,0
/PNUM,TABN,0
/PNUM,SVAL,0
/NUMBER,-1
!*
/PNUM,ELEM,0
```

```
/REPLOT
!*

! Count the number of nodes
!-----------------------------------------------------------------------------------------------------------
NSEL,ALL
*GET,NCOUNT,NODE,,COUNT
ALLSEL,ALL

! Create arrays for the Voronoi cell numbers and line numbers
!-----------------------------------------------------------------------------------------------------------
*DIM,CELLCOUNT,ARRAY,NCOUNT,1,0, , ,
*DIM,LINEINFO,ARRAY,NCOUNT,2,0, , ,

! Read grain number into cellcount array
!-----------------------------------------------------------------------------------------------------------
*CREATE,ansuitmp
*VREAD,CELLCOUNT,'2D_CELL_COUNT','csv',' ',IJK,NCOUNT,1,0, ,
(1F8.0)
*END
/INPUT,ansuitmp

CELL_CHECK=1
LINE_MIN=1
ALLSEL,ALL,ALL
KP_START=1          !Counter for #kp in cells


*DO,N,1,NCOUNT
        NSEL,S,,,N              ! Select next node
        KNODE,N,N               ! create keypoint at node
        ALLSEL,ALL,ALL

        *IF,CELL_CHECK,EQ,CELLCOUNT(N,1),THEN
                L,N-1,N         ! create lines bounding each cell
        *ELSE
                *GET,KP_COUNTER,KP,,COUNT
                L,KP_COUNTER-1,KP_START      !ensures cells are properly closed
                KP_START=KP_COUNTER
                *GET,LCOUNT,LINE,,COUNT
                CELL_CHECK=CELL_CHECK+1

        *ENDIF

*ENDDO
```

```
LPLOT

!Cleanup of erroneous lines (i.e. lines which extend outside a box measuring 1x1,
!and lines which cross over other grains)
!-----------------------------------------------------------------------------------------------------------
*GET,LCOUNT2,LINE,,COUNT

LDELE,LCOUNT+1,LCOUNT2,1    !Removal of duplicated lines
ALLSEL
*DO,X,1,LCOUNT              !Removal of lines which exceed half the length of the box
        LSEL,S,,,X
        LSUM
        *GET,LLENGTH,LINE,,LENG
        *IF,LLENGTH,GT,0.5,THEN
                LDELE,X
        *ENDIF
        ALLSEL
*ENDDO

LPLOT

RECTNG,0,1,0,1       !Create box
BTOL,1E-6
ASBL,ALL,ALL,,DELETE,DELETE      ! Divide box by lines to create grain areas


! Reactivate graphics
!-----------------------------------------------------------------------------------------------------------
/GOPR
IMMED,1
/SHOW,TERM

APLOT
SAVE

! NOTE: some cells may be missing borders. Manual cleanup may be required.

!-----------------------------------------------------------------------------------------------------------
! PART 2A: GRAIN BOUNDARY GAP CREATION
!-----------------------------------------------------------------------------------------------------------
! Separate all grains by a gap whose thickness is proportional to the
! areas of each grain
!-----------------------------------------------------------------------------------------------------------

!Compress all ID# to ensure proper sequencing of areas, lines, and keypoints
NUMCMP,ALL
```

```
/triad,off        ! turn off global CS label
/psymb,cs,0     ! turn off local CS labels

/NOPR
IMMED,0
/SHOW,OFF

! Cycle through all areas and calculate the centroids
! then duplicate areas and shrink around centroid to create grain boundary gap
! grain sizes are reduced relative to their area so that the grain boundary
! maintains an relatively equal thickness throughout

NUMSTR,KP,100000          ! begin KP numbering at 100k
NUMSTR,AREA,100000     ! begin Area numbering at 100k
NUMSTR,LINE,100000       ! begin line numbering at 100k


ALLSEL
*GET,AACOUNT,AREA,,COUNT              ! count total # areas
*DIM,AREAS,ARRAY,AACOUNT,1,0,     ! create array to store areas of grains
*DIM,RATIO,ARRAY,AACOUNT,1,0,     ! create array to store area ratios
AAVG=1/AACOUNT
EXTRA_GAP=2                                ! apply an extra thickness to the GB
                                                  ! (in micro m)

! SHRINK
*DO,X,1,AACOUNT,1
        ASEL,S,,,X
        ASUM
        *GET,AR,AREA,,AREA              ! get area of grain
        AREAS(X,1)=AR                     ! store area of grain in array AREAS
        RATIO(X,1)=AAVG/AR
        *GET,ACENT_X,AREA,,CENT,X                  ! get x-coord of centroid
        *GET,ACENT_Y,AREA,,CENT,Y                  ! get y-coord of centroid
        LOCAL,99+X,CART,ACENT_X,ACENT_Y        ! create local CS at centroid

        ! scale down proportional to grain size + additional "Extra_Gap"

        ARSCALE,X,,,(100-(EXTRA_GAP+RATIO(X,1)))/100,(100-
        (EXTRA_GAP+RATIO(X,1)))/100,1,,1,0    ! scale down grain to leave gap
        !ARSCALE,X,,,0.99,0.99,1,,1,0              ! alternative for scaling by a constant
        ADELE,X
        ALLSEL
*ENDDO
aplot
```

```
!COMPRESS ALL ID#
NUMCMP,ALL

RECTNG,0,1,0,1       ! Align edges
AINP,ALL             ! Pairwise boolean intersect areas

/GOPR                !Reactivate graphics
IMMED,1
/SHOW,TERM


ALLSEL
APLOT
SAVE

!-----------------------------------------------------------------------------------------------------------
! Part 3: LATH BLOCK GEOMETRY GENERATION
!-----------------------------------------------------------------------------------------------------------
! This section creates the parallel lath block geometry within each grain
!-----------------------------------------------------------------------------------------------------------

/PREP7

*GET,ACOUNT,AREA,,COUNT
ASUM,DEFAULT

!Remove warning & error messages
/UIS, MSGPOP, 4

BTOL,1E-7
BOPTN,KEEP,NO     !Boolean options


!Ensures random function "rand" is different everytime code is executed
!-----------------------------------------------------------------------------------------------------------
*GET,DIM,ACTIVE,0,TIME,WALL
DIM=DIM*3600
*DIM,DUMMY,ARRAY,DIM
*VFILL,DUMMY(1),RAND
*DEL,DIM
*DEL,DUMMY
!-----------------------------------------------------------------------------------------------------------

*DIM,CHOICE_COUNT,ARRAY,ACOUNT,1
EXTRA_INC=0.05     ! Dictates the thickness between parallel lines (0.01=1 micro m)
M=0                ! The kp ID# increment
```

```
! Speed up input reading by turning off graphics and output
!-----------------------------------------------------------------------------------------------------------
/NOPR
IMMED,0
/SHOW,OFF
AREA_START=1

NUMSTR,LINE,100000        ! begin line numbering at 100k

COUNT_3=0
LINC=0

*DO,N,1,acount,1                ! begins to cycle through individual grains
ASEL,S,,,N
LSLA
APLOT
NUMSTR,LINE,100000        ! begin line numbering at 100k
!-----------------------------------------------------------------------------------------------------------
!determines whether to have +ve or -ve sloping parallel lines

        CHOICE=RAND(0.4,0.6)
        CHOICE_COUNT(N,1)=CHOICE

        *IF,CHOICE,LT,0.5,THEN

                X1=-2                   ! start at intercept (-2,0)
                Y1=0
                SLOPE=RAND(0.1,1)


!-----------------------------------------------------------------------------------------------------------
! PARALLELL LINE CREATION (+VE SLOPE)
!-----------------------------------------------------------------------------------------------------------
                ! Cycle the extra from -2 to 2 every "extra_inc"
                *DO,EXTRA,-2,2,EXTRA_INC



                        Y1=X1*SLOPE+EXTRA

                        K,5000+M,X1,Y1              !Plot first kp with x1=-2
                        X1=2

                        Y1=X1*SLOPE+EXTRA      !Calculate y at x1=2
```

```
                K,5001+M,X1,Y1          !Plot kp at second point

                L,5000+M,5001+M         !Draw line

                COUNT_3=COUNT_3+1

                M=M+2
                X1=-2

        *ENDDO

!-------------------------------------------------------------------------------------------------------
    *ELSEIF,CHOICE,GE,0.5,THEN


        X1=-2
        Y1=0
        SLOPE=RAND(-1,-0.1)

!-------------------------------------------------------------------------------------------------------
! PARALLELL LINE CREATION (-VE SLOPE)
!-------------------------------------------------------------------------------------------------------
        !Cycle the extra from -2 to 2 every "extra_inc"
        *DO,EXTRA,-2,2,EXTRA_INC

            Y1=X1*SLOPE+EXTRA

            K,10000+M,X1,Y1         !Plot first kp with x1=-2
            X1=2

            Y1=X1*SLOPE+EXTRA       !Calculate y at x1=2

            K,10001+M,X1,Y1         !Plot kp at second point

            L,10000+M,10001+M       !Draw line

            M=M+2
            X1=-2

        *ENDDO
!-------------------------------------------------------------------------------------------------------

    *ENDIF

    APLOT                           ! slices the grain by the parallel lines
    ASBL,ALL,ALL,,DELE,DELE
```

```
        ALLSEL
        APLOT


*ENDDO

/GOPR
IMMED,1
/SHOW,TERM

!-----------------------------------------------------------------------------------------------------------
! PART 2B: CREATION OF GRAIN BOUNDARY
! This section fills the gap between grains with a solid geometry
!-----------------------------------------------------------------------------------------------------------

RECTNG,0,1,0,1       ! Create rectangle
APTN,ALL             ! Divide rectangle by newly created grains to create grain
                     ! boundaries

!COMPRESS ALL ID#
NUMCMP,ALL

APLOT

! remove grain boundaries and at borders and smooth edges
RECTNG,0.01,0.99,0.01,0.99
AINP,ALL                    ! Pairwise boolean intersect areas

SAVE

IGESOUT,GRAIN_MODEL,,1       !Write geometry to IGES file
```

Software Details and Computer Specifications:

Matlab [4]:

Matlab R2011a V 7.12.0.635

ANSYS [170]:

ANSYS 13.0, 2010
ANSYS Mechanical LS-DYNA Prepost 1.1.4 X64

LS-DYNA [5]:

LS-DYNA 9.71 R5.1 Non-linear Explicit Dynamics
LS-PrePost 4.1 X64 Alpha 2013

Computer:

Operating System: Windows 7 Home Premium 64-bit (6.1, Build 7601)
Processor: Intel® Core™ i5-2500K CPU @ 3.30 GHz (4 CPUs), ~ 3.3 GHz
Memory: 8192MB RAM

APPENDIX B

SAMPLE CODE FOR 3D GRAIN TESSELATION IN MATLAB, GENERATION OF 3D GEOMETRICAL GRAINS IN ANSYS APDL

```
%-------------------------------------------------------------------------------------------------------
% 3D Grain Model using Voronoi Tessellation in MATLAB
% by Ian Polyzois (C)
% May 2013
%
% This model creates a 3D Voronoi tessellation of volumes in a spherical Euclidian space
% defined by the number of grains with an average size (Gsize) which fit into a 100 cubic
% micrometer volume. It generates the Voronoi vertices, cells, and planar faces which
% encompass each cell and  outputs the data to be read by FEA software
%-------------------------------------------------------------------------------------------------------

function [cell_count]=Grains3D(Gsize)


% G = # grains/(100 micrometers)^3 with size Gsize
% creates a spherical volume of points based on euclidian distance

Gvol=(4/3)*pi*(Gsize/2)^3;
Box=100^3;
G=round(Box/Gvol)*2;
R=2;
P=rand(1,3);
k=1;
while k<G
        theta=2*pi*rand(1);
        phi=pi*rand(1);
        r = R*sqrt(rand(1));
% convert to cartesian
        x=r.*sin(theta).*cos(phi);
        y=r.*sin(theta).*sin(phi);
        z=r.*cos(theta);
        P1=[x y z];
        r=sqrt((x-0)^2+(y-0)^2+(z-0)^2);
        D = pdist2(P1,P,'euclidean');
 %euclidean distance

        if D>0.146*r^(2/3)
                P=[P;P1];
                k=k+1;
        end
end

[v,c] = voronoin(P);            % find voronoi verticies and cells

vert=[];
cells=[];
```

```
cell_count=1;
facets=[];
facet_cells=[];
KV_Array=[];

for k=1:length(c)                    %increment the cell #
   if all(c{k}~=1)                   %eliminate the inf values
      VertCell = v(c{k},:);          % verts of cell # c{k}

      for i=1:length(VertCell)       % create an array for cell and fill it VertCell rows
                                     % long
         cells=[cells; cell_count];
      end

      vert=[vert; VertCell];         %add VertCell to a larger array


      KVert = convhulln(VertCell);   % defines the facet vertices ID# for vertices in
                                     % VertCell

      KV_Array=[KV_Array; KVert]; %add KVert to larger array


      for m=1:length(KVert)          % row incrementation on KVert

         a=KVert(m,:);               %a=each row of kVert

         for j=1:length(a),           %increment columns in kVert (3 columns = 1
                                     % facet)

% 1 vertice (3 total for 1 facet)
            facets=[facets; VertCell(a(j),1),VertCell(a(j),2),VertCell(a(j),3)];

            facet_cells=[facet_cells; cell_count];
         end
      end

 patch('Vertices',VertCell,'Faces',KVert,'FaceColor','g','FaceAlpha',0.5)
      cell_count=cell_count+1;

% Note: cellcount size does not equal 'c' or 'P' because cells with infinite values
% are not counted

   end
```

```
end

for k=1:length(facets),
    facet_count=[facet_count; k];
end

% write the facet vertices coordinates and facet cell numbers to XLS for import by
% FEM software
% Note: Must convert ‘xlsx’ to ‘CSV’ format to be read by ANSYS

xlswrite('3D_Cell_Data.xlsx',facet_count,'3D_Cell_Data','A1');
xlswrite('3D_Cell_Data.xlsx',facets,'3D_Cell_Data','B1');
xlswrite('3D_Cell_Count.xlsx', facet_cells, '3D_Cell_Count', 'A1');

end
```

```
!*****************************************************************************
! ANSYS 13.0 APDL Code
! 3D Grain Model
!
! -Prior Austenite 3D Grain Geometry Generation, May 2013
!
! by Ian Polyzois (C)
!
! This model reads the Voronoi facet vertices and facet cell numbers
! from MATLAB output code Grains3D and generates 3D prior austenite
! grain geometry within a defined geometrical volume
! It outputs the geometry into an IGES file
!*****************************************************************************


/PREP7
/CLEAR
/UIS, MSGPOP, 4

! Read Nodal Data from File
!-----------------------------------
NRRANG,1,99999999,1,
NREAD,'3D_CELL_DATA','csv',' '


! Remove labels
/PNUM,KP,0
/PNUM,LINE,0
/PNUM,AREA,0
/PNUM,VOLU,0
/PNUM,NODE,0
/PNUM,TABN,0
/PNUM,SVAL,0
/NUMBER,-1
!*
/PNUM,ELEM,0
/REPLOT
!*

! count the number of generated nodes
NSEL,ALL
*GET,NCOUNT,NODE,,COUNT
ALLSEL,ALL

! create arrays for the facet cell count and facet area count
*DIM,CELLCOUNT,ARRAY,NCOUNT,1,0, , ,
```

```
*DIM,AREAINFO,ARRAY,NCOUNT,2,0, , ,

! read facet cell numbers from CSV file into array Cellcount

*CREATE,ansuitmp
*VREAD,CELLCOUNT,'3D_CELL_COUNT','csv',' ',IJK,NCOUNT,1,0, ,
(1F8.0)
*END
/INPUT,ansuitmp

CELL_CHECK=1
AREA_MIN=1

ALLSEL,ALL,ALL

! Each facet is a plane with 3 vertices. This check increments after each facet is generated
CHECK_3=0


*DO,N,1,NCOUNT

        NSEL,S,,,N              ! Select next node
        KNODE,N,N               ! Create keypoint at that node
        ALLSEL,ALL,ALL
        CHECK_3=CHECK_3+1

        *IF,CELL_CHECK,EQ,CELLCOUNT(N,1),THEN          !check if within the
                                                       ! same cell

                *IF,CHECK_3,EQ,3,THEN          !if 3 keypoints are created
                        A,N,N-1,N-2            !create area
                        CHECK_3=0              !set check to 0
                *ENDIF

        *ELSE                                  !if not in same cell
                *GET,ACOUNT,AREA,,COUNT              !get areas of completed cell

                AREAINFO(CELL_CHECK,1)=AREA_MIN      !store area count
                                                     !minimum
                AREAINFO(CELL_CHECK,2)=ACOUNT  !store total area count

                ALLSEL,ALL

                CELL_CHECK=CELL_CHECK+1
                AREA_MIN=ACOUNT+1
```

```
        *ENDIF

*ENDDO

*DO,X,1,CELL_CHECK,1

ASEL,S,,,AREAINFO(X,1),AREAINFO(X,2)      !select the areas that make the cell
AGLUE,ALL                                 !glue areas that make cell
VA,ALL                                    !create volume from areas
ALLSEL
*ENDDO


ALLSEL,ALL,ALL
ADELE,ALL
LDELE,ALL

VPLOT

! Create Cylindrical Geometry to encase the Voronoi Tesselation
!-----------------------------------------------------------------------------------------------------
*GET,VC,VOLU,,COUNT             ! count all the volumes

! start ID# at 100000 to ensure no overlaps
NUMSTR,LINE,100000
NUMSTR,KP,100000
NUMSTR,AREA,100000
NUMSTR,VOLU,100000

!create cylinder with radius R=1, and length L=+-0.5 from center
CYLIND,0.5,0,-0.5,0.5,0,360,

boptn,keep,no
vinp,all                  ! piece-wise volume overlap the cylinder with existing volumes

!*********************************************************************
! Note: this step may fail due to geometrical inconsistencies or very small volumes; in which
! chase the boolean tolerance 'btol' may need to be adjusted or manual removal of unstable
! volumes may need to be performed. Also some cleanup required here (manually delete
! volumes outside cylinder)
!*********************************************************************

! Compress Volume numbers
NUMCMP,VOLU

IGESOUT,3D_GRAIN_MODEL,,1          !Write geometry to IGES file
```

APPENDIX C

CONTRIBUTIONS TO KNOWLEDGE

CONFERENCE PROCEEDINGS AND REPORTS:

[1] M. N. Bassim, G. Nazimuddin, J. Delorme and I. Polyzois, “Characterization of impact behaviour of armour plate materials,” in DYMAT 2012 - 10th International Conference on the Mechanical and Physical Behaviour of Materials Under Dynamic Loading, Freiburg, Germany, 2012.

[2] G. Nazimuddin, I. Polyzois, M. Bolduc, and M. Bassim, “High strain rate studies of armor metals,” in Proceedings of Canadian Congress of Applied Mechanics Forum (CANCAM), Vancouver, BC, Canada, 2011

[3] I. Polyzois and M.N. Bassim, “Modeling the formation of adiabatic shear bands in armor steels at high strain rates and large strains,” in Proceedings of The Canadian Society for Mechanical Engineering Forum (CSME), Victoria, BC, Canada, 2010

[4] I. Polyzois, "Finite Element Modeling of the Behavior of Armor Materials Under High Strain Rates and Large Strains," Masters Thesis, University of Manitoba, Winnipeg, 2010.

REFERENCES

[1] T. Wright, The Physics and Mathemtaics of Adiabatic Shear Bands, Cambridge: University Press, 2002.

[2] R. Armstrong and S. Walley, "High strain rate properties of metals and alloys," *International Materials Reviews,* vol. 53, no. 3, pp. 105-128, 2008.

[3] D. Rittel, "A different viewpoint on adiabtic shear localization," *Journal of Physics D: Applied Physics,* vol. 42, p. 214009, 2009.

[4] *MATLAB 7.12,* The MathWorks Inc., Natick, Massachusetts, United States.

[5] *LS-DYNA 9.71,* Livermore Software Technology Corporation, Livermore, CA.

[6] F. Aurenhammer, "Voronoi Diagrams -- A Survey of a Funamental Geometrical Data Structure," *ACM Computing Surveys,* vol. 23, no. 3, pp. 345-405, 1991.

[7] A. Okabe, B. Boots, K. Sugihra and S. N. Chiu, Spacial Tesseltions -- Concepts and Applications of Voronoi Diagrams, 2nd Edition, John Wiley, 2000.

[8] R. Gingold and J. Monaghan, "Smoothed particle hydrodynamics: theory and application to non-spherical stars," *Mon. Not. R. Astron. Soc.,* vol. 181, pp. 375-389, 1977.

[9] L. Libersky and A. Petschek, "Smooth Particle Hydrodynamics with Strength of Materials, Advances in the Free Lagrange Method," *Lecture Notes in Physics,* vol. 395, pp. 248-257, 1990.

[10] L. Libersky, A. Petschek, T. Carney, J. Hipp, F. Allahdadi and F. High, "High Strain Lagrangian Hydrodynamics: A Three-Dimensional SPH Code for Dynamic Material Response," *J. Comput. Phys,* vol. 109, pp. 67-75, 1993.

[11] J. Johnson and W. Cook, "Fracture characteristics of three metals subjected to various strains, strain rates, temperatures and pressures," *Engineering Fracture Mechanics,* pp. 31-48, 1985.

[12] G. Camacho and M. Ortiz, "Adaptive Lagrangian modelling of ballistic penetration of metallic targets," *Int. J. Comput. Methods Appl. Mech. Engrg,* vol. 142, pp. 269-301, 1997.

[13] T. Børvik, O. Hopperstad, T. Berstad and M. Langseth, "A computational model of viscoplasticity and ductile damage for impact and penetration," *Eur. J. Mech. A/Solids,* vol. 20, pp. 685-712, 2001.

[14] H. Feng and M. Bassim, "Finite element modeling of the formation of adiabatic shear bands in AISI 4340 steel," *Material Science and Engineering: A*, vol. 266, no. 1-2, pp. 255-260, 1999.

[15] M. Bassim, "Study of the formation of adiabatic shear bands in steels," *Journal of Materials Processing Technology*, vol. 119, no. 1-3, pp. 234-236, 2001.

[16] V. Nesterenko, M. Meyers and H. Chen, "Shear localization in high-strain-rate deformation of granular alumina," *Acta Materialia*, vol. 44, no. 5, pp. 2017-2026, 1996.

[17] J. Barry and G. Byrne, "TEM study on the surface white later in two turned hardened steels," *Materials Science and Engineering: A*, vol. 325, no. 1-2, pp. 356-364, 2002.

[18] J. Hines and K. Vecchio, "Recrystallization kinetics within adiabatic shear bands," *Acta Materialia*, vol. 45, no. 2, pp. 635-649, 1997.

[19] J. Duffy and Y. Chi, "On the measurement of local strain and temperature during the formation of adiabatic shear bands," *Materials Sceince and Engineering: A*, vol. 157, no. 2, pp. 195-210, 1992.

[20] A. Marchand and J. Duffy, "An experimental study of the formation process of adiabatic shear bands in a structural steel," *Journal of Mechanics and Physics of Solids*, vol. 36, no. 3, pp. 251-283, 1988.

[21] A. Chokshi and M. Meyers, "The prospects of superplasticity at high strain rates: preliminary considerations and an example," *Scripta Metallurgical et Materialia*, vol. 24, no. 103, pp. 605-610, 1990.

[22] M. Meyers, Y. Chen, F. Marquis and D. Kim, "High-strain, high-strain-rate behaviour of tantalum," *Metallurgical and Materials Transactions A*, vol. 26, no. 10, pp. 2493-2501, 1995.

[23] M. Mataya, M. Carr and G. Krauss, "Flow localization and shear band formation in a precipation strengthened austenitic stainless steel," *Metallurgical and Materials Transactions A*, vol. 13, no. 7, pp. 1263-1274, 1982.

[24] R. Doherty, D. Hughes, J. Humphreys, D. Jenson, M. Kassner, W. King, T. McNelley, H. McQueen and A. Rollet, "Current Issues in Recrystallization: A Review," 1997.

[25] B. Derby and M. Ashby, "On dynamic recrystallization," *Scripta Metallurgica*, vol. 21, pp. 879-884, 1987.

[26] Q. Li, Y. Xu, Z. Lai, L. Shen and Y. Bai, "Dynamic recyrustallization induced by plastic deformation at high strain rate in a Monel alloy," *Materials Science and Engineering A.,* vol. 276, pp. 150-256, 2000.

[27] K. Cho, S. Lee, S. Nutt and J. Duffy, "Adiabatic shear band formation during dynamic torsional deformation of an HY-100 steel," *Acta Metallurgica et Materialia,* vol. 41, no. 3, pp. 923-932, 1993.

[28] M. Meyers and H. Pak, "Observation of an adiabatic shear band in titanium by high-voltage transmission electron microscopy," *Acta Metallurgica et Materiala,* vol. 34, no. 12, pp. 2493-2499, 1986.

[29] U. Andrade, M. Meyers, K. Vecchio and A. Chokshi, "Dynamic Recystallization in high-strain, high-strain-rate plastic deformation of copper," *Acta Metallurgica et Materialia,* vol. 42, no. 9, pp. 3183-3195, 1994.

[30] J. Hines, K. Vecchio and S. Ahzi, "A Model for Microstructure Evolution in Adiabatic Shear Bands," *Metallurgical and Materials Transactions A,* vol. 29A, pp. 191-203, 1998.

[31] J. Kerrisk, "A model for Shear-Band Formation and High-Explosive Initiation in Hydrodynamics Code," Los Alamos National Laboratory, 1996.

[32] F. Zhou, T. Wright and K. Ramesh, " A numerical methodology for investigating the formation of adiabatic shear bands," *Journal of the Mechanics and Physics of Solids,* vol. 54, pp. 904-926, 2006.

[33] X.-b. Wang, "Adiabatic Shear Localization for Steels Based on Johnson-Cook Model and Second- and Fourth-Order Gradient Plasticity Models," *Journal of Iron and Steel Research, International,* vol. 14, no. 5, pp. 56-61, 2007.

[34] L. Daridon, O. Oussouaddi and S. Ahzi, "Influence of the material constitutive models on the adiabatic shear band spacing: MTS, power law and Johnson-Cook models," *International Journal of Solids and Structures,* vol. 41, pp. 3109-3124, 2004.

[35] Y. Gao, "An implicit finite element method for simulating inhomogenous deforation and shear bands of amorphous alloys based on the free-volume model," *Modelling Simul. Mater. Sci. Eng.,* vol. 14, pp. 1329-1345, 2006.

[36] X.-b. Wang, "A method for calculating damage evolution in adiabatic shear band of titanium alloy," *Trans. Nonferrous Met. Soc. China,* vol. 19, pp. 1280-1285, 2009.

[37] Z. Zhu and R. Batra, "Shear band development in a thermally softening viscoplastic body," *Computers & Structures,* vol. 29, no. 5, pp. 459-472, 1991.

[38] H. Hallberg, M. Wallin and M. Ristinmaa, "Modeling of Continuous Dynamic Recrystallization in Commercial-Purity Aluminum," *Material Science and Engineering A,* vol. 572, pp. 1126-1134, 2010.

[39] N. Yazdipour, A. Dehghan-Manshadi, C. Davies and P. Hodgson, "Simulation of Dynamic Recrystallization using Irregular Cellular Automata," *Materials Forum,* vol. 31, pp. 164-176, 2007.

[40] J. Frenkel, "Zur Theorie der Elastizitatsgrenze und der Festigkeit Kristallinischer Korper," *Z. Phys,* vol. 37, pp. 572-609, 1926.

[41] D. Hull and D. J. Bacon, Introduction to Dislocations, Butterworth-Heinemann, 1984.

[42] W. D. J. Callister, Fundamentals of Materials Science and Engineering, Danvers, MA: John Wiley & Sons, 2005.

[43] A. C. Thomson, "High Strain Rate Characterization of Advanced High Strength Steels," Waterloo, 2006.

[44] A. Rusinek, J. Rodriquez-Martinez and A. Arias, "A Thermo-viscoplastic constitutive model for FCC metals with application to OFHC copper," *International Journal of Mechanical Sciences,* 2009.

[45] E. Hall, "The deformation and ageing of mild steel: III discussion of results," *Proceedings of The Royal Society B,* vol. 64, pp. 747-753, 1951.

[46] N. Petch, "Cleavage strength of polycrystals," *J. Iron Steel Inst.,* vol. 174, pp. 25-2, 1953.

[47] R. Abbaschian, L. Abbaschian and R. Reed-Hill, Physical Metallurgy Principles, Stamford, CT: Cengage Learning, 2009.

[48] R. Sandstrom and R. Lagneborg, "A model for hot working occuring by recrystallization," *Acta Metallurgrica,* vol. 23, no. 3, pp. 367-398, 1975.

[49] "Key to Metals, Classification of Carbon and Low-Alloy Steels," 2010. [Online]. Available: http://www.keytometals.com/Articles/Art62.htm. [Accessed 1 May 2014].

[50] eFunda, "Low-Carbon Steels," eFunda, 2014. [Online]. Available: http://www.efunda.com/materials/alloys/carbon_steels/low_carbon.cfm. [Accessed 1 May 2014].

[51] T. Bell, "The Effect of Alloying Agents on Steel Properties," 2014. [Online]. Available: http://metals.about.com/od/metallurgy/a/The-Effect-Of-Alloying-Agents-On-Steel-Properties.htm. [Accessed 1 May 2014].

[52] eFunda, "Alloy Steels," 2014. [Online]. Available: http://www.efunda.com/materials/alloys/alloy_steels/alloy.cfm. [Accessed 1 May 2014].

[53] "Key to Metals, High-Alloy Cast Steels," 2010. [Online]. Available: http://steel.keytometals.com/articles/art100.htm. [Accessed 1 May 2014].

[54] eFunda, "AISI 4340 Alloy Steel," 2014. [Online]. Available: http://www.efunda.com/glossary/materials/alloys/materials--alloys--steel--alloy_steel--aisi_4340.cfm. [Accessed 1 May 2014].

[55] W. F. Smith and J. Hashemi, Foundations of Materials Science and Engineering (4th ed.), McGraw-Hill, 2006.

[56] H. Pollack, Materials Science and Metallurgy (4th Edition), Prentice Hall, 1988.

[57] J. E. Garnham, "University of Cambridge: The Wear of Bainitic and Pearlitic Steels," 1995. [Online]. Available: http://www.msm.cam.ac.uk/phase-trans/2005/pearlite.html. [Accessed May 2014].

[58] F. Humphreys and M. Hatherly, Recrystallization and Related Annealing Phenomena, Oxford: Elsevier Science Ltd., 1995.

[59] H. Bhadeshia, "Materials Science & Metallurgy: Martensite in Steels," 2002. [Online]. Available: http://www.msm.cam.ac.uk/phase-trans/2002/martensite.html. [Accessed May 2014].

[60] G. Totten and M. Howes, Steel Heat Treatment Handbook, CRC Press, 1997.

[61] H. Bhadeshi, "Tempered Martensite," University of Cambridge, 2004. [Online]. Available: http://www.msm.cam.ac.uk/phase-trans/2004/Tempered.Martensite/tempered.martensite.html. [Accessed May 2014].

[62] Wikipedia, "Bainite," [Online]. Available: http://en.wikipedia.org/wiki/Bainite. [Accessed 4 May 2014].

[63] S. Murphy and J. Whiteman, "The precipitation of epsilon-carbide in twinned martensite," *Metallurgical Transaction 1*, pp. 843-848, 1970.

[64] P. Padmanabham and W. Wood, "Precipitation of ε carbide in martensite," *Materials Science and Engineering*, vol. 65, pp. 289-297, 1984.

[65] Y. Ohmori and I. Tamura, "Epsilon carbide precipitation during tempering o plain carbon martensite," *Metallurgical Transaction,* vol. 23A, pp. 2737-2751, 1992.

[66] S. Nagakura, Y. Hirotsu, M. Kosunoki, T. Suzuki and Y. Nakamura, "Crystallographic study of the tempering of martensitic carbon steel by electron microscopy and diffraction," *Metallurgical Transaction,* vol. 14A, pp. 1025-1031, 1983.

[67] S. Skrzypek, E. Kolawa, A. Sawicki and T. Tyliszczak, "A study of the retained austenite phase transformation in low alloy steel using conversion electron mössbauer spectroscopy and X-ray diffraction," *Materials Science and Engineering,* vol. 66, pp. 145-149, 1984.

[68] A. Kokosza and J. Pacyna, "Evaluation of retained austenite stability in heat treated cold work tool steel," *Journal of Materials Processing Technology,* Vols. 162-163, pp. 327-331, 2005.

[69] F. C. Campell, Elements of Metallurgy and Engineering Alloys, ASM International, 2008.

[70] H. Bhadeshia and D. Edmonds, "Tempered martensite embrittlement: Role of retained austenite and cementite," *Metal Science,* vol. 13, pp. 325-334, 1979.

[71] A. Odeshi, M. Bassim, S. Al-Ameeri and Q. Li, "Dynamic shear band propagation and failure in AISI 4340 steel," *Journal of Materials Processing Technology,* vol. 169, pp. 150-155, 2005.

[72] Q. Xue, X. Liao, Y. Zhu and G. Gray III, "Formation mechanisms of nanostructures in stainless steel during high-strain-rate severe plastic deformation," *Material Science and Engineering A,* Vols. 410-411, pp. 252-256, 2005.

[73] M. Meyers, U. Andrade and A. Chokshi, "The effect of grain size on the high-strain, high-strain-rate behaviour of copper," *Metallurgical and Materials Transactions A,* vol. 26, no. 11, pp. 2881-2893, 1995.

[74] J. Bailey and P. B. Hirsch, *Proc. Roy. Soc. Lond.,* vol. 267A, p. 11, 1962.

[75] J. Li, *J. Appl. Phys.,* vol. 33, p. 2958, 1962.

[76] H. Hu, in *Recovery and Recrystallizaiton of Metals,* L. Himmel, Ed., New York, Interscience Publishing, 1963, pp. 311-362.

[77] R. Doherty, *Met. Sci.,* vol. 8, p. 132, 1974.

[78] D. Rittel and S. Osovski, "Dynamic failure by adiabatic shear banding," *International Journal of Fracture,* vol. 161, no. 1, pp. 177-185, 2010.

[79] D. Rittel, P. Landau and A. Venkert, "Dynamic Recrystallization as a potential cause for adiabatic shear failure," *Physical Review Letters,* vol. 101, no. 16, p. 165501, 2008.

[80] Y. Xu, Y. Bai, Q. Xue and S. L.T., "Formation, Microstructure and Develeopment of the Localized Shear Deformation in Low-Carbon Steels," *Acta Materialia,* vol. 44, no. 5, pp. 1917-1926, 1996.

[81] S. Medyanik, W. Liu and S. Li, "On criteria for dynamic adiabatic shear band propagaion," *Journal of the Mechanics and Physics of Solids,* vol. 55, no. 7, pp. 1439-1461, 2007.

[82] M. Pérez-Prado, J. Hines and K. Vecchio, "Microstructural Evolution in Adiabatic Shear Bands in Ta and Ta-W Alloys," *Acta mater.,* vol. 49, pp. 2905-2917, 2001.

[83] M. Meyers, G. Subhash, B. K. Kad and L. Prasad, "Evolution of Microstructure and Shear Band Formation in a-hcp Titanium," *Mechanics of Materials,* vol. 17, pp. 175-193, 1994.

[84] M. Meyers, L. Meyer, K. Vecchio and A. U., "High Strain, HIgh Strain-Rate Deformation of Copper," *Journal de Physique,* vol. 1, no. 8, pp. 11-17, 1991.

[85] W. Crozier and W. Hume, "High-Velocity, Light-Gas Gun," *Journal of Applied Physics,* vol. 28, pp. 892-894, 1957.

[86] D. Hughes, L. Gourley and M. Gourley, "Shock-Wave Compression of Iron and Bsmuth," *J. Appl. Phys.,* vol. 32, p. 624, 1961.

[87] R. McQueen and S. Marsh, "Equation of State for Nineteen Metallic Elements from Shock-Wave Measurements to Two Megabars," *Journal of Applied Physics,* vol. 31, no. 7, pp. 1253-1269, 1960.

[88] S. G. Taylor and A. Whiffen, "The use of flat-ended projectiles for determining dynamic yield stress; I theoretical considerations; II tests on various metallic materials," *Royal Society Proceedings,* vol. 194, pp. 289-299, 1948.

[89] J. House, "Taylor Impact Testing," Air Force Armament Laboratory, United States Air force, Eglin Air Force Base, Florida, 1989.

[90] H. Kolsky, "An investigation of the mechancial properties of materials at very high rates of loading," *Proc. Phys. Soc. London,* vol. B62, pp. 676-700, 1949.

[91] W. Chen and B. Song, Split Hopkinson (Kolsky) Bar, New York: Springer, 2011.

[92] G. Gary, "High Strain Rate Testing: Classic Split-Hopkinson Pressure Bar Testing," in *ASM Handbook Vol. 8: Mechanical Testing and Evaluation*, ASM International, 2000, pp. 462-476.

[93] M. Meyers, Dynamic Behavior of Materials, Hoboken, NJ: John Wiley & Sons, 1994.

[94] S. Nemat-Nasser, "High Strain Rate Testing: Introduction to High Strain Rate Testing," in *ASM Handbook Vol. 8: Mechanical Testing*, ASM International, 2000, pp. 427-446.

[95] B. Song and W. Chen, "Split Hopkinson pressure bar techniques for characerizing soft materials," *Latin American Journal of Solids and Structures,* vol. 2, pp. 113-152, 2005.

[96] J. Foster, D. Frew, M. Forrestal, E. Nishida and W. Chen, "Shock testing accelerometers with a Hopkinson pressure bar," in *Experimental and Applied Mechanics, Volume 6*, Conference Proceedings of the Society for Experimental Mechanics Series 9999, 2011, pp. 229-237.

[97] R. Nakkalil, J. Hornaday Jr. and M. Bassim, "Characterization of the compression properties of rail steels at high temperatures and strain rates," *Materials Science and Engineering A,* vol. 141, pp. 247-260, 1991.

[98] F. Zerilli and R. Armstrong, "Dislocationc-mechanics-based constitutive relations for mataerial dynamic calculations," *J. Appl. Phys.,* vol. 61, pp. 11816-1825, 1987.

[99] R. Kapoor and S. Nemat-Nasser, "Comparison between high and low strain-rate deformation of tantalum," *Metallurgical and Materials Transactions A,* vol. 31, pp. 815-823, 2000.

[100] L. Schwer, "Optionl Strain-Rate Forms for the Johnson Cook Consitutive Model and teh Role of the Parameter Epsilon_0," in *LS-DYNA Anwenderforum 2007*, Frankenthal, 2007.

[101] H. Huh and W. Kang, "Crash-worthiness assessment of thin-walled structures with the high-strength steel sheet," *International Journal of Vehicle Design,* vol. 30, no. 1/2, pp. 1-21, 2002.

[102] D. Allen, W. Rule and S. Jones, "Optimizing material strength constants numerically extracted from Taylor Impact data," *Experimental Mechanics*, vol. 37, no. 3, pp. 333-338, 1997.

[103] G. Cowper and P. Symonds, "Strain hardening and strain rate effects in the impact loading of cantilever beams," Applied Mathematics Report, 1958.

[104] M. Cockroft and D. Latham, "Ductility and the workability of metals," *Journl of the Institute of Metals,* vol. 96, pp. 33-39, 1968.

[105] G. Taylor and H. Quinney, "The latent energy remaining in a metal after cold working," *Proc. Royal Soc. London,* vol. 143, no. 849, pp. 307-326, 1934.

[106] G. Ravichandran, A. Rosakis, J. Hodowany and P. Rosakis, "On the conversion of plastic work into heating during high-strain-rate deformation," in *Proc. 12th APS Topical Conference on Shock Compression of Condensed Matter*, 2001.

[107] F. Lederman, M. Salamon and L. Shacklette, "Experimental verification of scaling and test of the universality hypothesis from specifica heat data," *Phys. Rev. B,* vol. 9, no. 7, pp. 2981-2988, 1974.

[108] eFunda, "Properties of Alloy Steel AISI 4340," [Online]. Available: http://www.efunda.com/materials/alloys/alloy_steels/show_alloy.cfm?ID=AISI_4340&prop=all&Page_Title=AISI%204340.. [Accessed 12 December 2013].

[109] R. Y. Z. Judge, S. Jones and G. Beattie, "Numberical Simulation of Spiral-strand Cables Subjected to High Velocity Fragment Impact," in *8th European LS-DYNA Users Conference*, Strasbourg, 2011.

[110] P. Zang, M. Karompour, D. Balint and J. Lin, "Three dimensional virtual grain structure generation with grain size control," *Mechanics of Materials,* vol. 55, pp. 89-101, 2012.

[111] S. Kuriyama and M. Meyers, "Numerical Modeling of the Propagation of an Adiabatic Shear Band," *Metallurgical Transactions A,* vol. 17A, pp. 443-450, 1986.

[112] S. Kuriyama and M. Meyers, "Numerical Analysis of Adiabatic Shear Band in an Early Stage of Its Propagation," in *IUTAM Symposium on Macro- and Micro-Mechanics of High Velocity Deformation and Fracture*, Berlin, 1987.

[113] R. Smit, W. Brekelmans and H. Meijer, "Prediction of the mechanical behavior of nonlinear heterogeneous systems by multi-level finite element modeling," *Comput. Methods Appl. Mech. Engrg*, vol. 155, pp. 181-192, 1998.

[114] J. Besson, S. D. and W. Brocks, "Modeling of plain strain ductile rupture," *International Journal of Plasticity*, vol. 19, 2003.

[115] A. Gurson, "Continuum theory of ductile rupture by void nucleation and growth. Part I. Yield criteria and flow rules for porous ductile media," *J. Engng Mater Technol Trans ASME,* vol. 99, pp. 2-15, 1977.

[116] V. Tvergaard and A. Needleman, "Analysis of cup-cone fracture in a round tensile bar," *Acta Metall,* vol. 32, no. 1, pp. 157-69, 1984.

[117] L. Xue, "Consitutive modeling of void shearing effect in ductile fracture of porous materials," *Engineering Fracture Mechanics,* vol. 75, pp. 3343-3366, 2008.

[118] F. McClintock, S. Kaplan and C. Berg, "Ductile fracture by hole growth in shear bands," *Int. J. Fract. Mechan.*, vol. 2, no. 4, pp. 614-27, 1966.

[119] G. Schmitz, B. Bottger, J. Eiken, M. Apel, A. Viardin, A. Carre and G. Laschet, "Phase-field based simulation of microstructure evolution in technical alloy grades," *International Journal of Advances in Engineering Sciences and Applied Mathematics,* vol. 2, no. 4, pp. 126-139, 2011.

[120] P. Zhang, D. Balint and J. Lin, "Controlled Poisson Voronoi tessleation for virtual grain structure generation: a statistical evaluation," *Philosophical Magazine,* vol. 91, no. 36, pp. 4555-4573, 2011.

[121] Z. Fan, Y. Wu, X. Zhao and Y. Lu, "Simulation of polycrystalline structure with Voronoi diagram in Laguerre geometry based on random closed packing of spheres," *Computation Materials Science,* vol. 29, pp. 301-308, 2004.

[122] G. Liu and M. Liu, Smoothed Particle Hydrodynamics: A Meshfree Particle Method, Toh Tuck Link, Singapore: World Scientific Publishing Co. Pte. Ltd, 2003.

[123] J. Donea, A. Huerta, J.-P. Ponthot and A. Rodriguez-Ferran, "Volume 1: Chapter 14: Arbitrary Lagrangian-Eulerian Methods," in *Encyclopedia of Computational Mechanics*, Wiley InterScience, 2004.

[124] L. Lucy, "A numerical approach to the testing of fission hypothesis," *Astron. Journal,* vol. 82, pp. 1013-1024, 1977.

[125] P. Randles and L. Libersky, "Smoothed Particle Hydrodynamics: Some recent improvements and applications," *Comput. Meth. Appl Mech. Engrg.,* vol. 139, no. 1, pp. 375-408, 1996.

[126] J. L. Lacome, "Smooth Particle Hydrodynamics (SPH): A New Feature in LS-DYNA," in *6th International LS-DYNA Conference,* Detroit, 2000.

[127] S. Al-Qawbah, K. S. Rababa and A. Awad, "The Effect of Austenite Temperature on the Microstructure, Mechanical Behavior, Hardness, and Impact Toughness

of AISI D2 Tool Steel," *International Journal of Engineering Research and Application (IJERA),* vol. 2, no. 3, pp. 2890-2896, 2012.

[128] H. Chandler, Heat Treater's Guide: Practices and Procedures for Irons and Steel, ASM International, Dec 31, 1994.

[129] E. B. Kula and A. A. Anctil, "Tempered Martensite Embrittlement and Fracture Toughness in 4340 Steel," Metals Research for Army Material, U.S. Army Materials Reserach Agency, Watertown, MA, 1967.

[130] S. Morito, H. Tanaka, R. Konishi, T. Furuhara and T. Maki, "The morphology and crystallography of lath marteniste in Fe-C alloys," *Acta Materialia,* vol. 51, no. 6, pp. 1789-1799, 2003.

[131] S. Morito, X. Huang, T. Furuhara, T. Maki and N. Hansen, "The morphology and crystallography of lath martensite in allow steels," *Acta Materialia,* vol. 54, no. 19, pp. 5323-5331, 2006.

[132] F. B. Pickering, "Hardenability Concepts with Applications to Steel," D. Doane and K. J.S., Eds., Warrnedale, PA, American Institute of Min. Metall. and Petroleum Eng., 1978, pp. 179-228.

[133] S. Matsuda, T. Inoue, H. Mimura and Y. Okamura, "Proc. Int. Sympo. on Toward Improved Ductility and Toughness," in *The Iron and Steel Inst. of Japan,* Kyoto, Japan, 1971.

[134] S. Morooka, Y. Tomota, Y. Adachi, S. Morito and T. Kamiyama, "Hierarchical Characterization by EBSD and Neutron Diffraction on Heterogeneous Deformation Behavior of a Martensitic Steel," *Tetsu-to-Hagane,* vol. 94, no. 8, pp. 313-320, 2008.

[135] G. F. Vandervoort, "Revealing Prior-Austenite Grain Boundaries in Heat-treated Steels," [Online]. Available: http://www.georgevandervoort.com/metallography/specific/iron-and-steel-specific/20001306-revealing-prior-austenite-grain-boundaries-in-heat-treated-steels-article.html. [Accessed 14 July 2013].

[136] A. Ucisik, H. Feng and C. McMahon, "The influence of intercritical heat treatment on the temper emrbittlement of P-doped Ni-Cr steel," *Metallurgical Transactions,* vol. 9A, pp. 321-329, 1978.

[137] S. Bechet and L. Beaujard, "New reagent for the micrographical demonstration of the austenite grain of hardened or hardened-tempered steels," *Rev. Met.,* vol. 52, pp. 830-836, 1955.

[138] *IQMaterials,* MedyaCybernetics, Rockville, MD, 2011.

[139] ASTM, ASTM E112-10 Standard Test Methods for Determining Average Grain Size, ASTM International.

[140] N. Lim, C. Bang, S. Das, H. Jin, R. Ayer and C. Park, "Influence of Tempering Temperature on Both the Microstructural Evolution and Elemental Distribution in AISI 4340 Steels," *Met. Mater. Int.,* vol. 18, no. 1, pp. 87-94, 2012.

[141] G. Lai, W. Wood, R. Clark, V. Zackay and E. Parker, "The Effect of Austenitizing Temperature on the microstructure and Mechanical Properties of As-Quenched 4340 Steel," *Metallurgical Transactions,* vol. 5, pp. 1663-1670, 1974.

[142] R. Ritchie, B. Francis and W. Server, "Evaluation of Toughness in AISI 4340 Alloy Steel Austenized at Low and High Temperatures," *Metallurgical Transactions A,* vol. 7, pp. 831-838, 1976.

[143] K. Khan and W. Wood, "The effect of step quenching on the microstructure and fracture toughness of AISI 4340 steel," *Metallurgical and Materials Transactions A,* vol. 9, no. 7, pp. 899-907, 1978.

[144] Atlas of stress-strain curves, Materials Park OH: ASM International, 2002.

[145] ASM Handbook: Volume 4: Heat Treating, Materials Park, OH: ASM International, 1991.

[146] M. Born and K. Huang, Dynamical Theory of Crystal Lattices, London: Oxford University Press, 1954.

[147] D. S. Joshi, M. L. Bhatnagar and R. S. Shrivastava, "A simple technique for the determination of Young's Modulus," *Journal of Physics E: Scientific Instruments,* vol. 2, no. 9, p. 831, 1969.

[148] ASME, ASME B31.1 Power Piping ASME Code for Pressure Piping, American National Standard, 1995.

[149] H. Tomlinson, "The effect of Change of Temperature on the Velocity of Sound in Iron," *Nature,* vol. 33, pp. 582-582, 1886.

[150] K. Nowacki and W. Kasprzyk, "The Sound Velocity in an alloy Steel at High-Temperature Conditions," *Interntional Journal of Thermophysics,* vol. 31, pp. 101-112, 2010.

[151] F. Everett and J. Miklowitz, "Poisson's Ratio at High Temperatures," *Journal of Applied Physics,* vol. 15, pp. 592-597, 1944.

[152] M. A. Gebril, "Effect of austenization temperatures and times on hardness, microstructure and corrosion rate of high carbon steel," in *7th International*

Conference on Advanced Computational Engineering and Experimenting ACE-X 2013, Madrid, Spain, 2013.

[153] H. Kuhn, ASM Handbook: Volume 8: Mechanical Testing and Evaluation, Materials Park, OH: ASM International: The Materials Information Society, 2000.

[154] R. Steiner, ASM Handbook: Volume 1: Properties and Selections: Irons, Steels, and High Performance Alloys, Materials Park, OH: ASM International, 1990.

[155] ASM, ASM Handbook: Volume 2: Properties and Selections: Nonferrous Alloys & Special Purpose Materials, Materials Park, OH: ASM International, 1991.

[156] B. Banerjee, "The mechanical threshold stress model for various tempers of AISI 4340 steel," *International Journal of Solids and Structures,* vol. 44, pp. 834-859, 2007.

[157] R. Shivpuri, X. Cheng and Y. Mao, "Elasto-plastic pseudo-dynamic numerical model for the design of shot peening process paramters," *Maerials and Design*, vol. 30, pp. 3112-3120, 2009.

[158] "ASTM E140-07: Standard Hardness Conversion Tables for Metals Relationship Among Brinell Hardness, Vickers Hardness, Rockwell Hardness, Superficial Hardness, Knoop Hardness, and Scleroscope Hardness," ASTM International, West Conshohocken, PA, 2012.

[159] W.-S. Lee and G.-W. Yeh, "The plastic deformation behaviour of AISI 4340 alloy steel subjected to high temperature and high strain rate loading conditions," *Journal of Materials Processing Technology,* vol. 71, pp. 224-234, 1997.

[160] J. R. Davis, ASM Speciality Handbook: Tool Materials, 1996.

[161] G. Kay, "Failure Modeling of Titanium 6Al-4V and Aluminum 2024-T3 with the Johnson-Cook Material Model," DOT/FAA/AR-03/57, 2003.

[162] T. Wierzbicki, Y. L. Y.-W. Bao and Y. Bai, "Calibration and Evaluation of Seven Fracture Models," *International Journal of Mechanical Sciences,* vol. 47, pp. 719-743, 2005.

[163] Y. W. T. Bao, "On the Cut-Off Value of Negative Triaxiality for Failure," *Engineering Fracture Mechanics,* vol. 72, pp. 1049-1069, 2005.

[164] G. Johnson and T. Holmquist, "Test Data and Computational Strength and Fracture Modal Constants for 23 Materials Subject to Large Strain, High Strain Rates, and High Temperature," Los Alamos National Laboratory, 1989.

[165] K. Nahshon, M. Pontin, A. Evans, J. Hutchinson and F. Zok, "Dynamic Shear Rupture of Steel Plates," *Journal of Mechanics of Materials and Structures*, vol. 2, no. 10, pp. 2049-2066, 2007.

[166] A. Needleman and V. Tvergaard, "Mesh effects in the analysis of dynamic ductile crack growth," *Eng. Fract. Mech.*, vol. 47, no. 1, pp. 75-91, 1994.

[167] A. Gullerud, X. Gao, B. Dodds Jr. and R. Haj-Ali, "Simultion of ductile crack growth using computational cells: numerical aspects," *Eng. Fract. Mech.*, vol. 66, pp. 65-92, 2000.

[168] J. A. V. D. Avyle, "Correlation of Fractography, Microstructure and Fracture Toughness Behavior of High Strength Alloys," Massachusetts Institute of Technology, Cambridge, 1975.

[169] The Engineering Toolbox, "Friction and Coefficients of Friction," [Online]. Available: http://www.engineeringtoolbox.com/friction-coefficients-d_778.html. [Accessed 1 07 2014].

[170] *ANSYS® Academic Research, Release 13.0.*

[171] M. Bassim and A. Odeshi, "Shear strain localization and fracture in high strength structural materials," *Archives of Material Science and Engineering,* vol. 31, pp. 69-74, 2008.

[172] A. Odeshi and M. Bassim, "Evolution of adiabatic shear bands in dual-phase steel at very high strain rates," *Materials Science and Engineering: A,* vol. 488, no. 1-2, pp. 235-240, 2008.

[173] R. Batra and N. Wilson, "Adiabatic shear bands in plane strain deformations of WHA," *International Journal of PLasticiy,* vol. 14, no. 1-3, pp. 43-60, 1998.

[174] K. Cho, Y. Chi and J. Duffy, "Microscopic observations of adiabatic shear bands in three difference steels," *Metallurgical and Materials Transactions A,* vol. 21, no. 4, pp. 1161-1175, 1990.

[175] D. Rittel, Z. Wang and A. Dorogoy, "Geometrical imperfection and adiabatic shear banding," *International Journal of Impact Engineering,* vol. 35, no. 11, pp. 1280-1292, 2008.

[176] H. Hallberg, "processing and Properties of Bulk nanostructured Materials: Approaches to modeling of recrystallization," *Metals*, vol. 1, pp. 16-48, 2011.

[177] S. Illescas, J. Fernandez and J. Guilemany, "Kinetic analysis of the austenitic grain grown in HSLA steel with low carbon content," *Materials Letters,* vol. 62, pp. 3478-3480, 2008.

[178] A. Guimelli, "Austenite grain growth kinetics and the grain size distribution," UBC, Vancouver, B.C., 1995.

[179] A. Zurek, "The study of adiabatic shear band instability in a pearlitic 4340 steel using a dynamic punch test," *Metallurgical and Materials Transactions A,*, vol. 25, no. 11, pp. 2483-2489, 1994.

[180] S. Schoenfeld and T. Wright, "A failure criterion based on material instability," *International Journal of Solids and Structures,* vol. 40, no. 12, pp. 3021-3037, 2003.

[181] D. Hull and D. Bacon, "1 - Defects in Crystals," in *Introdcution to Dislocations (Fourth Edition),* Oxford, Butterworth-Heinemann, 2001, pp. 1-21.

[182] T. Wright, "Scaling laws for adiabatic shear bands," *International Journal of Solids and Structures,* vol. 32, no. 17-18, pp. 2745-2750, 1995.

[183] R. Valiev, E. kozlov, Y. Ivanov, J. Lian, A. Nazarov and B. Baudelet, "Deformation behaviour of ultra-fine grained copper," *Acta Metallurgica et Materialia,* vol. 42, no. 7, pp. 2467-2475, 1994.

[184] S. Morito, Y. Adachi and Y. Ohba, "Morphology and Crystallography of Sub-Blocks in Ultra-Low Carbon Lath Martensite Steel," *Materials Transactions,* vol. 50, no. 8, pp. 1919-1923, 2009.

[185] M. Meyers, Y. Xu, Q. Xue, M. Perez-Prado and T. McNelley, "Microstructural evolution in adiabatic shear localization in stainless steel," *Acta Materialia,* vol. 51, pp. 1307-1325, 2003.

[186] W.-S. Lee and T.-T. Su, "Mechanical properties and microstructural features of AISI 4340 high-strength alloy steel under quenched and tempered conditions," *Journal of Mateirals Processing Technology,* vol. 87, pp. 198-206, 1999.

[187] S. Lee, K.-M. Cho, K. Kim and W. Choi, "Adiabatic Shear Band Formation in Al-SiCw Composites," *Metallurgical Transactions A,* vol. 24A, pp. 895-900, 1993.

[188] D. Rittel, Z. Wang and M. Merzer, "Adiabatic Shear Failure and Dynamic Stored Energy of Cold Work," *Physical Review Letters,* vol. 96, p. 075502, 2006.

[189] A. Belyakov, K. Tsuzaki, H. Miura and T. Sakai, "Effect of initial microstructures on grain refinmenet in stainless steel by large strain deformation," *Acta Materialia,* vol. 51, pp. 847-861, 2003.

[190] J. Fowler, M. Worswick, A. Pilkey and H. Nahme, "Damage Leading to Ductile Fracture under High Strain-Rate Conditions," *Metallurgical and Materials Transactions A,* vol. 31A, pp. 831-844, 2000.

[191] A. Grebe, H.-R. Pak and M. Meyers, "Adiabatic Shear Localization in Titanium and Ti-6 Pct Al-4 Pct V Alloy," *Metallurgical Transactions A,* vol. 16A, pp. 761-775, 1985.

[192] C. Mason and M. Worswick, "Adiabatic shear in annealed and shock-hardened iron and in quenched and tempered 4340 steel," *International Journal of Fracture III,* pp. 29-51, 2001.

[193] C. Duan, Y. Cai, M. Wang and G. Li, "Microstructural study of adiabatic shear bands formed in serrated chips during high-speed machining of hardened steel," *Journal of Material Science,* vol. 44, pp. 897-902, 2009.

[194] A. Odeshi, S. Al-ameeri, S. Mirfakhraei, F. Yazdani and M. Bassim, "Deformation and failure mechanism in AISI 4340 steel under ballistic impact," *Theoretical and Applied Fracture Mechanics,* vol. 45, pp. 18-24, 2006.

[195] N. Bourne, J. Millett and G. Gray III, "On the shock compression of polycrystalline metals," *Journal of Material Science,* vol. 44, pp. 3319-3343, 2009.

[196] C. Meyers Jr., "Strain-Hardening Effects in BCC, FCC, and HCP Metals Loaded at Very High Rates," *Journal of Materials Science,* vol. 4, pp. 1-9, 1969.

[197] X. Teng, T. Wierxbicki and H. Couque, "On the transition from adiabatic shear banding to fracture," *Mechanics of Mateirals,* vol. 39, pp. 107-125, 2007.

[198] M. El Wahabi, L. Gavard, F. Montheillet, J. Cabrera and J. Prado, "Effect of initial grain size on dynamic recrystallization in high purity austenitic stainless steels," *Acta Materialia,* vol. 53, pp. 4605-4612, 2005.

[199] C. Wittman, M. Meyers and H. Pak, "Observation of an Adiabatic Shear Band in AISI 4340 Steel by High-Voltage Transmission Electron Microscopy," *metallurgical Transactions A,* vol. 21A, pp. 707-716, 1990.

[200] M. Dolinski, D. Rittel and A. Dorogoy, "Modeling Adiabatic Shear Failure From Energy Considerations," *J. Mech. Phys. Solids,* 2010.

[201] D. Curran and L. Seaman, "Computational Models for Nucleation, Growth, and Coalescence of Adiabatic Shear Bands," *Journal de Physique,* vol. 46, pp. 395-401, 1985.

[202] G. Gray III, S. Chen, W. Wright and M. Lopez, "Consitutive Equations for Annealed Metals Under Compression at High Strian Rates and High Temperatures," Los Alamaos National Laboratory, 1994.

[203] D. Mohr, G. Gary and B. Lundberg, "Evaluation of stress-strain curve esitmates in dynamic experiments," *International Journal of Impact Engineering,* vol. 2010, pp. 161-169, 2010.

[204] A. Khan and R. Liang, "Behaviors of three BCC metal over a wide range of strain rates and temperatures: experiments and modeling," *International Journal of Plasticity,* vol. 15, pp. 1089-1109, 1999.

[205] A. Gilat and C.-S. Cheng, "Modleing torsional split Hopkinson bar tests at strain rates above 10,000 s-1," *International Jounral of Plasticity,* vol. 18, pp. 787-799, 2002.

[206] A. Molinari and G. Ravichandran, "Constitutive modeling of high-strain-rate deformation in metals based on the evolution of an effective microstructural length," *Mechanics of Materials*, vol. 37, pp. 737-752, 2005.

[207] S. Ghosh, K. Lee and S. Moorthy, "Two scale analysis of heterogeneous elastic-plastic materials with asymptotic homogenization and Voronoi cell finite element model," *Comput. Methods Appl. Mech. Engrg.* , vol. 132, pp. 63-116, 1996.

[208] Z. Zheng, J. Yu and J. Li, "Dynamic crushing of 2D cellular structures: A finite element study," *International Journal of Impact Engineering,* vol. 32, pp. 650-664, 2005.

[209] J. Klepaczko, "Plastic shearing at high and very high strain rates," *Journal De Physique IV,* pp. 35-40, 1994.

[210] J. Lins, H. Sandim, H.-J. Kestenbach, D. Raabe and K. Vecchio, "A microstructural investivation of adiabatic shear bands in an interstitial free steel," *Material Scince and Engineering A,* vol. 457, pp. 205-218, 2007.

[211] M. Fermen-Coker, "Numerical Simulation of Adiabatic Shear Bands in Ti-6Al-4V Alloy due to Fragment Impact," U.S. Army Research Laboratory Aberdeen Proving Ground, MD, 2004.

[212] Z. Basinski, "Thermally activated glide in face-centered cubic metals and its application to the theory of strain hardening," *Philosophical Magazine,* vol. 4, pp. 393-432, 1959.

[213] *Split-Hopkinson Pressure Bar Apparatus: A Historic Mechanical Engineering Landmark,* Designation Ceremony, Southwest Research Institute. Texas: The American Society of Mechanical Engineers ASME, 2006.

[214] S. Gourdet and F. Montheillet, "A model of conitnuous dynamic recrystallization," *Acta Materialia,* vol. 51, no. 9, pp. 2685-2699, 2003.

[215] D. Smith, "Interaction of Dislocations with Grain Boundaries," *Journal de Physique,* vol. 43, no. 12, pp. 225-237, 1982.

[216] D. R. Askeland, P. P. Fulay and D. K. Bhattacharya, Essentials of Materials Science and Engineering, 2nd Edition, SI, Stamford, CT: Cengage Learning, 2010.

[217] D. H. Herring, "A Discussion of Retained Austenite," The Heat Treat Doctor, March 2005. [Online]. Available: http://www.heat-treat-doctor.com/documents/RetainedAustenite.pdf. [Accessed 1 May 2014].

[218] M. Durand-Charre, Microstructure of Steels and Cast Irons, Springer, 2004.

[219] D. Lesuer, C. Syn and O. Sherby, "Nano-subgrain Strengthening in Ball-milled Iron," *Materials Science and Engineering A,* 2006.

[220] T. Massalski, Binary Alloy Phase Diagrams, 2nd Edition, Vol. 1, 1990.

[221] H. Bhadeshia, "Interpretation of the Microstructure of Steels," Postech Graduate Institute of Ferrous Technology (GIFT), [Online]. Available: http://cml.postech.ac.kr/2008/Steel_Microstructure/SM2.html. [Accessed May 2014].

[222] M. Umemoto, Y. Todaka and K. Tsuchiya, "Mechanical properties of cementite and fabiraction of artificial pearlite," *Materials Science Forum,* Vols. 426-432, pp. 859-864, 2003.

[223] Suresh, *Ironmaking and Steelmaking,* vol. 30, pp. 379-384, 2003.

[224] "Key to Metals, Structure of Plain Steel," September 2000. [Online]. Available: http://www.keytometals.com/page.aspx?ID=CheckArticle&site=kts&NM=3. [Accessed 1 May 2014].

[225] E. Davenport and E. Bain, *Trans. AIME,* vol. 90, pp. 117-154, 1930.

[226] "Key to Metals, The Tempering of Martensite: Part One," 2010. [Online]. Available: http://steel.keytometals.com/Articles/Art127.htm. [Accessed May 2014].

[227] R. von Mises, "Mechanik der festen Körper im plastisch deformablen Zustand," *Göttin, Nachr. Math. Phys,* vol. 1, pp. 582-592, 1913.

[228] G. Johnson and T. Holmquist, "A computational constitutive model for brittle materials subjected to large strains," in *Shock-wave and High Strain-rate Phenomena in Materials*, M. Meyers, L. Murr and K. Staudhammer, Eds., New York, Marcel Dekker Inc., 1992, pp. 1075-1081.

[229] G. Johnson and T. Holmquist, "An improved computational consitutive model for brittle materials," *High-Pressure Science and Technology, American Institute of Physics,* 1994.

[230] C. Jiang, S. Srinivasan, A. Caro and S. Maloy, "Structural, elastic and electronic properties of Fe_3C from first-principles," Cornell University.

[231] "Modern Steels and Their Properties," in *Handbook 2757, 7th Ed.*, Bethlehem Steel Corporation, 1972.

[232] R. Deniz and R. Yildirim, "Ballistic Penetration of Hardnened Steel Plates," in *27th International Symposium on Ballistics*, Freiburg, Germany, 2013.

[233] D. Fitzgibbon, "Semiannual Report on Pressure Vessel Design Criteria," Space Techology Laboratories, Air Force Ballistic Missile Division, 1959.

[234] A. Medved and A. Bryukhanov, "The variation of Young's modulus and the hardness with tempering of some quenched chromium steels," *Metal Science and Heat Treatment,* vol. 11, no. 9, pp. 706-708, 1969.

[235] I. A. C. Tkalcec, S. Crevoiserat and D. Mari, "Tempering effects on a mrtensitic high carbon steel," *Materials Science and Engineering A,* Vols. 387-389, pp. 352-356, 2004.

[236] Wilson, "Wilson Hardness ASTM Conversion Chart," 2011. [Online]. Available: http://www.wilson-hardness.com/Resources/WallChartRequest.aspx. [Accessed 2014].

[237] M. Wisti and M. Hingwe, "Tempering of Steel," in *ASM Handbook - Heat Treating*, J. Davis, G. Davidson, S. Lampman, T. Zorc, J. Daquila and A. Ronke, Eds., Materials Park, OH, OH: ASM International, 1991, pp. 121-36.

[238] J. Nelson, "The use of wetting agents in metallographic etchants," *Praktische Metallographie,* vol. 4, pp. 192-198, 1967.